# Measuring cosmological weak lensing using the Advanced Camera for Surveys on board the Hubble Space Telescope

DISSERTATION

zur
Erlangung des Doktorgrades (Dr. rer. nat)
der
Mathematisch–Naturwissenschaftlichen Fakultät
der
Rheinischen Friedrich–Wilhelms–Universität Bonn

vorgelegt von

TIM RICHARD WALTER SCHRABBACK–KRAHE
GEB. SCHRABBACK
aus
Bad Ems

Bonn, 2007

Angefertigt mit Genehmigung der Mathematisch–Naturwissenschaftlichen Fakultät der Rheinischen Friedrich–Wilhelms–Universität Bonn

1. Referent: Prof. Dr. Peter Schneider (Universität Bonn)

2. Referent: Prof. Dr. Yannick Mellier (Institut d'Astrophysique de Paris)

Tag der Promotion: 15. Februar 2008

Diese Dissertation ist auf dem Hochschulschriftenserver der ULB Bonn
http://hss.ulb.uni-bonn.de/diss_online elektronisch publiziert.

Erscheinungsjahr: 2008

# Contents

# Summary

During the last eight years cosmological weak lensing, the gravitational lensing effect caused by the inhomogeneous large-scale matter distribution, developed into a powerful probe of cosmology. By studying the distortions which are imprinted onto the observed shapes of distant galaxies, the power spectrum of matter fluctuations can be constrained free of assumptions on the relation between luminous and dark matter. However, due to the weakness of the effect it is challenging to measure and can only be detected statistically from an ensemble of coherently lensed background galaxies. In addition, a careful correction for systematic effects is indispensable, first of all for the image point-spread-function (PSF).

In this PhD thesis I present a detailed cosmological weak lensing analysis using deep observations from the Advanced Camera for Surveys (ACS) on board the Hubble Space Telescope (HST). Including data from the ACS Parallel Cosmic Shear Survey, the HST/GEMS Survey, and the HST/COSMOS Survey, this data set constitutes the largest survey used to measure cosmological weak lensing from space today. Space-based weak lensing studies are not affected by Earth's atmosphere, whose blurring effect ("seeing") strongly limits the number density of sufficiently resolved galaxies in ground-based surveys. The higher number density obtained from space helps to locally beat down the shape noise induced by the intrinsic ellipticities of the source galaxies. This is particularly important in order to constrain the small-scale power spectrum and reconstruct the projected matter distribution.

Before being able to use the ACS data for weak lensing studies, it was necessary to develop several technical tools and carefully test our weak lensing pipeline: Firstly, we developed an image reduction pipeline for ACS data, which fulfils the strict requirements weak lensing places on the data quality, e.g. regarding careful image registration and bad pixel masking. This pipeline has also been used in several independent studies. Secondly, the detection of strong temporal variations of the ACS PSF, which are interpreted as focus changes due to thermal breathing of the telescope, led to the development of a new PSF correction scheme. Classically, PSF variations across the field-of-view are modelled by interpolating measured stellar shape parameters using polynomial functions. However, due to the small field-of-view of ACS ($3\farcm3 \times 3\farcm3$), high galactic latitude fields contain only of order 10 stars, which are too few for a direct interpolation. In our correction scheme we fit the stars present in a galaxy field with PSF models derived from dense stellar fields. We determine the correction on the basis of single exposures in order to obtain an optimal time-dependence of the solution and exclude noise in the ellipticity measurement caused by resampling. Using a principal component analysis we verify that most of the PSF variation indeed occurs in a one-dimensional parameter space, which can be related to the focus position.

We estimate that our PSF correction scheme reduces the systematic contribution to the shear correlation functions due to PSF distortions to $< 2 \times 10^{-6}$ for galaxy fields containing at least 10 stars. This corresponds to $\lesssim 5\%$ of the cosmological signal expected on scales of a single ACS field. Thirdly, we carefully tested our weak lensing pipeline using simulated images from the Shear TEsting Programme[1] (STEP), which have been analysed by several independent groups in blind tests. After eliminating biases identified in the first round of simulations (Heymans et al. 2006b), our pipeline performed among the most accurate methods with an average (relative) shear recovery accuracy of $\sim 2\%$ on the second simulation set (Massey et al. 2007a). As the only method we achieve the same average accuracy for the third set of STEP simulations (Rhodes et al. in prep.), which features space-based weak lensing data, partially with ACS-like properties. In this test our pipeline also yields a good correction as a function of galaxy size and magnitude ($\sim \pm 5\%$ variation), which is important if one aims at measuring the shear signal as a function of source redshift. Concluding from STEP, the systematic accuracy of our pipeline should be well within the statistical noise of the ACS weak lensing data.

The analysis of the ACS data was done in two steps: We first present results from a pilot study published in Schrabback et al. (2007), in which we test the capabilities of ACS for cosmological weak lensing measurements with early parallel observations and the combined GEMS and GOODS ACS mosaic of the *Chandra* Deep Field South (CDFS). We perform a number of diagnostic tests indicating that the remaining level of systematics is consistent with zero for the GEMS and GOODS data confirming the success of our PSF correction scheme. For the parallel data we detect a low level of remaining systematics which we interpret to be caused by a lack of sufficient dithering of the data. Combining our shear estimate of the GEMS and GOODS observations using 96 galaxies arcmin$^{-2}$ with the photometric redshift catalogue of the GOODS-MUSIC sample, we determine a *local single field estimate* for the mass power spectrum normalisation $\sigma_8 = 0.59^{+0.13}_{-0.17}\,(\mathrm{stat}) \pm 0.07\,(\mathrm{sys})$ (68% confidence assuming Gaussian sampling variance) at a fixed matter density $\Omega_\mathrm{m} = 0.24$ for a $\Lambda$CDM cosmology, where we marginalise over the uncertainty of the Hubble constant and the redshift distribution. This estimate agrees only marginally with the WMAP-3 result of $\sigma_8 = 0.761^{+0.049}_{-0.048}$ (Spergel et al. 2007) and is significantly below values found by recent ground-based surveys (e.g. Benjamin et al. 2007). From this discrepancy we conclude that the CDFS is subject to strong sampling variance with a significant under-density of compact foreground structures. This is consistent with a recent study by Phleps et al. (2007), who find a strong deficiency of red galaxies in this field.

As a second step we present a preliminary cosmological weak lensing analysis of the HST/COSMOS Survey. With 1.64 deg$^2$ its sky area is approximately seven times larger than GEMS. The significantly increased statistical accuracy revealed previously undetectable residual systematic errors indicated by a significant B-mode signal. So far we have not been able to unambiguously identify its origin, but note that similar indications for remaining systematics have been found in an independent analysis of the same data by Massey et al. (2007c). Using only B-mode-free scales ($> 1'$ in the shear two-point correlation function), we find $\sigma_8 = 0.71 \pm 0.09$ (68% confidence) from COSMOS for fixed $\Omega_\mathrm{m} = 0.24$, where the error includes the uncertainties in the redshift distribution, the Hubble constant, and the shear calibration, as well as a Gaussian

[1] `http://www.physics.ubc.ca/~heymans/step.html`

estimate for sampling variance. This result is in excellent agreement with the WMAP-3 constraints, but is significantly below the estimates found by Massey et al. (2007c). Due to the presence of remaining systematics our COSMOS analysis is still preliminary, leaving room for further development in the time after the PhD project.

In addition to the cosmological weak lensing analysis we present a projected mass map for the COSMOS field, as well as first results from a weak lensing analysis of the HST/STAGES Survey targeting the galaxy super-cluster Abell 901/902. Furthermore, I briefly summarise ACS studies of galaxy clusters led by some of my collaborators, which make use of the developed data reduction and weak lensing pipeline.

# Chapter 1

# Introduction

Cosmology is currently experiencing a dramatic transition: Although being based on solid theory, many observational constraints used to be weak until large surveys and new probes were launched in the late 1990s. The dawn of precision cosmology can probably be pinpointed to the year 2003, when the first-year results of the *Wilkinson Microwave Anisotropy Probe* (WMAP) were published measuring the anisotropies of the Cosmic Microwave Background (CMB) with unprecedented accuracy (Bennett et al. 2003). These measurements of the early Universe are particularly powerful when combined with constraints from the local (present day) Universe, lifting degeneracies between different cosmological parameters. Tight constraints were found in combination with the *2 degree Field Galaxy Redshift Survey* (2dFGRS) or the *Sloan Digital Sky Survey* (SDSS), which investigate the large-scale distribution of galaxies in the relatively nearby Universe (Spergel et al. 2003; Tegmark et al. 2004b). The recently published three-years results of WMAP (WMAP-3) tighten the parameter constraints further (Spergel et al. 2007) leading to the current standard model of cosmology, where the spatial geometry of the Universe is close to Euclidean (flat) with a total energy content consisting of 4% normal matter (baryons) and 20% non-baryonic dark matter. The remaining 76% consist of a field or substance named dark energy, which is responsible for the observed accelerated expansion of the Universe.

Although this relative distribution can be measured with good accuracy, we are still lacking physical understanding for the Universe's dominant constituents: Not interacting electromagnetically, dark matter can only be detected via its gravitational influence on nearby luminous matter or its distortion of the surrounding space-time metric. The latter is measurable through the effect of gravitational lensing, which describes the deflection and distortion of light bundles emitted from distant objects in the gravitational potential of foreground structures. Therefore, it provides a way to constrain the projected foreground mass using well understood physics without any assumptions on the relation between luminous and dark matter. Gravitational lensing has already provided substantial contributions to our understanding of dark matter, showing for example that dark matter is well-traced by luminous matter on large scales (see e.g. Massey et al. 2007c). Another important finding was the observation of dark matter separated from the major baryonic mass component in the special environment of the merging "Bullet" galaxy cluster (Clowe et al. 2006; Bradač et al. 2006), which was announced as the first "direct" proof for the existence of dark matter also yielding constraints on the cross-section for dark matter

self-interaction (Randall et al. 2007). Affirmed by these and further findings nowadays most cosmologists and physicists have a rather clear expectation of dark matter consisting of one or more types of elementary particles, which might be detected directly in upcoming particle physics experiments.

On the other hand fundamental physics is currently unable to provide any convincing explanation for dark energy: In order to allow for stationary cosmological models, it was first introduced by Einstein as the special case of a *cosmological constant* in the field equations of General Relativity. Yet, it was dropped after Hubble discovered the expansion of the Universe in 1929. 70 years later measurements of the expansion history using supernovae of type Ia as standard candles provided first convincing evidence that this expansion is in fact accelerating (Riess et al. 1998; Perlmutter et al. 1999), bringing the cosmological constant back into the discussion. However, the only natural explanation coming from quantum physics, which interprets dark energy as ground-state energy of the vacuum, yields an estimate for its energy density which is too large by a factor of $\sim 10^{120}$, indicating that our theories of fundamental physics and gravity are either incorrect or incomplete. Due to this extremely low density, dark energy properties can never be observed in particle physics experiments, but only by studying the expansion history and structure growth in the Universe. It is this potential for new physics which has strongly boosted the interest in observational cosmology, and has led to the planning and conduction of new and ambitious surveys over the next $\sim$ 12 years. One of the key questions is whether the equation-of-state parameter $w$, the ratio of pressure and density of dark energy is truly $-1$, as would be the case for a cosmological constant, or if it differs from this value, with a possible time dependence. Using WMAP-3 in combination with SDSS data and results from the Supernova Legacy Survey (SNLS), Spergel et al. (2007) are able to place the currently best constraints on the equation-of-state parameter $w = -1.08 \pm 0.12$, assuming it to be constant.

The Dark Energy Task Force (DETF, Albrecht et al. 2006) and the ESA-ESO Working Group on Fundamental Cosmology (Peacock et al. 2006) compare different techniques concerning their prospects to constrain and study the evolution of dark energy arriving at consistent conclusions: It will be necessary to combine the precise measurements of the CMB soon provided by the PLANCK satellite with probes of the expansion history and structure growth at lower redshifts. The DETF identifies the four major probes: baryonic acoustic oscillations, galaxy cluster surveys, supernova surveys, and weak gravitational lensing surveys as being most promising for this task, with the distinction that weak lensing surveys will potentially be able to yield the tightest constraints, if systematic errors prove to be well enough controllable.

In the weak lensing regime gravitational shear distortions are small and can only be measured statistically from a large ensemble of background source galaxies. This is relevant in the outer regions of galaxy clusters and, in particular, for gravitational lensing of the large-scale-structure itself, which is also termed “cosmic shear” or “cosmological weak lensing”. Measuring the latter provides a powerful tool to constrain the power spectrum of the total matter density field. If the source population can accurately be split into redshift bins, the change of the shear signal with redshift additionally yields constraints on the power spectrum evolution which depends on the evolution of dark energy properties. Due to the weakness of cosmological shear it is, however, challenging to measure, with the first detections only reported seven years ago (Bacon et al. 2000; Kaiser et al. 2000; Van Waerbeke et al. 2000; Wittman et al. 2000). Since then cosmic shear has

developed into a flourishing field of cosmology, where growing surveys and better corrections for systematic effects do not only yield constraints on the matter content $\Omega_m$ and the normalisation of the power spectrum $\sigma_8$ (Maoli et al. 2001; Van Waerbeke et al. 2001, 2002, 2005; Hoekstra et al. 2002a; Refregier et al. 2002; Bacon et al. 2003; Brown et al. 2003; Jarvis et al. 2003; Hamana et al. 2003; Heymans et al. 2004, 2005; Rhodes et al. 2004; Massey et al. 2005; Hetterscheidt et al. 2007; Massey et al. 2007c; Schrabback et al. 2007; Benjamin et al. 2007) but recently also on the dark energy equation of state parameter $w$ (Jarvis et al. 2006; Hoekstra et al. 2006; Semboloni et al. 2006; Kitching et al. 2007).

Given that the typical cosmic shear signal-to-noise ratio per background galaxy is only of order $1/30$, a proper correction for systematic effects is indispensable, first of all for the image point-spread-function (PSF). The PSF dilutes the shear signal by isotropic blurring and creates spurious signal due to anisotropy, which can easily exceed the cosmological signal. This is particularly important in view of the next generation of cosmic shear surveys, which will provide the statistical power to measure cosmological shear with percent and sub-percent level accuracy aiming at precision measurements of dark energy properties. This will only be possible if the methods used to extract the shear signal by measuring galaxy shapes have a comparable systematic accuracy. In order to assess the accuracy of existing methods and to provide a platform for further development the Shear TEsting Programme[1] (STEP) was launched in 2004, with first results published by Heymans et al. (2006b) and Massey et al. (2007a). So far blind analyses of simulated images containing a hidden shear signal were conducted. From these we conclude that several shape measurement techniques already reach a systematic accuracy of a few percent, which is sufficient for current studies, but substantial development is still required for upcoming surveys.

Both the majority of the previous cosmic shear measurements were, and most of the planned surveys will be, conducted using ground-based wide-field imaging data. Ground-based data are however strongly affected by the variable conditions of Earth's atmosphere, where image blurring due to atmospheric turbulence (seeing) erases the shape information of small galaxies. Alternative concepts for future space-based wide-field imaging missions such as DUNE[2] or SNAP[3] are currently being proposed to funding agencies. These would provide shear information without the disturbing influence of the atmosphere, which would be enormously helpful concerning the high systematic accuracy sought when targeting dark energy. In addition, the resolution of space-based imaging provides a substantially higher number density of usable background galaxies, which is important both for measurements of the small-scale power spectrum and for dark matter mapping. Space missions can furthermore provide deep infrared imaging, which is very valuable for an accurate estimate of the source redshift distribution via the technique of photometric redshifts.

In order to prepare for this future generation of space-based surveys it is not only important to improve and develop shape measurement methods, but also to test existing methods on currently available data, in order to better assess the feasibility and identify possible obstacles.

[1] http://www.physics.ubc.ca/~heymans/step.html
[2] http://dune-mission.net/
[3] http://snap.lbl.gov/

The only currently available space telescope useful for weak lensing measurements is the *Hubble Space Telescope* (HST). Cosmic shear studies have already been carried out with the HST cameras WFPC2 (Rhodes et al. 2001; Refregier et al. 2002; Casertano et al. 2003) and STIS (Hämmerle et al. 2002; Rhodes et al. 2004; Miralles et al. 2005). With the installation of the *Advanced Camera for Surveys* (ACS) *Wide-Field Channel* (WFC) detector in March 2002, a camera combining improved sensitivity (48% total throughput at 660 nm) and a relatively large field-of-view ($\sim 3\farcm3 \times 3\farcm3$) with good sampling ($0\farcs05$ per pixel) became available. This unique tool for weak lensing measurements at small angular scales has already provided exceptional results for the study of galaxy clusters (Jee et al. 2005a,b, 2006, 2007; Lombardi et al. 2005; Clowe et al. 2006; Bradač et al. 2006; Leonard et al. 2007) and galaxy-galaxy lensing (Heymans et al. 2006a; Gavazzi et al. 2007).

In this thesis project I have now conducted a cosmological weak lensing analysis using images from the ACS archive, which provides the largest available dataset for space-based cosmic shear measurements. With a total area of approximately two square degrees this dataset is smaller than most current ground-based surveys, but the substantially higher number density of background sources provides the capability for competitive constraints on the small scale power spectrum. In addition, the analysis of the ACS archive provides a pathfinder role for future space-based surveys. During the course of this project independent analyses of two subsets of these data have been published, the GEMS (Heymans et al. 2005) and COSMOS (Massey et al. 2007c) surveys, allowing for independent tests of the different analysis pipelines.

A large fraction of the data in the ACS archive is provided with rudimental calibration only. On the other hand weak lensing places very high demands on data quality. Therefore a major aspect of this work was the development of a sophisticated data reduction pipeline for ACS, which additionally has been used in several other projects. Besides the work on ACS data, a large portion of the thesis project has been devoted to the testing and improvement of the applied shape measurement method within the STEP project.

This manuscript is organised as follows: I will first summarise the theoretical background on cosmology and structure formation in Chapter 2, followed by an introduction to gravitational lensing in Chapter 3. Chapter 4 will be devoted to shape measurement tests conducted within the STEP project. I will detail on the instrument, data, and data reduction in Chapter 5. The cosmic shear analysis is divided into a pilot study conducted with early data from the *ACS Parallel Survey* and the *GEMS Survey*, as described in Chapter 6, and a preliminary analysis of the ACS COSMOS data presented in Chapter 7. I will briefly summarise further projects which make use of our ACS pipeline in Chapter 8 and finally conclude in Chapter 9.

# Chapter 2

# Cosmology and structure formation

In this Chapter I will summarise aspects of cosmology and structure formation, which are relevant for the understanding of this thesis. In the first Section I will give a brief introduction to standard cosmology, which describes the evolution of the Universe as a whole, assuming that it is homogenous and isotropic. I will then proceed with the theory of structure formation describing the evolution of density inhomogeneities in Section 2.2. Both theories are presented in-depth for example in the extensive monograph by Peacock (1999). A detailed description, particularly of structure formation, is also given by Dodelson (2003). The chapter will be completed with a summary of different probes for cosmological parameter estimation in Section 2.3.

## 2.1 Cosmology

In the *Theory of General Relativity* Einstein (1916) describes the Universe by a four dimensional space-time, which is characterised by its metric tensor $g_{\alpha\beta}$. The geometry and the energy content of the Universe are interrelated by *Einstein's field equations*

$$G_{\alpha\beta} = -\frac{8\pi G}{c^2} T_{\alpha\beta} - \Lambda g_{\alpha\beta}\,, \tag{2.1}$$

where the *Einstein tensor* $G_{\alpha\beta}$ is a function of the metric and its first and second derivatives. $G$ and $c$ are the gravitational constant and the speed of light in vacuum. The energy-momentum tensor for the matter and radiation $T_{\alpha\beta}$ is that of an ideal fluid, which can be characterized by its density $\rho(\vec{x}, t)$ and pressure $p(\vec{x}, t)$. $\Lambda$ is a possible *cosmological constant*.

### 2.1.1 Homogeneous and isotropic world models

Although Einstein's field equations cannot be solved generally, solutions can easily be found if one imposes two strong constraints on their possible form, which are also referred to as the *cosmological principle*: It postulates that the matter distribution and motion is *isotropic* on sufficiently large scales as seen by a comoving observer, who participates in the cosmic expansion without any peculiar velocity, and that every comoving observer experiences the same history of

the Universe. The latter characteristic is also named *observer homogeneous*. While it is not a priori clear if these assumptions are really justified, observations show that the matter distribution and motion indeed appear to be isotropic on sufficiently large scales $\gtrsim 200$ Mpc (see Section 2.2). In the discussion we will thus follow the "standard" approach to examine the impact of a smoothed homogeneous density $\rho(t)$ and pressure $p(t)$ field on the space-time metric, which is justified by the argument that the Universe is much larger than this scale. However, note that this approach is currently questioned in the literature (e.g. Kolb et al. 2006; Wiltshire 2007).

Robertson (1935) and Walker (1936) showed independently that the most general form for a line element d$s$ fulfilling the cosmological principle is given by

$$\mathrm{d}s^2 = g_{\alpha\beta}\mathrm{d}x^\alpha \mathrm{d}x^\beta = c^2\mathrm{d}t^2 - a^2(t)\mathrm{d}r^2; \quad \mathrm{d}r^2 = \mathrm{d}\chi^2 + f_K^2(\chi)\left(\mathrm{d}\theta^2 + \sin^2\theta \mathrm{d}\Phi^2\right), \tag{2.2}$$

with the time $t$ measured by a comoving observer, the cosmic scale factor $a(t)$, and the comoving line element d$r$ of a three-dimensional space with constant curvature. This line element d$r$ depends on a radial coordinate $\chi$ and two angular coordinates $\Phi$ and $\theta$. Under the assumption that the Universe is homogeneous and isotropic, $K$ has to be uniform. Then $f_K(\chi)$ takes the form

$$f_K(\chi) = \begin{cases} \frac{1}{\sqrt{K}}\sin\left(\sqrt{K}\chi\right) & K > 0 \\ \chi & K = 0 \\ \frac{1}{\sqrt{-K}}\sinh\left(\sqrt{-K}\chi\right) & K < 0 \end{cases}. \tag{2.3}$$

Assuming homogeneity the scale factor $a$ may only depend on time $t$, and all distances in three-dimensional space scale directly with $a(t)$. With these constraints, (2.1) simplifies to the *Friedman equations*

$$\left(\frac{\dot{a}}{a}\right)^2 = \frac{8\pi G}{3}\rho - \frac{Kc^2}{a^2} + \frac{\Lambda}{3}, \tag{2.4}$$

and

$$\frac{\ddot{a}}{a} = -\frac{4\pi G}{3}\left(\rho + \frac{3p}{c^2}\right) + \frac{\Lambda}{3}, \tag{2.5}$$

which describe the evolution of the cosmic scale factor with time. The left-hand side of (2.4) is the square of the *Hubble parameter*

$$H(t) = \frac{\dot{a}(t)}{a(t)}. \tag{2.6}$$

Its value at the present epoch $t_0$ is the *Hubble constant* $H_0$, which interrelates the distances and apparent recession velocities of objects in the nearby Universe. Since the distance of a nearby object can be approximated by $D \approx a(t_0)\chi$, its apparent recession velocity is then given by

$$v = \dot{a}(t_0)\chi = \frac{\dot{a}(t_0)}{a(t_0)}D = H_0 D. \tag{2.7}$$

$H_0$ is of order $70\,\mathrm{km\,s^{-1}\,Mpc^{-1}}$ (see Sect. 2.3.1), where the uncertainty in its value is usually parameterised as $H_0 = 100\,h\,\mathrm{km\,s^{-1}\,Mpc^{-1}}$. The inverse of the Hubble constant is called *Hubble time* ${H_0}^{-1} \approx 10h^{-1}$ Gyr and would be equal to the age of the Universe if the expansion rate

would have been constant. The maximum distance a photon could have travelled during this time defines the *Hubble radius* $R_\mathrm{H} = c/H_0 \approx 3\,h^{-1}$ Gpc.

As detailed in Sect. 2.3.2, several independent probes confirm that the expansion of the Universe is currently accelerating with $\ddot{a} > 0$. With (2.5) this implies that either

1. The cosmological constant is indeed non-zero, or
2. A particle or field with negative pressure such that $\left(\rho + \frac{3p}{c^2}\right) < 0$ dominates the Universe, or
3. The underlying theory of General Relativity is wrong or incorrectly applied.

For the second case the unknown constituent has been named *dark energy*. We define the *equation-of-state parameter*

$$w = \frac{p}{c^2\rho}\,, \tag{2.8}$$

which must be smaller than $-1/3$ for dark energy. Combining the time-derivative of (2.4) with (2.5) yields

$$\dot{\rho} = -3H\left(\rho + \frac{p}{c^2}\right), \tag{2.9}$$

which holds for each contributor to the energy density separately. For constant $w$ we find

$$\dot{\rho} = \dot{a}\frac{\mathrm{d}\rho}{\mathrm{d}a} = -3\frac{\dot{a}}{a}(1+w)\rho\,, \tag{2.10}$$

so that $\mathrm{d}\rho/\mathrm{d}a = -3(1+w)(\rho/a)$ and

$$\rho = \rho_0 a^{-3(1+w)}\,, \tag{2.11}$$

where $\rho_0$ denotes the contributor's density today and we normalise the cosmic scale factor to today, $a(t_0) = 1$.

For non-relativistic matter, which is often called dust, $w$ is of order $(v/c)^2$, and can be ignored, whereas relativistic particles and radiation have significant pressure $p_\mathrm{r} = \rho_\mathrm{r}c^2/3$ yielding $w = +1/3$. From (2.11) follows the dependence of the dust, radiation, and dark energy density on the scale factor

$$\begin{aligned} \rho_\mathrm{m} &\propto a^{-3} \\ \rho_\mathrm{r} &\propto a^{-4} \\ \rho_\mathrm{X} &\propto a^{-3(1+w)}\,. \end{aligned} \tag{2.12}$$

For normalisation we define the *critical density*

$$\rho_\mathrm{cr} = \frac{3H_0^2}{8\pi G} \tag{2.13}$$

and the dimensionless parameters

$$\Omega_\mathrm{m} = \frac{\rho_\mathrm{m}}{\rho_\mathrm{cr}},\ \Omega_\mathrm{r} = \frac{\rho_\mathrm{r}}{\rho_\mathrm{cr}},\quad \Omega_\mathrm{X} = \frac{\rho_\mathrm{X}}{\rho_\mathrm{cr}}\,. \tag{2.14}$$

Then (2.4) can be rewritten as

$$H^2(t) = H_0^2 \left[ \Omega_\mathrm{r} a(t)^{-4} + \Omega_\mathrm{m} a(t)^{-3} - \frac{Kc^2}{H_0^2} a(t)^{-2} + \Omega_\mathrm{X} a(t)^{-3(1+w)} \right] , \tag{2.15}$$

where the case of a cosmological constant instead of a dark energy field is absorbed in $\Omega_\mathrm{X}(w = -1) = \Omega_\Lambda = \Lambda/(3H_0^2)$. At present constraints on $w$ are rather weak and unable to distinguish from $w = -1$. To shorten the notation we will therefore use $\Omega_\Lambda$ instead of $\Omega_\mathrm{X}$ when $w = -1$ is implicitly assumed.

While $\Omega_\mathrm{m}$ and $\Omega_\Lambda$ are both of order unity (see Sect. 2.3.2), $\Omega_\mathrm{r} \approx 10^{-5}$ can be neglected at the present epoch[1]. Radiation played an important role only in much earlier phases of the Universe. For the rest of the chapter we will therefore neglect $\Omega_\mathrm{r}$. The geometry of the Universe depends on the total sum of the density parameters:

$$\Omega_\mathrm{tot} = \Omega_\mathrm{m} + \Omega_\mathrm{X} . \tag{2.16}$$

If we insert $t = t_0$, the curvature today follows from (2.15)

$$K = \left( \frac{H_0}{c} \right)^2 (\Omega_\mathrm{m} + \Omega_\mathrm{X} - 1) = \left( \frac{H_0}{c} \right)^2 (\Omega_\mathrm{tot} - 1) . \tag{2.17}$$

The different signs that $K$ can have correspond to different geometries of the Universe:

$$\begin{aligned} \Omega_\mathrm{tot} < 1 \quad &\Longleftrightarrow \quad K < 0 \quad \text{open universe} , \\ \Omega_\mathrm{tot} = 1 \quad &\Longleftrightarrow \quad K = 0 \quad \text{flat universe} , \\ \Omega_\mathrm{tot} > 1 \quad &\Longleftrightarrow \quad K > 0 \quad \text{closed universe} . \end{aligned} \tag{2.18}$$

The special case of a flat universe with $\Omega_\mathrm{m} = 1$ and $\Omega_\mathrm{X} = 0$ is called *Einstein–de Sitter* (EdS) universe. Eliminating $K$ in (2.15) by inserting (2.17) leads to

$$H^2(t) = H_0^2 \left[ \Omega_\mathrm{m} a(t)^{-3} + (1 - \Omega_\mathrm{m} - \Omega_\mathrm{X}) a(t)^{-2} + \Omega_\mathrm{X} a(t)^{-3(1+w)} \right] . \tag{2.19}$$

For the case of a time-dependent $w$ the dark energy dependence on the scale factor can be generalised as

$$a(t)^{-3(1+w)} \longrightarrow \exp\left( 3 \int_a^1 \frac{\mathrm{d}a'}{a'} [1 + w(a')] \right) . \tag{2.20}$$

### 2.1.2 Redshift and distances

Due to the expansion of space-time photons are redshifted on their way through the Universe. The *redshift* of a source is defined as

$$z \equiv \frac{\lambda_\mathrm{obs} - \lambda_\mathrm{em}}{\lambda_\mathrm{em}} , \tag{2.21}$$

[1] The dominant contribution to $\Omega_\mathrm{r}$ at the present time comes from the photons of the Cosmic Microwave Background (see Section 2.1.3) with $\Omega_\mathrm{CMB} \approx 2.4 \times 10^{-5} h^{-2}$.

with the emitted wavelength $\lambda_{\rm em}$ and observed wavelength $\lambda_{\rm obs}$ of a photon travelling from the source to the observer. Redshift and scale factor are directly related by

$$1 + z = \frac{a(t_0)}{a(t_{\rm em})} = \frac{1}{a(t_{\rm em})} \,. \tag{2.22}$$

Different measurement prescriptions for distances exist, yielding the same results in static Euclidian space, as was tacitly assumed in (2.7). However, they can give different results in an expanding or curved space-time. Thus one clearly has to define which measurement prescription is applied, if distances are used in cosmology.

Most important for this thesis is the *angular diameter distance* relating the cross-section $\delta A$ of an object to the solid angle $\delta\Omega$ under which it appears

$$D_{\rm ang} = \left(\frac{\delta A}{\delta\Omega}\right)^{1/2} \,. \tag{2.23}$$

It is defined such that the relation between the physical separation $X$ of two light rays and the angle $\theta$ between them, remains valid also in curved space-time:

$$D_{\rm ang} = \frac{X}{\theta} \,. \tag{2.24}$$

Thus it is the appropriate distance definition for gravitational lensing theory (see Section 3.1). The angular diameter distance between an objects at redshift $z_2$ and an observer at redshift $z_1$ is given by

$$D_{\rm ang}(z_1, z_2) = a(z_2)\, f_K\left[\chi(z_2) - \chi(z_1)\right] \,, \tag{2.25}$$

which can be expressed in terms of the density parameters as

$$D_{\rm ang}(z_1, z_2) = \frac{1}{1+z_2}\, f_K\left[\frac{c}{H_0}\int_{z_1}^{z_2} \frac{{\rm d}z'}{\sqrt{(1-\Omega_{\rm m}-\Omega_{\rm X})\,(1+z')^2 + \Omega_{\rm m}\,(1+z')^3 + \Omega_{\rm X}\,(1+z')^{3(1+w)}}}\right] . \tag{2.26}$$

In the special case of an EdS universe (2.26) can be integrated to

$$D_{\rm ang}(z_1, z_2) = \frac{2c}{H_0(1+z_2)}\left((1+z_1)^{-1/2} - (1+z_2)^{-1/2}\right) . \tag{2.27}$$

The *luminosity distance* is defined via the ratio between the luminosity $L$ of a source at redshift $z_2$ and the flux $S$ measured by an observer at redshift $z_1$

$$D_{\rm lum} = \sqrt{\frac{L}{4\pi S}} \,, \tag{2.28}$$

which is related to the angular diameter distance as

$$D_{\rm lum}(z_1, z_2) = \left(\frac{1+z_2}{1+z_1}\right)^2 D_{\rm ang}(z_1, z_2) \,. \tag{2.29}$$

The extent of structures in the Universe at different redshifts is usually compared in terms of the *comoving distance*. This distance scale expands together with the Universe and is defined on the spatial hypersurface $t = t_0$ between the world lines of the source and the observer. With $a(t_0) = 1$ it is directly given by $\Delta D_{\rm com} = \Delta\chi$. From the metric (2.2) follows $c\,{\rm d}t = -a\,{\rm d}\chi$, because light rays propagate with ${\rm d}s = 0$. By inserting (2.19) into ${\rm d}D_{\rm com} = -a^{-1}\,c\,{\rm d}t = -c\,{\rm d}a\,(\dot{a}\,a)^{-1} = -c\,{\rm d}a\,(a^2\,H)^{-1}$ we find that the comoving distance between a source at $z_2$ and an observer at $z_1$ is given by

$$D_{\rm com}(z_1, z_2) = \frac{c}{H_0}\int_{a(z_1)}^{a(z_2)} \left[\Omega_{\rm m} a' + (1 - \Omega_{\rm m} - \Omega_{\rm X})a'^2 + \Omega_{\rm X} a'^{1-3w}\right]^{-1/2} {\rm d}a' \,. \tag{2.30}$$

### 2.1.3 The Cosmic Microwave Background

With the Universe expanding today, the cosmic scale factor must haven been smaller in the past, with higher photon energies due to redshifting. This leads to the conclusion that the Universe originated from a dense and hot state with much higher particle interaction rates than today. At early times photons and electromagnetically interacting particles were in thermal equilibrium, with photon energies described by the Planck distribution. Once electrons and protons combined to create neutral hydrogen, and photon energies became too low to ionise the hydrogen atoms again, the cross-section for photon-particle interactions dropped strongly. After passing this *last scattering surface*, the photons travelled almost freely through the expanding Universe, continuously being redshifted. It can be shown that photon energies described by a Planck distribution at an initial time $t_i$, still follow a Planck distribution after being redshifted with the new temperature

$$T(t) = T(t_i)\frac{a(t_i)}{a(t)} \,. \tag{2.31}$$

In the present Universe this radiation can be observed as the *Cosmic Microwave Background Radiation* (CMB), which was first detected by Penzias & Wilson (1965). The absolute temperature of the CMB was measured very precisely by the *Cosmic Background Explorer* (COBE) to be $T(t_0) = 2.728 \pm 0.004$K (Fixsen et al. 1996). Comparing the temperature in different directions, fluctuations of the order $\frac{\Delta T}{T} \lesssim 10^{-5}$ have been detected by many different experiments. The currently most precise all-sky map of the CMB fluctuations was measured by the *Wilkinson Microwave Anisotropy Probe* (WMAP, Bennett et al. 2003), see Fig. 2.1. The analysis of the WMAP data yielded unprecedented constraints on numerous cosmological parameters (see Sect. 2.3), including the redshift of photon-baryon decoupling $z_{\rm dec} = 1088^{+1}_{-2}$, which corresponds to the peak in the photon visibility function. The FWHM of the visibility function can be used to define the effective thickness of the decoupling surface $\Delta z_{\rm dec} = 194 \pm 2$ (Spergel et al. 2003).

## 2.2 Structure formation

In Section 2.1 we assumed that the Universe is isotropic and homogeneous. This assumption is obviously wrong on scales of our ordinary lives. Also in stars, galaxies, and galaxy clusters the

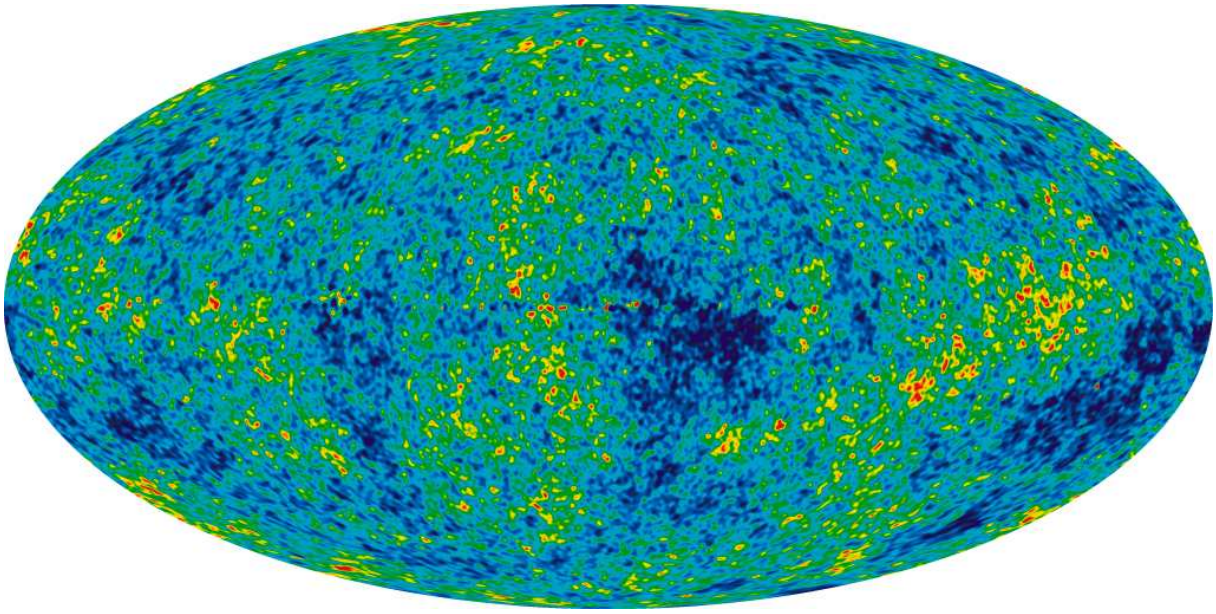

Figure 2.1: All-sky map of the temperature fluctuations in the Cosmic Microwave Background as measured by the WMAP satellite with 13′ FWHM resolution (WMAP-3). In this plot a linear scale is used ranging from $-200\mu$K (dark blue) to $+200\mu$K (red) deviation from the average temperature. For this map, measurements in five different frequency bands have been combined in order to subtract foreground contaminations. Note that there is a chance alignment of a particularly warm feature and a cool feature near the Galactic plane. Figure from http://map.gsfc.nasa.gov. Credit: NASA/WMAP Science Team.

matter distribution is very concentrated and thus inhomogeneous. Observations of the large-scale distribution of galaxies, like the *2dF Galaxy Redshift Survey* (2dFGRS) or the *Sloan Digital Sky Survey* (SDSS), show that galaxies are located preferentially along *filaments*, which are separated by almost empty regions called *voids* (see Fig. 2.2). At the intersections of filaments one often finds galaxy clusters. Together with the underlying dark matter distribution, the large-scale galaxy distribution is termed *large-scale-structure*. Smoothed over regions of approximately $200\,h^{-1}$Mpc, the matter distribution appears to be largely homogeneous, justifying the use of the mean density $\rho(t)$ in the Friedman equations.

A useful quantity to describe the growth of structures is the *density contrast*

$$\delta(\vec{r},t) = \frac{\rho(\vec{r},t) - \overline{\rho}(t)}{\overline{\rho}(t)}\,, \tag{2.32}$$

which is defined as the relative deviation of the density $\rho(\vec{r},t)$ from the average density $\overline{\rho}(t) = \overline{\rho}(t_0)/a^3$, and is always $\geq -1$ given that $\rho \geq 0$. As the CMB temperature fluctuations are of order $\Delta T/T \sim 10^{-5}$, we also expect that $|\delta| \ll 1$ at $z \sim 1100$. On the hand massive galaxy clusters in the present Universe have $\delta \gtrsim 200$ in their central $\sim 1.5$ Mpc. The growth of these inhomogeneities is driven by gravitational instability: while the dynamic of cosmic Hubble expansion is controlled

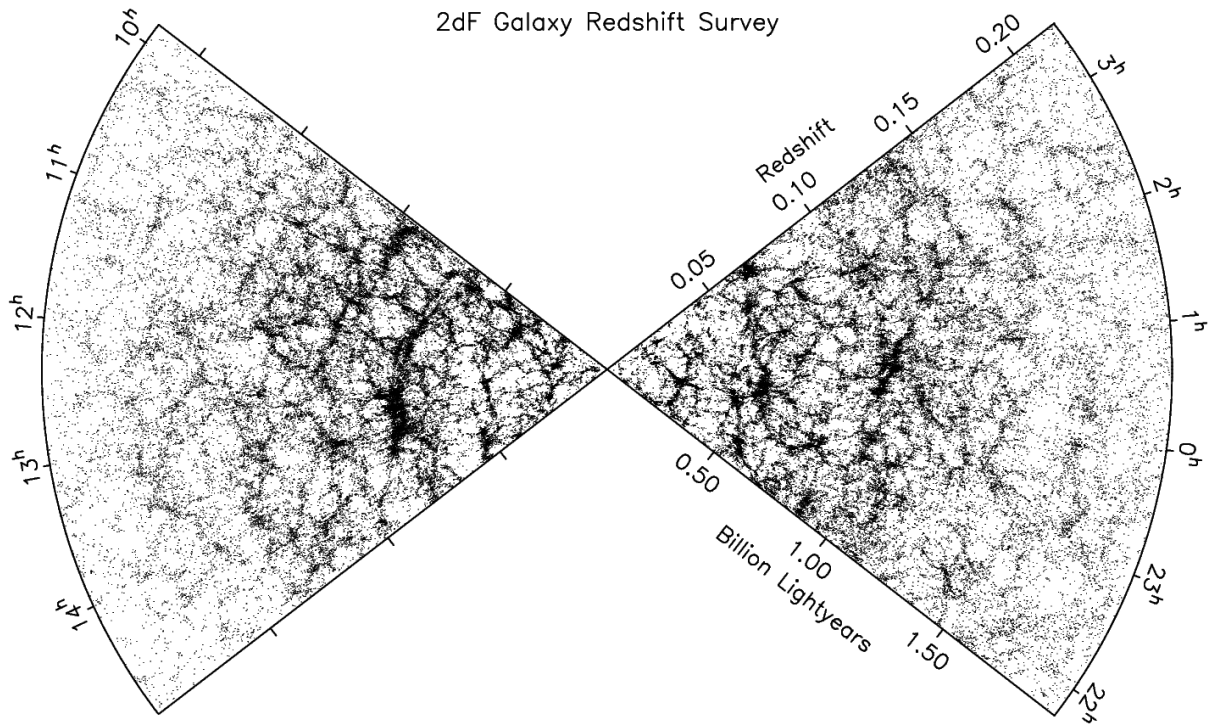


Figure 2.2: Redshift distribution of the galaxies in the complete 2dF Galaxy Redshift Survey. In the survey reliable redshifts have been measured for 221,414 galaxies. The projected map clearly shows the large-scale structure of the luminous matter, traced by galaxy clusters, filaments and voids. (Image credits: M. Colless et al., 2dF Galaxy Redshift Survey)

by the mean density $\bar{\rho}(t)$, the density deviation $\Delta\rho(\vec{r},t) = \rho(\vec{r},t) - \bar{\rho}(t)$ creates an additional gravitational field. For $\Delta\rho > 0$ and hence $\delta > 0$ the stronger field leads to a slower local expansion. Therefore, the density decreases slower than the mean density $\bar{\rho}(t)$, leading to a further increase in $\delta$.

The origin of the initial density fluctuations is still under debate, but it is most widely assumed that they arose from quantum fluctuations in the very early Universe ($\sim 10^{-43}$ s), which were inflated during a phase of exponentially accelerated expansion called *inflation*. In this scenario, the statistics of the original density fluctuations can be described by Gaussian random fields.

### 2.2.1 Linear structure growth

For $|\delta| \ll 1$ the growth of structures can be described by linear perturbation theory, where we make two additional simplifications:

- We only consider length scales much smaller than the Horizon $r_{\mathrm{H}}$, which is given by the maximum distance a photon can have travelled since the Big Bang. Hence, we only consider scales which are much smaller than any scale relevant for the Universe as a whole, enabling us to apply Newtonian gravity.

- We limit the discussion to non-relativistic pressure-less matter (dust).

Furthermore, we only consider the case of dark energy as a pure cosmological constant here.

The non-relativistic matter can be treated as a pressureless fluid with density $\rho(\vec{r},t)$ moving with velocity $\vec{u}(\vec{r},t)$ under the influence of a gravitational field, which obeys the following set of differential equations:

$$\frac{\partial\rho}{\partial t} + \nabla_r \cdot [\rho\vec{u}] = 0 \qquad \text{Continuity equation} \tag{2.33}$$

$$\frac{\partial\vec{u}}{\partial t} + (\vec{u}\cdot\nabla_r)\,\vec{u} = -\nabla_r\phi \qquad \text{Euler equation} \tag{2.34}$$

$$\nabla_r^2\phi = 4\pi G\rho - \Lambda \qquad \text{Poisson equation}\,, \tag{2.35}$$

where $\phi$ denotes the gravitational potential. The Poisson equation has been modified to allow for a cosmological constant, where the form has been chosen to reproduce the Friedmann equation (2.5). The homogeneous solution of this set of equations is given by the Hubble expansion

$$\rho(\vec{r},t) = \bar{\rho}(t) = \rho_0 a^{-3} \tag{2.36}$$

$$\vec{u}(\vec{r},t) = \frac{\dot{a}}{a}\,\vec{r} \tag{2.37}$$

$$\phi(\vec{r},t) = \frac{1}{6}\,(4\pi G\bar{\rho} - \Lambda)\,|\vec{r}|^2\,. \tag{2.38}$$

For $|\delta| \ll 1$ deviations from the Hubble expansion will be small. Hence, general solutions can be found as linear perturbations of the homogeneous solution. For this we transform to comoving coordinates $\vec{x} = \vec{r}/a$, decompose the velocity into homogeneous expansion and peculiar velocity $\vec{u}(\vec{r}(\vec{x}),t) = \dot{a}\vec{x}+\vec{v}(\vec{x},t)$, define the comoving potential $\Phi(\vec{x},t) = \phi(a\vec{x},t)+(\ddot{a}a/2)\,|\vec{x}|^2$, and substitute the density by the density contrast, so that (2.33) to (2.35) read

$$\frac{\partial\delta}{\partial t} + \frac{1}{a}\nabla_x \cdot [(1+\delta)\vec{v}] = 0 \qquad \text{Continuity equation} \tag{2.39}$$

$$\frac{\partial\vec{v}}{\partial t} + \frac{\dot{a}}{a}\vec{v} + \frac{1}{a}\,(\vec{v}\cdot\nabla_x)\,\vec{v} = -\frac{1}{a}\nabla_x\Phi \qquad \text{Euler equation} \tag{2.40}$$

$$\nabla_x^2\Phi = \frac{3H_0^2\Omega_\mathrm{m}}{2a}\delta \qquad \text{Poisson equation}\,. \tag{2.41}$$

We consider only small perturbations $|\delta| \ll 1$ and therefore neglect terms non-linear in $\delta$ und $\vec{v}$. By combining the time derivative of (2.39), and the divergence of (2.40) with (2.41), we find the linearised evolution equation of the density perturbations:

$$\ddot{\delta} + \frac{2\dot{a}}{a}\dot{\delta} - \frac{3H_0^2\Omega_\mathrm{m}}{2a^3}\delta = 0\,. \tag{2.42}$$

This equation no longer has an explicit dependence on $\vec{x}$. Hence, the temporal and spatial dependences of the solution factorise. The general solution of the second-order differential equation (2.42) is therefore given by

$$\delta(\vec{x},t) = D_+(t)\Delta_+(\vec{x}) + D_-(t)\Delta_-(\vec{x})\,, \tag{2.43}$$

where $D_\pm(t)$ are the two linearly independent solutions of $D(t)$ obeying

$$\ddot{D} + \frac{2\dot{a}}{a}\dot{D} - \frac{3H_0^2\Omega_\mathrm{m}}{2a^3}D = 0\,. \tag{2.44}$$

With $D_+(t)$ we denote the *growing mode* which increases with time, while $D_-(t)$ refers to the decreasing *decaying mode*. Any early contribution of $D_-(t)$ will have faded away at current epochs so that only the growing mode is present, which we normalise to $D_+(t_0) = 1$ for today.

In the special case of an EdS universe the time-dependence of the scale factor is given by $a(t) = (t/t_0)^{2/3}$ with $t_0 = 2/(3H_0)$, leading to the solutions $D_+ = (t/t_0)^{2/3}$ and $D_- = (t/t_0)^{-1} = (3t_0/2)\,H(t)$. By computing $\frac{\mathrm{d}}{\mathrm{d}t}(\dot{H} + H^2)$ it can be shown that the Hubble parameter $H(t)$ generally provides one solution of (2.44), which, however, refers to the decaying mode. With it the growing solution can be constructed using Sturm-Liouville theory as

$$D_+(t) \propto H(t)H_0^2 \int_0^t \frac{\mathrm{d}t'}{a^2(t')H^2(t')}\,. \tag{2.45}$$

The explicitly computed growing solution of the EdS universe also provides a very rough approximation for other cosmologies (see Fig. 2.3). Since we observe large density contrasts $\delta \gg 1$ today, we would expect $\delta(z = 1100) \gtrsim 10^{-3}$ leading to $\Delta T/T \gtrsim 10^{-3}$ at the time the CMB radiation was emitted. However, the observed fluctuations in the CMB are weaker by approximately two orders of magnitude (see Section 2.1.3). This is a very strong indication that the major fraction of the matter is not in baryonic form, but has to be dark matter which only interacts gravitationally. At the time the CMB was emitted, the dark matter must already have formed stronger density fluctuations, whereas the distribution of the baryonic matter was smoother due to the pressure of the matter-radiation fluid.

In the linear perturbation theory applied above, the spatial distribution $\Delta_+(\vec{x})$ of the initial fluctuations does not change in comoving coordinates, while only the amplitude of the fluctuations grows in time with $D_+(t)$. Thus, fluctuations on different scales do not mix. With the normalisation $D_+(t_0) = 1$ chosen, $\Delta_+(\vec{x})$ would describe the present day fluctuations, *if* the evolution had been linear. We will discuss the impact of non-linear evolution in Sect. 2.2.6.

### 2.2.2 Statistical properties of the density field

Due to the clustering of matter it is more likely to find an overdense region near to another one than at a random location. In real-space this is typically described in terms of correlation functions.

While the expectation value for the density at location $\vec{x}$ is simply given by the mean density $\langle\rho(\vec{x})\rangle = \bar{\rho}$, the expectation value for the product of the densities at locations $\vec{x}$ and $\vec{y}$ becomes

$$\langle\rho(\vec{x})\,\rho(\vec{y})\rangle = \bar{\rho}^2\langle[1+\delta(\vec{x})]\,[1+\delta(\vec{y})]\rangle = \bar{\rho}^2\,(1 + \langle\delta(\vec{x})\,\delta(\vec{y})\rangle =: \bar{\rho}^2\,(1+\xi(\vec{x},\vec{y}))\,, \tag{2.46}$$

where we have defined the *two-point correlation function* of matter fluctuations $\xi(\vec{x},\vec{y})$ and used $\langle\delta(\vec{x})\rangle = 0$. Due to the homogeneity of the Universe $\xi$ may only depend on the separation vector $(\vec{x}-\vec{y})$, and isotropy further limits its dependence to the modulus $r = |\vec{x}-\vec{y}|$ of this vector.

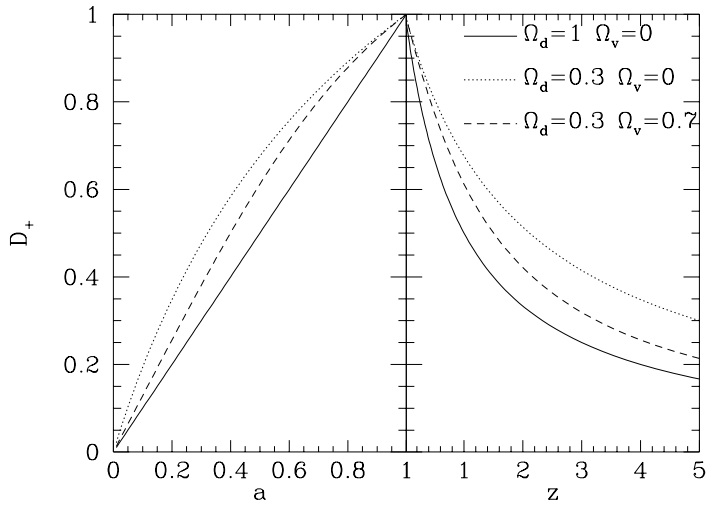


Figure 2.3: Growth factor $D_+(t)$ for three different cosmological models in dependence of the scale factor $a$ (*left*) and the redshift $z$ (*right*). Source: P. Schneider.

Alternatively, the description can be performed in Fourier-space with the transformed density contrast

$$\hat{\delta}(\vec{k},t) = \int \mathrm{d}^3x\, \mathrm{e}^{\mathrm{i}\vec{k}\cdot\vec{x}}\delta(\vec{x},t)\,, \tag{2.47}$$

where $\vec{k}$ denotes the comoving wave vector, and the *power spectrum*

$$P(|\vec{k}|) = \int \mathrm{d}^3x\, \mathrm{e}^{-i\vec{k}\cdot\vec{x}}\xi(|\vec{x}|) = 2\pi \int_0^\infty \mathrm{d}r\; r^2\, \frac{\sin kr}{kr}\, \xi(r)\,. \tag{2.48}$$

The larger its value is for a mode $k$, the larger is the amplitude of fluctuations at length scale $L \simeq 1/k$.

Both $\xi(r)$ and $P(k)$ are time-dependent, evolving as structures grow. As they dependent quadratically on $\delta$, which evolves as

$$\delta(\vec{x},t) = D_+(t)\Delta_+(\vec{x})\,, \tag{2.49}$$

their *linear* time evolution reads

$$\xi(x,t) = D_+^2(t)\,\xi(x,t_0) \tag{2.50}$$

$$P(k,t) = D_+^2(t)\,P(k,t_0) =: D_+^2(t)\,P_0(k)\,, \tag{2.51}$$

where we have defined $P_0(k)$ as the *linearly extrapolated* present day power spectrum.

### 2.2.3 The initial power spectrum

The currently most popular scenario for the origin of the observed density fluctuations are quantum fluctuations in the early Universe, which can be described by Gaussian random fields and have been exponentially enlarged during the phase of inflation.

At very early times *after* inflation, all length scales which are relevant today, have been much larger than the horizon $r_{\rm H}$. Hence, there was no distinguished length scale, so that the initial power spectrum could only have the form of a power law

$$P(k) \propto k^{n_{\rm s}} \,, \tag{2.52}$$

with the *spectral index* $n_{\rm s}$. For $n_{\rm s} = 1$ the fluctuation in the potential and hence space-time become scale independent, leading to the *Harrison-Zeldovich spectrum*

$$P(k, t_i) = A k^{n_{\rm s}} \,; \quad n_{\rm s} = 1 \,, \tag{2.53}$$

where the normalisation $A$ cannot be predicted but only determined by observations. Indeed a detailed quantitative treatment of inflation predicts $n_{\rm s}$ close to, but slightly smaller than 1 (see e.g. Dodelson 2003).

### 2.2.4 Transfer function

So far we have only considered sub-horizon matter fluctuations, which in a matter-dominated flat cosmology grow with $\delta \propto a$. A generalised treatment, for example discussed in Dodelson (2003), shows that this is also the case for super-horizon fluctuations, if matter dominates the expansion.

On the other hand the early expansion history was dominated by radiation, which can be seen from (2.15). The transition from radiation to matter dominance happens at

$$z_{\rm eq} = a_{\rm eq}^{-1} - 1 \simeq 23900 \Omega_{\rm m} h^2 \,. \tag{2.54}$$

For $a \ll a_{\rm eq}$ modes of scale $L$ grow as

$$\delta \propto a^2 \qquad \text{if} \quad L \gg r_{\rm H} \,, \text{and} \tag{2.55}$$

$$\delta \approx \text{const} \qquad \text{if} \quad L \ll r_{\rm H} \,, \tag{2.56}$$

where the suppression of growth for $L \ll r_{\rm H}$ originates from the radiation dominated expansion entering in (2.44).

We define the scale factor $a_{\rm enter}(L)$, at which the length scale $L$ of a fluctuation enters into the co-moving horizon, or – more correct – the horizon grows above the length scale $L$:

$$r_{\rm H}(a_{\rm enter}(L)) = L \,. \tag{2.57}$$

Small-scale fluctuations enter into the horizon earlier and are hence stronger suppressed, as illustrated in Fig. 2.4. We define the special length scale $L_0$ for which $a_{\rm eq} = a_{\rm enter}(L_0)$:

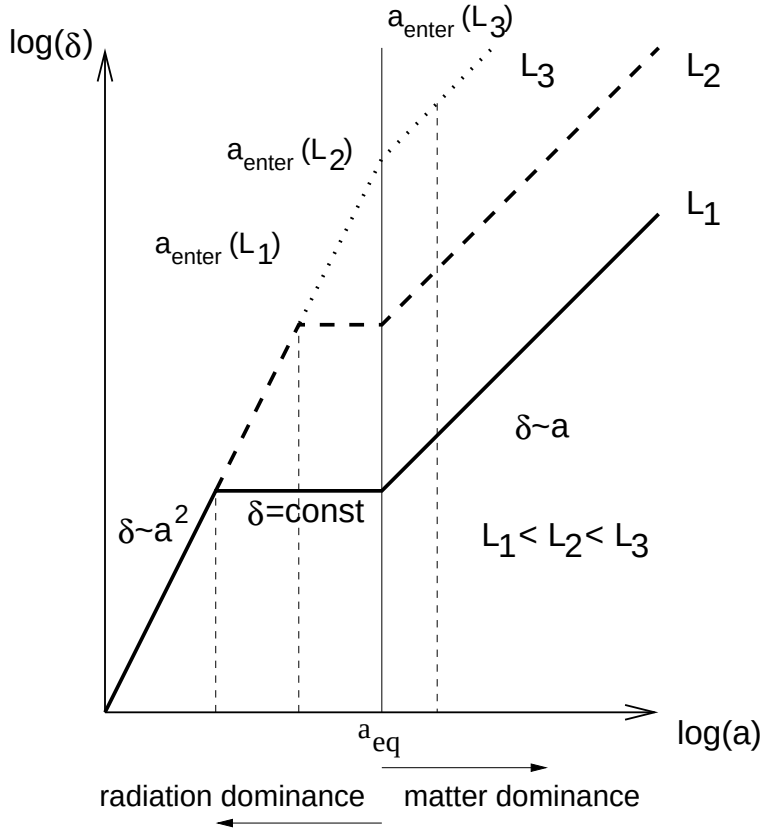


Figure 2.4: Growth of density fluctuations as a function of scale factor $a$ for three different co-moving length scales $L_1 < L_2 < L_3$. After entering the horizon at $a = a_{\rm enter}(L)$ the growth is suppressed during radiation dominance until $a = a_{\rm eq}$. The fluctuation of scale $L_1$ enters the horizon first leading to the strongest suppression. The $L_3$-fluctuation enters the horizon after the time of matter and radiation equality and is therefore not suppressed.

$$L_0 = r_{\rm H}(a_{\rm eq}) = \frac{c}{\sqrt{2}H_0}\,\frac{1}{\sqrt{\Omega_{\rm m}}}a_{\rm eq}^{1/2} = \frac{c}{\sqrt{2}H_0}\,\frac{1}{\sqrt{23900\Omega_{\rm m}h}} \simeq 12\left(\Omega_{\rm m}h^2\right)^{-1}\,{\rm Mpc}\,. \tag{2.58}$$

Scales smaller than $L_0$ are suppressed by the factor $[a_{\rm enter}(L)/a_{\rm eq}]^2$.

Furthermore, structure growth depends on the nature of dark matter. The theory of linear structure growth as summarised above correctly applies to so-called "cold" dark matter (CDM) consisting of non-relativistic particles. Dark matter particles which are relativistic or "hot" (HDM) are not bound to the potential wells. Hence, if all dark matter was hot, small-scale fluctuations would be washed out due to free streaming. In this scenario large structures would form first, later fragmenting into smaller ones. Different observations such as the presence of galaxies at $z \sim 6$ show that this cannot be the case and the dominant part of dark matter must be cold. Nonetheless, a small contribution of hot dark matter is expected from neutrinos, which were relativistic at $z_{\rm eq}$.

Corrections to structure growth, such as the ones discussed, but also effects due to pressure

and dissipation, are summarised in the *transfer function* $T_k$ defined as

$$T_k = \frac{\delta(k, t_0)}{\delta(k, t_{\rm ini}) D_+(t_{\rm ini})}\,, \tag{2.59}$$

with the linear growth factor $D_+$ between an initial time $t_{\rm ini}$ and the present $t_0$. The initial time is arbitrary, as long as it refers to a time before any scale of interest became smaller than the horizon.

For a CDM-only Universe Efstathiou et al. (1992) derive a fitting formula:

$$T_k = \left[1 + \left(6.4q + (3.0q)^{3/2} + (1.7q)^2\right)^\nu\right]^{-1/\nu}\,, \text{ with } \nu = 1.13\,, \tag{2.60}$$

which depends on the dimensionless parameter

$$q = \frac{k}{\Omega_{\rm m} h^2 {\rm Mpc}^{-1}} = \frac{k/(h{\rm Mpc}^{-1})}{\Gamma}\,, \tag{2.61}$$

with the *shape parameter*

$$\Gamma = \Omega_{\rm m} h\,. \tag{2.62}$$

For large $k$ and $q$ (2.60) reproduces the suppression of sub-horizon modes $\propto k^{-2}$. The shape parameter corresponds to the wave mode $k/(h{\rm Mpc}^{-1})$, where the transfer function turns over from a constant to this suppression. Sugiyama (1995) provide a modification of the shape parameter in the presence of baryons

$$\Gamma = \Omega_{\rm m} h \exp\left[-\Omega_{\rm b}(1 + \sqrt{2h}/\Omega_{\rm m})\right]\,, \tag{2.63}$$

where $\Omega_{\rm b}$ denotes the baryonic matter content.

Taking the transfer function into account, the time-dependent *linearly extrapolated* power spectrum reads

$$P(k, t) = D_+^2(t) T_k^2 A k^{n_{\rm s}}\,. \tag{2.64}$$

### 2.2.5 Power spectrum normalisation

The normalisation of the power spectrum $A$ cannot be predicted, but has to be determined from observations. While $A$ is often used in the context of CMB science, observations in the low-redshift Universe usually use an alternative normalisation given by

$$\sigma_8 = \sigma(\delta)_{[R=8h^{-1}{\rm Mpc}]} = \sqrt{\langle\delta^2\rangle_{[R=8h^{-1}{\rm Mpc}]}}\,, \tag{2.65}$$

which measures the dispersion of the *linearly extrapolated* density contrast $\delta$ determined in spheres of radius $R = 8h^{-1}$Mpc. This at first sight arbitrary length scale was chosen because the dispersion of the number of galaxies measured in this volume is of order unity, so that also $\sigma_8$ should be of order unity assuming that galaxies trace the underlying dark matter well.

### 2.2.6 Non-linear evolution and simulations

The theory of linear structure growth breaks down for $\delta \gtrsim 1$, and hence fails to explain, for example, the formation of galaxies and galaxy clusters. Here an analytic treatment is only possible in special cases such as the spherical collapse model (e.g. Peacock 1999). For the general case one has to rely on numerical N-body simulations, where the state-of-the-art is currently given by the Millennium Simulation containing $10^{10}$ particles (Fig. 2.5). Such simulations of cold dark matter particles in a universe with cosmological constant ($\Lambda$CDM) efficiently reproduce the filamentary *cosmic web* observed in galaxy redshift surveys.

In contrast to linear structure growth, perturbations of different scales (different $k$-modes) interact in non-linear evolution creating non-Gaussian features in the density field. Hence, the statistical properties of the density field are no longer fully described by the power-spectrum, but higher-order statistics have to be taken into account. Based on numerical simulations Peacock & Dodds (1996) found a fitting function for the power spectrum in the non-linear regime, which was later revised by Smith et al. (2003) to better describe the small-scale signal.

In Fig. 2.6 the predicted power spectrum is plotted for different CDM cosmologies, once considering only linear structure growth and once taking non-linear corrections by Peacock & Dodds (1996) into account. The cosmological parameters used in the different models are listed in Table 2.1.

Table 2.1: Overview of cosmological parameters used in Fig. 2.6.

| $\Omega_m$ | $\Omega_\Lambda$ | $\Gamma$ | $\sigma_8$ | **model name** |
|---|---|---|---|---|
| 1.0 | 0 | 0.25 | 0.6 | EdS(0.6,0.25) |
| 0.3 | 0 | 0.25 | 1.0 | OCDM(1.0,0.25) |
| 0.3 | 0.7 | 0.25 | 1.0 | $\Lambda$CDM(1.0,0.25) |
| 1.0 | 0 | 0.25 | 1.0 | EdS(1.0,0.25) |
| 1.0 | 0 | 0.5 | 0.6 | EdS(0.6,0.5) |

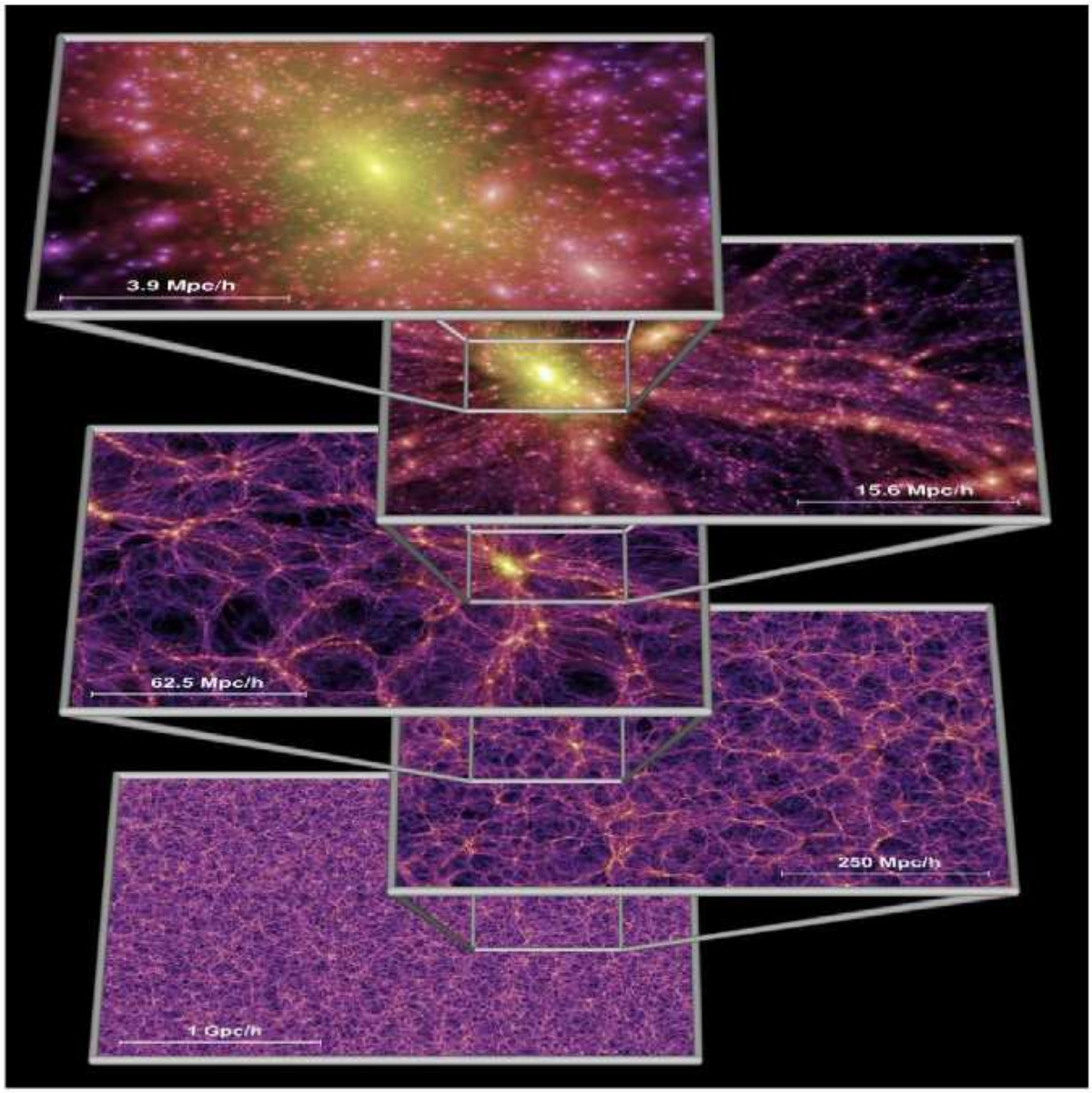


Figure 2.5: Dark matter density field in the Millennium Simulation projected within slices of $15h^{-1}$ Mpc. The simulation has a side-length of $500h^{-1}$ Mpc and contains $10^{10}$ particle. For the lower two panels slices taken at different angles were combined to obtain the large side-length while avoiding replicating structures (from Springel et al. 2005).

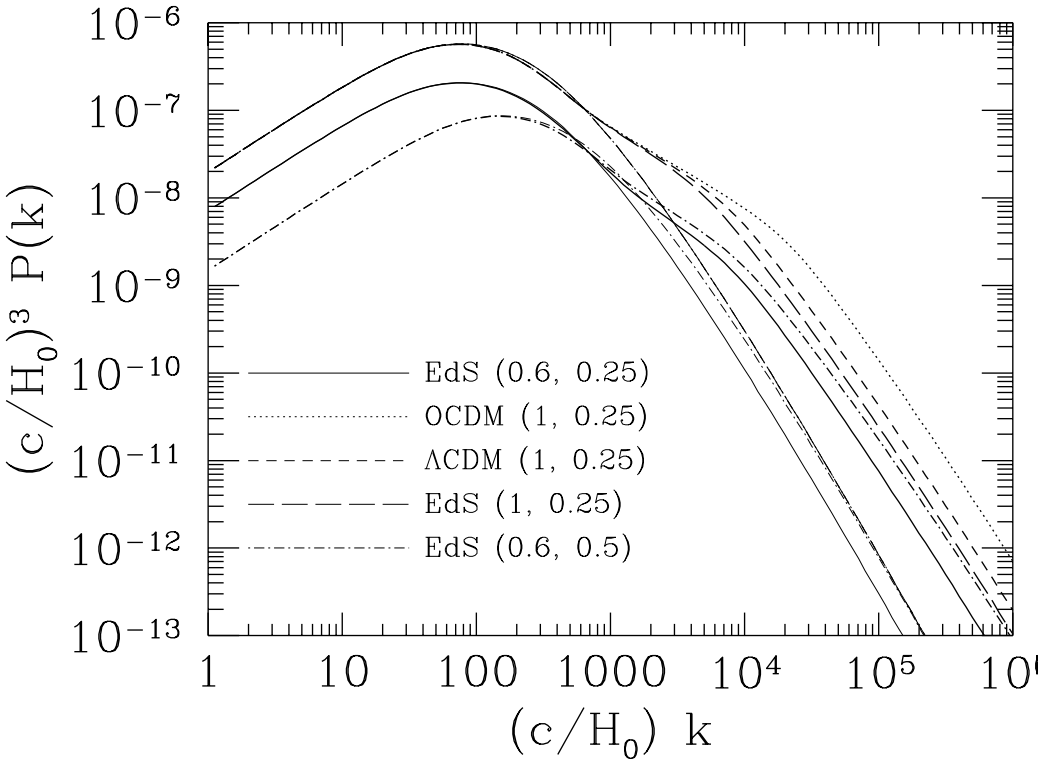


Figure 2.6: Power spectrum for five different cosmological models, with parameters detailed in Table 2.1. Thin lines display the linearly extrapolated power spectrum, whereas the non-linear corrections given by Peacock & Dodds (1996) were taken into account for the thick lines. At small $k$ the models show the $\propto k^{n_s}$ dependence of the initial power spectrum. Close to $(c/H_0)k = 100$ the power spectrum turns over due to the suppression of sub-horizon modes during radiation dominance. Non-linear corrections are important for large $k$ (source: P. Schneider).

## 2.3 Measurement of cosmological parameters

Nowadays many different techniques are used to constrain cosmological parameters. As a description of all of them is beyond the scope of this work I will limit the discussion to a non-exhaustive list of important parameters and probes.

### 2.3.1 Hubble constant

Hubble (1929) first measured a positive Hubble constant of approximately $500\,\mathrm{km\,s^{-1}\,Mpc^{-1}}$ and thus realised that the Universe is actually expanding. However, the estimated value of the Hubble constant was far too large, given that Hubble under-estimated the brightness of cepheids used as distance indicator for nearby galaxies. Later the necessary distinction between cepheids of different stellar populations was found by Baade (1956). Additionally, Hubble's measurement was strongly influenced by the peculiar velocities of the observed galaxies and galaxy groups.

More recent measurements from the *HST Key Project* (see Fig. 2.7) yield a value of the Hubble constant of $72 \pm 3\,(\mathrm{stat}) \pm 7\,(\mathrm{sys})\,\mathrm{km\,s^{-1}\,Mpc^{-1}}$ (Freedman et al. 2001). This is in good agreement with recent measurements of Cepheid distances to nearby galaxies hosting type Ia supernovae, which yield $H_0 = 73 \pm 4\,(\mathrm{stat}) \pm 5\,(\mathrm{sys})\,\mathrm{km\,s^{-1}\,Mpc^{-1}}$ (Riess et al. 2005), and combined Sunyaev-Zeldovich and X-ray measurements of galaxy clusters, where Bonamente et al. (2006) find $H_0 = 77^{+4}_{-3}\,(\mathrm{stat})\,^{+10}_{-8}\,(\mathrm{sys})\,\mathrm{km\,s^{-1}\,Mpc^{-1}}$. Under the assumptions of a spatially flat geometry and pure cosmological constant the WMAP-3 results also yield tight constraints $H_0 = 73 \pm 3\,\mathrm{km\,s^{-1}\,Mpc^{-1}}$ (Spergel et al. 2007).

Another, purely geometric approach to estimate $H_0$ comes from the measurement of time-delays between the different images of multiply-imaged quasars in strong lensing systems (see Sect. 3.1). While constraints on $H_0$ from individual systems are often limited by degeneracies with the radial mass profile of the lensing galaxy, estimates from a larger ensemble seem to be promising, see Oguri (2007) who finds $H_0 = 68 \pm 6\,(\mathrm{stat}) \pm 8\,(\mathrm{sys})\,\mathrm{km\,s^{-1}\,Mpc^{-1}}$ from 16 measured time delays. Currently several large observing programmes such as COSMOGRAIL[2] and HOLIGRAIL[3] are conducted, in order to increase the number of accurately know time-delays and improve $H_0$ estimates from lensing.

### 2.3.2 Density parameters

The density parameters $\Omega_\mathrm{m}$ and $\Omega_\Lambda$ can be constrained in various ways, which can be grouped into probes examining the expansion history of the Universe, probes constraining the geometry of the Universe, and probes measuring the power spectrum of density fluctuations.

During the last decade supernovae of type Ia have been used as standard candles to probe the expansion of the Universe. Almost simultaneously the Supernova Cosmology Team (Perlmutter et al. 1999) and the High–$z$ Supernova Search Team (Riess et al. 1998) found evidence for

[2] http://www.cosmograil.org/

[3] http://www.astro.uni-bonn.de/~holigrail

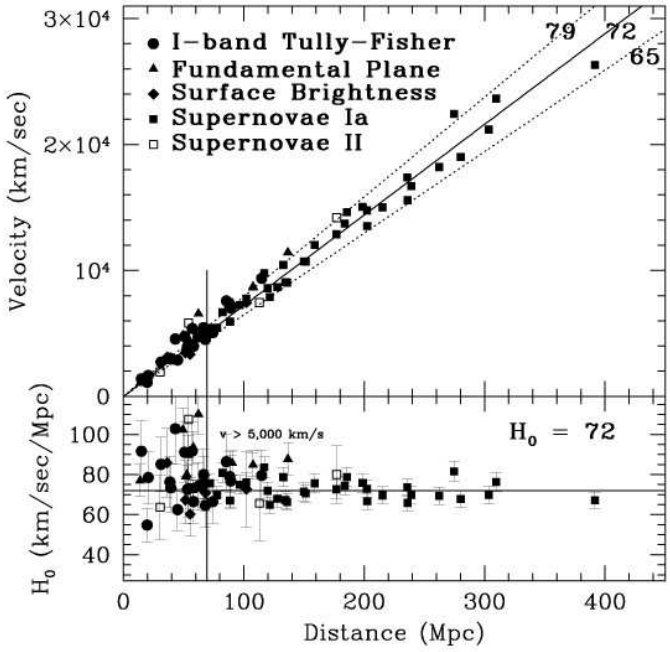


Figure 2.7: *Top:* A Hubble diagram of distance versus velocity for secondary distance indicators calibrated by cepheids. A slope of $H_0 = 72\,\mathrm{km\,s^{-1}\,Mpc^{-1}}$ is shown, flanked by lines of 10% error. Beyond 5,000 $\mathrm{km\,s^{-1}}$ (indicated by the vertical line), both numerical simulations and observations suggest that the effects of peculiar motions are small. *Bottom:* Value of the Hubble constant $H_0$ as a function of distance (Fig. 4 of Freedman et al. 2001).

an accelerating expansion, which is only possible in the presence of dark energy or a positive cosmological constant.

The geometry of the Universe and hence $\Omega_{\mathrm{tot}}$ can be constrained best using the CMB. The angular power spectrum of CMB temperature fluctuations contains characteristic accoustic peaks, which originate from accoustic oscillations of the baryon-photon fluid. These oscillations are driven by the gravitational potential of the dark matter concentrations on the one hand, and the photon pressure on the other. The physical size of the largest oscillation mode depends on the well-known scale of the horizon at the time of last scattering. The angular scale of this mode is then determined by the angular diameter distance to the surface of last scattering $D_{\mathrm{ang}}(z_{\mathrm{rec}})$, which depends on the geometry of the Universe. Hence, the geometry can be well constrained by measuring the location of the first accoustic peak in the CMB power spectrum, which was first determined by the ballon experiments BOOMERANG (de Bernardis et al. 2000) and MAXIMA (Hanany et al. 2000) to be at $\ell \sim 200$ consistent with a spatially flat geometry of the Universe. These results were confirmed with better accuracy by the WMAP satellite, which yielded $\Omega_{\mathrm{k}} = 1-\Omega_{\mathrm{tot}} = -0.014 \pm 0.017$ when combined with the HST Key Project estimate for $h$ (Spergel et al. 2007).

Density parameters, particularly $\Omega_{\mathrm{m}}$, can also be constrained by measuring the statistical

properties of the large-scale structure (see Sect. 2.3.3), for example using galaxy clusters or the large-scale distribution of galaxies. The analysis of supernovae, CMB, and large-scale structure data yields remarkably consistent and hence independently confirmed parameter constraints (see Fig. 2.8), which is often termed *concordance cosmology*.

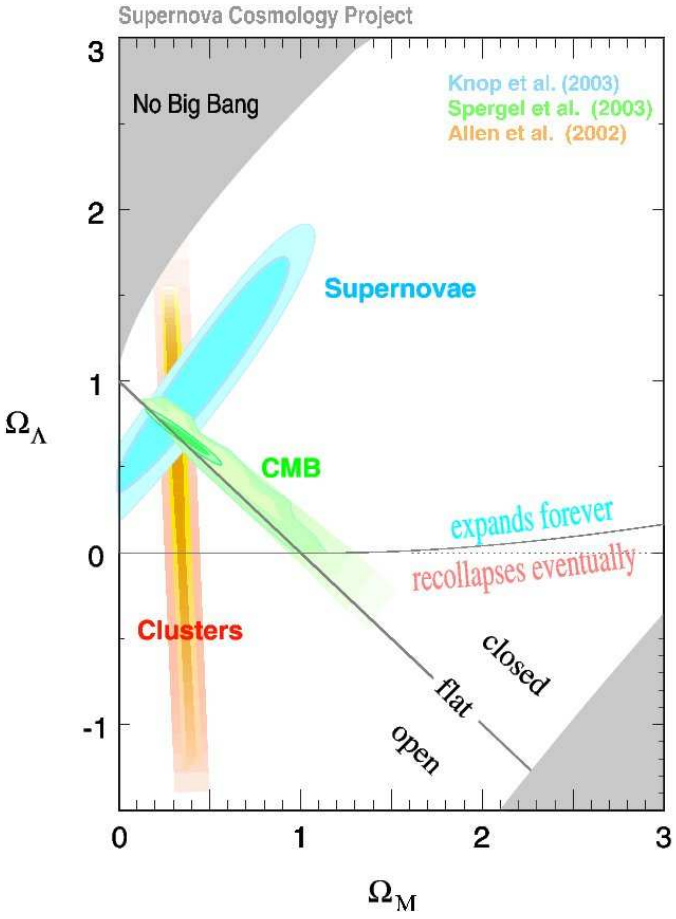


Figure 2.8: Consistent constraints on $\Omega_m$ and $\Omega_\Lambda$ from supernovae, CMB, and galaxy cluster data. Figure from Knop et al. (2003).

The tightest overall constraints were so far found using the WMAP-3 data, which can be well fit using a flat ΛCDM cosmology with parameters $(\Omega_m h^2, \Omega_b h^2, h, n_s, \tau, \sigma_8) = (0.1277^{+0.0080}_{-0.0079}, 0.02229 \pm 0.00073, 0.732^{+0.031}_{-0.032}, 0.958 \pm 0.016, 0.089 \pm 0.030, 0.761^{+0.049}_{-0.048})$ (WMAP3 only, Spergel et al. 2007). $\tau$ denotes the optical depth for scattering of CMB photons at free electrons which were released in the so-called phase of reionisation. Hence, we live in a Universe which is dominated by dark energy ($\Omega_\Lambda \approx 0.76$), and for which only $\sim 1/6$ of total matter content $\Omega_m \approx 0.24$ is in baryonic form ($\Omega_b \approx 0.042$). Given these parameters and assuming that dark energy really behaves like a cosmological constant, the Universe will accelerate and expand forever.

### 2.3.3 Power spectrum estimation

Different techniques can be used to contrain the power spectrum of matter density fluctuations. The main features one aims to extract are

1. the overall normalisation expressed as $A$ or $\sigma_8$;
2. the spectral index $n_s$ defining the slope of the inital fluctuation power law;
3. the shape parameter $\Gamma$ defining the turn-over point of the power spectrum;
4. cosmological parameters affecting the growth factor $D_+(t)$.

It is important to note that currently good predictions only exist for the linear and moderately non-linear part of the power spectrum. At highly non-linear scales (physical scales $\lesssim 300$ kpc) fitting formulas derived from dark matter simulations are expected to fail, as the impact of baryons on the power spectrum becomes important, which is still difficult to model (Rudd et al. 2007).

Different techniques often have very different dependencies on cosmological and power spectrum parameters, so that parameter degeneracies can be efficiently broken by combining different probes. Techniques to extract power spectrum information include:

- Under the assumption that galaxies trace the dark matter fluctuations, their distribution can be used to probe the power spectrum. The currently largest galaxy redshift surveys, the 2dFGRS and the SDSS have been used to probe the power spectrum on a wide range of scales (Cole et al. 2005; Percival et al. 2007, and reference therein). A problem of this method is that the exact bias between galaxies and dark matter, which is expressed in the bias factor $b$, is unknown and has to be estimated.

- The temperature anisotropies measured in the CMB (see Section 2.1.3) can be used to study the power spectrum at $z \sim 1100$ out to very large physical scales and thus small $k$ (see e.g. Jones et al. 2006; Spergel et al. 2007; Page et al. 2007; Hinshaw et al. 2007).

- The power spectrum can also be normalised by measuring the abundance and mass function of galaxy clusters (see for example Reiprich & Böhringer 2002; Bahcall et al. 2003; Sievers et al. 2003; Viana et al. 2003; Henry 2004). This probes the power spectrum on scales of the order 10 $h^{-1}$ Mpc.

- The Ly$-\alpha$ forest in quasar spectra can be used to investigate how clumpy intergalactic hydrogen is distributed. This can be used to probe the power spectrum on very small physical scales at $z \lesssim 6$ (see e.g. Gnedin & Hamilton 2002; Jena et al. 2005; Seljak et al. 2005; Desjacques & Nusser 2005).

- During the last years weak gravitational lensing became a powerful tool to probe the power spectrum. We will discuss this in detail in Section 3.3.

In Figure 2.9 some recent measurements with different techniques are shown, which can be translated into the power spectrum under certain assumptions.

A relatively young technique which makes use of a special feature of the power spectrum are baryonic acoustic oscillations: The baryonic oscillations observed in the CMB leave a weak but non-vanishing impact on the total matter power spectrum, which can still be observed in the present day Universe, hence providing a standard ruler at two very different redshifts. After Eisenstein et al. (2005) detected this effect for the first time in the SDSS data, Percival et al. (2007) use it in combination with the peak location in the CMB data to constrain the matter density to $\Omega_\mathrm{m} = 0.256^{+0.029}_{-0.024}$.

### 2.3.4 Dark energy equation of state parameter

Most studies assumed so far that dark energy behaves like a cosmological constant. Deviations from $w = -1$ lead to modifications both of the expansion history and the rate of structure growth. Yet, with current data the subtle differences are challenging to measure, where currently the tightest constraints have been found by combining high-$z$ type Ia supernovae with further probes to constrain the expansion history: Wood-Vasey et al. (2007) analyse data from the ESSENCE Supernova Survey yielding $w = -1.05^{+0.13}_{-0.12}(\mathrm{stat.}) \pm 0.11(\mathrm{sys.})$, where they assume flatness and include priors from baryon acoustic oscillations. This is consistent with a combined analysis of WMAP-3, SDSS, and supernovae data from the Supernova Legacy Survey (SNLS) yielding $w = -1.08 \pm 0.12$ (Spergel et al. 2007).

Weaker constraints have also been found by other probes such as weak gravitational lensing (see Sect. 3.3). The Dark Energy Task Force (DETF, Albrecht et al. 2006) identifies four major probes as being most promising for future constraints on $w$ and its time-dependence, namely baryonic acoustic oscillations, supernova surveys, galaxy cluster surveys, and weak gravitational lensing surveys. Aiming at precision measurements of $w$ the combination of several of these techniques will be a key issue, both to break parameter degeneracies and provide external checks for systematics. Additionally, it will be important to verify if the impact of dark energy on the expansion history (to which all probes are sensitive) agrees with its impact on structure growth (to which only the latter two are sensitive). Any deviation might provide an essential clue for our understanding of the nature of dark energy.

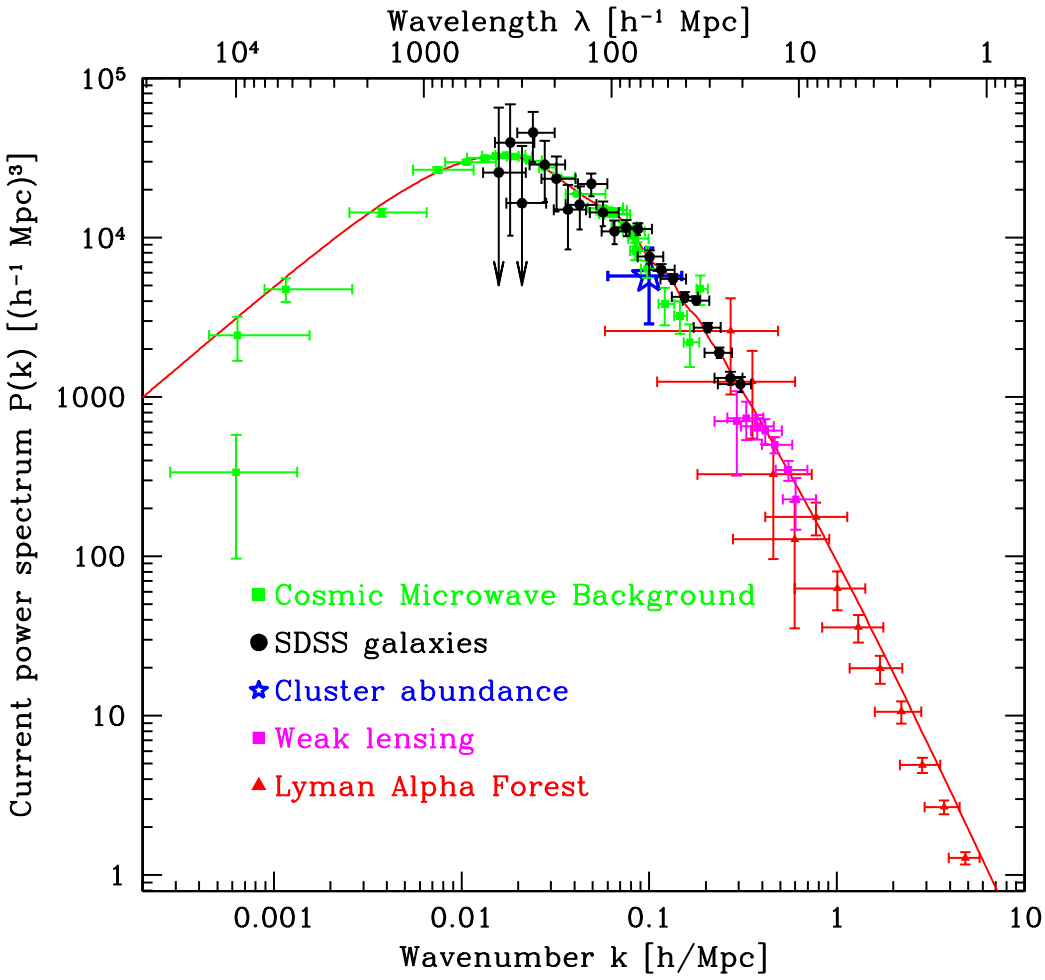


Figure 2.9: Measurements of the power spectrum with different methods. The CMB data combines the Boomerang, MAXIMA, DASI, CBI, VSA, ACBAR, and WMAP data (Hinshaw et al. 2003). The points of the SDSS galaxies are from Tegmark et al. (2004a). The point of the cluster abundance reflects the spread in the recent literature. The plotted weak lensing data are from the Red-Sequence Cluster Survey (Hoekstra et al. 2002a). The Ly$\alpha$ forest points are from Gnedin & Hamilton (2002). Note that the location of CMB, cluster abundance, weak lensing, and the Ly$\alpha$ forest points depends on the density parameters, and for the CMB additionally on the reionisation optical depth $\tau$. This figure is for the case of a so-called "vanilla" flat scalar scale-invariant model with $\Omega_m = 0.28$, $h = 0.72$, $\Omega_b/\Omega_m = 0.16$, and $\tau = 0.17$. A bias factor $b = 0.92$ is assumed for the SDSS galaxies (Figure 37 from Tegmark et al. 2004a).

# Chapter 3

# Gravitational lensing

According to Einstein's Theory of General Relativity, light rays propagate along null geodesics of the space-time metric. Thus, light is deflected by the inhomogeneous gravitational potential of the matter distribution in the Universe.

In many applications of the theory of gravitational lensing, single galaxies or galaxy clusters deflect light of background sources. As their extend along the line-of-sight is much smaller than the distances involved, the lens effect can be approximated by a single kink. In the first two sections of this chapter gravitational lensing in this *thin lens approximation* is discussed. After introducing some general terminology and formalisms of gravitational lensing in Sect. 3.1, I will summarise *weak gravitational lensing* in Sect. 3.2. Here the distortions are weak and can only be measured statistically from an ensemble of coherently lensed galaxies. In Section 3.3 I will then describe *cosmic shear*, the gravitational lensing effect by large-scale structure, which is also termed *cosmological weak lensing*. In this case the thin lens approximation cannot be used and a more general treatment is required. I will conclude this chapter with a discussion of practical issues concerning gravitational shear measurements in Sect. 3.4.

For a detailed description of gravitational lensing and its derivation from General Relativity, the reader is referred to the monograph by Schneider et al. (1992). A review about weak lensing was published by Bartelmann & Schneider (2001). Cosmic shear has been reviewed e.g. by Refregier (2003) and Van Waerbeke & Mellier (2003).

In this chapter three-dimensional vectors $\vec{x}$ are denoted by an arrow over the symbols, whereas bold-face is used for two-dimensional vectors $\boldsymbol{x}$.

## 3.1 Basics of lensing in the thin lens approximation

### 3.1.1 The lens equation

In the *thin lens approximation*, light emitted from a background source is deflected in the gravitational potential of a single localised foreground mass distribution on its way to the observer. Such a situation is sketched in Fig. 3.1, where a mass distribution at distance $D_\mathrm{L}$ from the observer acts as gravitational lens and deflects light rays emitted by a source at distance $D_\mathrm{S}$. Given that the

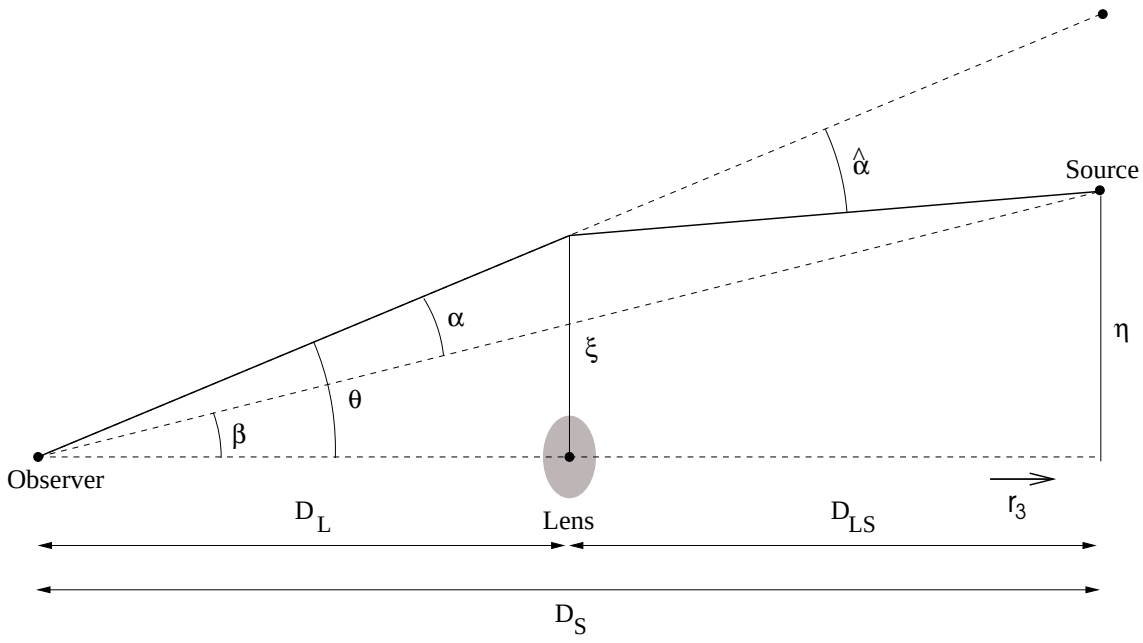


Figure 3.1: Geometry of gravitational lensing in the thin lens approximation: $D_\mathrm{L}$, $D_\mathrm{S}$, and $D_\mathrm{LS}$ are the angular diameter distances from the observer to the lens, from the observer to the source, and from the lens to the source. Without lensing the source would be observed at an angular position $\boldsymbol{\beta}$. Due to lensing, a light ray passing the lens at distance $\boldsymbol{\xi}$ will be deflected by an angle $\hat{\boldsymbol{\alpha}}$. Thus, the image will be observed at angular position $\boldsymbol{\theta}$. Angular positions are measured relative to the line-of-sight from the observer to an arbitrary image centre of the lens. The planes perpendicular to this axis at the distance of the lens $D_\mathrm{L}$ and the source $D_\mathrm{S}$ are called lens and source plane, respectively.

region in which a light ray is actually curved is much smaller than $D_\mathrm{L}$ and the distance between lens and source $D_\mathrm{LS}$, the deflection can be approximated by a single kink near the deflector (thin lens approximation). $\boldsymbol{\eta}$ and $\boldsymbol{\xi}$ denote the two-dimensional angular position of the source and the kink respectively from the line-of-sight to the lens. In this context all distance definitions refer to angular diameter distances (see Sect. 2.1.2), for which we can read off the following relation from Fig. 3.1

$$\boldsymbol{\eta} = \frac{D_\mathrm{S}}{D_\mathrm{L}}\boldsymbol{\xi} - D_\mathrm{LS}\hat{\boldsymbol{\alpha}}(\boldsymbol{\xi})\,, \tag{3.1}$$

with the *deflection angle* $\hat{\boldsymbol{\alpha}}(\boldsymbol{\xi})$. Inserting angular coordinates $\boldsymbol{\beta} = D_\mathrm{S}^{-1}\boldsymbol{\eta}$ and $\boldsymbol{\theta} = D_\mathrm{L}^{-1}\boldsymbol{\xi}$ into (3.1) leads to the *lens equation*

$$\boldsymbol{\beta} = \boldsymbol{\theta} - \frac{D_\mathrm{LS}}{D_\mathrm{S}}\hat{\boldsymbol{\alpha}}(D_\mathrm{L}\boldsymbol{\theta}) \equiv \boldsymbol{\theta} - \boldsymbol{\alpha}(\boldsymbol{\theta})\,, \tag{3.2}$$

where we have defined the *scaled deflection angle* $\boldsymbol{\alpha}(\boldsymbol{\theta})$. According to the lens equation, a source at the true position $\boldsymbol{\beta}$ will be seen by an observer at an angular position $\boldsymbol{\theta}$, if it satisfies (3.2).

### 3.1.2 From the deflection angle to the deflection potential

We will first consider the case of gravitational light deflection by a point mass $M$. Under the assumption that the impact parameter $\xi = |\boldsymbol{\xi}|$ is much larger than the Schwarzschild radius of the lens, $\xi \gg R_S = 2GMc^{-2}$, the gravitational field is weak, and the absolute value of the deflection angle $\hat{\alpha}$ can be calculated from General Relativity to be

$$\hat{\alpha} = \frac{4GM}{c^2 \xi} \,. \tag{3.3}$$

Due to the assumed weak field, the field equations of General Relativity can be linearised. In order to determine the deflection angle of an extended matter distribution with density $\rho(\vec{r})$, we can then simply add up the deflection caused by each mass element $\mathrm{d}m(\vec{r}) = \rho(\vec{r})\mathrm{d}V$ of the matter distribution. If we choose the coordinate system such that the line-of-sight to the lens is in the $r_3$ direction, the total deflection angle is

$$\hat{\boldsymbol{\alpha}}(\boldsymbol{\xi}) = \frac{4G}{c^2} \int \mathrm{d}^2\xi' \int \mathrm{d}r'_3 \, \rho(\xi'_1, \xi'_2, r'_3) \frac{\boldsymbol{\xi} - \boldsymbol{\xi}'}{|\boldsymbol{\xi} - \boldsymbol{\xi}'|^2} = \frac{4G}{c^2} \int \mathrm{d}^2\xi' \, \Sigma(\boldsymbol{\xi}') \frac{\boldsymbol{\xi} - \boldsymbol{\xi}'}{|\boldsymbol{\xi} - \boldsymbol{\xi}'|^2} \,, \tag{3.4}$$

where we have defined the *surface mass density*

$$\Sigma(\boldsymbol{\xi}) = \int \mathrm{d}r_3 \, \rho(\xi_1, \xi_2, r_3) \,. \tag{3.5}$$

A gravitational lens is called *strong*, if it is capable to produce multiple images, meaning that there is more than one angular position $\boldsymbol{\theta}$ for a certain $\boldsymbol{\beta}$ obeying (3.2). To quantify this, we define the dimensionless *convergence*

$$\kappa(\boldsymbol{\theta}) = \frac{\Sigma(D_L \boldsymbol{\theta})}{\Sigma_{cr}} \,, \tag{3.6}$$

with the *critical surface mass density*

$$\Sigma_{cr} = \frac{c^2}{4\pi G} \frac{D_S}{D_L D_{LS}} \,. \tag{3.7}$$

If a lens has $\kappa \geq 1$ somewhere, it produces multiple images for certain source positions[1]. An example for these *strong lensing* effects is shown in Fig. 3.2.

From (3.4) and the definition of $\kappa$, we find that the scaled deflection angle can be written as

$$\boldsymbol{\alpha}(\boldsymbol{\theta}) = \frac{1}{\pi} \int \mathrm{d}^2\theta' \kappa(\boldsymbol{\theta}') \frac{\boldsymbol{\theta} - \boldsymbol{\theta}'}{|\boldsymbol{\theta} - \boldsymbol{\theta}'|^2} \,. \tag{3.8}$$

If we define the two-dimensional scalar *deflection potential*

$$\Psi(\boldsymbol{\theta}) = \frac{1}{\pi} \int \mathrm{d}^2\theta' \kappa(\boldsymbol{\theta}') \ln|\boldsymbol{\theta} - \boldsymbol{\theta}'| \,, \tag{3.9}$$

the scaled deflection angle is given as its gradient $\boldsymbol{\alpha}(\boldsymbol{\theta}) = \nabla_{\boldsymbol{\theta}} \Psi$. The deflection potential is the two-dimensional analogue of the three-dimensional Newtonian gravitational potential. It obeys the Poisson equation

$$\nabla^2_{\boldsymbol{\theta}} \Psi(\boldsymbol{\theta}) = 2\kappa(\boldsymbol{\theta}) \,. \tag{3.10}$$

[1] Note that $\kappa \geq 1$ is sufficient, but not necessary for multiple images to occur.

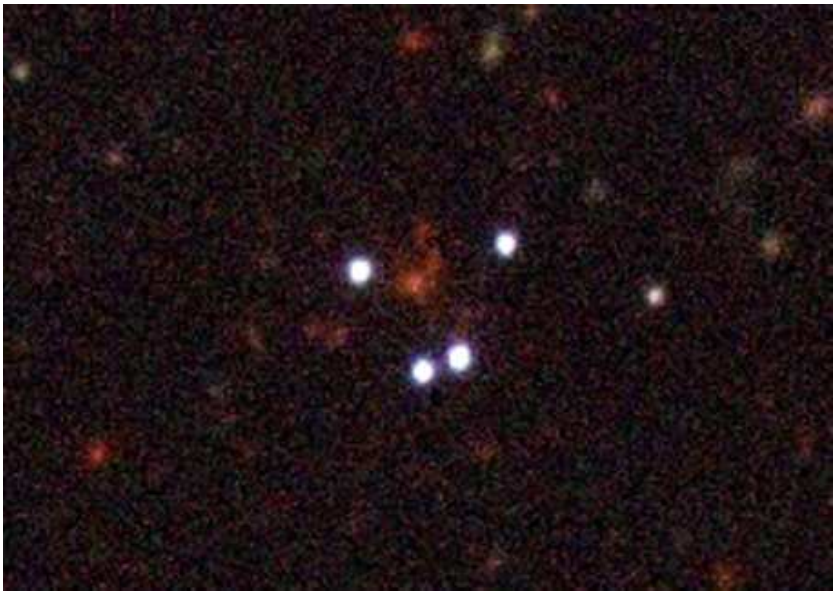

Figure 3.2: Gravitational lens SDSS1004+4112: A quasar at redshift $z_s = 1.734$ is quadruply lensed by a galaxy cluster at redshift $z_l = 0.68$. Between the quasar images the central galaxy and a further cluster member are visible. Image taken with the Hoher List 1m-telescope (credits: Schrabback, Joachimi; AIfA).

### 3.1.3 Image distortion and magnification

The lens equation (3.2) yields the image positions $\boldsymbol{\theta}$ of a source at angular position $\boldsymbol{\beta}$. Since photons are neither absorbed nor emitted in gravitational light deflection, lensing conserves surface brightness. Therefore the surface brightness distribution in the source plane $I^{(s)}(\boldsymbol{\beta})$ and the lens plane $I(\boldsymbol{\theta})$ must be equal, $I^{(s)}(\boldsymbol{\beta}(\boldsymbol{\theta})) = I(\boldsymbol{\theta})$. If we assume that the source is small compared to the scale on which the mass distribution of the lens varies, we can locally linearise the lens mapping. Then the surface brightness at a point $\boldsymbol{\theta}$ in the lens plane is given by

$$I(\boldsymbol{\theta}) = I^{(s)}\left[\boldsymbol{\beta}_0 + \mathcal{A}(\boldsymbol{\theta}_0)\cdot(\boldsymbol{\theta}-\boldsymbol{\theta}_0)\right], \tag{3.11}$$

where $\boldsymbol{\beta}_0$ is a reference point within the source which is mapped onto $\boldsymbol{\theta}_0$. The distortion of the lensed images is then described by the Jacobian matrix

$$\mathcal{A} \equiv \frac{\partial\boldsymbol{\beta}}{\partial\boldsymbol{\theta}} = \left(\delta_{ij} - \frac{\partial\alpha_i(\boldsymbol{\theta})}{\partial\theta_j}\right) = \left(\delta_{ij} - \frac{\partial^2\Psi(\boldsymbol{\theta})}{\partial\theta_i\partial\theta_j}\right), \tag{3.12}$$

which we can decompose into a diagonal and a trace-free part

$$\begin{aligned}\mathcal{A} &= \begin{pmatrix} 1-\kappa-\gamma_1 & -\gamma_2 \\ -\gamma_2 & 1-\kappa+\gamma_1 \end{pmatrix} \\ &= (1-\kappa)\begin{pmatrix} 1 & 0 \\ 0 & 1 \end{pmatrix} - |\gamma|\begin{pmatrix} \cos 2\phi & \sin 2\phi \\ \sin 2\phi & -\cos 2\phi \end{pmatrix}.\end{aligned} \tag{3.13}$$

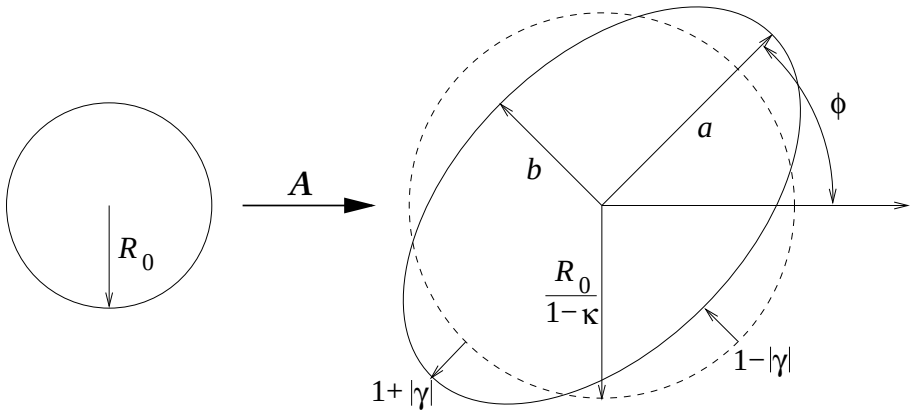


Figure 3.3: Illustration of the first order effect of convergence $\kappa$ and shear $\gamma$ on an intrinsically round source with un-lensed radius $R_0$. The convergence produces an isotropic magnification, whereas the shear creates an anisotropic distortion.

Here we have introduced the *shear* $\gamma = \gamma_1 + \mathrm{i}\gamma_2$, which is a complex number with modulus $|\gamma| = \left(\gamma_1^2 + \gamma_2^2\right)^{1/2}$ and polar angle $\phi$. The convergence and the shear can be expressed as derivatives of the deflection potential

$$\kappa = \frac{1}{2}\left(\Psi_{,11} + \Psi_{,22}\right), \quad \gamma_1 = \frac{1}{2}\left(\Psi_{,11} - \Psi_{,22}\right), \quad \gamma_2 = \Psi_{,12} = \Psi_{,21}\,. \tag{3.14}$$

Their different effects in lens mapping are illustrated in Fig. 3.3. While the convergence produces an isotropic magnification, the image is anisotropically distorted by the shear. An intrinsically round source with un-lensed radius $R_0$ is mapped onto an ellipse with major and minor semi-axes

$$a = \frac{R_0}{1 - \kappa - |\gamma|}, \quad b = \frac{R_0}{1 - \kappa + |\gamma|}\,. \tag{3.15}$$

The total flux observed from the source in the lensed and un-lensed case is given by the integral over the corresponding brightness distribution. From (3.11) follows that the *magnification factor* of the source is given by

$$\mu = \frac{1}{\det \mathcal{A}} = \frac{1}{(1 - \kappa^2) - |\gamma|^2}\,, \tag{3.16}$$

where $\mu$ can have either sign, depending on the parity of the lensed image with respect to the unperturbed image. The flux of the source is magnified by $|\mu|$. Regions with different parity are separated by *critical curves* in the lens plane, which are defined by $\det \mathcal{A} = 0$. Critical curves are mapped back onto *caustics* in the source plane. Formally the magnification is infinite on critical curves. However, real sources are extended. Therefore, the magnification has to be calculated by averaging $\mu$ over the source, weighted by the surface brightness. Additionally the geometrical-optics approximation fails near critical curves. In a wave-optics description also the magnification of a point source remains finite (e.g. Schneider et al. 1992). Nevertheless the

magnification can still attain large values ($\lesssim 100$) in real images. Very prominent features are the giant luminous arcs in the strong lensing regions of galaxy clusters (compare Fig. 3.4), where faint background galaxies are highly magnified. Some of these sources would be too faint to be observable without lensing. Thus galaxy clusters can be regarded as natural *gravitational telescopes*.

Obviously this magnification effect influences the local number density of background galaxies. Galaxies which are intrinsically too faint to be observed, can be magnified above the detection threshold. This increases the observed number density of galaxies. However, the magnification effect also stretches the sky locally, resulting in an effective decrease of the number density. Which of both competing effects wins depends on the shape of the luminosity function of the source population. The lensed number counts $n(>S,z)$ of sources at redshift $z$, which are above a flux limit $S$, are related to the un-lensed counts $n_0(>S,z)$ by

$$n(>S,z) = \frac{1}{\mu(\boldsymbol{\theta},z)} n_0\left(> \frac{S}{\mu(\boldsymbol{\theta},z)}, z\right) . \tag{3.17}$$

If one neglects the redshift dependence and assumes that the source counts follow a power law $n_0(>S) = N_0 S^{-\alpha}$, the relation between the lensed und un-lensed number counts in a certain region of the sky with magnification $\mu$ is given by

$$\frac{n(>S)}{n_0(>S)} = \mu^{\alpha-1} . \tag{3.18}$$

Thus for $\alpha > 1$ the source counts are enhanced, otherwise they are depleted. While the number counts are enhanced for bright quasars, a depletion is expected for the faint galaxies used in weak lensing studies (see Sect. 3.2).

In principle this *magnification bias* could be used to measure the local strength of the distortion, for example in galaxy clusters. Although a depletion in local number counts has been reported for some clusters (Fort et al. 1997; Dye et al. 2002; Taylor et al. 1998; Dye et al. 2001), this approach is limited by our lack of knowledge of the un-lensed galaxy number counts at a particular position (galaxies tend to be clustered, see Sect. 2.2). A much more successful approach is to estimate the local shear from the ellipticities of background galaxies, which will be discussed in the next section.

## 3.2 Principles of weak gravitational lensing

In the close vicinity of massive galaxy clusters, highly distorted images of background galaxies can be observed (see Fig. 3.4). Further away from the central regions, the tidal gravitational forces distort the images only slightly. This *weak lensing* effect cannot be measured from single galaxies, but can only be studied statistically by investigating an ensemble of background galaxies.

The goal of basically all weak lensing studies is to learn something about the matter distribution of the lens and thus the convergence field $\kappa$, which however cannot be measured directly. In Section 3.2.1, I will first illustrate how the local shear field can be measured from the ellipticities

Figure 3.4: HST/ACS image of the most X-ray-luminous galaxy cluster RXJ1347–1145. Around the bright cluster galaxies several giant arcs and arclets can be seen, which are highly distorted and magnified images of faint background galaxies. (Credits: Schrabback, Erben; NASA, ESA, AIfA)

of background galaxies. In Section 3.2.2, I will then show that $\kappa$ can in principle be inferred from the shear field $\gamma$, up to the so-called mass-sheet degeneracy (see Eq. 3.31). The practical difficulties for measuring the shear are discussed in Section 3.4. I will limit the discussion to the case $\kappa \ll 1$ and $|\gamma| \ll 1$. This limitation may not be correct in the inner regions of massive galaxy clusters, but is perfectly applicable in cosmic shear studies (see Sect. 3.3).

### 3.2.1 Ellipticities as a measure of shear

The local gravitational shear distorts the image of background sources. As discussed in Sect. 3.1.3, round sources are transformed into ellipses. Thus, if all galaxies were intrinsically circular, the shear could directly be estimated from the shape of the observed galaxies. However, with galaxies being intrinsically elliptical, the shear cannot be measured from single galaxies. Yet, it is reasonable to assume that the intrinsic orientation of galaxies is random. Thus the local shear can be estimated by averaging over an ensemble of background galaxies, if the strength of the shear exceeds the Poisson noise from the intrinsic ellipticities.

The shapes of galaxies can be very irregular, in which case they are only poorly represented by ellipses. Since gravitational lensing conserves surface brightness, it is convenient to define the ellipticity of a galaxy in terms of its second-order brightness moments:

$$Q_{ij} = \frac{\int \mathrm{d}^2\theta\, \theta_i \theta_j I(\boldsymbol{\theta})}{\int \mathrm{d}^2\theta\, I(\boldsymbol{\theta})}\,, \quad i,j \in \{1,2\}\,, \tag{3.19}$$

with the surface brightness distribution $I(\boldsymbol{\theta})$. $\boldsymbol{\theta}$ is the position relative to the centre of the galaxy, which is chosen such that the first moment of the brightness distribution vanishes:

$$\int \mathrm{d}^2\theta\, \boldsymbol{\theta} I(\boldsymbol{\theta}) = 0\,. \tag{3.20}$$

The shape of a galaxy is usually quantified by a complex ellipticity, for which the most widely used definitions are given by

$$\chi = \chi_1 + \mathrm{i}\chi_2 = \frac{Q_{11} - Q_{22} + 2\mathrm{i}Q_{12}}{Q_{11} + Q_{22}}\,, \tag{3.21}$$

$$\epsilon = \epsilon_1 + \mathrm{i}\epsilon_2 = \frac{Q_{11} - Q_{22} + 2\mathrm{i}Q_{12}}{Q_{11} + Q_{22} + 2\sqrt{Q_{11}Q_{22} - Q_{12}^2}}\,. \tag{3.22}$$

The ellipticity definitions are interrelated as

$$\chi = \frac{2\epsilon}{1 + |\epsilon|^2}\,, \quad \epsilon = \frac{\chi}{1 + \sqrt{1 - |\chi|^2}}\,. \tag{3.23}$$

For an image with elliptical isophotes these ellipticity definitions are connected to the ratio of the major and minor axes of the ellipse $a$ and $b$, and to the position angle of the major axis $\phi$ by

$$\chi = \frac{1 - r^2}{1 + r^2} \mathrm{e}^{2\mathrm{i}\phi}\,, \quad r \equiv \frac{b}{a} \tag{3.24}$$

$$\epsilon = \frac{1 - r}{1 + r} \mathrm{e}^{2\mathrm{i}\phi}\,, \tag{3.25}$$

where the factor $2\phi$ in the exponent signifies that an ellipse is invariant under rotations by $\pi$.

Seitz & Schneider (1995) showed that the transformation between the source ellipticity $\chi^{(s)}$ and the image ellipticity $\chi$ is given by

$$\chi^{(s)} = \frac{\chi - 2g + g^2\chi^*}{1 + |g|^2 - 2\Re(g\chi^*)}\,, \tag{3.26}$$

where the asterisk denotes complex conjugation, and we have defined the reduced shear

$$g = \frac{\gamma}{1-\kappa}\,. \tag{3.27}$$

In terms of the ellipticity $\epsilon$ the transformation (3.26) reads

$$\epsilon^{(s)} = \begin{cases} \frac{\epsilon - g}{1 - g^*\epsilon} & \text{for } |g| \leq 1 \\ \frac{1 - g\epsilon^*}{\epsilon^* - g^*} & \text{for } \quad |g| > 1\,, \end{cases} \tag{3.28}$$

as shown by Seitz & Schneider (1997).

Assuming the Universe is statistically isotropic, the intrinsic orientation of galaxies is random, and hence the expectation value of the source ellipticity is zero:

$$\langle \chi^{(s)} \rangle = 0 = \langle \epsilon^{(s)} \rangle\,. \tag{3.29}$$

Therefore, in the weak lensing regime ($\kappa \ll 1$, $|\gamma| \ll 1$, and thus $|g| \ll 1$) the expectation value of the observed ellipticity is given by

$$\frac{1}{2}\langle \chi \rangle \approx \langle \epsilon \rangle = g = \frac{\gamma}{1-\kappa} \approx \gamma\,. \tag{3.30}$$

Hence, the ellipticity of each galaxy is an unbiased, but very noisy, estimator for the local (reduced) shear.

The reduced shear $g$ is invariant under the transformation

$$\kappa \mapsto \kappa' : \kappa' = \lambda\kappa + (1 - \lambda)\,, \tag{3.31}$$

which is equivalent to multiplying $\mathcal{A}$ in (3.13) by a factor $\lambda$ implying a transformation $\gamma \mapsto \gamma'$ : $\gamma' = \lambda\gamma$. Thus, replacing $\kappa$ by a scaled version of $\kappa$ and adding a mass–sheet of constant surface mass density does not change the measured ellipticities. This means that from the observed image distortions alone, $\kappa$ can only be inferred up to this so-called *mass–sheet degeneracy*.

From (3.16) follows $\mu \propto \lambda^{-2}$. Therefore the mass–sheet degeneracy can be lifted, if magnification effects are also taken into account, e.g. by measuring the magnification bias (see Sect. 3.1.3). According to Eqs. (3.6) and (3.7), $\kappa$ depends on the distances in the lens system. Thus, the discussion above strictly holds only if all sources are at the same redshift. By observing galaxies which are distributed in redshift, the mass–sheet degeneracy is in fact weakly broken (Seitz & Schneider 1997; Bradač et al. 2004).

### 3.2.2 Mass reconstruction

According to (3.14), both the convergence and the shear are second derivatives of the deflection potential. Therefore, the convergence field can in principle be recovered from the shear field. However, such a reconstruction is limited by the mass–sheet degeneracy, which was discussed in the last subsection. If we take the Fourier transforms of the fields involved

$$\hat{\kappa}(\boldsymbol{l}) = \int \mathrm{d}^2\theta\, \kappa(\boldsymbol{\theta})\, \mathrm{e}^{\mathrm{i}\boldsymbol{l}\cdot\boldsymbol{\theta}}\,, \quad \hat{\gamma}_j(\boldsymbol{l}) = \int \mathrm{d}^2\theta\, \gamma_j(\boldsymbol{\theta})\, \mathrm{e}^{\mathrm{i}\boldsymbol{l}\cdot\boldsymbol{\theta}}\,, \quad \hat{\Psi}(\boldsymbol{l}) = \int \mathrm{d}^2\theta\, \Psi(\boldsymbol{\theta})\, \mathrm{e}^{\mathrm{i}\boldsymbol{l}\cdot\boldsymbol{\theta}}\,, \tag{3.32}$$

with $j \in \{1, 2\}$ and the two-dimensional wave vector $\boldsymbol{l}$, Eqs. (3.14) read in Fourier space

$$\begin{aligned} \hat{\kappa}(\boldsymbol{l}) &= -\frac{1}{2}(l_1^2 + l_2^2)\hat{\Psi}(\boldsymbol{l}) \\ \hat{\gamma}_1(\boldsymbol{l}) &= -\frac{1}{2}(l_1^2 - l_2^2)\hat{\Psi}(\boldsymbol{l}) \\ \hat{\gamma}_2(\boldsymbol{l}) &= -l_1 l_2 \hat{\Psi}(\boldsymbol{l})\,. \end{aligned} \tag{3.33}$$

Thus, in Fourier space the convergence and the shear are related as

$$\hat{\kappa} = \frac{1}{l_1^2 + l_2^2}\left((l_1^2 - l_2^2)\hat{\gamma}_1 + (2l_1 l_2)\hat{\gamma}_2\right)\,. \tag{3.34}$$

(3.34) is not defined for $|\boldsymbol{l}| = 0$, which actually leads to the mass-sheet degeneracy. By transforming (3.34) back into real space we find that the convergence can be expressed as a convolution of the shear

$$\kappa(\boldsymbol{\theta}) - \kappa_0 = \frac{1}{\pi}\int_{\mathbb{R}^2} \mathrm{d}^2\theta'\, \mathcal{D}^*(\boldsymbol{\theta} - \boldsymbol{\theta}')\gamma(\boldsymbol{\theta}') \tag{3.35}$$

with the complex kernel

$$\mathcal{D}(\boldsymbol{\theta}) = \frac{\theta_2^2 - \theta_1^2 - 2\mathrm{i}\theta_1\theta_2}{|\boldsymbol{\theta}|^4}\,, \tag{3.36}$$

which was first found by Kaiser & Squires (1993). Here the asterisk denotes the complex conjugate. In principle, $\kappa(\boldsymbol{\theta})$ should be real. However, noise in real data can produce an imaginary component. To ensure that $\kappa$ is real, usually only the real part of the integrand in (3.35) is taken into account. Since the integration in (3.14) has to be performed over the entire $\boldsymbol{\theta}'$ plane, this method should not be applied to finite and thus realistic data fields. Different finite field inversion algorithms have been developed to solve this problem (Kaiser 1995; Seitz & Schneider 2001; Hu & Keeton 2002).

Schneider (1996) introduced the *aperture mass* or $M_{\mathrm{ap}}$ statistic

$$M_{\mathrm{ap}}(\boldsymbol{\theta}) = \int \mathrm{d}^2\theta'\, \kappa(\boldsymbol{\theta}')U(\boldsymbol{\theta} - \boldsymbol{\theta}')\,, \tag{3.37}$$

which measures a weighted integral of the local surface mass density around a point $\boldsymbol{\theta}$. Often a circular aperture and a compensated filter function $U(\theta = |\boldsymbol{\theta} - \boldsymbol{\theta}'|)$ with

$$\int_0^{\vartheta} \mathrm{d}\theta\, \theta\, U(\theta) = 0 \tag{3.38}$$

and $U(\theta) = 0$ for $\theta > \vartheta$ are used. Schneider (1996) showed that $M_{\rm ap}$ can then be expressed in terms of the *tangential component* of the shear

$$\gamma_{\rm t} = -\Re\left(\gamma \mathrm{e}^{-2\mathrm{i}\phi}\right), \tag{3.39}$$

with the polar angle $\phi$ relative to the centre of the aperture. The aperture mass is then given by

$$M_{\rm ap}(\boldsymbol{\theta}) = \int_{|\boldsymbol{\theta}-\boldsymbol{\theta}'|\le\vartheta} \mathrm{d}^2\theta' \gamma_{\rm t}(\boldsymbol{\theta}') Q(|\boldsymbol{\theta}-\boldsymbol{\theta}'|), \tag{3.40}$$

where the filter function $Q(\theta)$ is given in terms of the filter function $U(\theta)$ by

$$Q(\theta) = \frac{2}{\theta^2}\int_0^\theta \mathrm{d}\theta'\, \theta' U(\theta') - U(\theta). \tag{3.41}$$

Analogously we define

$$M_\perp(\boldsymbol{\theta}) = \int_{|\boldsymbol{\theta}-\boldsymbol{\theta}'|\le\vartheta} \mathrm{d}^2\theta' \gamma_\times(\boldsymbol{\theta}') Q(|\boldsymbol{\theta}-\boldsymbol{\theta}'|) \tag{3.42}$$

for the *cross component* of the shear relative to the centre of the aperture

$$\gamma_\times = -\Im\left(\gamma\, \mathrm{e}^{-2\mathrm{i}\phi}\right). \tag{3.43}$$

Note that $M_\perp(\boldsymbol{\theta})$ is expected to vanish for pure lensing (see Sect. 3.3.3).

For the filter functions we use a form proposed by Schneider et al. (1998)

$$U(\theta) = \frac{9}{\pi\vartheta^2}\left[1-\left(\frac{\theta}{\vartheta}\right)^2\right]\left[\frac{1}{3}-\left(\frac{\theta}{\vartheta}\right)^2\right]\mathrm{H}(\vartheta-\theta), \tag{3.44}$$

where $\mathrm{H}(\vartheta-\theta)$ denotes the Heaviside step function, leading to

$$Q(\theta) = \frac{6}{\pi\vartheta^2}\left(\frac{\theta}{\vartheta}\right)^2\left[1-\left(\frac{\theta}{\vartheta}\right)^2\right]\mathrm{H}(\vartheta-\theta). \tag{3.45}$$

## 3.3 Cosmological weak lensing

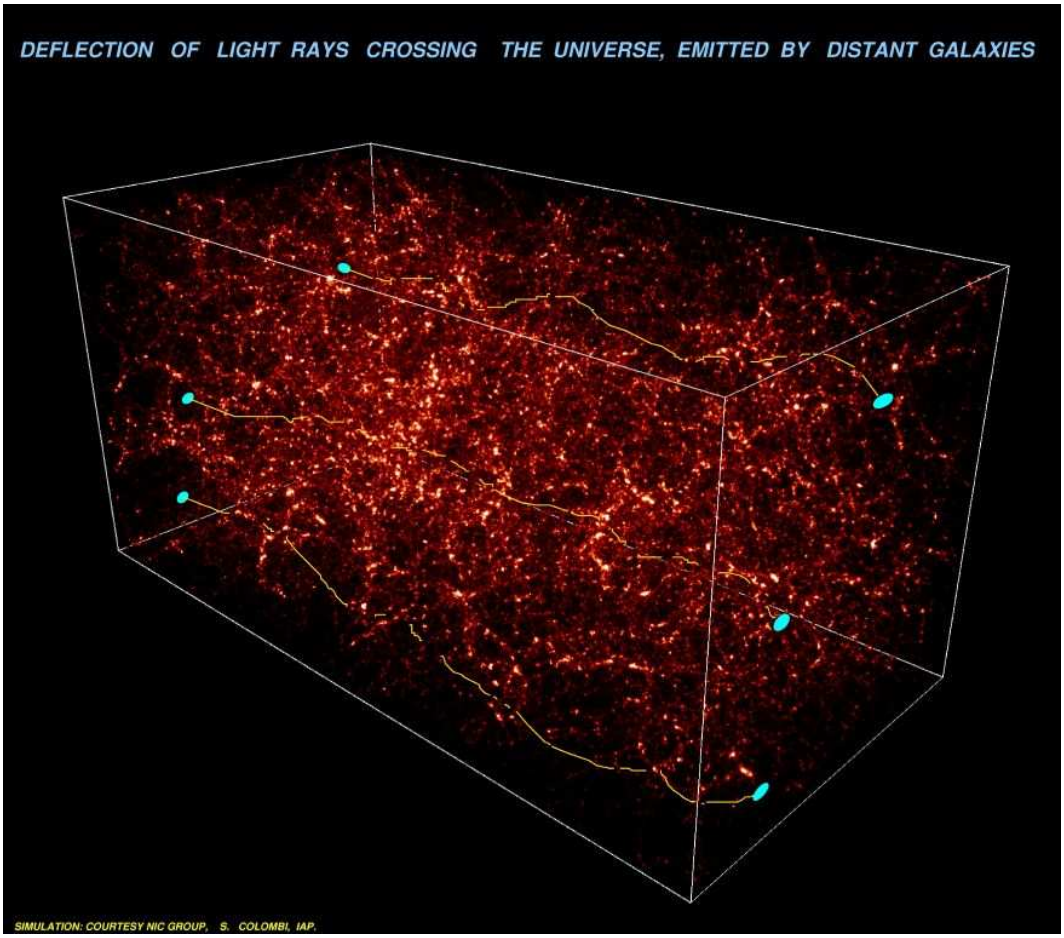


Figure 3.5: Illustration of cosmic shear: In this figure N–body simulations of dark matter particles by S. Colombi are shown. Brighter colours indicate denser regions. The three blue ellipses in the rear represent distant galaxies. Light rays emitted from these galaxies are continuously deflected and distorted due to the inhomogeneous gravitational field created by the matter density fluctuations. The deflections shown here are highly exaggerated to illustrate the effect. (Image credit: DESCART project at IAP, France)

In the previous sections, I summarised gravitational lensing by relatively localised lenses, which can be approximated by a single mass sheet. This approximation can be made, if very massive objects like galaxy clusters act as lenses, since they dominate the integrated mass on the line-of-sight to background galaxies. In this section, I will summarise the theory of *cosmic shear*, which is also termed *cosmological weak lensing* and describes weak lensing by large-scale structure. Here, light rays are continuously deflected and distorted while travelling through the inhomogeneous gravitational potential created by the density fluctuations (illustrated in Figure

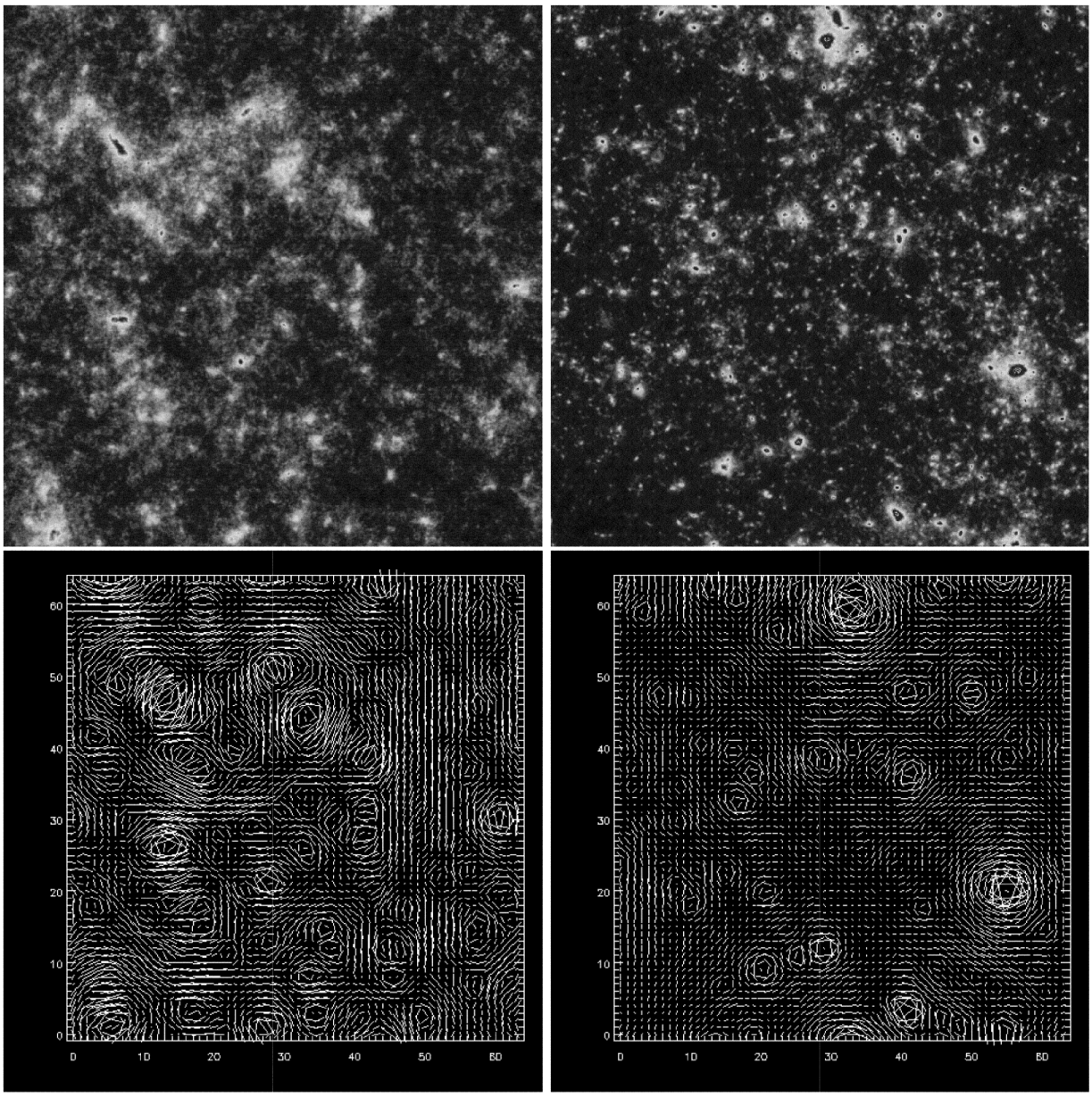


Figure 3.6: Ray tracing through N-body simulations by Jain, Seljak, & White (2000). The top two panels show the magnification, whereas the lower two panels indicate the corresponding shear field for sources at a redshift $z_s = 1$. The *left* panels correspond to an Einstein-de Sitter cosmology and the *right* panels to an open model with $\Omega_m = 0.3$. The two cosmological models can be distinguished from the statistics of the shear field, which is stronger correlated for the EdS model. The field size is $1^\circ \times 1^\circ$. (Figures 5 and 6 of Jain, Seljak, & White 2000)

3.5). Thus a more general theoretical description is required. The statistics of the shear field reflect the statistics of the large-scale structure of the Universe. Therefore, measurements of the strength of cosmic shear are a powerful tool to probe the dark matter distribution of the Universe and therewith distinguish between different cosmological models. Jain, Seljak, & White (2000) demonstrated this with ray tracing calculations through N-body simulations for two different cosmological models, shown in Fig. 3.6. In this section I will partially follow the train of thought as presented in Schneider et al. (2006).

### 3.3.1 Gravitational lensing by the 3-D matter distribution

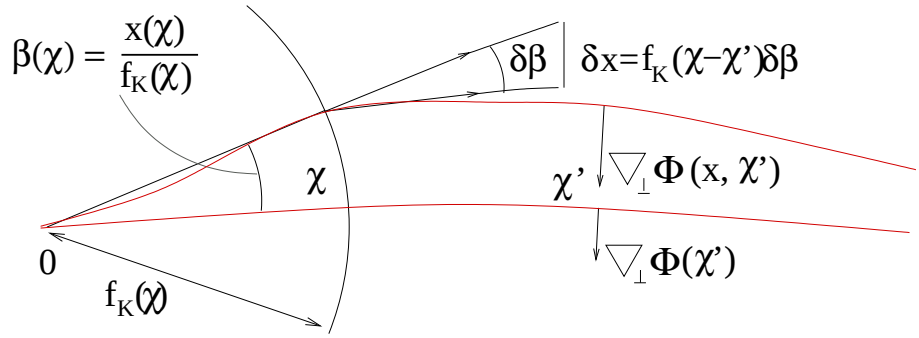


Figure 3.7: Illustration of light propagation in an inhomogeneous universe: In this sketch two light rays are shown, which intersect at the position $\chi = 0$ of an observer. The propagation of the upper light ray is considered relatively to the lower fiducial ray. At a comoving distance $\chi$ the light rays have a transverse separation $\boldsymbol{x}(\chi)$, which in the absence of lensing would appear under an angular separation $\boldsymbol{\beta}(\chi)$ as seen by the observer. Both light rays are continuously deflected by the gravitational potential of the mass inhomogeneities in the universe, where the relative deflection depends on the difference of the transverse gradient $\nabla_\perp$ of the Newtonian potential along both paths.

In order to investigate the deflection of light in the inhomogeneous Universe, we consider a light ray propagating from a source relative to a fiducial ray (Fig. 3.7). For the relevant case of weak gravitational fields ($\Phi \ll c^2$), which typically vary on scales much smaller than the curvature scale of the Universe, and matter with non-relativistic motions, the comoving separation $\boldsymbol{x}(\boldsymbol{\theta},\chi)$ between the two light rays, which are separated by an angle $\boldsymbol{\theta}$ at the observer, obeys the propagation equation

$$\frac{\mathrm{d}^2\boldsymbol{x}}{\mathrm{d}\chi^2} + K\boldsymbol{x} = -\frac{2}{c^2}\left[\nabla_\perp\Phi(\boldsymbol{x}(\boldsymbol{\theta},\chi),\chi) - \nabla_\perp\Phi^{(0)}(\chi)\right], \tag{3.46}$$

with the comoving radial distance $\chi$, the spatial curvature $K$ as defined in (2.17), and the Newtonian gravitational potential along the light ray $\Phi(\boldsymbol{x}(\boldsymbol{\theta},\chi),\chi)$ and along the fiducial ray $\Phi^{(0)}(\chi)$. $\nabla_\perp = (\partial/\partial x_1, \partial/\partial x_2)$ denotes the transverse comoving gradient operator. A derivation of (3.46) can for example be found in Bartelmann & Schneider (2001).

(3.46) can formally be solved by the method of Green's functions yielding

$$\boldsymbol{x}(\boldsymbol{\theta},\chi) = f_K(\chi)\,\boldsymbol{\theta} - \frac{2}{c^2}\int_0^\chi \mathrm{d}\chi'\, f_K(\chi-\chi')\left[\nabla_\perp\Phi(\boldsymbol{x}(\boldsymbol{\theta},\chi'),\chi') - \nabla_\perp\Phi^{(0)}(\chi')\right], \tag{3.47}$$

where $f_K(\chi)$ was defined in (2.3). Without lensing the source would be seen at the angular separation $\boldsymbol{\beta}(\chi) = \boldsymbol{x}(\chi)/f_K(\chi)$ from the fiducial ray. Therefore, $\boldsymbol{\beta}$ can be interpreted as the unlensed angular position in a hypothetical source plane at a comoving distance $\chi$. In analogy with standard lens theory we can then calculate the Jacobian matrix

$$\begin{aligned}\mathcal{A}_{ij}(\boldsymbol{\theta},\chi) &= \frac{\partial\beta_i}{\partial\theta_j} = \frac{1}{f_K(\chi)}\frac{\partial x_i}{\partial\theta_j} \\ &= \delta_{ij} - \frac{2}{c^2}\int_0^\chi \mathrm{d}\chi'\,\frac{f_K(\chi-\chi')f_K(\chi')}{f_K(\chi)}\frac{\partial^2\Phi(\boldsymbol{x}(\boldsymbol{\theta},\chi'),\chi')}{\partial x_i\partial x_k}\mathcal{A}_{kj}(\boldsymbol{\theta},\chi')\end{aligned} \tag{3.48}$$

to describe the locally linearised lens mapping. Expanding $\mathcal{A}$ in powers of $\Phi$ and truncating non-linear terms yields

$$\mathcal{A}_{ij}(\boldsymbol{\theta},\chi) = \delta_{ij} - \frac{2}{c^2}\int_0^\chi \mathrm{d}\chi'\,\frac{f_K(\chi-\chi')f_K(\chi')}{f_K(\chi)}\frac{\partial^2\Phi(\boldsymbol{x}=f_K(\chi')\boldsymbol{\theta},\chi')}{\partial x_i\partial x_j}\,. \tag{3.49}$$

Therefore, in first-order of $\Phi$, the distortion can be approximated by an integral along the unperturbed ray $\boldsymbol{x} = f_K(\chi)\boldsymbol{\theta}$, whereas corrections are of order $\Phi^2$. This approach corresponds to the Born approximation, and is justified because the expected deflections are small. We define the deflection potential

$$\Psi(\boldsymbol{\theta},\chi) \equiv \frac{2}{c^2}\int_0^\chi \mathrm{d}\chi'\,\frac{f_K(\chi-\chi')}{f_K(\chi)f_K(\chi')}\Phi(f_K(\chi')\boldsymbol{\theta},\chi')\,, \tag{3.50}$$

for which

$$\mathcal{A}_{ij} = \delta_{ij} - \frac{\partial^2\Psi}{\partial\theta_i\partial\theta_j} \tag{3.51}$$

holds similarly to (3.12) in the thin lens approximation. Hence, lensing by the large-scale structure can be treated as lensing by a lens plane with effective deflection potential $\Psi$. Correspondingly to (3.14) we define the effective mass density $\kappa$ and shear $\gamma$ as

$$\kappa = \frac{1}{2}\left(\Psi_{,11}+\Psi_{,22}\right), \text{and} \tag{3.52}$$

$$\gamma = \frac{1}{2}\left(\Psi_{,11}-\Psi_{,22}\right) + \mathrm{i}\Psi_{,12}\,. \tag{3.53}$$

Using the three-dimensional Poisson equation in comoving coordinates

$$\Delta\Phi = \frac{3H_0^2\Omega_\mathrm{m}}{2}\frac{\delta}{a}\,, \tag{3.54}$$

we can express $\kappa$ in terms of the density contrast $\delta$ as

$$\begin{aligned}\kappa(\boldsymbol{\theta}, w) &= \frac{1}{c^2}\int_0^{\chi} \mathrm{d}\chi' \, \frac{f_K(\chi-\chi')\, f_K(\chi')}{f_K(\chi)} \left[\frac{\partial^2}{\partial x_1^2} + \frac{\partial^2}{\partial x_2^2}\right] \Phi(f_K(\chi')\boldsymbol{\theta}, \chi') \\ &= \frac{3H_0^2\Omega_\mathrm{m}}{2c^2}\int_0^{\chi} \mathrm{d}\chi' \, \frac{f_K(\chi-\chi')\, f_K(\chi')}{f_K(\chi)} \frac{\delta(f_K(\chi')\boldsymbol{\theta}, \chi')}{a(\chi')}\,, \end{aligned} \tag{3.55}$$

where we used the fact that the line-of-sight integration of $(\partial^2/\partial x_3^2)\Phi$ gives an average contribution of zero.

The convergence $\kappa$ depends on the distance $\chi$ to the source. For sources distributed in redshift according to $p_z(z)\mathrm{d}z = p_\chi(\chi)\mathrm{d}\chi$, the effective surface mass density reads

$$\kappa(\boldsymbol{\theta}) = \int \mathrm{d}\chi \, p_\chi(\chi)\kappa(\boldsymbol{\theta}, \chi) = \frac{3H_0^2\Omega_\mathrm{m}}{2c^2}\int_0^{\chi_\mathrm{h}} \mathrm{d}\chi \, g(\chi) f_K(\chi) \frac{\delta(f_K(\chi)\boldsymbol{\theta}, \chi)}{a(\chi)}\,, \tag{3.56}$$

with the effective source-redshift weighted lens efficiency factor

$$g(\chi) = \int_\chi^{\chi_\mathrm{h}} \mathrm{d}\chi' \, p_\chi(\chi') \frac{f_K(\chi'-\chi)}{f_K(\chi')}\,, \tag{3.57}$$

where $\chi_\mathrm{h} = D_\mathrm{com}(0, \infty)$ denotes the distance to the horizon.

We define the power spectrum $P_\kappa(l)$ of the convergence by

$$\langle \hat{\kappa}(\boldsymbol{l})\hat{\kappa}(\boldsymbol{l}')\rangle = (2\pi)^2 \delta_\mathrm{D}(\boldsymbol{l}+\boldsymbol{l}')P_\kappa(l)\,, \tag{3.58}$$

where $\hat{\kappa}$ is the Fourier transform of the convergence as defined in (3.32). The convergence power spectrum is related to the three-dimensional power spectrum $P_\delta$, which was discussed in Sect. 2.2, by

$$P_\kappa(l) = \frac{9H_0^4\Omega_\mathrm{m}^2}{4c^4}\int_o^{\chi_\mathrm{h}} \mathrm{d}\chi \frac{g^2(\chi)}{a^2(\chi)} P_\delta\left(\frac{l}{f_K(\chi)}, \chi\right). \tag{3.59}$$

Therefore, observations which constrain $P_\kappa$ also yield information about $P_\delta$. Theoretical predictions for the convergence power spectrum are plotted in Fig. 3.8. From these plots it can be seen that the non-linear evolution dominates the power spectrum for angular scales below $30'$, which correspond to wave numbers $l \geq 200$. A derivation of (3.59) can be found in Kaiser (1998).

Following from the definitions of the convergence and the shear in Eqs. (3.52) and (3.53), their Fourier transforms are related by

$$\hat{\gamma}(\boldsymbol{l}) = \mathrm{e}^{2\mathrm{i}\phi}\hat{\kappa}(\boldsymbol{l})\,, \tag{3.60}$$

with the polar angle $\phi$ of the wave vector $\boldsymbol{l}$. Hence, the two-point correlation functions of the Fourier transformed convergence and shear are identical:

$$\langle \hat{\gamma}(\boldsymbol{l})\hat{\gamma}^*(\boldsymbol{l}')\rangle = \langle \hat{\kappa}(\boldsymbol{l})\hat{\kappa}^*(\boldsymbol{l}')\rangle\,, \tag{3.61}$$

and the convergence power spectrum can directly be calculated from the shear correlation function.

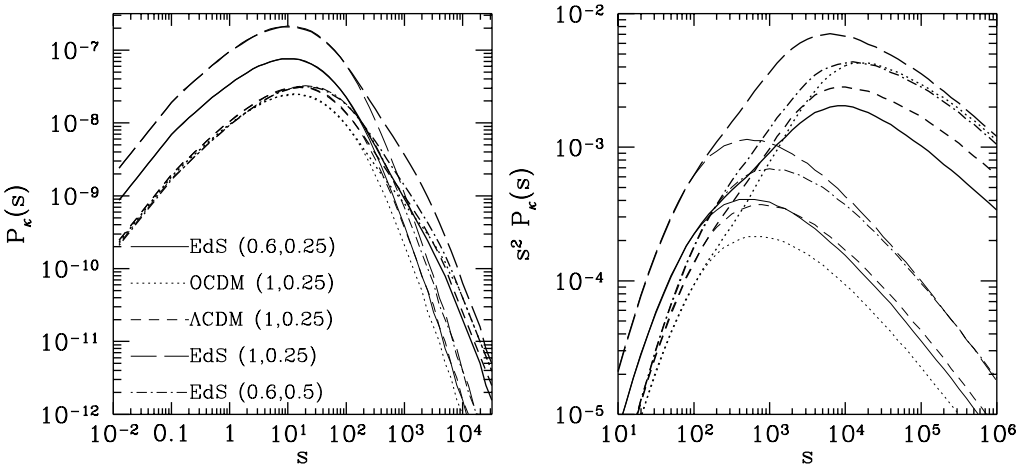


Figure 3.8: The convergence power spectrum $P_\kappa(l)$ (*left* panel) and its dimensionless form $l^2 P_\kappa(l)$ (*right* panel) plotted for different cosmological models (abbreviations see Table 2.1). For the power spectra shown, a mean redshift of the galaxy distribution of $\langle z_s \rangle = 1.5$ was assumed. While the thin curves were calculated taking into account linear evolution only, the thick curves were derived using the fully non-linear evolution according to Peacock & Dodds (1996). For wave numbers $l \geq 200$, which correspond to angular scales below $30'$, the non-linear evolution leads to much stronger power. (Figure from Schneider et al. 1998)

## 3.3.2 Cosmic shear measures and theoretical predictions

In this subsection I will discuss statistical measures for the shear and theoretical predictions for their values on different scales.

### 3.3.2.1 The shear dispersion

By measuring the mean shear $\overline{\gamma}(\theta)$ in a circular aperture of radius $\theta$, we can define the shear dispersion $\langle|\overline{\gamma}|^2\rangle(\theta) = \langle\overline{\gamma}\overline{\gamma}^*\rangle(\theta)$. Here the average denoted by $\langle ... \rangle$ is defined as the ensemble average over many independent circular apertures, which all contain different realisations of the shear field. When the shear dispersion is practically measured, it has to be ensured that many independent lines-of-sight are probed, in order to reduce the influence of cosmic variance. It can be shown that the shear dispersion is related to the convergence power spectrum by

$$\langle|\overline{\gamma}|^2\rangle(\theta) = \langle\overline{\gamma}\overline{\gamma}^*\rangle(\theta) = \frac{1}{2\pi}\int \mathrm{d}l\, l P_\kappa(l) W_{\mathrm{TH}}(l\theta)\,, \tag{3.62}$$

with the top-hat filter function $W_{\mathrm{TH}}(\eta) = 4\mathrm{J}_1^2(\eta)/\eta^2$. $\mathrm{J}_n$ denotes the $n^{\mathrm{th}}$-order Bessel function of the first kind. In Figure 3.9, the predicted shear dispersion for different cosmological models is plotted in dependence of the aperture radius $\theta$. The shear dispersion increases towards small $\theta$ for all cosmological models, which is due to the fact that light rays coming from galaxies closely separated in the sky travel through similar regions of the large-scale structure. The predicted

shear dispersion is plotted both for the case of purely linear structure growth and for the case of non-linear evolution according to the description of Peacock & Dodds (1996). On scales below $10'$ the non-linear evolution becomes important and creates a much stronger shear signal.

By comparing measurements of the shear dispersion at different scales with these theoretical predictions, one can discriminate between different cosmological models. To first order, the amplitude of the shear signal is proportional to $\sigma_8\Omega_\mathrm{m}^{0.6}$. Qualitatively these dependencies can easily be understood, since an increase of the normalisation $\sigma_8$ directly increases $P_\delta$ and therefore also $P_\kappa$. A higher $\Omega_\mathrm{m}$ also leads to an increase of the shear signal, since gravitational lensing depends on $\Delta\rho$ and not only the relative density contrast $\delta = \Delta\rho/\rho$. The quantitative dependence on $\Omega_\mathrm{m}^{0.6}$ is only approximate and has been found by fitting likelihood contours in cosmological parameter estimations (e.g. Heymans et al. 2005). The shear signal additionally increases with the mean value of the source redshift distribution, which is due to two effects: First, higher redshift galaxies are deflected along a longer path through the inhomogeneous matter distribution. Second, the lens efficiency given by (3.57), which depends on the factor $f_K(\chi' - \chi)/f_K(\chi')$, increases for sources at higher redshifts $z(\chi')$.

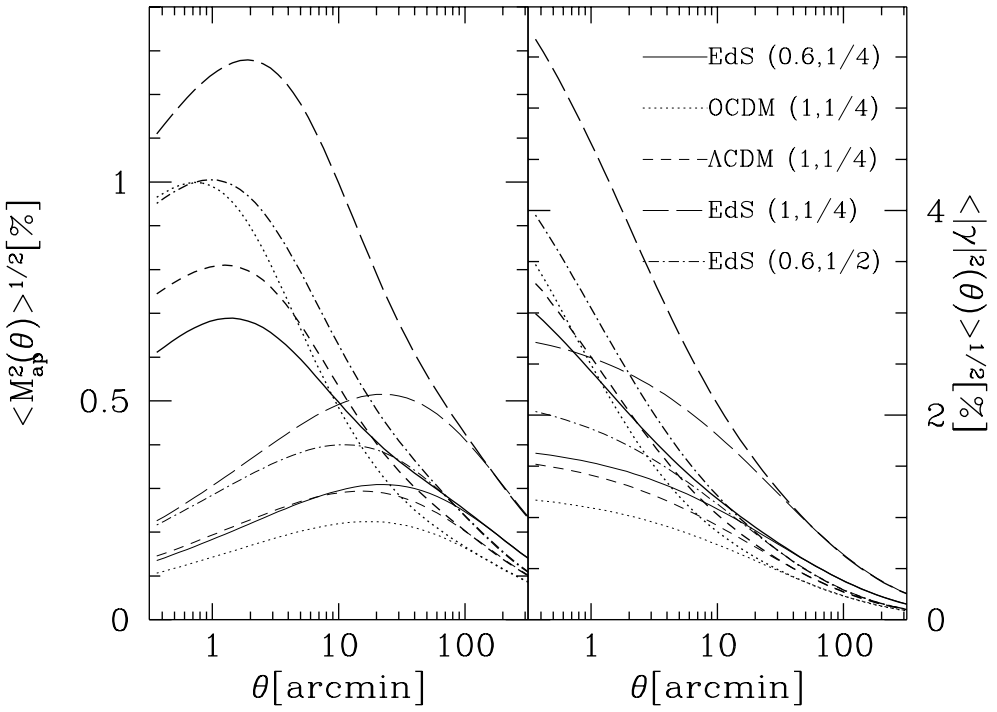


Figure 3.9: The square root of the aperture mass dispersion (*left*) and the shear dispersion (*right*) in dependence of the aperture radius $\theta$ for the same cosmological models as in Fig. 3.8. Again thin curves correspond to purely linear structure growth, whereas the thick curves have been calculated with the fully non-linear evolution as described in Peacock & Dodds (1996). (Figure from Schneider et al. 1998)

#### 3.3.2.2 The aperture mass dispersion

Similarly to the shear dispersion one can define the dispersion of the aperture mass in a circular aperture with radius $\theta$ as given in (3.40), which is related to the convergence power spectrum by

$$\langle M_{\rm ap}^2\rangle(\theta) = 2\pi \int_0^\infty {\rm d}l l P_\kappa(l) \left[\int_0^\theta {\rm d}\vartheta \vartheta U(\vartheta) {\rm J}_0(l\vartheta)\right]^2 , \tag{3.63}$$

where $\langle ...\rangle$ again denotes the ensemble average. For weight functions $U$ and $Q$ as defined in Eqs. (3.44) and (3.45), (3.63) reads

$$\langle M_{\rm ap}^2\rangle(\theta) = \frac{1}{2\pi} \int_0^\infty {\rm d}l\, l\, P_\kappa(l) W_{\rm ap}(\theta l) , \tag{3.64}$$

with

$$W_{\rm ap}(\eta) \equiv \frac{576}{\eta^4} {\rm J}_4^2(\eta) . \tag{3.65}$$

The theoretically predicted aperture mass dispersion is plotted in Fig. 3.9 for various cosmological models and the cases of purely linear and also non-linear structure growth. The dependence on the cosmological parameters is similar to the dependence of the shear dispersion as discussed above. Note that the filter function $W_{\rm ap}$ in (3.64) is much more localised than the wide filter function $W_{\rm TH}$ used for the shear dispersion. Therefore, the aperture mass dispersion measures the convergence power spectrum highly localised at a scale of $l \sim 5/\theta$ (Schneider et al. 1998). However, the higher resolution is gained on the cost of less power, since only a narrow range of wave numbers $l$ contributes.

#### 3.3.2.3 The shear correlation functions

A very important estimate for the cosmic shear is the shear two-point correlation function $\langle\gamma\gamma\rangle_\theta$ for pairs of points with separation $\theta$ (e.g. pairs of galaxies). With the polar angle $\varphi$ of their separation vector, we define the tangential and cross-component of the shear at their positions for this pair as

$$\gamma_{\rm t} = -\Re(\gamma\, {\rm e}^{-2{\rm i}\varphi}) , \quad \gamma_\times = -\Im(\gamma\, {\rm e}^{-2{\rm i}\varphi}) , \tag{3.66}$$

and the following shear correlation functions

$$\xi_\pm(\theta) = \langle\gamma_{\rm t}\gamma_{\rm t}\rangle(\theta) \pm \langle\gamma_\times\gamma_\times\rangle(\theta) , \quad \xi_\times(\theta) = \langle\gamma_{\rm t}\gamma_\times\rangle(\theta) . \tag{3.67}$$

Under parity transformation $\xi_\times$ changes sign. Thus, it is expected to vanish if estimated from sufficiently many fields. The shear correlation functions are related to the convergence power spectrum by

$$\xi_+(\theta) = \frac{1}{2\pi} \int_0^\infty {\rm d}l\, l\, {\rm J}_0(l\theta) P_\kappa(l) , \quad \xi_-(\theta) = \frac{1}{2\pi} \int_0^\infty {\rm d}l\, l\, {\rm J}_4(l\theta) P_\kappa(l) . \tag{3.68}$$

#### 3.3.2.4 Interrelations of the shear measures

All of the second-order shear estimates discussed measure the convergence power spectrum, although with different filter functions. Therefore it can be expected that they are actually interrelated. This can be shown by first inverting (3.68) using the orthonormality of Bessel functions:

$$P_\kappa(l) = 2\pi \int_0^\infty \mathrm{d}\theta\, \theta\, \xi_+(\theta) \mathrm{J}_0(l\theta) = 2\pi \int_0^\infty \mathrm{d}\theta\, \theta\, \xi_-(\theta) \mathrm{J}_4(l\theta)\,, \tag{3.69}$$

which we can plug into (3.68) to yield the interrelation of the correlation functions:

$$\xi_+(\theta) = \xi_-(\theta) + \int_\theta^\infty \frac{\mathrm{d}\vartheta}{\vartheta} \xi_-(\vartheta) \left(4 - 12\frac{\theta^2}{\vartheta^2}\right), \tag{3.70}$$

$$\xi_-(\theta) = \xi_+(\theta) + \int_0^\theta \frac{\mathrm{d}\vartheta\,\vartheta}{\theta^2} \xi_+(\vartheta) \left(4 - 12\frac{\vartheta^2}{\theta^2}\right). \tag{3.71}$$

By inserting (3.69) into the equations for the shear dispersion (3.62) and the aperture mass dispersion (3.64), we find:

$$\langle|\overline{\gamma}|^2\rangle(\theta) = \int_0^{2\theta} \frac{\mathrm{d}\vartheta\,\vartheta}{\theta^2} \xi_+(\vartheta) S_+\left(\frac{\vartheta}{\theta}\right) = \int_0^\infty \frac{\mathrm{d}\vartheta\,\vartheta}{\theta^2} \xi_-(\vartheta) S_-\left(\frac{\vartheta}{\theta}\right), \tag{3.72}$$

$$\langle M_{\mathrm{ap}}^2\rangle(\theta) = \int_0^{2\theta} \frac{\mathrm{d}\vartheta\,\vartheta}{\theta^2} \xi_+(\vartheta) T_+\left(\frac{\vartheta}{\theta}\right) = \int_0^{2\theta} \frac{\mathrm{d}\vartheta\,\vartheta}{\theta^2} \xi_-(\vartheta) T_-\left(\frac{\vartheta}{\theta}\right), \tag{3.73}$$

with $S_\pm$ and $T_\pm$ as given in Schneider et al. (2002):

$$\begin{aligned}
S_+(x) &= \frac{1}{\pi}\left[4\arccos\left(\frac{x}{2}\right) - x\sqrt{4-x^2}\right]\mathrm{H}(2-x)\,,\\
S_-(x) &= \frac{x\sqrt{4-x^2}(6-x^2) - 8(3-x^2)\arcsin(x/2)}{\pi x^4}\,\mathrm{H}(2-x)\\
&\quad + \frac{4(x^2-3)}{x^4}\,\mathrm{H}(x-2)\,,\\
T_+(x) &= \left\{\frac{6(2-15x^2)}{5}\left[1 - \frac{2}{\pi}\arcsin\left(\frac{x}{2}\right)\right]\right.\\
&\quad \left. + \frac{x\sqrt{4-x^2}}{100\pi}(120 + 2320x^2 - 754x^4 + 132x^6 - 9x^8)\right\}\mathrm{H}(2-x)\,,\\
T_-(x) &= \frac{192}{35\pi}x^3\left(1 - \frac{x^2}{4}\right)^{7/2}\mathrm{H}(2-x)\,,
\end{aligned}$$

where H denotes the Heaviside function.

#### 3.3.2.5 Advantages of the shear correlation functions

For several reasons, the shear correlation functions $\xi_\pm$ are nowadays the preferred shear measure:

- The correlation functions contain the full information about the convergence power spectrum, which also allows one to calculate the other estimators directly from $\xi_\pm$ as seen above.

- Real data contains regions which cannot be used for the analysis, for example due to bright stars or CCD defects, making it difficult to employ circular apertures on the field. On the other hand, the correlation functions at scale $\theta$ can simply be measured by selecting all usable pairs of background galaxies on an image within a separation bin of width $\Delta\theta$ around the separation $\theta$.

- Practically, also the computing time for the correlation function is much shorter than e.g. for the shear dispersion, if estimated in many angular bins.

### 3.3.3 E-modes and B-modes

The deflection potential $\Psi$, which is given in (3.50), is a one-component (real) quantity, whereas the shear field $\gamma$, which is given in terms of $\Psi$ in (3.53), is a two-component (or complex) quantity. This implies that the two components of the shear cannot be independent. From Eqs. (3.52) and (3.53) follows

$$\nabla\kappa = \begin{pmatrix} \gamma_{1,1} + \gamma_{2,2} \\ \gamma_{2,1} - \gamma_{1,2} \end{pmatrix} = \boldsymbol{u}\,, \tag{3.74}$$

where we defined the gradient field $\boldsymbol{u}$. Although $\boldsymbol{u}$ is expected to be curl-free for pure lensing, noise in the data produces a curl component. A significantly non-zero curl component can be created by various effects like artefacts from the image co-addition or anisotropy correction, but also intrinsic alignment of sources. The gradient and the curl part of $\boldsymbol{u}$ can be projected out by taking another derivate

$$\nabla^2\kappa^{\mathrm{E}} = \nabla\cdot\boldsymbol{u}\,, \quad \nabla^2\kappa^{\mathrm{B}} = \nabla\times\boldsymbol{u} = u_{2,1} - u_{1,2}\,, \tag{3.75}$$

where we have defined the E-mode and B-mode components of $\kappa$, which are named after the similar decomposition of CMB polarisation into electric curl-free and magnetic curl modes. An alternative way to define these components is to introduce a complex part in (3.35)

$$\kappa^{\mathrm{E}}(\boldsymbol{\theta}) + \mathrm{i}\kappa^{\mathrm{B}}(\boldsymbol{\theta}) - \kappa_0 = \frac{1}{\pi}\int_{\mathbb{R}^2} \mathrm{d}^2\theta'\,\mathcal{D}^*(\boldsymbol{\theta}-\boldsymbol{\theta}')\gamma(\boldsymbol{\theta}')\,. \tag{3.76}$$

The different effects of E/B-modes are sketched in Fig. 3.10. In principle one can then define the E/B-mode components of the deflection potential $\psi(\boldsymbol{\theta}) = \psi^{\mathrm{E}}(\boldsymbol{\theta}) + \mathrm{i}\psi^{\mathrm{B}}(\boldsymbol{\theta})$ and the convergence power spectra $P_{\mathrm{E}}$ and $P_{\mathrm{B}}$ in full analogy to the case of pure lensing.

Crittenden et al. (2002) show that $\xi_\pm$ can be decomposed into the curl-free E-mode component $\xi^E(\theta)$ and the curl B-mode component $\xi^B(\theta)$ as

$$\xi^E(\theta) = \frac{\xi_+(\theta) + \xi'(\theta)}{2}\,, \quad \xi^B(\theta) = \frac{\xi_+(\theta) - \xi'(\theta)}{2}\,, \tag{3.77}$$

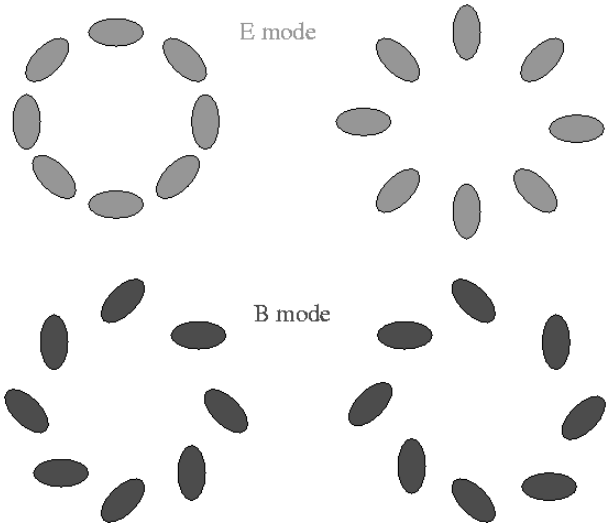


Figure 3.10: Illustration of the effect of curl-free shear modes (E-modes, *top* patterns) and curl modes (B-modes, *bottom* patterns) on intrinsically circular sources. E-modes can be produced by gravitational lensing. The *upper left* pattern corresponds to a local matter over-density and the *upper right* pattern to a local under-density. Probably, observed B-modes are due to systematic effects in the data analysis or intrinsic alignment of sources (figure from Van Waerbeke & Mellier 2003).

with

$$\xi'(\theta) = \xi_-(\theta) + 4\int_\theta^\infty \frac{\mathrm{d}\vartheta}{\vartheta}\xi_-(\vartheta) - 12\theta^2\int_\theta^\infty \frac{\mathrm{d}\vartheta}{\vartheta^3}\xi_-(\vartheta)\,. \tag{3.78}$$

Note that the integral in (3.78) formally extends to infinity. Thus, due to finite field size, real data require the substitution of the measured $\xi_-(\theta)$ with theoretical predictions for large $\theta$.

This problem does not occur for the aperture mass statistics, for which Crittenden et al. (2002) show that $M_{\rm ap}$ purely measures the E-mode signal, whereas $M_\perp$ contributes to the B-mode only:

$$\langle M_{\rm ap}^2\rangle(\theta) = \frac{1}{2\pi}\int_0^\infty \mathrm{d}l\, l\, P_{\rm E}(l) W_{\rm ap}(\theta l)\,, \tag{3.79}$$

$$\langle M_\perp^2\rangle(\theta) = \frac{1}{2\pi}\int_0^\infty \mathrm{d}l\, l\, P_{\rm B}(l) W_{\rm ap}(\theta l)\,. \tag{3.80}$$

Thus, $M_{\rm ap}$ is sensitive to E-modes only, whereas $M_\perp$ measures B-modes only. As in the case of pure E-modes both can be calculated from the shear correlation functions:

$$\langle M_{\rm ap}^2\rangle(\theta) = \frac{1}{2}\int_0^{2\theta} \frac{\mathrm{d}\vartheta\,\vartheta}{\theta^2}\left[\xi_+(\vartheta)T_+\left(\frac{\vartheta}{\theta}\right) + \xi_-(\vartheta)T_-\left(\frac{\vartheta}{\theta}\right)\right], \tag{3.81}$$

$$\langle M_\perp^2\rangle(\theta) = \frac{1}{2}\int_0^{2\theta} \frac{\mathrm{d}\vartheta\,\vartheta}{\theta^2}\left[\xi_+(\vartheta)T_+\left(\frac{\vartheta}{\theta}\right) - \xi_-(\vartheta)T_-\left(\frac{\vartheta}{\theta}\right)\right]. \tag{3.82}$$

Since lensing is expected to produce a pure E-mode signal, it is an important test for the data analysis to check whether a B-mode is present in the final data catalogues. Many systematic effects introduced by errors in the image reduction or an incomplete anisotropy correction will create both a spurious E-mode and B-mode shear signal. Therefore, the strength of B-modes present should give a rough estimate of the contamination of the shear signal with systematics.

But not all B-modes are due to systematic effects. The clustering of sources can produce a finite B-mode (Schneider et al. 2002). Also the application of the Born approximation (see Sect. 3.3.1) might not be fully sufficient, which can be tested with ray-tracing simulations (e.g. Jain et al. 2000). However, these two effects are expected to produce only very small B-modes. Additionally, intrinsic alignment of sources can produce finite B-modes. Although this is expected to have major influence on shallow cosmic shear surveys, deep surveys should only be affected at a $\lesssim 10\%$ level (Heymans et al. 2006c).

## 3.4 Practical concerns for measuring shear

### 3.4.1 Measurement difficulties

The observed galaxy images are not only distorted by gravitational shear, but are additionally affected by various effects of the telescope and the camera used for the observation, and in case of ground-based observations also by the atmosphere. These effects have to be accounted for properly. Otherwise they can lead to a wrong estimate of the gravitational shear.

- Different effects cause a point-like source to be imaged as an extended object. Observed images are a convolution of the unperturbed images with the *point-spread-function* (PSF), which summarises these effects. For ground-based observations the major contribution comes from the isotropic blurring caused by atmospheric turbulence. Space-based observations have a much higher resolution, which is mainly determined by the diffraction limit of the telescope. Coma, chromatic aberrations, astigmatism, and field curvature of the telescope optics also affect the PSF, as well as charge diffusion in the CCD camera. Usually one decomposes the PSF into isotropic smearing and anisotropic distortions. An anisotropic PSF can be created by astigmatism, field curvature, wrong offsets in the image co-addition (see Sect. 5.2.2), tracking errors, or wind at the telescope site. Whereas isotropic smearing dilutes the signal, an anisotropic PSF can mimic a false shear signal.

- Optical and near infrared observations are usually done with CCD cameras. Here the information is discretised into pixels. Ideally, the size of the pixels is much smaller than the width of the PSF, which is then well sampled. However, for cost optimisation the PSF is often only poorly sampled, with a PSF FWHM of $\sim 2$ pixels ("Nyquist-sampling") or less, making proper PSF correction particularly challenging. For under-sampled data, the effective sampling and resolution can be somewhat improved by using dithered observations, where several images are taken with sub-pixel shifts (see Sect. 5.2.3).

- Furthermore, observations are affected by various sources of noise, like sky background,

read-out electronics, dark current, and photon noise, but also image defects like cosmic rays and hot or cold pixels (see Sect. 5.1.6).

- A particularly unpleasant systematic effect is the degradation of the charge-transfer-efficiency (CTE), the efficiency with which the pixel charges are transfered during read-out. If the efficiency degrades, objects loose a fraction of their electrons to neighbouring pixels creating CTE-trails. This is particularly problematic for space-based cameras, where the continuous bombardment with cosmic rays create charge traps reducing the CTE substantially.

## 3.4.2 The KSB+ method

The correction of PSF effects is of fundamental importance for weak lensing studies. A correction is in principle possible, if the PSF is properly sampled on the pixel grid and across the image. Kaiser, Squires, & Broadhurst (1995); Luppino & Kaiser (1997); Hoekstra et al. (1998) (hereafter referred to as KSB+) developed a formalism for the PSF correction, which is still the most widely used weak lensing shape measurement technique. In this method, stars are used to model the PSF across the field, since they are practically point sources. Then the galaxy ellipticities are corrected for smearing and anisotropy. Whereas I only summarise the KSB+ formalism in this subsection, a more detailed description is given in App. A. Although the KSB+ method was developed for ground-based data dominantly affected by smearing due to atmospheric turbulence, Hoekstra et al. (1998) showed that it can also be applied to space-based images. In Chapter 4 I will present detailed tests of the algorithm carried out in the frame of STEP project, also for simulated space-based images.

### 3.4.2.1 General description

In Sect. 3.2.1 we defined the ellipticity parameters of galaxies in terms of the second-order brightness moments $Q_{ij}$, which were defined in (3.19) by an integral over the whole image plane. In real images the integration has to be replaced by a sum over pixel values and has to be truncated due to neighbouring objects. The truncation is done with a weight function $W$, which gives low weight at large distances from the galaxy centre. Then the second-order brightness moments are defined in analogy to (3.19) as

$$Q_{ij} = \int \mathrm{d}^2\theta\, W(\theta^2)\theta_i\theta_j I(\boldsymbol{\theta})\,,\ i,j \in \{1,2\}\,, \tag{3.83}$$

where the weight function usually depends only on the distance from the object centre $\theta = |\boldsymbol{\theta}|$ and is typically chosen to be a Gaussian with filter scale $r_\mathrm{g}$. The centre of the coordinate system is again chosen such that the first moment of the surface brightness vanishes

$$\int \mathrm{d}^2\theta\, W(\theta^2)\boldsymbol{\theta} I(\boldsymbol{\theta}) = 0\,. \tag{3.84}$$

The appropriate filter scale $r_\mathrm{g}$ depends on the size of the objects and is determined in the process of object detection (see Sect. 3.4.2.2). From now on we will use $Q_{ij}$ as defined with a weight

function in (3.83). The complex ellipticity is then defined from the second-order brightness moments as in (3.21). To indicated that this ellipticity has, in contrast to $\chi$, been measured with a weight function, we denote it as $e$:

$$e = e_1 + \mathrm{i}e_2 = \frac{Q_{11} - Q_{22} + 2\mathrm{i}Q_{12}}{Q_{11} + Q_{22}} \,. \tag{3.85}$$

The total response of a galaxy ellipticity to the reduced shear $g$ and PSF effects is given by

$$e_\alpha - e^{\mathrm{s}}_\alpha = P^g_{\alpha\beta} g_\beta + P^{\mathrm{sm}}_{\alpha\beta} q^*_\beta \,, \tag{3.86}$$

with the intrinsic source ellipticity $e^{\mathrm{s}}$, the "pre-seeing" *shear polarisability*

$$P^g_{\alpha\beta} = P^{\mathrm{sh}}_{\alpha\beta} - P^{\mathrm{sm}}_{\alpha\gamma} \left[ (P^{\mathrm{sm}*})^{-1}_{\gamma\delta} \, P^{\mathrm{sh}*}_{\delta\beta} \right] , \tag{3.87}$$

and the *shear* and *smear polarisability tensors* $P^{\mathrm{sh}}$ and $P^{\mathrm{sm}}$, which are calculated from higher-order brightness moments as detailed in Hoekstra et al. (1998) and App. A. The *anisotropy kernel* $q^*(\boldsymbol{\theta})$ describes the anisotropic component of the PSF and has to be measured from stellar images (denoted with the asterisk), which are not affected by gravitational shear and have $e^{\mathrm{s}*} = 0$:

$$q^*_\alpha = (P^{\mathrm{sm}*})^{-1}_{\alpha\beta} e^*_\beta \,. \tag{3.88}$$

We define the *anisotropy corrected ellipticity*

$$e^{\mathrm{ani}}_\alpha = e_\alpha - P^{\mathrm{sm}}_{\alpha\beta} q^*_\beta \,, \tag{3.89}$$

and the *fully corrected ellipticity* as

$$e^{\mathrm{iso}}_\alpha = (P^g)^{-1}_{\alpha\beta} e^{\mathrm{ani}}_\beta \,, \tag{3.90}$$

which is an unbiased estimator for the reduced gravitational shear $\langle e^{\mathrm{iso}} \rangle = g$, assuming a random orientation of the intrinsic ellipticity $e^{\mathrm{s}}$. For the weak distortions measured in cosmic shear $\kappa \ll 1$, and hence

$$\langle e^{\mathrm{iso}} \rangle = g \simeq \gamma \,. \tag{3.91}$$

The KSB+ formalism relies on the assumption that the image PSF can be described as a convolution of an isotropic part with a small anisotropy kernel. Thus, it is ill-defined for several realistic PSF types (Kaiser 2000), being of particular concern for diffraction limited space-based PSFs. This shortcoming incited the development of alternative methods (Rhodes et al. 2000; Kaiser 2000; Bernstein & Jarvis 2002; Refregier & Bacon 2003; Massey & Refregier 2005; Kuijken 2006; Nakajima & Bernstein 2007). Nevertheless Hoekstra et al. (1998) demonstrated the applicability of the formalism for HST/WFPC2 images, if the filter scale $r_{\mathrm{g}}$ used to measure stellar shapes is matched to the filter scale used for galaxy images.

As stated above, the anisotropy kernel $q^*$ has to be measured from stellar images. The amplitude and direction of this kernel typically varies smoothly across the field of view, with possible discontinuities between chips, e.g. created by different chip heights. Thus, $q^*$ has to be interpolated for the galaxy positions, for example with a low-order polynomial fit, if enough stars are present in the image. If this is not the case, an often attempted approach is to fit the PSF in different observations with more stars present (e.g. of globular clusters), and then apply this fit to the galaxy fields. However, this works only if the PSF variation is sufficiently stable in time. I will discuss the situation for the ACS/WFC PSF in detail in Sect. 6.2.

#### 3.4.2.2 Special features of the KSB+ implementation

Our analysis is based on the Erben et al. (2001) implementation of the KSB+ formalism, with further modifications. There are currently several independent KSB implementations in use, which differ in the details of the computation, yielding slightly different results (see Heymans et al. 2006b and Chapter 4 for a comparison of several implementations).

Before shapes can actually be measured, objects have to be detected. For this purpose the Erben et al. (2001) pipeline uses `SExtractor` (Bertin & Arnouts 1996), which also provides a first estimates of the centroid position. Then the pipeline refines the centroid position iteratively until (3.84) is fulfilled.

As a particular feature the Erben et al. (2001) implementation splits each pixel into $4\times4$ sub-pixels linearly interpolating the pixel flux. The KSB integrals in the computation of $Q_{ij}$, $P^{\rm sm}_{\alpha\beta}$, and $P^{\rm sh}_{\alpha\beta}$ are then evaluated at the sub-pixel centres using the float value of the distance to the object centre. For poorly sampled data this approach yields results which are more stable with respect to the relative position of the object centre on the pixel grid.

In principle the Gaussian filter scale $r_{\rm g}$ can be chosen arbitrarily. However, in order to maximise the signal-to-noise of the shape measurement, $r_{\rm g}$ should be somehow related to the true size of the galaxy. In the pipeline $r_{\rm g}$ can be defined as a function of the `SExtractor` `FLUX_RADIUS` parameter

$$r_{\rm g} = X \cdot \texttt{FLUX\_RADIUS}\,, \tag{3.92}$$

where we typically set $X = 1.0$.

In addition to the KSB+ quantities Erben et al. (2001) compute for each object the half-light radius $r_{\rm h}$ and the signal-to-noise ratio

$$\mathrm{S/N} = \frac{\int \mathrm{d}^2\theta\, W_{r_{\rm g}}(|\boldsymbol{\theta}|)\, I(\boldsymbol{\theta})}{\sigma_1 \sqrt{\int \mathrm{d}^2\theta\, W^2_{r_{\rm g}}(|\boldsymbol{\theta}|)}}\,, \tag{3.93}$$

which is based on the same filter function as the one used for shape measurements and depends on the single-pixel dispersion of the sky background $\sigma_1$. Stars and galaxies are usually selected with cuts in the magnitude–$r_{\rm h}$ plane.

Erben et al. (2001) also propose a weighting scheme, to down-weight the shear estimate from low signal-to-noise galaxies, which we adopt in parts of the analysis. Here they define a distance measure between galaxies in a two-dimensional parameter space, for which we use magnitude and ${r_{\rm h}}^2$. The weight $w_i$ for each galaxy is then given by the inverse variance of the shear estimate of the galaxy and its $N$ neighbours in the parameter space, where we typically use $N = 20$ or $N = 50$

$$w_i \propto \langle (e^{\rm iso})^2 \rangle^{-1}_N (r_{\rm h}, \mathrm{mag})\,. \tag{3.94}$$

As a modification to the original Erben et al. (2001) pipeline, we measures all stellar quantities needed for the correction of the galaxy ellipticities as a function of the filter scale $r_{\rm g}$ following

[2]For mag in magnitudes and $r_{\rm h}$ in pixels a simple Euclidian distance measure is usually sufficient, as applied in this work. However, if parameters are used which vary over several orders of magnitudes, such as flux, a reasonable distance definition can, for example, be found by sorting the galaxies in each quantity and defining the one-dimensional distance between neighbours to be unity.

Hoekstra et al. (1998). For the calculation of $P^g_{\alpha\beta}$ in (3.87) and its inversion in (3.90) we usually use the approximations

$$\left[(P^{\rm sm*})^{-1}_{\gamma\delta}\, P^{\rm sh*}_{\delta\beta}\right] \approx \frac{{\rm Tr}\left[P^{\rm sh*}\right]}{{\rm Tr}\left[P^{\rm sm*}\right]}\delta_{\gamma\beta}\,, \quad (P^g)^{-1}_{\alpha\beta} \approx \frac{2}{{\rm Tr}\left[P^g\right]}\delta_{\alpha\beta}\,, \tag{3.95}$$

as the trace-free part of the tensor is much smaller than the trace (Erben et al. 2001). Only if we explicitly refer to a "full tensor correction" this approximation has not been applied. To simplify the notation we define

$$T^* \equiv \frac{{\rm Tr}\left[P^{\rm sh*}\right]}{{\rm Tr}\left[P^{\rm sm*}\right]}\,. \tag{3.96}$$

Note that the KSB+ correction scheme can lead to unphysical ellipticities due to noise in the data. Small galaxies can have small or even negative ${\rm Tr}P^g/2$ leading to $|e_{\rm iso}| > 1$. Thus, they must be down-weighted or rejected with appropriate cuts either in ${\rm Tr}P^g/2$ or $|e_{\rm iso}|$.

We have extensively tested and optimised this implementation using image simulations of the STEP project, as detailed in Chapter 4.

### 3.4.3 Practical shear estimators

In this section I will discuss practical estimators of the second-order shear statistics, which are actually used to measure the shear from the data. In practise, the KSB+ algorithm is first applied to correct the measured ellipticities for PSF effects (see Sect. 3.4.2). The fully corrected galaxy ellipticity $e^{\rm iso}$ is an unbiased estimator of the local shear $\gamma$ as is the ellipticity $\epsilon$. Here I will present the discussion in terms of $\epsilon$, as it is usually done in the literature. In practice, the estimator of the correlation function is calculated from $e^{\rm iso}$.

According to (3.28), the ellipticity $\epsilon_i$ of a galaxy at position $\boldsymbol{\theta}_i$ is related to the shear $\gamma$ (for $|\gamma| \ll 1$) as

$$\epsilon_i = \epsilon^{\rm s}_i + \gamma(\boldsymbol{\theta}_i)\,, \tag{3.97}$$

where $\epsilon^{\rm s}_i$ denotes the intrinsic ellipticity of the galaxy. The shear two–point correlation function is calculated in bins of angular width $\Delta\vartheta$. It is convenient to introduce the function $\Delta_\vartheta(\phi) = 1$ for $\vartheta - \Delta\vartheta/2 < \phi \le \vartheta + \Delta\vartheta/2$, and zero otherwise, which defines the angular bin. If we allow weight factors $w_i$ assigned to each galaxy, an estimator for the correlation function $\xi_+(\vartheta)$ is given by

$$\hat{\xi}_+(\vartheta) = \frac{\sum_{ij} w_i w_j (\epsilon_{i{\rm t}}\epsilon_{j{\rm t}} + \epsilon_{i\times}\epsilon_{j\times})\Delta_\vartheta(|\boldsymbol{\theta}_i - \boldsymbol{\theta}_j|)}{\sum_{ij} w_i w_j \Delta_\vartheta(|\boldsymbol{\theta}_i - \boldsymbol{\theta}_j|)}\,, \tag{3.98}$$

where the denominator corresponds to an effective number of pairs considered in the angular bin. Under the assumption that the source ellipticities are randomly oriented, it follows that

$$\langle \epsilon_{i{\rm t}}\epsilon_{j{\rm t}} + \epsilon_{i\times}\epsilon_{j\times}\rangle = \sigma^2_\epsilon \delta_{ij} + \xi_+(|\boldsymbol{\theta}_i - \boldsymbol{\theta}_j|)\,, \tag{3.99}$$

with the dispersion of the intrinsic galaxy ellipticity $\sigma_\epsilon$. Since $\delta_{ij}\Delta_\vartheta(|\boldsymbol{\theta}_i - \boldsymbol{\theta}_j|)$ vanishes for all pairs $i$, $j$, it follows that $\hat{\xi}_+$ is an unbiased estimator of $\xi_+$: $\langle\hat{\xi}_+\rangle(\vartheta) = \xi_+(\vartheta)$. Correspondingly

$$\hat{\xi}_-(\vartheta) = \frac{\sum_{ij} w_i w_j (\epsilon_{i{\rm t}}\epsilon_{j{\rm t}} - \epsilon_{i\times}\epsilon_{j\times})\Delta_\vartheta(|\boldsymbol{\theta}_i - \boldsymbol{\theta}_j|)}{\sum_{ij} w_i w_j \Delta_\vartheta(|\boldsymbol{\theta}_i - \boldsymbol{\theta}_j|)} \tag{3.100}$$

is an unbiased estimator for $\xi_-$: $\langle\hat{\xi}_-\rangle(\vartheta) = \xi_-(\vartheta)$. As explained in Sect. 3.3.2, the correlation function $\xi_\times$ defined in (3.67) is expected to vanish. Thus, also its estimator

$$\hat{\xi}_\times(\vartheta) = \frac{\sum_{ij} w_i w_j \epsilon_{i\mathrm{t}} \epsilon_{j\times} \Delta_\vartheta(|\boldsymbol{\theta}_i - \boldsymbol{\theta}_j|)}{\sum_{ij} w_i w_j \Delta_\vartheta(|\boldsymbol{\theta}_i - \boldsymbol{\theta}_j|)} \tag{3.101}$$

is expected to vanish. Instead of $\hat{\xi}_\pm$ sometimes the correlation between the tangential- and cross-components of the ellipticities are considered directly in the literature

$$\langle\gamma_\mathrm{t}\gamma_\mathrm{t}\rangle(\vartheta) = \frac{\sum_{ij} w_i w_j \epsilon_{i\mathrm{t}} \epsilon_{j\mathrm{t}} \Delta_\vartheta(|\boldsymbol{\theta}_i - \boldsymbol{\theta}_j|)}{\sum_{ij} w_i w_j \Delta_\vartheta(|\boldsymbol{\theta}_i - \boldsymbol{\theta}_j|)}\,, \tag{3.102}$$

$$\langle\gamma_\times\gamma_\times\rangle(\vartheta) = \frac{\sum_{ij} w_i w_j \epsilon_{i\times} \epsilon_{j\times} \Delta_\vartheta(|\boldsymbol{\theta}_i - \boldsymbol{\theta}_j|)}{\sum_{ij} w_i w_j \Delta_\vartheta(|\boldsymbol{\theta}_i - \boldsymbol{\theta}_j|)}\,, \tag{3.103}$$

which are unbiased estimators for $\gamma_\mathrm{t}\gamma_\mathrm{t}(\vartheta)$ and $\gamma_\times\gamma_\times(\vartheta)$.

As shown in Sect. 3.3.2, the shear dispersion and the aperture mass dispersion can be calculated from the correlation function. Accordingly, their estimators can be determined from $\hat{\xi}_+$ and $\hat{\xi}_-$. If the centres of the bins, in which the correlation function is calculated, are given by $\vartheta_n = (n - 1/2)\Delta\vartheta$, and the aperture radius $\theta$ is an integer multiple of the bin width ($\theta = m\Delta\vartheta$), the integrals in Eqs. (3.72) and (3.73) can be replaced by sums over the bins. This yields the estimators

$$\mathcal{S}(\theta) = \frac{\Delta\vartheta}{\theta^2}\left[K_+ \sum_{n=1}^{2m} \vartheta_n \hat{\xi}_+(\vartheta_n) S_+\left(\frac{\vartheta_n}{\theta}\right) + (1 - K_+) \sum_{n=1}^{\infty} \vartheta_n \hat{\xi}_-(\vartheta_n) S_-\left(\frac{\vartheta_n}{\theta}\right)\right], \tag{3.104}$$

$$\mathcal{M}(\theta) = \frac{\Delta\vartheta}{\theta^2} \sum_{n=1}^{2m} \vartheta_n \left[K_+ \hat{\xi}_+(\vartheta_n) T_+\left(\frac{\vartheta_n}{\theta}\right) + (1 - K_+) \hat{\xi}_-(\vartheta_n) T_-\left(\frac{\vartheta_n}{\theta}\right)\right], \tag{3.105}$$

where $\mathcal{S}$ and $\mathcal{M}$ are unbiased estimators for the shear dispersion $\langle|\gamma|^2\rangle(\theta)$ and aperture mass dispersion $\langle M_\mathrm{ap}^2\rangle(\theta)$ respectively. $K_+$ describes the relative contributions of the two expressions in Equations (3.72) and (3.73). Due to the infinite support of $S_-$, $\mathcal{S}(\theta)$ should be calculated from $\hat{\xi}_+$ only. Note, that it is then sensitive both to E-modes and B-modes. To separate E-modes and B-modes, $\mathcal{M}(\theta)$ can be calculated with $K_+ = 1/2$. Then it is sensitive to E-modes only. The strength of the B-modes can then be measured from the estimator $\mathcal{M}_\perp(\theta)$

$$\mathcal{M}_\perp(\theta) = \frac{\Delta\vartheta}{2\theta^2} \sum_{n=1}^{2m} \vartheta_n \left[\hat{\xi}_+(\vartheta_n) T_+\left(\frac{\vartheta_n}{\theta}\right) - \hat{\xi}_-(\vartheta_n) T_-\left(\frac{\vartheta_n}{\theta}\right)\right], \tag{3.106}$$

which is an unbiased estimator for $\langle M_\perp^2(\theta)\rangle$. Note that in real data the correlation functions can only be measured from a minimal separation, e.g. due to confusion between neighbouring galaxies. Hence, the summation has a lower cut-off, which can lead to biased estimates and E–/B–mode mixing (Kilbinger et al. 2006). However, for space-based data the impact of this effect is small due to the high resolution and galaxy number density.

In order to simplify the notation we will relax the distinction between the shear statistics and their estimators when plotting actual estimates, e.g. we will write $\langle M_\mathrm{ap}^2\rangle(\theta)$ instead of $\langle\mathcal{M}(\theta)\rangle(\theta)$.

# Chapter 4

# Testing and improving KSB+ with the STEP simulations

A major part of this thesis project was the stepwise testing and improvement of the applied KSB+ implementation using the simulations of the Shear TEsting Programme (STEP). The conclusion of this study is that the KSB+ formalism can reach a systematic average relative accuracy at the 2% level, with a deviation $\lesssim 5\%$ as a function of galaxy magnitude and size, if slightly tweaked and carefully applied. This is well within the statistical errors of the ACS cosmic shear project. However, due to a number of fundamental limitations of the method it seems unlikely that its accuracy can be further improved substantially. Hence, it most likely cannot serve as a proper tool for future generations of weak lensing surveys aiming at sub-percent-level accuracy. Given that more advanced techniques are still in development, it is, however, likely that KSB+ will still be applied within the next few years for upcoming surveys. Hence, the in-depth analysis presented here may prove valuable for this transient period.

This chapter is organised as follows: I will first introduce the STEP Project in Sect. 4.1. In Sections 4.2 to 4.4 I will then summarise the results of three subsequent rounds of blind shear analyses with increasingly complex image simulations (STEP1, STEP2, STEP3), where STEP3 was particularly designed to mimic space-based data, partially with ACS-like properties. The blind analyses were followed by a central evaluation of the catalogues submitted by the different collaborators. When referring to this first shear analysis and central evaluation I use the term "original" analysis, to distinguish from followed non-blind tests and analyses conducted by myself to improve the method. I will then conclude this chapter in Sect. 4.5.

## 4.1 Introduction

Erben et al. (2001); Bacon et al. (2001) and Hoekstra et al. (2002b) presented the first detailed tests of shape measurement pipelines on image simulations containing an artifical shear signal. They all used the KSB+ method, but arrived at somewhat different conclusions: Bacon et al. (2001) found that they could recover the input shear with $\sim 5\%$ accuracy, if they apply a calibration factor of $0.85^{-1}$ to increase the KSB shear estimate. On the other hand Erben et al.

(2001) found an accuracy of 10 – 15% without the need of a calibration factor. Hoekstra et al. (2002b) concluded that they could recover the input shear with better than 10% accuracy. The differences between these results are important: although they all use the same KSB+ method, subtle differences in the implementation lead to significantly different results. This underlines the importance to test every shear measurement pipeline on simulations.

Systematic errors of order 10% were at best comparable to the statistical errors of surveys conducted at the time of the tests mentioned in the previous paragraph. However, statistical errors of large present day surveys have already shrunken below this value, and for upcoming and future surveys the shear measurement accuracy will have to drop to the percent and sub-percent level.

With this perspective the Shear TEsting Programme[1] (STEP) was launched in 2004. The first goal of STEP was to test various shear measurement techniques on different sets of image simulations, hence providing benchmarks on the current accuracy. In these tests the input shear was kept secret to ensure a fair and creditable comparison. The number of independent groups and methods who participated in the tests is impressive, and nowadays all seriously developed shear measurement methods have been tested on the simulations of at least one of the STEP projects.

As part of this thesis work, I tested our KSB+ pipeline in all previous STEP analyses, starting with relatively simple simulations of ground-based data (STEP1, Sect. 4.2). Several biases identified with this first blind test were fixed for the analysis of the second set of simulations (STEP2, Sect. 4.3), which includes more realistic PSF models and galaxy morphology. Finally the third set of simulations (STEP3, Sect. 4.4) resembles space-based data, providing a test which is particularly useful for this thesis project.

## 4.2 STEP1: Simple simulations of ground-based data

The STEP1 analysis has been published by Heymans, Van Waerbeke, Bacon, Berge, Bernstein, Bertin, Bridle, Brown, Clowe, Dahle, Erben, Gray, Hetterscheidt, Hoekstra, Hudelot, Jarvis, Kuijken, Margoniner, Massey, Mellier, Nakajima, Refregier, Rhodes, Schrabback, & Wittman (2006b), which I abbreviate as H06 henceforth. Here I will focus the discussion on the results of different KSB+ pipelines. For a more detailed description also concerning the results of other shape measurement methods see the original publication. Additionally, I will present results from subsequent tests conducted on the STEP1 data with our pipeline.

In total 13 different shear measurement methods or implementations have been tested in the original analysis of the STEP1 image simulations (Table 4.1), including several implementations of KSB+ which differ in subtle details of the coding, see Appendix A of H06 for a detailed comparison. The analysis was carried out blindly by all authors except LV, CH, and KK.

[1] http://www.physics.ubc.ca/~heymans/step.html

Table 4.1: Shear measurement methods and implementations tested in the original analysis of the STEP1 image simulations.

| **Author** | **Key** | **Method** |
|---|---|---|
| Bridle | SB | im2shape (Bridle et al. 2002) |
| Brown | MB | KSB+ (Bacon et al. 2000 pipeline) |
| Clowe | C1&C2 | KSB+ |
| Dahle | HD | K2K (Kaiser 2000) |
| Hetterscheidt | MH | KSB+ (Erben et al. 2001 pipeline) |
| Heymans | CH | KSB+ |
| Hoekstra | HH | KSB+ |
| Jarvis | MJ | Bernstein & Jarvis (2002): Rounding kernel method |
| Kuijken | KK | Kuijken (2006): Shapelets to 12th order |
| Margoniner | VM | Wittman et al. (2001): Elliptical weight function |
| Nakajima | RN | Bernstein & Jarvis (2002): Deconvolution fitting method |
| Schrabback | TS | KSB+ (Erben et al. 2001 pipeline + modifications) |
| van Waerbeke | LV | KSB+ |

### 4.2.1 Skymaker simulations

The STEP1 image simulations were created by Ludovic van Waerbeke using the SKYMAKER[2] package. Galaxies were populated in redshift space and modelled as a sum of an exponential disk and a de Vaucouleurs-type bulge, hence neglecting further substructure and morphology. The source ellipticity $(e_1^{(s)}, e_2^{(s)})$ was randomly drawn from a zero mean Gaussian distribution with $\sigma_e = 0.3$. To these galaxies five different shears were applied with $\gamma_1 = (0.0, 0.005, 0.01, 0.05, 0.1)$, $\gamma_2 = 0.0$.

After adding $\sim 10$ stars $/[']^2$ the images were convolved with six different ground-based PSFs

[2] http://terapix.iap.fr/cplt/oldSite/soft/skymaker

Table 4.2: Overview of the PSF models used in the STEP1 image simulations (compare to Fig. 4.1).

| **PSF** | **Seeing** | **PSF type** | **Ellipticity** |
|---|---|---|---|
| 0 | 0.″9 | no anisotropy | 0.00 |
| 1 | 0.″7 | coma | $\sim 0.04$ |
| 2 | 0.″7 | jitter, tracking error | $\sim 0.08$ |
| 3 | 0.″7 | defocusing | $\sim 0.00$ |
| 4 | 0.″7 | astigmatism | $\sim 0.00$ |
| 5 | 0.″7 | triangular | $\sim 0.00$ |

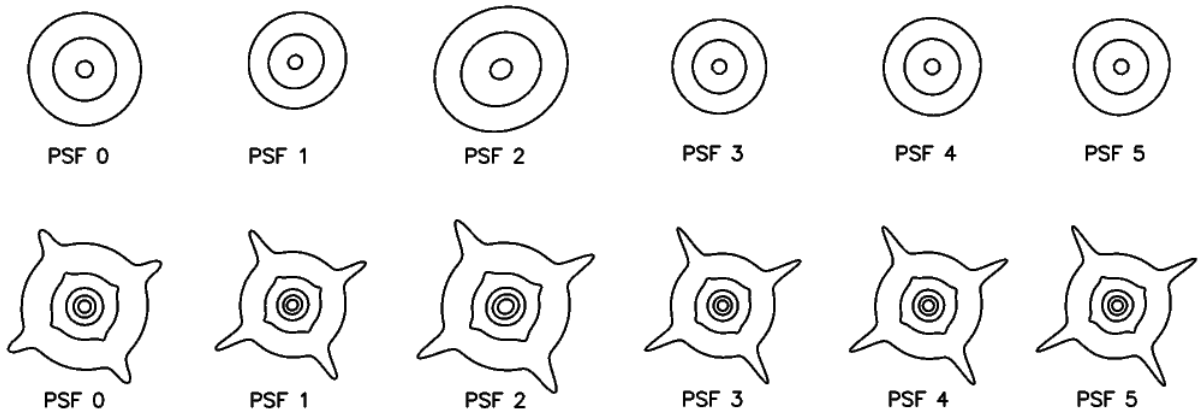


Figure 4.1: STEP1 SKYMAKER PSF models, as described in Table 4.2. The upper panel shows the PSF core, with contours marking 3, 25, and 90 per cent of the peak intensity. The lower panel shows the extended diffraction spikes, with 0.003, 0.03, 0.3, and 25 per cent contours (adapted from H06).

that are listed in Table 4.2 and shown in Fig. 4.1. These PSF models were selected to provide a realistic representation of the types of PSF distortions seen in ground-based observations. They were realised through ray-tracing models of the optical plane. Additionally, they include atmospheric turbulence (seeing) yielding an effective stellar FWHM $\sim 0\farcs9$. The ellipticity of PSF1 is a good representation for typical realistic ground-based surveys. For comparison PSF2 is very elliptical featuring tracking errors. The other PSFs are used to test the impact of non-Gaussian PSF distortions. The simulations have a pixel scale of $0\farcs206$, hence the PSFs are well sampled. A uniform background ($19.2\,\mathrm{mag}/[\arcsec]^2$) was added to the data, with uncorrelated Poisson photon shot-noise and Gaussian read-out noise. A small cutout of one simulated image is shown in Fig. 4.2.

Each of the $5 \times 6$ shear and PSF combinations contain 64 images with $4096 \times 4096$ pixels and an effective galaxy number density $N \sim 15/[']^2$ yielding a total of $\sim 1.7 \cdot 10^5$ galaxies per combination. Hence, shot noise due to the intrinsic ellipticities was reduced to the $\simeq 0.1\%$-level.

### 4.2.2 Shear estimation

We used our KSB+ pipeline with special characteristics detailed in Sect. 3.4.2.2 to determine shear estimates for the galaxies in all data sets. For object detection with SExtractor we used a Gaussian filter function (gauss_2.5_5x5) and required objects to comprise at least 4 adjacent pixels (DETECT_MINAREA) which are $1.2\sigma$ (DETECT_THRESH) above the sky background.

To exclude stars and poorly resolved galaxies we applied a very conservative cut $r_\mathrm{h} > 1.2 r_\mathrm{h}^*$, where $r_\mathrm{h}^*$ denotes the half-light radius of stars (see Fig. 4.3). In addition, we select galaxies with cuts $|e^\mathrm{iso}| \leq 0.8$, $\mathrm{Tr}P^g/2 > 0$, and $\mathrm{S/N} > 4$. We performed the PSF correction twice, once using a third-order polynomial interpolation, and once assuming that the PSF was constant across the field-of-view, with only marginal differences for the final shear estimate.

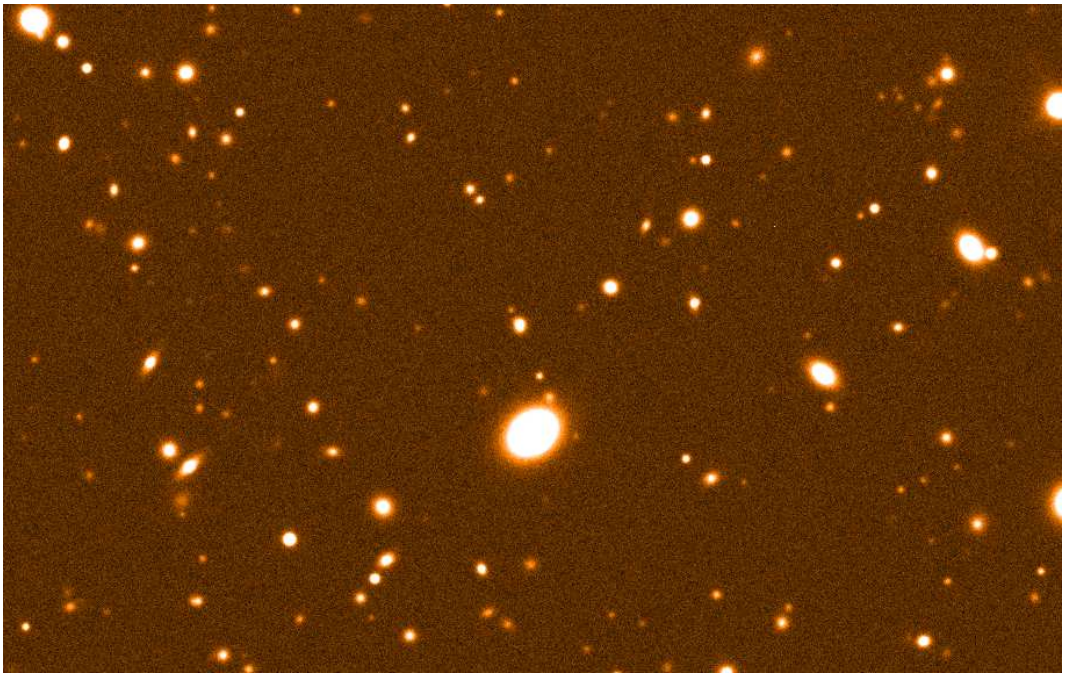

Figure 4.2: Cutout of one SKYMAKER STEP1 image with PSF 0 (width 3′).

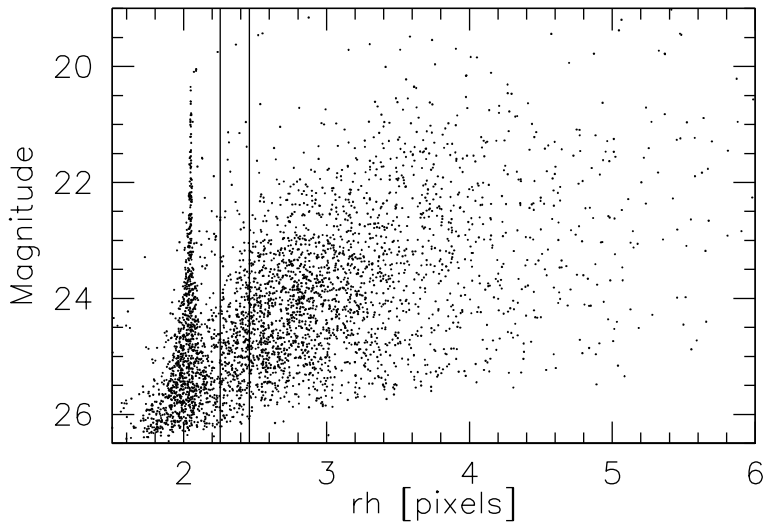


Figure 4.3: $r_{\rm h}$–magnitude distribution of objects in one of the STEP1 PSF 1 frames with $\gamma_1 = 0.0$. The stellar locus is clearly visible at $r_{\rm h}^* \sim 2.05$ pixels. The lines indicate cuts to select galaxies at $1.1r_{\rm h}^*$ and $1.2r_{\rm h}^*$.

Table 4.3: Table to compare the different number densities $N_{\rm gal}/[']^2$, percentage of stellar contamination and false detection, and detection software for the different pipelines tested in STEP1. $S/N_s$ gives the signal-to-shot-noise for the shear estimate in the $\gamma_1 = 0.005$ simulations. $S/N_s'$ has been calculated taking weights into account if provided (adapted from Table 4 in H06).

| **Author** | $N_{\rm gal}/[']^2$ | **% stars** | **%false** | **Software** | $S/N_s$ | $S/N_s'$ |
|---|---|---|---|---|---|---|
| SB | 18 | 1.9 | 3.8 | SExtractor | 7 | 6 |
| MB | 14 | 7.1 | 0.1 | hfindpeaks | 10 | – |
| C1 | 12 | 2.7 | 0.0 | hfind + SExt | 9 | 11 |
| C2 | 12 | 2.8 | 0.0 | hfind + SExt | 9 | 11 |
| HD | 17 | 44.9 | 0.0 | hfindpeaks | 8 | – |
| MH | 14 | 3.9 | 0.0 | SExtractor | 11 | 14 |
| CH | 12 | 3.0 | 0.0 | SExtractor | 11 | – |
| HH | 16 | 10.8 | 0.1 | hfindpeaks | 10 | 11 |
| MJ | 9 | 0.1 | 3.6 | SExtractor | 8 | 22 |
| KK | 9 | 0.8 | 0.0 | SExtractor | 10 | 12 |
| VM | 13 | 3.8 | 0.0 | SExtractor | 10 | – |
| RN | 9 | 0.9 | 0.4 | SExtractor | 10 | 24 |
| TS | 10 | 1.4 | 0.0 | SExtractor | 11 | 14 |
| LV | 13 | 0.0 | 0.0 | hfindpeaks | 11 | 12 |

### 4.2.3 Analysis

The joint analysis of the submitted blind catalogues was conducted by CH.

#### 4.2.3.1 Object detection

For the different methods the galaxy number densities, contaminations with stars and false detections, and achieved signal-to-shot-noise are listed in Table 4.3. The conservative selection criteria applied in our analysis led to a low contamination with stars (1.4%) and false detections (0.0%) on the cost of a rather low galaxy number density (10 galaxies $/[']^2$). However, the rejection of the noisy galaxies did not lead to a lower unweighted signal-to-noise of the shear estimate (11). Also, the weighted signal-to-noise (14) ranks among the highest values after the MJ and RN estimates, which use a very aggressive weighting scheme introducing a problematic non-linear response (see Sect. 4.2.3.2).

#### 4.2.3.2 Calibration bias and PSF contamination

For each method and PSF model the data were fitted as

$$\langle\gamma_1\rangle = q \cdot (\gamma_1^{\rm true})^2 + (1+m)\cdot\gamma_1^{\rm true} + c_1 \quad \langle\gamma_2\rangle = c_2\,, \tag{4.1}$$

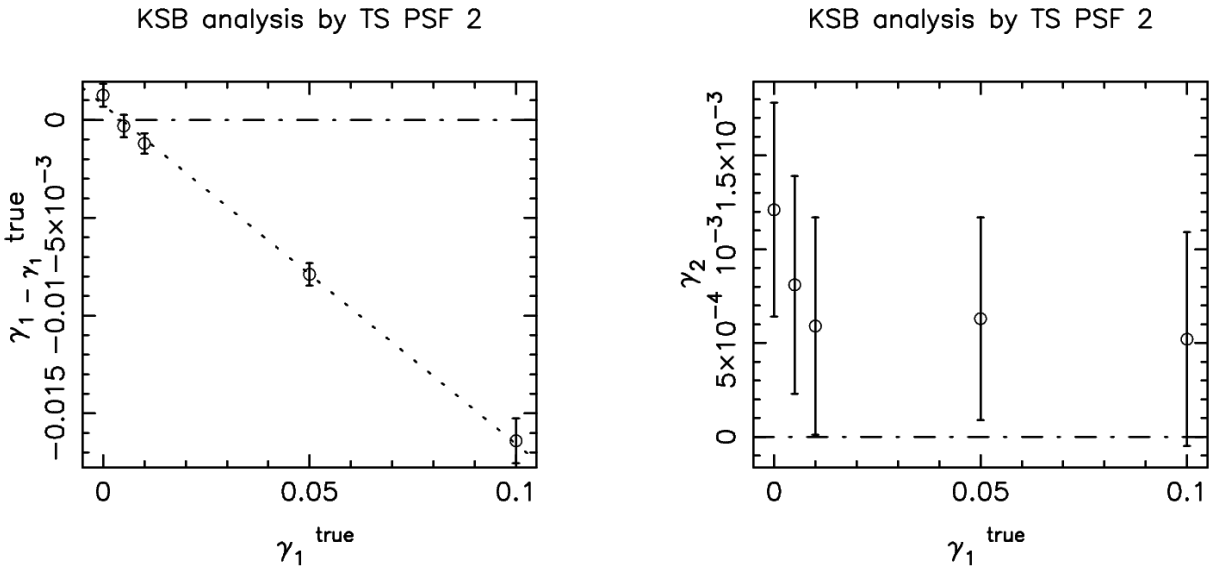


Figure 4.4: Difference of input and measured shear as a function of input shear for the TS analysis of the STEP1 simulations with PSF 2. For $\gamma_1$ the short-dashed line shows the estimated linear fit (plot by CH).

where $\langle\gamma_{1,2}\rangle$ denotes the mean shear estimate computed from all galaxies with the same input shear. For a perfect method $\langle\gamma_1\rangle$ would be consistent with $\gamma_1^{\rm true}$ and $\langle\gamma_2\rangle$=0, hence $q = m = c_1 = c_2 = 0$. For a method which systematically under- or over-estimates the shear a calibration bias is present with $m \neq 0$. If a method shows non-linear response to the shear signal $q \neq 0$. Residuals in the PSF anisotropy correction will show up independently of the input shear as non-zero constants $c_{1,2}$. If $q$ is consistent with zero the fit was repeated without quadratic dependence. As an example we plot the fit for the TS analysis of the highly elliptical PSF 2 in Fig. 4.4. The method shows a linear response to shear, with a systematic under-estimation by $m \sim -16\%$, and good correction for PSF anisotropy with $|c_{1,2}| \sim 0.001$.

From all PSF types we compute the mean calibration bias $\langle m\rangle$, the mean non-linear coefficient $\langle q\rangle$ (if significant), and the dispersion $\sigma_c$ from $c_1$ and $c_2$, which provides an estimate for PSF anisotropy residuals. This allows us to compare the performance of the different methods condensed into a single plot (Fig. 4.5). While our KSB+ implementation (TS) ranks among the best methods concerning PSF anisotropy correction without introducing a non-linear shear response, it suffers from a substantial under-estimation of the shear with $\langle m\rangle = -0.167 \pm 0.011$. An interesting comparison can be made with the MH analysis, which stems from the same `SExtractor` catalogue and also applies the Erben et al. (2001) KSB+ implementation, but uses different selection criteria and, in particular, does not perform the PSF anisotropy correction as a function of filter scale $r_g$. The reduction of PSF anisotropy residuals $\sigma_c$ by more than a factor of two for our method compared to the MH analysis clearly shows the advantage of a scale-dependent anisotropy correction, which we hence recommend for all KSB+ implementations.

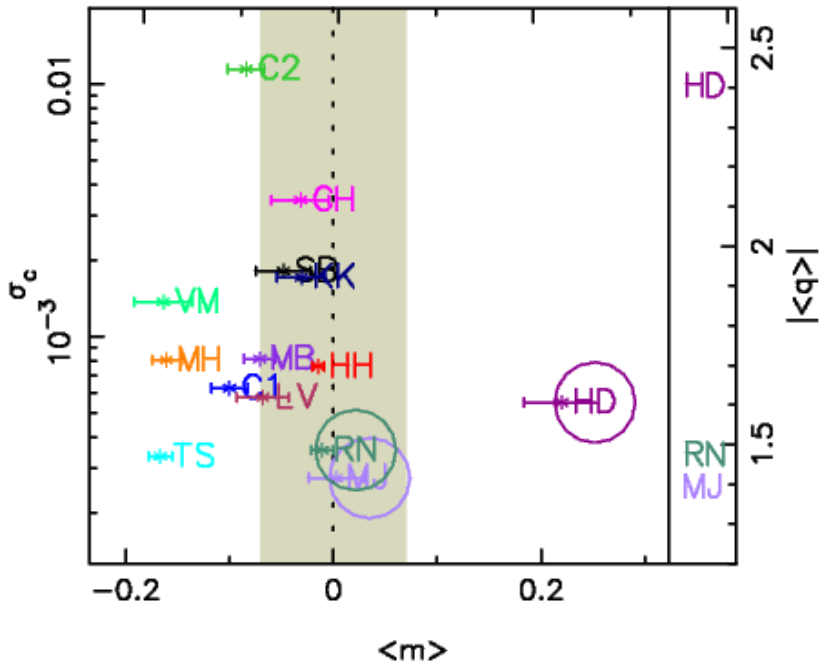


Figure 4.5: STEP1 measures of calibration bias $\langle m \rangle$, PSF residuals $\sigma_c$, and non-linearity $\langle q \rangle$ for the methods listed in Table 4.1. For the non-linear cases where $\langle q \rangle \neq 0$ (points enclosed within a large circle), $\langle q \rangle$ is shown with respect to the right-hand scale. Results in the shaded region suffer from less than 7 per cent calibration bias (Fig. 3 from H06).

#### 4.2.3.3 Selection bias

Weak lensing measurements rely on the fact that the mean intrinsic source ellipticity vanishes $\langle e_\alpha^{(s)} \rangle = 0$ when averaged over many galaxies. Therefore it is very important that no selection biases are introduced in the compilation of source catalogues, which might alter the mean ellipticity of the source galaxies.

Kaiser (2000) points out, that there is a preference to select galaxies oriented in the direction of the PSF anisotropy, which have a higher surface brightness after PSF convolution than galaxies oriented perpendicular to the PSF. Detection algorithms which require objects to have a certain number of pixels above a given threshold (such as `SExtractor`) might then lead to a *PSF selection bias*. This can be avoided by first choosing a low detection threshold in combination with a later rejection of noisy objects using significance or signal-to-noise cuts.

In addition, there is a preference to select objects which are anti-aligned with the shear. This *shear selection bias* was first described by Hirata & Seljak (2003). The overall magnification of a source is independent of the direction of the shear. Additionally, surface brightness is conserved under gravitational shear (in contrast to the effect of PSF ellipticity). Hence, if objects were selected purely by the number of pixels above a certain threshold, no bias would be introduced. However, usually images are smoothed with a Gaussian kernel before object detection, in order to reduce the impact of noise. This will, however, lead to a preferred detection of round objects, and hence galaxies anti-oriented with the shear. In addition, object detection or shape measurement methods might fail to converge for highly elliptical objects, again introducing shear selection bias. Furthermore, shear selection bias can also be created when cuts are applied to reject highly elliptical galaxies.

In order to test the different STEP1 analyses for selection bias, we reject the false and stellar detections from the catalogues and perform a similar fit as in (4.1), but use the intrinsic input source ellipticity $e_\alpha^{(s)}$ instead of the shear estimate

$$\langle e_1^{(s)} \rangle_{\rm selc} = m_{\rm selc} \gamma_1^{\rm true} + c_1 \quad \langle e_2^{(s)} \rangle_{\rm selc} = c_2 \,, \tag{4.2}$$

from which we compute the mean shear selection bias $\langle m_{\rm selc} \rangle$ and the dispersion $\sigma_c^{\rm s}$ from all PSF models. PSF-anisotropy-dependent selection bias as estimated from $\sigma_c^{\rm s}$ was found to be very low for all methods with $\sigma_c^{\rm s} < 0.001$. In contrast, shear selection bias $\langle m_{\rm selc} \rangle$ is significantly non-zero for several methods including our KSB+ analysis, for which $\langle m_{\rm selc} \rangle = -0.045 \pm 0.006$. For our analysis the selection bias is mainly due to the cuts applied to the data, as discussed in Sect. 4.2.4 and 4.2.6.

In Fig. 4.6 we compare the shear selection bias $\langle m_{\rm selc} \rangle$ to the calibration bias $\langle m_{\rm uncontaminated} \rangle$, which is computed similarly to $\langle m \rangle$ in (4.1), but after rejection of false and stellar detections. Given the low contamination rate of our catalogues (see Table 4.3), $\langle m_{\rm uncontaminated} \rangle = -0.158 \pm 0.010$ differs only marginally from the contaminated $\langle m \rangle$. For our analysis selection bias accounts for $\langle m_{\rm selc} \rangle / \langle m_{\rm uncontaminated} \rangle \sim 28\%$ of the total calibration bias, while the rest must either be due to a systematic bias in the shear estimate of individual galaxies, or due to *weight bias*, which we discuss next.

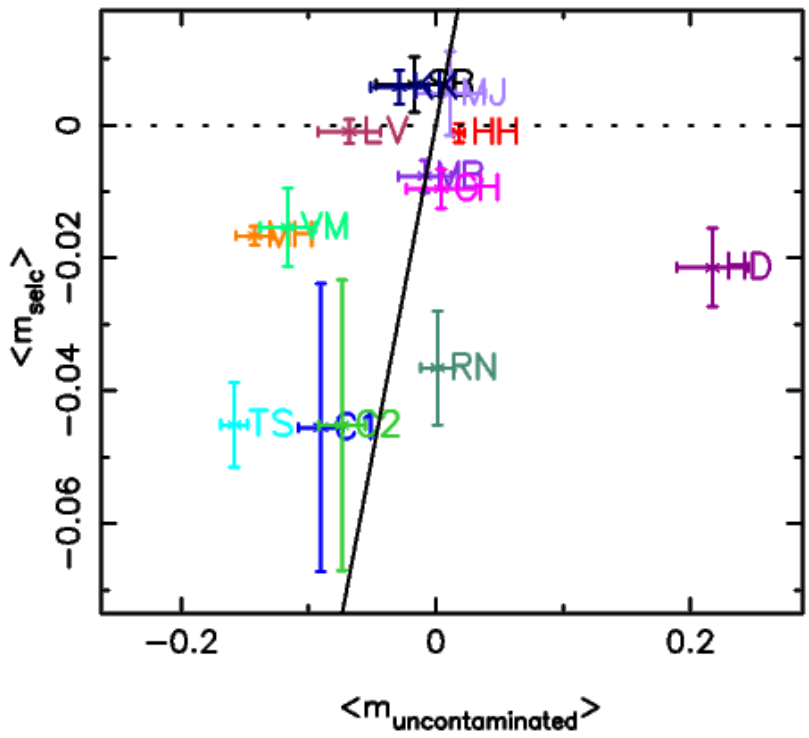


Figure 4.6: STEP1 measures of shear selection bias $\langle m_{\rm selc}\rangle$ compared to calibration bias measured rejecting false detections and stars, but taking weights into account ($\langle m_{\rm uncontaminated}\rangle$). Methods for which the calibration bias is solely due to selection lie on the 1:1 line over-plotted (Fig. 4 from H06).

#### 4.2.3.4 Weight bias

Ideally, weights should reduce noise in the shear estimate without introducing bias. To test for a possible bias, we perform a fit to

$$\langle e_1^{(s)}\rangle_{\rm selc} - \langle e_1^{(s)}\rangle'_{\rm selc} = m_{\rm weight}\gamma_1^{\rm true} + c_1\,, \tag{4.3}$$

where $\langle e_1^{(s)}\rangle_{\rm selc}$ denotes the unweighted and $\langle e_1^{(s)}\rangle'_{\rm selc}$ the weighted average of the intrinsic input source ellipticity. Note the unusual sign definition in (4.3), where a weight leading to an underestimation of the shear has a positive bias. We keep this convention to be consistent with H06.

From the fit we find that $c_1$ is consistent with zero for all methods, hence there is no PSF-dependent weight bias as expected. The mean shear-dependent weight bias $\langle m_{\rm weight}\rangle$ is at or below percent level for most methods, with exceptions being the KK shapelet code ($0.020 \pm 0.002$), our KSB+ implementation ($0.024 \pm 0.003$), and the MH KSB+ method ($0.032 \pm 0.003$). Hence, about $0.024/0.167 = 14\%$ of the total calibration bias in our analysis is caused by the weighting scheme (3.94), which also has been used by MH. This bias might originate from a possible correlation between half-light radius $r_{\rm h}$ and ellipticity modulus. Regions in $r_{\rm h}$–space with a lower ellipticity modulus receive a higher weight. However, lower ellipticity moduli are preferentially found for galaxies oriented orthogonal to the shear, which introduces the bias. One might therefore prefer to apply a different weighting scheme, such as the one proposed by Hoekstra et al. (1998).

### 4.2.4 Dependence on galaxy properties and scale factor $X$

Future weak lensing surveys aim at measuring the redshift dependence of the shear signal. Hence, a shear calibration bias depending on redshift-dependent quantities, such as magnitude or galaxy size, will mimic an evolution of the shear power spectrum which can easily doom any measurement of $w$. Also for surveys not using redshift bins ("2D–lensing"), a redshift-dependent calibration bias will for example lead to a wrong estimate of $\sigma_8$ due to the dependence of the shear power spectrum on the source redshift distribution (van Waerbeke et al. 2006). Hence, besides being negligible on average, calibration bias should also be negligible as a function of all properties used as redshift proxies.

In the H06 analysis the different shear catalogues were briefly tested for dependencies of the calibration bias on magnitude or flux radius. Different significant trends were detected for most methods, but not discussed in detail.

Here we present a more thorough analysis based on our shear catalogue for the simulations with PSF model 1 (to also test the dependence of anisotropy residuals) and the strongest shear $\gamma_1^{\rm true} = 0.1$, which provides the highest discriminating power. We plot the estimate for $\langle e_\alpha^{\rm iso}\rangle$ as a function of half-light radius, magnitude, and signal-to-noise ratio in Fig. 4.7, where the middle row corresponds to the default scale factor $X = 1.0$, see (3.92), which was also used in our original analysis. The upper (lower) row corresponds to a smaller (larger) value $X = 0.7$ ($X = 1.5$), which we additionally tested. As it can be seen from Fig. 4.7 and Table 4.4, the choice of $X$ has a significant impact on the overall average shear calibration bias, with a more negative bias for smaller $X$.

**Dependence on half-light-radius** For all three values of $X$ there is a striking dependence of the shear estimate $\langle e_1^{\rm iso}\rangle$ on $r_{\rm h}$, where a larger value for $r_{\rm h}$ corresponds to stronger under-estimation of the shear. For the SExtractor FLUX_RADIUS parameter, a similar, even slightly stronger trend was observed. Hence, different cuts on these parameters introduce different selection bias, which can also be seen from Fig. 4.6: The MH analysis, which includes all objects larger than the upper limit of the stellar $r_{\rm h}$ interval, suffers from relatively little selection bias ($\langle m_{\rm selc}\rangle = -0.017 \pm 0.001$) on the cost of higher stellar contamination (3.9%). On the other hand we use a more conservative selection $r_{\rm h} > 1.2 r_{\rm h}^*$ leading to lower contamination (1.4%) but higher selection bias $\langle m_{\rm selc}\rangle = -0.045 \pm 0.006$.

A possible $r_{\rm h}$ dependence of the shear estimate is not too surprising, given that the half-light-radius of an object does not only depend on the overall scale, but also the shape of the object. Half-light-radius is additionally measured from the PSF convolved image. Hence, an $r_{\rm h}$ dependence does not automatically imply a dependence on intrinsic galaxy size, which would be problematic for the cosmological application. This has to be tested independently, which will be done for the STEP2 simulations (Sect. 4.3.6). Nevertheless one wishes to avoid selection bias, and should therefore ideally apply no cuts in half-light-radius. This is, however, not feasible due to the required star rejection. One therefore has to find a trade-off between rejecting stars and hardly resolved galaxies on the one hand, and selection bias on the other. When plotting the $r_{\rm h}$ dependence in Fig. 4.7, we include all objects with $r_{\rm h} > 1.1 r_{\rm h}^*$. A peculiar behaviour can be seen for the first bin, where $\langle e_1^{\rm iso}\rangle$ drops while $\langle e_2^{\rm iso}\rangle$ is significantly positive, which indicates a contamination with poorly PSF corrected stars and/or galaxies. In order to exclude this peculiarity, we recommend a cut at $r_{\rm h} > 1.15 r_{\rm h}^*$, which is indicated by the vertical line. This should provide a sufficient rejection while introducing little bias. In any case it is preferable to select galaxies with cuts in $r_{\rm h}$ compared to FLUX_RADIUS, as the latter introduces a slightly stronger bias.

**Dependence on magnitude, signal-to-noise, and scale factor** $X$ Within the fit interval $21.5 <$ MAG_AUTO $< 25.5$ our shear estimate changes only weakly by $\sim 0.0025$ in shear corresponding to a $\sim 2.5\%$ calibration bias. For the relatively low number of even fainter galaxies we observe a deterioration of the shear estimate both for $X = 1.0$ and $X = 1.5$. Most of these galaxies also have a low signal-to-noise, which shows a similar trend of a stronger bias for lower S/N values. However, here the degradation is less abrupt, with a steeper slope over the total relevant lg(S/N) range. Hence, the problematic faint galaxies affected by strong bias can more efficiently be rejected with cuts in magnitude than S/N.

For $X = 0.7$ the S/N dependence is much flatter compared to the larger values of $X$, and no deterioration occurs at the faint magnitude or S/N end. Here it is important to realise that for individual objects S/N depends on the size of the Gaussian filter function and hence on $X$. Although the exact behaviour depends on the slope of the object brightness profile, a smaller value of $X$ will make the analysis more sensitive to the inner bright core of the object, increasing the S/N estimate. Hence, the applied cut S/N $> 3.0$ will not yield exactly the same object selection for the different values of $X$.

The downside of the better behaved S/N and magnitude trend is given by a larger overall calibration bias and stronger leakage of PSF anisotropy indicated by $\langle e_2^{\rm iso}\rangle$ (see also Table 4.4).

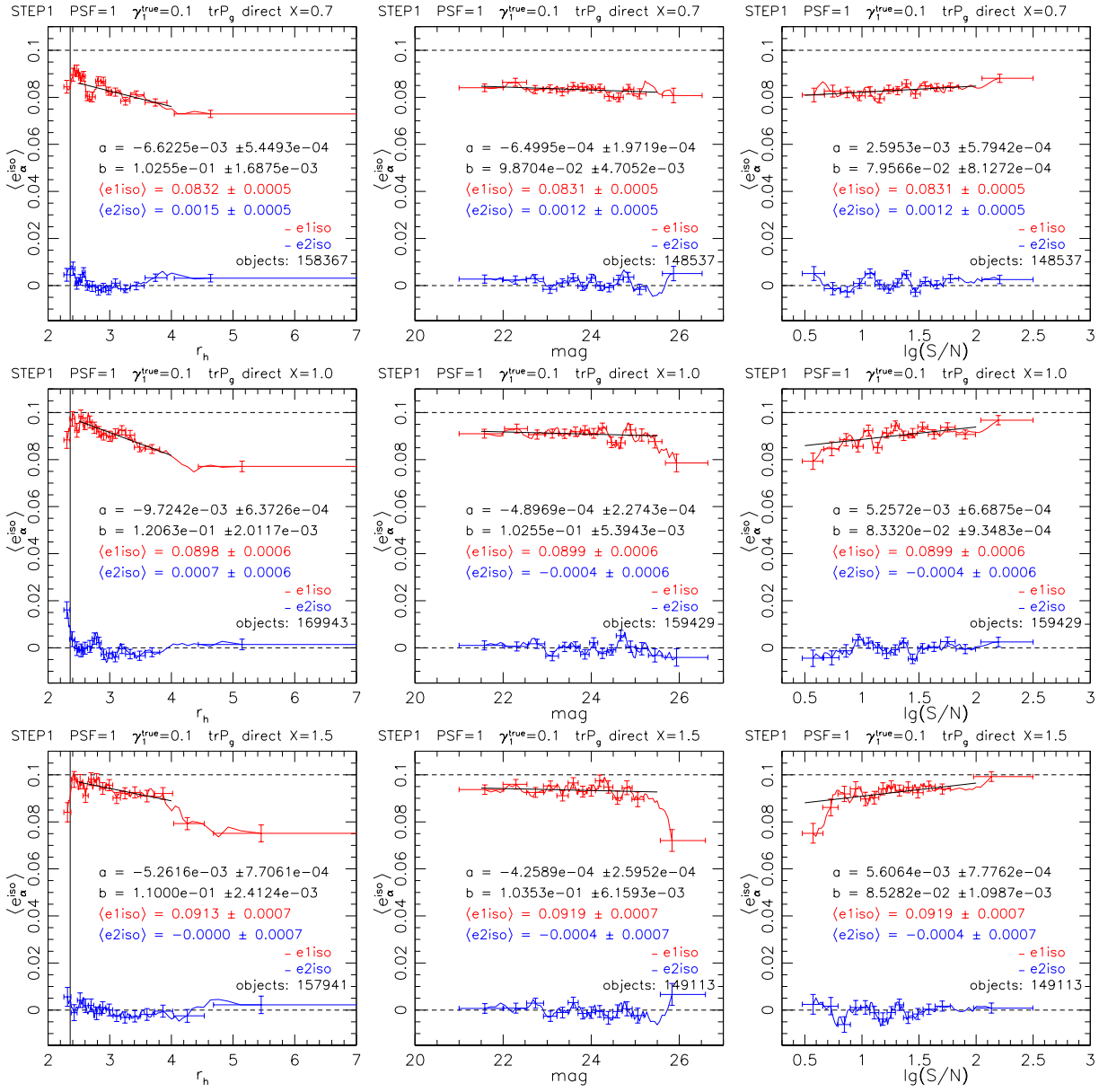


Figure 4.7: Dependence of the shear estimate for the STEP1 PSF1 simulations with $\gamma_1^{\rm true} = 0.1$ on half-light radius $r_{\rm h}$ (*left*), magnitude (`MAG_AUTO`, *middle*) and signal-to-noise S/N (*right*), for three scale factors $X$ specifying the KSB Gaussian filter scale. The curves show a box-average of the data, where the error-bars indicate individual bins. The bin width was chosen such that all bins receive equal numbers of galaxies. The deviation of $\langle e_1^{\rm iso} \rangle$ from $\gamma_1^{\rm true} = 0.1$ is due to shear calibration bias. A deviation of $\langle e_2^{\rm iso} \rangle$ from $\gamma_2^{\rm true} = 0.0$ is an indication for residual PSF anisotropy contamination. For the plots as a function of $r_{\rm h}$ the vertical line indicates the suggested cut at $1.15 r_{\rm h}^*$, which has been applied for the other panels. For all plots galaxies have additionally been selected with S/N $> 3.0$, tr$P_g/2 > 0.0$, and $|e^{\rm iso}| < 2.0$. Hence, the selection criteria were relaxed compared to the H06 analysis to reduce selection bias and increase the number density of galaxies. The black lines show a linear fit to the binned $\langle e_1^{\rm iso} \rangle$ points, where the length of the line indicates the region considered. The slope $a$ and offset $b$ of the linear fit are also given.

Table 4.4: Dependence of the overall (average) shear calibration bias $m_1$, PSF anisotropy residuals indicated by $\langle e_2^{\rm iso}\rangle$, and the selected number of galaxies $N_{\rm gal}$ on different selection and analysis parameters for the STEP1 PSF1 simulations with $\gamma_1^{\rm true} = 0.1$. We ignore the influence of PSF anisotropy in the computation of $m_1 = (\langle e_1^{\rm iso}\rangle - \gamma_1^{\rm true})/\gamma_1^{\rm true}$ due to the dominance of the gravitational shear. "full tensor" indicates a full tensor inversion of $P^g$, while modification (4.5) has been applied for "HH cor". For the two bottom rows $\mathrm{Tr}P^g/2$ has been fit using third-order polynomials in $r_{\rm h}$ and magnitude or ellipticity respectively.

| $X$ | $r_{\rm h}^{\rm min}/r_{\rm h}^*$ | $(\mathrm{S/N})_{\rm min}$ | $\lvert e^{\rm iso}\rvert_{\rm max}$ | $m_1$ | $\langle e_2^{\rm iso}\rangle$ | $N_{\rm gal}$ | special |
|---|---|---|---|---|---|---|---|
| 1.0 | 1.2 | 4.0 | 0.8 | $-0.114 \pm 0.005$ | $-0.0007 \pm 0.0005$ | 138461 | |
| 1.0 | 1.2 | 4.0 | 2.0 | $-0.105 \pm 0.006$ | $-0.0003 \pm 0.0006$ | 140411 | |
| 1.0 | 1.1 | 4.0 | 2.0 | $-0.095 \pm 0.006$ | $-0.0002 \pm 0.0006$ | 152676 | |
| 1.0 | 1.15 | 4.0 | 2.0 | $-0.095 \pm 0.006$ | $-0.0002 \pm 0.0006$ | 152676 | |
| 1.0 | 1.15 | 3.0 | 2.0 | $-0.101 \pm 0.006$ | $-0.0004 \pm 0.0006$ | 159429 | |
| 0.7 | 1.15 | 3.0 | 2.0 | $-0.169 \pm 0.005$ | $0.0012 \pm 0.0005$ | 148537 | |
| 0.7 | 1.15 | 4.0 | 2.0 | $-0.165 \pm 0.005$ | $0.0010 \pm 0.0005$ | 142462 | |
| 1.5 | 1.15 | 3.0 | 2.0 | $-0.081 \pm 0.007$ | $-0.0004 \pm 0.0007$ | 149113 | |
| 1.5 | 1.15 | 4.0 | 2.0 | $-0.074 \pm 0.007$ | $-0.0007 \pm 0.0007$ | 142585 | |
| 1.0 | 1.15 | 3.0 | 0.8 | $-0.107 \pm 0.005$ | $-0.0025 \pm 0.0006$ | 140980 | full tensor |
| 1.0 | 1.15 | 3.0 | 1.4 | $0.016 \pm 0.007$ | $0.0015 \pm 0.0007$ | 152627 | full tensor |
| 1.0 | 1.15 | 3.0 | 2.0 | $0.057 \pm 0.008$ | $0.0039 \pm 0.0008$ | 155523 | full tensor |
| 1.0 | 1.15 | 3.0 | 2.0 | $-0.062 \pm 0.006$ | $0.0008 \pm 0.0006$ | 159172 | HH cor |
| 1.0 | 1.15 | 3.0 | 2.0 | $-0.115 \pm 0.005$ | $-0.0010 \pm 0.0005$ | 159424 | $P^g(r_{\rm h}, \mathrm{mag})$ |
| 1.0 | 1.15 | 3.0 | 2.0 | $-0.114 \pm 0.005$ | $-0.0012 \pm 0.0005$ | 159429 | $P^g(r_{\rm h}, \lvert e^{\rm iso}\rvert)$ |

The latter can easily by understood: By choosing a smaller $X$ one is more sensitive to the galaxy cores, whose shape is more strongly affected by PSF effects. The increased overall bias is surprising and maybe provides hints concerning the actual origin of the bias. This trend would be expected, if the bias originates from pixelisation effects, which will be enhanced for less resolved objects. Alternatively, an under-estimation of the PSF smearing correction would be enhanced for smaller $X$, which amplifies PSF effects.

### 4.2.5 Improving the cuts

In order to reduce the impact of selection bias we modified our selection criteria when revising our pipeline after the original H06 analysis. In particular, we decided to use less conservative cuts for the star rejection, where a cut $r_\mathrm{h} > 1.15 r_\mathrm{h}^*$ seems to be preferable, as shown in Sect. 4.2.4. We also relax the cut on the corrected ellipticity, where $|e^\mathrm{iso}| < 2.0$ performs well in combination with $\mathrm{tr}P_g/2 > 0.0$. As can be seen from Table 4.4, each of both modifications change the overall calibration bias by $\sim 1\%$. Reducing the cut in half-light radius further to $1.1 r_\mathrm{h}^*$ does not improve the calibration significantly, but introduces undesired PSF anisotropy leakage.

We also tested the usage of a lower signal-to-noise cut $\mathrm{S/N} > 3.0$, which works best if the faintest galaxies in the magnitude-incomplete tail are additionally rejected ($\sim 5 - 10\%$), see Fig. 4.7. Note that the conservative cut $\mathrm{S/N} > 4.0$ applied in the original analysis led to a high signal-to-noise in the shear measurement, while using a rather low number of galaxies (Table 4.3). On the contrary, the faintest galaxies significantly add noise leading to little gain in the overall signal-to-noise.

We decided not to change the selected scale factor $X = 1.0$. While reducing it improves the behaviour at the faint end on the cost of stronger overall bias and more PSF anisotropy leakage, increasing it would reduce the average bias, but introduce a stronger deterioration at the faint end plus slightly largen the errors in the shear estimate (see Table 4.4). Hence, keeping $X = 1.0$ seems to be a good compromise. Yet, it might be interesting to investigate this previously ignored effect in further detail in the future.

### 4.2.6 Understanding the different KSB+ results seen in STEP1

At first sight, the different performances of the various KSB+ implementations in the original STEP1 analysis (see Table 4.5) might appear disconcerting. However, a closer look reveals that most of the differences can be well understood. Here we base the analysis on the calibration bias $\langle m_\mathrm{uncontaminated} \rangle$ after rejection of stars and false detections. Their impact is obvious and can be minimised by optimising the selection. In order to understand the bias in the actual shape measurement we estimate the shape measurement bias

$$m_\mathrm{shape} \simeq \langle m_\mathrm{uncontaminated} \rangle - \langle m_\mathrm{select} \rangle + \langle m_\mathrm{weight} \rangle \,. \tag{4.4}$$

Note that this provides only an approximation, which we expect to be accurate to the $1 - 2\%$ level. This is however sufficient when one aims to understand the large discrepancies between the methods.

Concerning PSF anisotropy residuals our approach to model the PSF anisotropy kernel as a function of filter scale $r_\mathrm{g}$ shows by far the best performance of all tested KSB+ codes. Hence, we generally recommend this approach.

#### 4.2.6.1 Performance of the different pipelines

**MB** The MB analysis is based on the Bacon et al. (2000) KSB+ pipeline, which utilises a shear calibration factor $\gamma_\mathrm{cor} = \gamma/0.85$ found from image simulations. *Without* this calibration factor

Table 4.5: Performance of the KSB+ implementations used in the original STEP1 analysis, where each author's key is given in the first column. $\langle m \rangle$ denotes the overall calibration bias, while false detections and stars have been excluded for $\langle m_{\rm uncontaminated} \rangle$. $\sigma_c$ is an estimate for PSF anisotropy residuals. $\langle m_{\rm select} \rangle$ and $\langle m_{\rm weight} \rangle$ denote selection and weight bias. We also compute the shape measurement bias $m_{\rm shape} \simeq \langle m_{\rm uncontaminated} \rangle - \langle m_{\rm select} \rangle + \langle m_{\rm weight} \rangle$ (based on Table 5 in H06).

| | $\langle m \rangle$ | $\sigma_c$ | $\langle m_{\rm uncontaminated} \rangle$ | $\langle m_{\rm select} \rangle$ | $\langle m_{\rm weight} \rangle$ | $m_{\rm shape}$ |
|---|---|---|---|---|---|---|
| MB | $-0.071 \pm 0.015$ | 0.0008 | $-0.009 \pm 0.021$ | $-0.008 \pm 0.002$ | – | $-0.001 \pm 0.021$ |
| C1 | $-0.100 \pm 0.018$ | 0.0006 | $-0.090 \pm 0.018$ | $-0.046 \pm 0.022$ | $0.011 \pm 0.004$ | $-0.033 \pm 0.029$ |
| C2 | $-0.084 \pm 0.018$ | 0.0115 | $-0.074 \pm 0.018$ | $-0.045 \pm 0.022$ | $0.010 \pm 0.003$ | $-0.019 \pm 0.029$ |
| MH | $-0.161 \pm 0.014$ | 0.0008 | $-0.142 \pm 0.015$ | $-0.017 \pm 0.001$ | $0.032 \pm 0.003$ | $-0.093 \pm 0.015$ |
| CH | $-0.032 \pm 0.028$ | 0.0035 | $0.004 \pm 0.027$ | $-0.010 \pm 0.003$ | – | $0.014 \pm 0.027$ |
| HH | $-0.015 \pm 0.006$ | 0.0008 | $0.018 \pm 0.004$ | $-0.001 \pm 0.001$ | $0.006 \pm 0.001$ | $0.025 \pm 0.004$ |
| TS | $-0.167 \pm 0.011$ | 0.0003 | $-0.158 \pm 0.010$ | $-0.045 \pm 0.006$ | $0.024 \pm 0.003$ | $-0.089 \pm 0.012$ |
| LV | $-0.068 \pm 0.025$ | 0.0006 | $-0.068 \pm 0.025$ | $-0.001 \pm 0.002$ | $0.005 \pm 0.001$ | $-0.062 \pm 0.025$ |

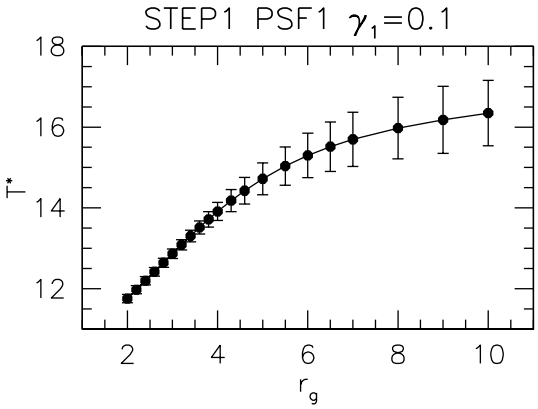


Figure 4.8: Dependence of $T^* = {\rm Tr}\left[P^{\rm sh*}\right]/{\rm Tr}\left[P^{\rm sm*}\right]$ on the Gaussian filter scale $r_{\rm g}$ computed from stars in the STEP1 PSF1 simulations with $\gamma_1^{\rm true} = 0.1$. The error-bars indicate the scatter between the different stars.

their analysis would yield $m_{\rm shape} \sim -15\%$. MB do not measure $P^{\rm sm*}$ and $P^{\rm sh*}$ as a function of filter scale. Given that $T^* = {\rm Tr}\left[P^{\rm sh*}\right]/{\rm Tr}\left[P^{\rm sm*}\right]$ increases for larger $r_{\rm g}$ (see Fig. 4.8), this will lead to an over-estimation of $P^g$ and hence an under-estimation of the shear. The quantitative impact of this effect can be estimated by comparing the C1 and C2 analysis. In the MB analysis ${\rm Tr}P^g/2$ was fit as a function of $r_{\rm g}$.

**C1/C2** For the two analyses by Clowe a calibration factor $\gamma_{\rm cor} = \gamma/0.95$ was applied, which would imply a shape measurement bias of $\sim -8\%$ for C1 and $\sim -7\%$ for C2 if no calibration factor had been used. The major difference between the two catalogues is the measurement of $P^{\rm sm*}$ and $P^{\rm sh*}$ as a function of filter scale in C2 but not C1. Hence, the additional under-estimation by $\sim 1.5\%$ in C1 can be accounted to the negligence of its scale dependence. We expect that the bias measured for the MB analysis has a similar contribution from the neglected

scale dependence. In the C1/C2 analysis $\mathrm{Tr}P^g/2$ is fit as a function of $r_\mathrm{g}$ and ellipticity.

**MH, TS** The MH analysis differs from our analysis (TS) only in the galaxy selection and PSF anisotropy correction. Hence it is expected that the shape measurement bias corrected for selection bias agree very well. No calibration factor has been applied in both analyses, which then consistently yield $m_\mathrm{shape} \sim -9\%$.

**CH** The CH KSB+ implementation yields a shape measurement bias which is consistent with zero without applying a calibration factor. However, in the computation of the $P^\mathrm{sh}$ and $P^\mathrm{sm}$ tensors this implementation approximates the separation between the object centre and each pixel by the integer separation to the central pixel. Preliminary tests done with an adapted version of our pipeline indicate that this approximation can effectively boost the average shear signal by a few percent. Hence, without this "correction" the CH pipeline would probably also yield a slightly negative shear measurement bias.

**HH** The HH pipeline yields a slightly positive shape measurement bias of $\sim 2.5\%$. In earlier studies with simulations HH found a significant dependence of $P^\mathrm{sh}$ on ellipticity. In order to compensate this effect they introduce an ellipticity dependent correction factor

$$P^\mathrm{sh} \rightarrow (1 - e^2/2)P^\mathrm{sh} \,. \tag{4.5}$$

Applying this factor in our analysis of the STEP1 PSF1 data with $\gamma^\mathrm{true} = 0.1$ boosts the shear signal by $\sim 4\%$ (see Table 4.4). Hence, without this correction the HH pipeline would probably also yield a slightly negative shear measurement bias. Besides the MH and TS pipelines, the HH implementation is the only tested KSB+ implementation which uses sub-pixel interpolation. In the HH analysis $\mathrm{Tr}P^g/2$ is fit as a function of $r_\mathrm{g}$.

**LV** The major differences between the LV implementation and our method are that LV does not use sub-pixel interpolation, but applies a fit of $\mathrm{Tr}P^g/2(r_\mathrm{g}, \mathrm{mag})$. His method yields a shear measurement bias of $\sim -6\%$.

#### 4.2.6.2 A common trend but differences in details

Ignoring all the "corrections", which are applied to boost the shear signal, all KSB+ pipelines show a trend to provide an under-estimated shear measurement. This shear measurement bias ranges from a few per cent (HH, CH) to $\sim -15\%$ for the MB implementation. A part of this bias can be understood due to the negligence of the $r_\mathrm{g}$ dependence of $P^{\mathrm{sm}*}$ and $P^{\mathrm{sh}*}$ for the methods MB and C1.

One might suspect that pixelisation gives rise to the overall trend that shear is under-estimated. This becomes, however, unlikely if one realises that both methods that do and methods that do not use sub-pixel interpolation suffer from large bias (MH and TS versus MB). Also, among the methods yielding rather small bias some do and some do not apply sub-pixel interpolation (HH versus CH).

In addition, we performed tests with our pipeline using simple simulations with Gaussian profiles, for which the measured KSB quantities can be compared to analytic predictions (Erben et al. 2001). These tests indicate that pixelisation can introduce systematic size-dependent biases, which can be as big as $\sim$ 10% for certain KSB+ parameters. In particular, the ellipticity and diagonal components of the $P^{\rm sm}$ tensor are typically under-estimated, whereas the diagonal elements of the $P^{\rm sh}$ tensor are typically over-estimated. Linear interpolation makes the KSB estimates more stable with respect to the relative position of the object centroid on the pixel grid, but does not correct for the bias. However, galaxies and stars are affected in a similar way, so that – at least in the Gaussian case – the impact on the final shear estimate partially cancels.

It seems likely that the dominant reason for the overall trend to under-estimate the shear is connected with the $P^g$–correction, which we will discuss in the next subsection. However, it is important to note that probably several other effects depending on the detailed coding are responsible for the remaining large scatter between the methods. A very good example is given by the $X$ dependence of our method, where a change from $X = 1.5$ to $X = 0.7$ worsens the bias from $\sim -8\%$ to $\sim -17\%$ (for S/N $> 4.0$, see Table 4.4).

### 4.2.7 Impact of the $P^g$–correction

In the original STEP1 analysis all KSB+ implementations use the trace approximation (3.95) for the inversion of the $P^g$ tensor to reduce noise. Several of the methods additionally fit Tr$P^g/2$ as a function of size, magnitude, and/or ellipticity, in order to further reduce noise (see Sect. 4.2.6.1).

#### 4.2.7.1 Tensor correction

Hetterscheidt (2007) argues that the trace inversion of $P^g$ leads on average to an under-estimation of the shear compared to the tensor inversion. We test this prediction by applying the full tensor inversion to our analysis of the PSF1 images with $\gamma_1^{\rm true} = 0.1$. Indeed, this leads to a substantially increased shear measurement with $m_1 \sim +5\%$ for $|e^{\rm iso}| < 2.0$ (Table 4.4). However, the results become very noisy and unstable with a strong dependence on the ellipticity cut. We therefore do not follow this approach for our science analysis. Nonetheless, the negligence of the trace-free part of $P^g$ is a very good candidate for the overall trend to under-estimate the shear. In fact, this agrees with the observed dependence of the bias on $X$, which was enhanced for small $X$ where the analysis is more strongly affected by PSF effects.

#### 4.2.7.2 $P^g$–fitting

Tr$P^g/2$ is a noisy quantity. Hence its inversion might introduce a bias. The MB, C1, C2, HH, and LV implementations of KSB+ attempt to reduce this bias by fitting Tr$P^g/2$ as a function of less noisy observables, such as magnitude and size. The fact that methods with weak, but also methods with strong bias belong to this group indicates that fitting does not solve the overall problem. It might, however, be useful to better control the dependence of the shear estimate on size or magnitude. To test this, we re-applied our analysis using two-dimensional third-order polynomial fits of Tr$P^g/2$ as a function of $r_{\rm h}$ and magnitude, and $r_{\rm h}$ and uncorrected ellipticity, where

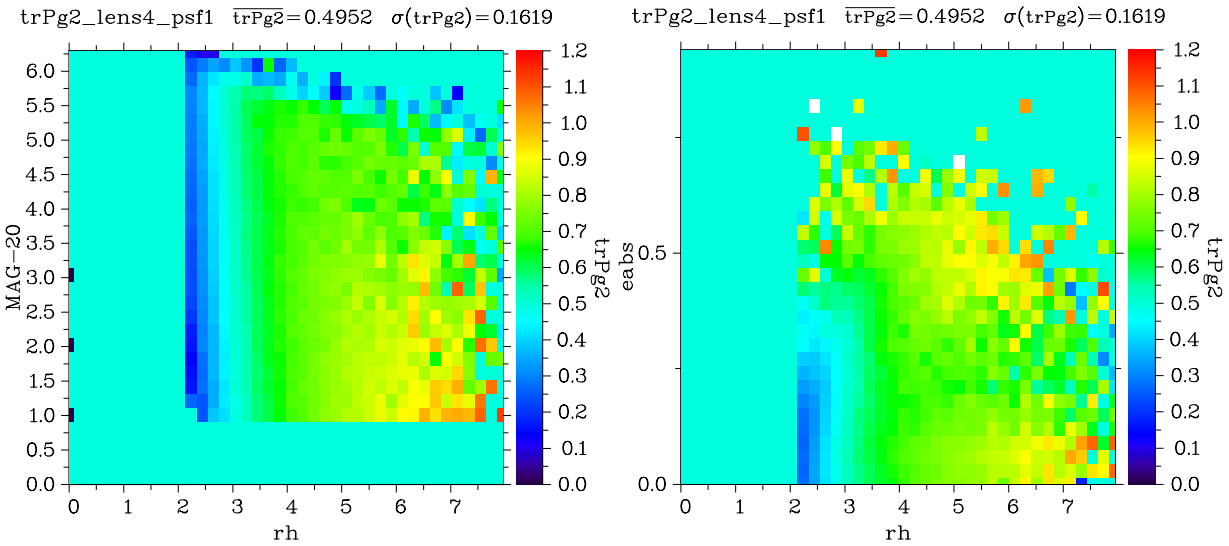


Figure 4.9: Dependence of $\langle \mathrm{Tr}P^g/2 \rangle$ on $r_\mathrm{h}$ and magnitude (*left*) as well as $r_\mathrm{h}$ and the modulus of the un-corrected ellipticity $|e|$ (*right*) for the STEP1 PSF1 $\gamma_1^\mathrm{true} = 0.1$ galaxies. Bins without galaxies show the mean value.

outliers have been rejected at the $3\sigma$–level. The variation of the mean $\mathrm{Tr}P^g/2$ in this parameter space is shown in Figure 4.9. In both cases fitting changes the overall bias only marginally (Table 4.4). If $\mathrm{Tr}P^g/2$ is fit as a function of $r_\mathrm{h}$ and ellipticity, the slope of the shear calibration bias as a function of magnitude and signal-to-noise is, however, significantly increased (Figure 4.10). In fact, this provides a slight overkill, with a shear signal increasing with magnitude.

### 4.2.8 Conclusions from STEP1

In the original H06 STEP1 analysis the different KSB+ pipelines show a remarkably different performance, with systematic average calibration errors ranging from $\sim -2\%$ to $\sim -17\%$. For several methods a large fraction of this bias arises from easily correctable effects, namely stellar contamination, false detections, selection bias due to cuts, and possibly bias due to the weighting scheme. Subtracting these effects and compensating for artificially included corrections to boost the shear signal, we estimate the true bias in the object shape measurement for each method, which ranges from $-2\%$ to $-15\%$, and amounts to $\sim -9\%$ for our method. We conclude that the overall trend for all tested KSB+ implementations to have a negative shear measurement bias probably originates from the negligence of the trace-free component in the inversion of the $P^g$ tensor. Fitting of $\mathrm{Tr}P^g/2$ seems to have little impact on the overall average bias. The large remaining scatter between the different methods probably stems from subtle differences in the coding, e.g. the treatment of pixelisation, possibly using sub-pixel interpolation. In particular, we identify a strong dependence of the shear calibration bias on the scale factor $X$ relating the flux-radius of an object to the filter scale $r_\mathrm{g}$ used for shape measurements.

We estimate that with optimised selection criteria (Sect. 4.2.5) a bias of $\sim -1\%$ will remain

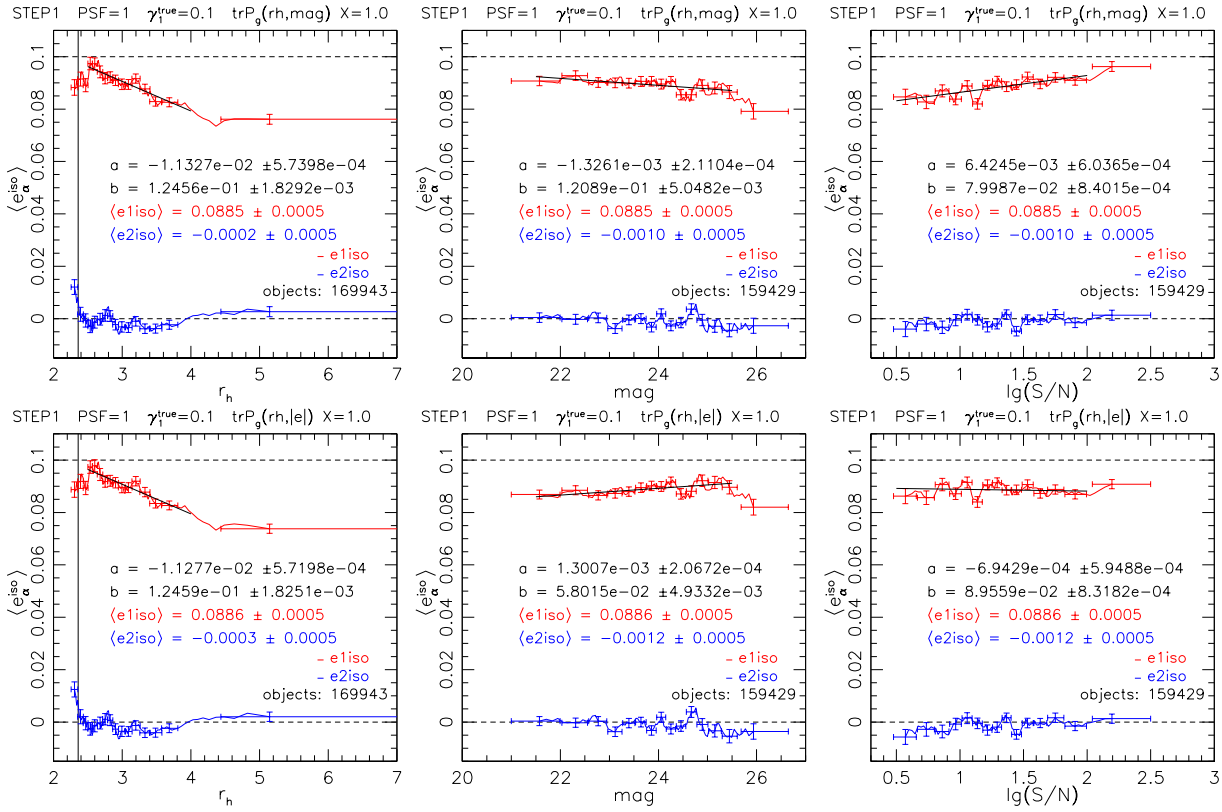


Figure 4.10: Dependence of the shear estimate for the STEP1 PSF1 simulations with $\gamma_1^{\rm true} = 0.1$ on half-light radius $r_{\rm h}$ (*left*), magnitude (`MAG_AUTO`, *middle*) and signal-to-noise S/N (*right*), for $\mathrm{Tr}P^g/2$ fit as a function of $r_{\rm h}$ and magnitude (*top*) as well as $r_{\rm h}$ and the modulus of the uncorrected ellipticity $|e|$ (*bottom*). Compared to Figure 4.7 $\mathrm{Tr}P^g/2(r_{\rm h}, \mathrm{mag})$–fitting has only little influence, whereas fitting as a function of $r_{\rm h}$ and $|e|$ significantly increases the slope of the shear estimate depending in magnitude and signal-to-noise.

from stellar contamination and selection bias for our method. Hence, the overall shear calibration bias in our analysis amounts to $\sim -10\%$. As the origin of this bias seems to be understood, and given that it appears to be stable between different PSF models on the $1-2\%$ level (see Table 4.5), it is reasonable to compensate this bias by the introduction of a shear calibration factor, where we define the corrected estimator

$$\gamma_\alpha = c_{\rm cal} e_\alpha^{\rm iso}\,, \tag{4.6}$$

with $c_{\rm cal} = 1/0.91$. Therefore, we decided to use this factor in the analysis of the STEP2 simulations (Sect. 4.3). Nonetheless, the actual value of the calibration obviously depends on the details of the implementation. Hence, we urge everybody using KSB+ to test their own implementation on image simulations, instead of blindly using calibration factors found for other pipelines.

In the original STEP1 analysis dependencies of the shear estimate on flux-radius and magnitude were identified, which we investigated further in this work. In particular, there is a strong dependence of the shear signal on half-light-radius $r_{\rm h}$, which can introduce selection bias if the cut to reject stars and poorly resolved galaxies is chosen too high. We find that a cut at $1.15 r_{\rm h}^*$ provides a good compromise between selection bias on the one hand, and PSF anisotropy leakage and stellar contamination on the other.

In our default KSB+ pipeline a deterioration of the shear estimate at the faint magnitude end occurs. For a low signal-to-noise cut $\mathrm{S/N} > 3.0$ this can be efficiently cured by rejecting the faintest $\sim 5-10\%$ of the galaxies with a magnitude cut. The same effect could be achieved by reducing the filter scale factor to $X = 0.7$, which however increases the overall bias and introduces PSF anisotropy leakage and is hence not recommended. Besides this deterioration we find a weak decline of the shear estimate with magnitude, amounting to a calibration bias of $\sim 2.0\%$ over the magnitude range $21.5 < \texttt{MAG\_AUTO} < 25.5$, which is unproblematic for current weak lensing analyses, but could be of concern for future constraints on $w$. A possible way to correct for this trend might be given by fitting $\mathrm{Tr}P^g/2$ as a function of $r_{\rm h}$ and ellipticity, which in the currently tested version however over-does the job. We will test this further using the STEP2 simulations in Sect. 4.3.8.

Concerning PSF anisotropy correction our approach to model the stellar anisotropy kernel as a function of filter scale provides the best correction of all KSB+ implementations. Hence, we recommend this approach for all methods.

## 4.3 STEP2: High precision simulations

After improving shear measurement methods based on the STEP1 results, the collaboration conducted a second blind analysis of simulated ground-based images. These simulations comprise a number of more realistic refinements such as galaxy morphology and more complex PSFs. In this analysis we achieved a significantly improved statistical measurement accuracy via a combination of more extensive simulations and pairs of galaxy images which have been rotated with respect to each other by $\pi/2$, efficiently reducing noise due to intrinsic ellipticities. This allowed us to split the data into subsets enabling tests for several effects which might affect future high-precision cosmic shear analyses, such as calibration bias which differs for different galaxy populations.

The detailed analysis has been published in Massey, Heymans, Bergé, Bernstein, Bridle, Clowe, Dahle, Ellis, Erben, Hetterscheidt, High, Hirata, Hoekstra, Hudelot, Jarvis, Johnston, Kuijken, Margoniner, Mandelbaum, Mellier, Nakajima, Paulin-Henriksson, Peeples, Roat, Refregier, Rhodes, Schrabback, Schirmer, Seljak, Semboloni, & van Waerbeke (2007a), which I will abbreviate as M07. Here I will mostly limit the discussion to the KSB+ performance and detail on further tests conducted with our method.

The tested methods and associated authors are listed in Table 4.6.

### 4.3.1 Shapelet simulations

The STEP2 simulations have been created by Richard Massey and William High using the Massey et al. (2004) simulation package. Based on the shapelet algorithm, which (de-)composes images of galaxies and stars using sets of orthogonal 2D functions, it allows for the inclusion of complex PSF models and galaxy morphology. Image parameters have been chosen to mimic deep $r$–band data taken in good conditions with the Suprime-Cam camera on the Subaru telescope.

For STEP2 six types of images with different PSF or galaxy types have been modelled, whose properties are summarised in Table 4.7, and which are plotted in Figure 4.11. Each set of simulations contains 128 $7' \times 7'$ images with pixel scale $0\farcs2$. For each set, the images have been split into two halves, which feature the same patch of the sky, but where the second half has been rotated by 90 degrees compared to the first half. The images have been sheared by a random amount given by a flat PDF with $|\gamma^{\rm input}| < 0.06$, where corresponding images between the different halves have been equally sheared.

In ordinary simulations the error in the estimated mean shear decreases with the number of galaxies $N$ as $\sqrt{\langle|e_i^{\rm int}|^2\rangle/N}$, where $e_i^{\rm int}$ denotes the intrinsic ellipticity of galaxy $i$, and $\sqrt{\langle|e_i^{\rm int}|^2\rangle} \sim 0.1$ for the STEP2 simulations.

Due to the rotated pairs we can form a shear estimator for each galaxy pair

$$\tilde{\gamma} = \frac{e^{\rm obs,unrot} + e^{\rm obs,rot}}{2} \,. \tag{4.7}$$

Table 4.6: Shear measurement methods and implementations tested in the analysis of the STEP2 image simulations (Table 2 from M07).

| **Author** | **Key** | **Method** |
|---|---|---|
| Bergé | JB | Shapelets (Massey & Refregier 2005) |
| Clowe | C1 | KSB+ (same PSF model used for all galaxies) |
| Clowe | C2 | KSB+ (PSF weight size matched to galaxies) |
| Hetterscheidt | MH | KSB+ (Erben et al. 2001 pipeline) |
| Hoekstra | HH | KSB+ |
| Jarvis | MJ | Bernstein & Jarvis (2002) |
| Jarvis | MJ2 | Bernstein & Jarvis (2002) (new weighting scheme) |
| Kuijken | KK | Shapelets (Kuijken 2006) |
| Mandelbaum | RM | Reglens (Hirata & Seljak 2003) |
| Nakajima | RN | Bernstein & Jarvis (2002) (deconvolution fitting) |
| Paulin-Henrikson | SP | KSB+ |
| Schirmer | MS1 | KSB+ (scalar shear susceptibility) |
| Schirmer | MS2 | KSB+ (tensor shear susceptibility) |
| Schrabback | TS | KSB+ |
| Semboloni | ES1 | KSB+ (shear susceptibility fitted from populations) |
| Semboloni | ES2 | KSB+ (shear susceptibility for individual galaxies) |

Table 4.7: Summary of the different PSF and galaxy types used in the STEP2 image simulations (Table 1 from M07).

| **Image set** | **PSF description** | **Galaxy type** |
|---|---|---|
| A | Typical Subaru PSF ($\sim 0\farcs6$) | shapelets |
| B | Typical Subaru PSF ($\sim 0\farcs6$) | pure exponential |
| C | Enlarged Subaru PSF ($\sim 0\farcs8$) | shapelets |
| D | Elliptical PSF ($x$-axis) | shapelets |
| E | Elliptical PSF (45°) | shapelets |
| F | Circularly symmetric Subaru PSF | shapelets |

Inverting (3.28) and considering that for the rotated pairs $e^{\rm int,unrot} = e^{\rm int} = -e^{\rm int,rot}$, we find

$$\tilde{\gamma} = \left( \frac{e^{\rm int} + \gamma}{1 + \gamma^* e^{\rm int}} + \frac{-e^{\rm int} + \gamma}{1 - \gamma^* e^{\rm int}} \right) /2 = \frac{\gamma - \gamma^* (e^{\rm int})^2}{1 - \gamma^* (e^{\rm int})^2} \,, \tag{4.8}$$

where we again approximate $\gamma \simeq g$ due to the weak shears applied. Averaging this shear estimator over $N/2$ galaxy pairs yields the significantly reduced shot-noise error in $\langle\tilde{\gamma}\rangle$ of

$$\sigma_{\langle\tilde{\gamma}\rangle} = |\gamma| \sqrt{\frac{\langle |e_i^{\rm int}|^4 \rangle}{N/2}} \,, \tag{4.9}$$

where $\sqrt{\langle |e_i^{\rm int}|^4 \rangle} \sim 0.05$ and $|\gamma| < 0.06$ for the STEP2 simulations.

The shapelet-generated galaxy images are based on the size–magnitude morphology distribution estimated from galaxies in the HST COSMOS survey. As these data have not been deconvolved for the ACS PSF, small galaxies in the simulations are intrinsically slightly rounder than in reality. To test the impact of morphology, the galaxies in simulation set B have be realised using simple exponential profiles with concentric, elliptical isophotes.

In contrast to the STEP1 simulations, STEP2 images contain correlated noise to mimic drizzled stacked images. This has been realised by smoothing the sky noise, which has an rms of 4.43 counts $s^{-1}$, with a Gaussian kernel of FWHM 3.5 pixels.

### 4.3.2 Shear measurement

For the STEP2 analysis we used our KSB+ pipeline as detailed in Sect. 3.4.2.2, but applied improved selection criteria derived from STEP1. For object detection with `SExtractor` we used a Gaussian filter function (gauss_4.0_7x7.conv) and required objects to comprise at least 10 adjacent pixels (`DETECT_MINAREA`) which are $1.5\sigma$ (`DETECT_THRESH`) above the sky background. We selected galaxies with cuts $|e^{\rm iso}| \leq 2.0$, ${\rm Tr}P^g/2 > 0.1$ (which has only minimal impact compared to ${\rm Tr}P^g/2 > 0.0$), S/N > 4, and with $r_{\rm h} > 1.05 r_{\rm h}^{*,{\rm upper}}$, where $r_{\rm h}^{*,{\rm upper}}$ denotes the upper limit of the 0.1 pixel wide interval for star selection, which approximately corresponds to $r_{\rm h} > 1.1 r_{\rm h}^*$. When measuring PSF quantities from stars we integrate to a radius of 4 stellar flux-radii in order to properly account for the scale dependence of the shapelet PSFs. The noise correlation has not been taken into account in the computation of the sky rms or S/N, but led to the raised detection thresholds. In order to take account for the stable calibration bias detected in STEP1, we applied a constant shear calibration factor of $0.91^{-1}$. We do not apply a weighting scheme for our STEP2 analysis.

### 4.3.3 Analysis

The joint analysis of the shear catalogues created in the blind test has been performed by Richard Massey and Catherine Heymans. After the extensive tests for selection and weight bias conducted in STEP1, the main STEP2 analysis was based on the matched rotated-pairs catalogue, which strongly reduces selection and weight bias isolating the actual shape measurement bias.

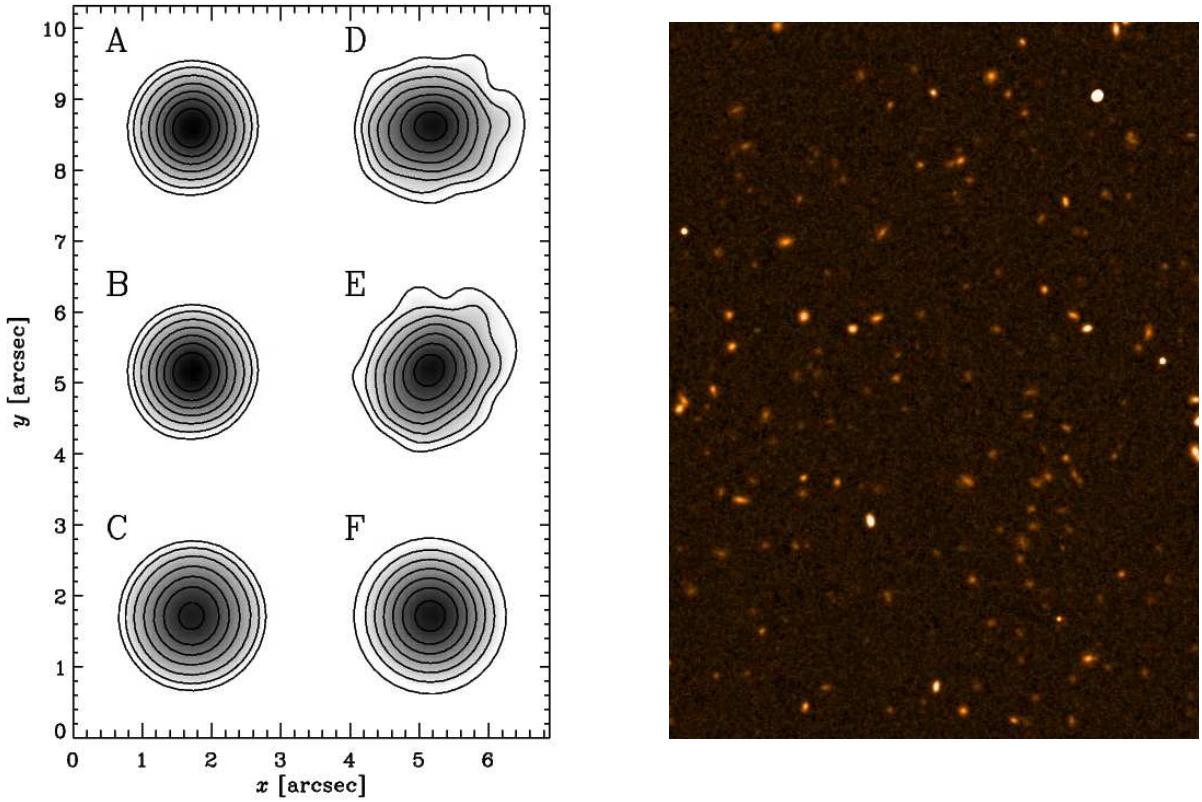


Figure 4.11: *Left:* The PSFs used for the six different sets of STEP2 image simulations. The colour scale and contour spacing is logarithmic (Figure 1 from M07). *Right:* 1.′5 wide cutout from one image of simulation set A.

Table 4.8: Estimates of stellar parameters from the TS KSB+ pipeline. $r_f$ denotes the stellar flux radius from `SExtractor`. The stellar ellipticities $e^*_\alpha$ have been measured with a filter scale $r_g = 3$ pixels (Table 5 from M07).

| Set | $r_f$ | $e^*_1/\%$ | $e^*_2/\%$ |
|---|---|---|---|
| A | 0.″334 | $-0.68 \pm 0.10$ | $1.21 \pm 0.07$ |
| B | 0.″334 | $-0.66 \pm 0.07$ | $1.28 \pm 0.05$ |
| C | 0.″406 | $-0.47 \pm 0.07$ | $0.97 \pm 0.06$ |
| D | 0.″390 | $11.49 \pm 0.11$ | $2.20 \pm 0.14$ |
| E | 0.″390 | $-2.21 \pm 0.14$ | $11.29 \pm 0.16$ |
| F | 0.″392 | $-0.01 \pm 0.12$ | $0.01 \pm 0.01$ |

#### 4.3.3.1 Object detection

In STEP2 contamination with stars or false detections was low except for the SP implementation of KSB+, which suffers from a $\sim$ 30% contamination. The number density of galaxies in our matched catalogue for image set A amounts to $36/\mathrm{arcmin}^2$, which is significantly above the average of all methods ($31/\mathrm{arcmin}^2$). For details see Table 6 in M07.

#### 4.3.3.2 PSF modelling

An interesting effect identified in the STEP2 analysis is PSF anisotropy leakage between the two ellipticity components. The two PSFs D and E are highly elliptical ($\sim$ 11%), but according to the input shapelet model they should contain a pure $e_1$ ellipticity (D) or $e_2$ ellipticity (E) respectively. Table 4.8 summarises PSF properties measured with our KSB+ implementation. For PSFs D and E, a $\sim$ 20% cross-contamination of the measured ellipticity is observed between the two components, which is not expected from the input model. This effect already occurs during the stellar ellipticity measurement and hence cannot be caused by neglected off-diagonal components of the $P^{\mathrm{sm}}$ tensor. The mixing might be caused by skewness in the PSF.

#### 4.3.3.3 Shear calibration bias and PSF anisotropy contamination

As for STEP1, the performance of the methods was estimated with fits to test for calibration bias $m_\alpha$ and PSF anisotropy residuals $c_\alpha$. Given that now also $\gamma_2 \neq 0$, the calibration bias could be tested independently for both ellipticity components. The analysis was conducted twice, once keeping the rotated image pairs separate but using only galaxies which were detected in both sets, and once including the rotated-pair analysis providing the increased sensitivity. By default values given in the test refer to the rotated-pair analysis, and errors of the mean calibration bias give the scatter between the different PSF models and shear components.

The performance of our pipeline and the HH implementation of KSB+ are compared in Figure 4.12 for the different image sets and ellipticity components. For the round or moderately elliptical PSFs A, B, C, and F our pipeline performs very well, with PSF residuals and calibra-

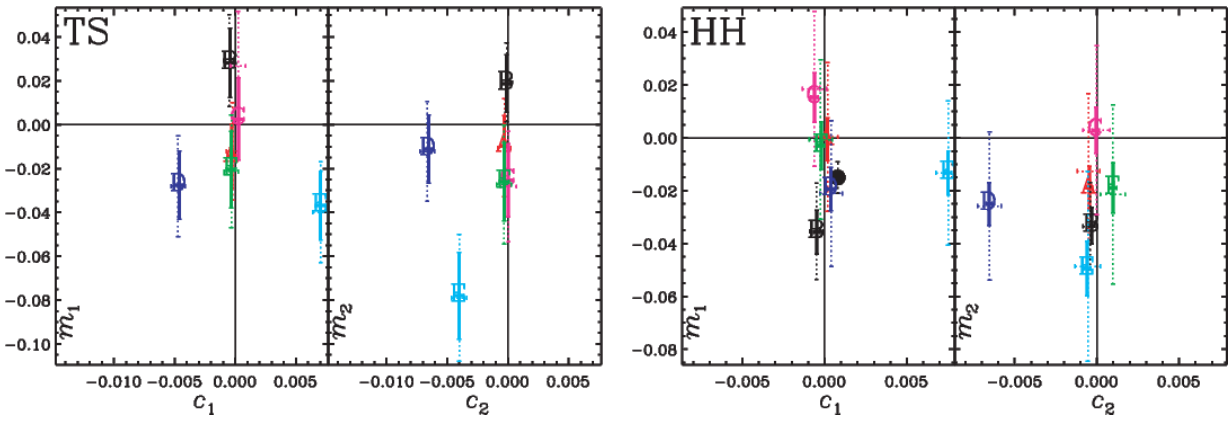


Figure 4.12: Fitted values of calibration bias $m_\alpha$ and PSF anisotropy residuals $c_\alpha$ for the TS (*left*) and HH (*right*) implementations of KSB+. For each method the *left* sub-panel corresponds to the $\gamma_1$ component, whereas the *right* sub-panel refers to $\gamma_2$. The dotted error-bars show rms errors computed without the rotated-pairs shear estimator, but only including common detections between the rotated and unrotated sets. The solid errors have been obtained after removal of the intrinsic ellipticity using the rotated-pairs shear estimator. The red, black, pink, dark blue, light blue, and green points correspond to image sets A, B, C, D, E, and F respectively. Note the different axis scales in the two panels (from Figure 5 in M07).

tion bias $\langle m \rangle = (-0.6 \pm 1.9)\%$ consistent with zero. This confirms the robustness of the shear calibration factor estimated from the STEP1 simulations. For the highly elliptical PSFs D and E we under-estimate the shear on average by $(-3.8 \pm 2.5)\%$, where the bias is strongest for the $e_2$ component of PSF E with $m_2 = -(7.8 \pm 2.0)\%$. Additionally, for these PSFs significant PSF anisotropy residuals are measured, indicated by non-zero values of $c_\alpha$. In particular, we measure a significantly negative $c_2$ for PSF D and positive $c_1$ for PSF E. From the shapelet input PSF models these components should not be affected by PSF anisotropy. The reason for this spurious signal is probably given by the false cross-terms found in the stellar ellipticity measurement (Sect. 4.3.3.2), which are then (falsely) subtracted from the the galaxy ellipticities. For PSFs D and E significant PSF anisotropy residuals have been detected for all methods, see e.g. the HH analysis in Figure 4.12. The presence of these residuals is disturbing but not too worrying for current surveys, given the fact that these PSF models have such a strong PSF ellipticity that similar data would probably be rejected for real cosmic shear surveys. The most effective PSF anisotropy suppression has been achieved by the MJ implementation of the Bernstein & Jarvis (2002) method reaching $c_\alpha < 0.002$.

A comparison of all methods achieving shear calibration errors smaller than 7% is given in Figure 4.13, where the mean calibration $\langle m \rangle$ is compared to the mean PSF anisotropy residuals $\langle c \rangle$. Note that this parameterisation is somewhat misleading given that anisotropy residuals with opposite signs partially cancel, which, however, is not the case for real data.

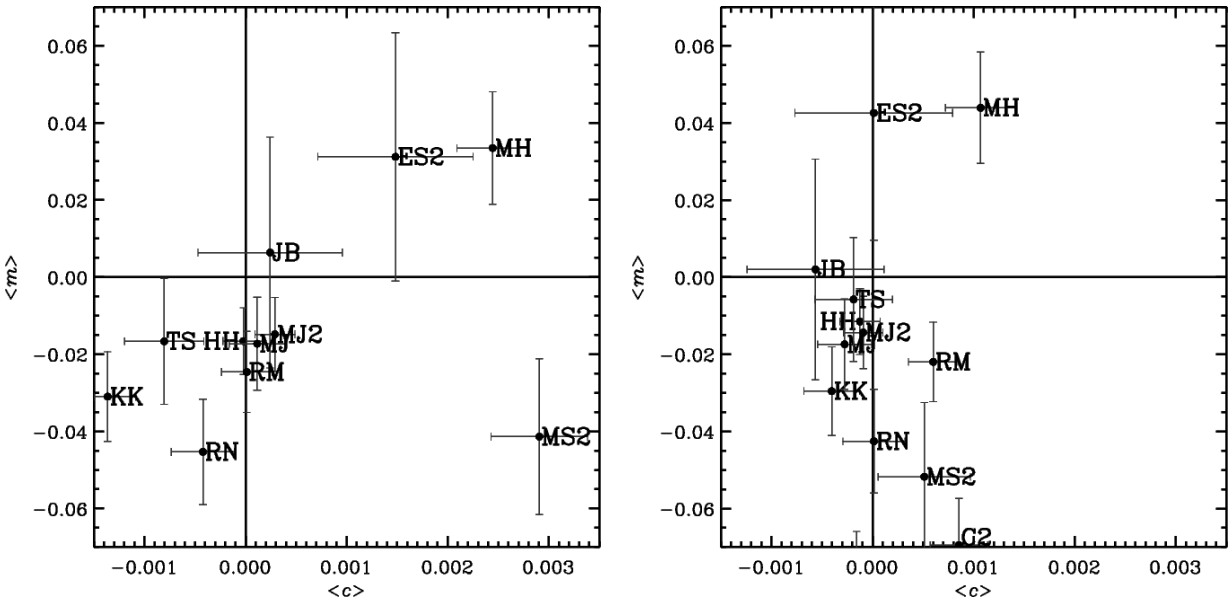


Figure 4.13: Comparison of the different STEP2 analyses in terms of their mean shear calibration bias $\langle m \rangle$ and PSF anisotropy residuals $\langle c \rangle$, also averaged over the two shear components. In the *left* panel all image sets have been considered, whereas the highly elliptical PSFs D and E have been excluded in the *right* panel. Note that methods with $\langle c \rangle$ consistent with zero may still have significant residuals for the individual PSF models, which then average out. The results from C1, SP, MS1, and ES1 are not shown here (Figure 6 from M07).

#### 4.3.3.4 Performance of the other KSB+ pipelines

Concerning calibration bias the KSB+ pipelines already tested in STEP1 perform with similar results: The HH implementation still achieves accuracy at the $1-2\%$ level with $\langle m\rangle = (-1.7 \pm 1.8)\%$, still including the ad-hoc correction to $P^{\rm sh}$. Similarly to our method the MH implementation has optimised the selection criteria and introduced a shear calibration factor $1/0.88$, which is slightly overzealous with $\langle m\rangle = (3.8 \pm 2.5)\%$, as expected from the STEP1 comparison, where the MH analysis yields similar shape measurement bias as our method (Table 4.5). The C1/C2 methods yield an under-estimation of the shear with $\langle m\rangle = (-12.1 \pm 4.6)\%$ for C1 and $\langle m\rangle = (-7.7 \pm 2.6)\%$ for C2. As this already includes the $1/0.95$ shear calibration factor, the calibration bias seems to be slightly enhanced compared to STEP1. The new SP implementation of KSB+ numerically integrates within pixels and uses a trace inversion of $P^g$. Its performance is very interesting, with a strong $(-11.7 \pm 2.2)\%$ bias for the $\gamma_1$ component, but only $(-6.1 \pm 2.1)\%$ bias for $\gamma_2$. The MS1 and MS2 methods use sub-pixel integration and fit $P^g$ as a function of $r_{\rm g}$ and magnitude, where MS1 applies a trace inversion, whereas MS2 uses the full $P^g$ tensor. As seen from our tests on STEP1, the full tensor correction yields a substantially higher shear estimate with a mean bias $\langle m\rangle = (-4.1 \pm 4.8)\%$ for MS2 compared to MS1 with $\langle m\rangle = (-15.7 \pm 3.5)\%$. The ES1 and ES2 implementations use sub-pixel integration and a trace inversion of $P^g$, where $\mathrm{Tr}P^g/2$ has been smoothed as a function of $r_{\rm g}$ and magnitude for ES1. They achieve a typical negative bias $\langle m\rangle = (-16.3 \pm 4.3)\%$ for ES1, but interestingly a slightly positive bias $\langle m\rangle = (3.1 \pm 6.9)\%$ for ES2. This might suggest that smoothing of $P^g$ instead of fitting is more effective. However, the method shows a disturbingly large scatter between the different PSF models.

### 4.3.4 Pixelisation effects

For most methods $\gamma_1$ is estimated more accurately than $\gamma_2$ with $m_1 > m_2$ (typically $\langle m_1\rangle - \langle m_2\rangle \sim (1-5)\%$), which is the case even for the circular PSF F. Here, the only preferred direction is given by the pixel grid, indicating that the difference might originate from pixelisation. For the square pixels, the $\gamma_1$-direction is sampled better than the $\gamma_2$-direction by a factor $\sqrt{2}$, which could explain the better estimates. However, this does not explain the reverse trend observed for the SP method.

### 4.3.5 Galaxy morphology

Complex galaxy morphologies included in the shapelet galaxies seem to slightly hinder the shape measurement accuracy for the majority of the KSB+ implementations. This can be seen by comparing image set A (shapelet galaxies) with set B (simple exponential profiles). For set A the KSB+ implementations C1, C2, MH, SP, MS1, TS, and ES1 yield a more negative calibration bias than for set B, while the trend is reversed only for the HH and MS2 methods. In the case of our method the difference amounts to $4.2 \pm 2.1\%$. The reason for this trend is probably given by the fact that KSB measures ellipticity for one window scale only. Several of the newer methods

tested in STEP2 deal with the complex morphologies very well, particularly the KK, MJ, and MJ2 methods.

### 4.3.6 Magnitude and size dependence

Due to the high discriminating power the STEP2 data could be split into several subsets to study calibration bias and PSF anisotropy residuals as a function of different parameters. Figure 4.14 shows the dependence on the input magnitude and galaxy size for the HH and our implementation of KSB+, where the galaxy size $R$ was computed according to equation (53) in Massey & Refregier (2005)

$$R^2 = \frac{\int_{\mathbb{R}^2} \mathrm{d}^2x\, |\boldsymbol{x}|^2 f(\boldsymbol{x})}{\int_{\mathbb{R}^2} \mathrm{d}^2x\, f(\boldsymbol{x})}\,, \tag{4.10}$$

with the position relative to the object centre $\boldsymbol{x}$ and surface brightness $f(\boldsymbol{x})$. For both methods the calibration bias becomes more negative for fainter magnitudes and weakly increases with galaxy size, where both effects are more pronounced for our analysis. Our method over-estimates the shear by $\sim 6\%$ at the bright end while under-estimating it by $\sim (20-30)\%$ for faint galaxies. Trends to under-estimate the shear for faint galaxies have been detected for all methods tested in STEP2, and are particularly problematic for 3D shear analyses. The method which was least affected is the ES2 implementation of KSB+ showing a $\sim 5\%$ decline. We will further investigate the detected dependencies in Sect. 4.3.7. As expected PSF anisotropy residuals are most strongly pronounced for small galaxies.

### 4.3.7 Impact of noise correlations

In the original STEP2 analysis all methods suffer from a degradation of the shear estimate for faint galaxies. We will see that – at least for our KSB+ implementation – this is mostly due to the negligence of the noise correlations when applying signal-to-noise cuts.

In the case of uncorrelated noise the dispersion of the sum of the pixel values over $N$ pixels scales as

$$\sigma_N = \sqrt{N}\sigma_1\,, \tag{4.11}$$

where $\sigma_1$ is the dispersion computed from single pixel values. Drizzling, or convolution in the case of the STEP2 simulations, reduces $\sigma_1$ but introduces correlations between neighbouring pixels. For example, even for pure noise it becomes more likely to find a "high" pixel value near to another "high" pixel than at a random position. The signal-to-noise of an object is usually defined as the ratio of the summed object flux convolved with some window or weight function, divided by an rms estimate for the noise in an equal area convolved with the same weight function. If the noise estimate is computed from $\sigma_1$ and scaled according to (4.11), or a version taking the weight function into account such as (3.93), the correlations are neglected and the noise estimate is too small compared to the uncorrelated case.

Together with the sheared images, the STEP2 simulations include one image without objects providing a pure noise realisation. We use this image to estimate the effective influence of the

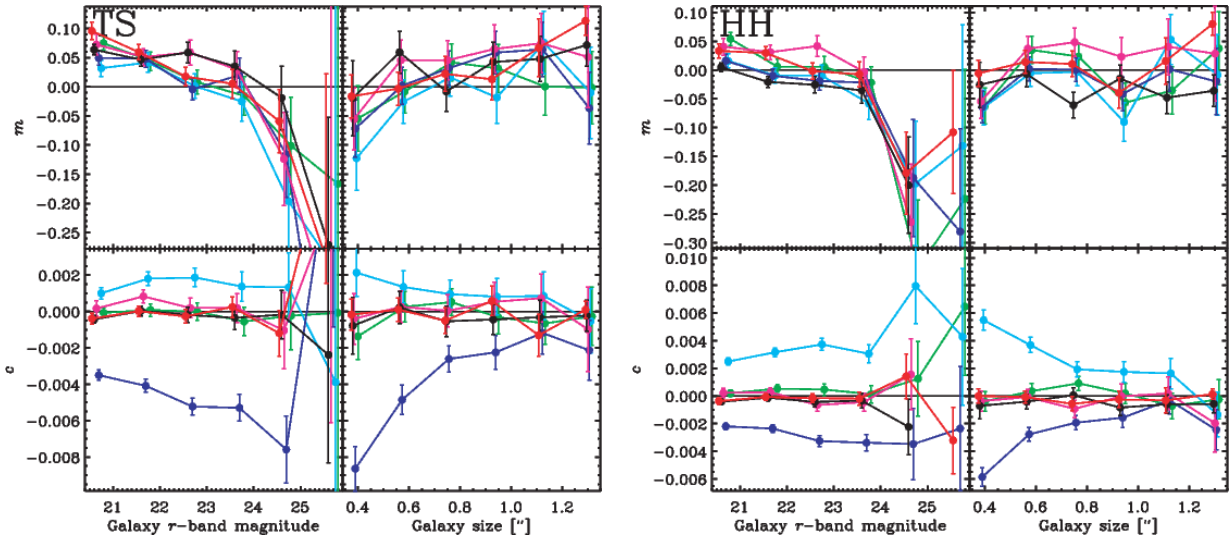


Figure 4.14: Shear calibration bias (*top*) and PSF anisotropy residuals (*bottom*) computed from galaxy bins in input magnitude and size for the TS (*left*) and HH (*right*) implementation of KSB+. Measurements of the two components have been averaged. The red, black, pink, dark blue, light blue, and green points correspond to image sets A, B, C, D, E, and F respectively (extracted from Figure 7 in M07).

noise correlations. Here we compute the rms of the pixel sum $\sigma_N^{\rm measure}$ in independent quadratic subregions of the image with side length $M = \sqrt{N}$. We then determine the ratio

$$r = \frac{\sigma_N^{\rm measure}}{\sqrt{N}\sigma_1^{\rm measure}}\,, \tag{4.12}$$

which in the absence of correlated noise would be equal to 1 for all $N$. In the presence of noise correlations it will converge for large $N$ to the factor by which $\sigma_1^{\rm measure}$ under-estimates the uncorrelated $\sigma_1$. This can be understood as drizzling or (normalised) convolution typically re-distributes pixel flux within a relatively small area. As soon as this is much smaller than the area spanned by $M^2$ pixels, the correlations become unimportant for the area pixel sum. The estimated $r(M)$ is plotted in Figure 4.15. Extrapolating for $M \to \infty$ we estimate that ordinary noise estimates based on the single pixel dispersion ignoring the noise correlation will over-estimate the signal-to-noise of objects by a factor $r \simeq 2.8$ for the STEP2 simulations. Hence, our selection criterion $\mathrm{S/N} > 4.0$ corresponds to a rather brave true cut $\mathrm{S/N^{true}} \gtrsim 1.4$ and includes objects with much lower true signal-to-noise than in STEP1.

We plot the dependence of our STEP2 shear estimate on the (uncorrected) S/N in the top left panel of Figure 4.16. For $\mathrm{S/N} \lesssim 7$, corresponding to $\mathrm{S/N^{true}} \lesssim 2.5$, a significant deterioration of the shear signal occurs, with a calibration bias $\langle m \rangle \sim -10\%$ and a large scatter between the different PSF models. Hence, this probably marks the limit where our KSB+ implementation can yield reasonable shear estimates. This also agrees with the STEP1 results, where shear estimates appeared to be stable with only moderate bias down to the applied cut $\mathrm{S/N^{true}} = 3.0$. We therefore reject the very noisy and strongly biased STEP2 galaxies with a modified cut $\mathrm{S/N} > 7.0$.

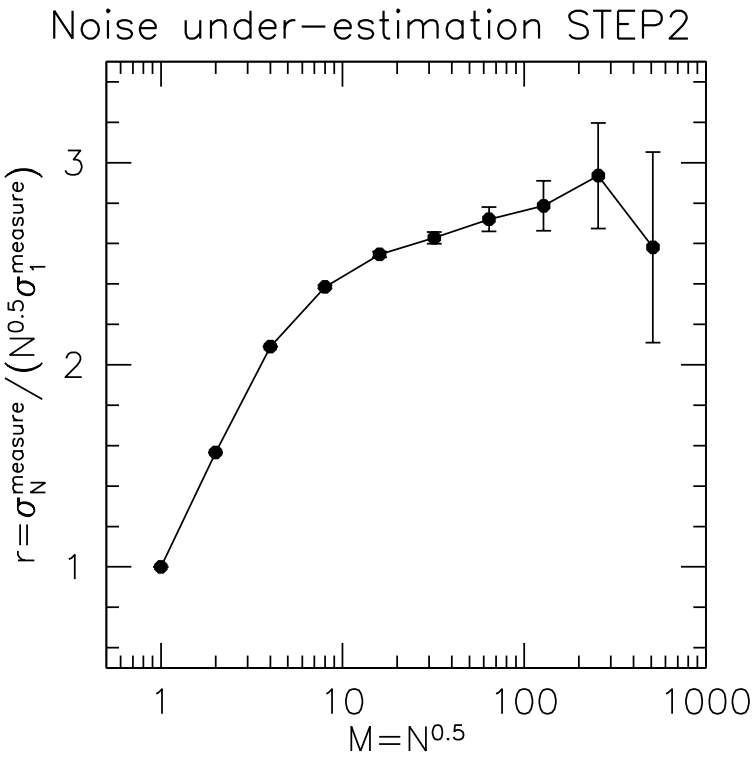


Figure 4.15: Ratio of the dispersion $\sigma_N^{\rm measure}$ measured from large areas of $N = M^2$ pixels to the estimate from the normal single dispersion $\sqrt{N}\sigma_1^{\rm measure}$ as a function of $M$, determined from an object-free STEP2 image. In the absence of noise correlations $r = 1$ for all $M$. The value $r \simeq 2.8$ for $M \to \infty$ gives the factor by which an object signal-to-noise is over-estimated when measured from the single pixel dispersion $\sigma_1^{\rm measure}$ ignoring the correlations.

Table 4.9: Calibration bias $m_\alpha$ and PSF anisotropy residuals $c_\alpha$ for different correction and cut schemes for the modified TS KSB+ analysis of the STEP2 data. The first line for each scheme gives $m_\alpha$ and $c_\alpha$ computed from all image sets, whereas the highly elliptical PSFs D and E have been excluded for the second line. The errors correspond to the scatter between the different image sets. In all cases a modified calibration factor $1/0.93$ and cuts $|e^{\rm iso}| < 2.0$, $\mathrm{Tr}P^g/2 > 0.1$ were applied. The first row corresponds to the standard correction with $\mathrm{Tr}P^g/2$ from individual galaxies, whereas $\mathrm{Tr}P^g/2$ has been fit as a function of $r_{\rm h}$ and mag from the galaxies with S/N > 7 for the other rows (compare to Figure 4.16, Figure 4.17, and Figure 4.19). In the table mag refers to `MAG_AUTO` from `SExtractor`.

| **Correction** | **Cuts** | $\langle m_1\rangle/\%$ | $\langle c_1\rangle \times 10^{-3}$ | $\langle m_2\rangle/\%$ | $\langle c_2\rangle \times 10^{-3}$ |
|---|---|---|---|---|---|
| $\mathrm{Tr}P^g/2$ no fit | S/N > 7 | $0.6 \pm 3.8$ | $3.0 \pm 4.9$ | $0.4 \pm 2.5$ | $-0.4 \pm 0.1$ |
| | mag < 24.4 | $2.4 \pm 2.6$ | $-0.4 \pm 0.1$ | $2.0 \pm 1.3$ | $0.1 \pm 0.3$ |
| $\mathrm{Tr}P^g/2$ fit | S/N > 4 | $1.2 \pm 4.9$ | $3.2 \pm 4.8$ | $-0.6 \pm 4.6$ | $-1.9 \pm 2.8$ |
| $(r_{\rm h}, \mathrm{mag})_{\rm S/N>7}$ | | $4.0 \pm 3.0$ | $-0.2 \pm 0.4$ | $2.3 \pm 2.1$ | $0.1 \pm 0.1$ |
| $\mathrm{Tr}P^g/2$ fit | S/N > 7 | $0.0 \pm 5.0$ | $2.6 \pm 4.7$ | $-0.5 \pm 3.8$ | $-1.6 \pm 2.9$ |
| $(r_{\rm h}, \mathrm{mag})_{\rm S/N>7}$ | mag < 24.4 | $2.6 \pm 2.4$ | $-0.6 \pm 0.3$ | $1.9 \pm 1.3$ | $0.2 \pm 0.3$ |

The remaining galaxies are best corrected with a slightly reduced calibration factor $c_{\rm cal} = 0.93^{-1}$ leading to a mean calibration bias $\langle m_1\rangle = (0.6 \pm 3.8)\%$ and $\langle m_2\rangle = (0.4 \pm 2.5)\%$ (see Table 4.9). If the highly elliptical PSFs D and E are excluded, the biases rises to $\langle m_1\rangle = (2.4 \pm 2.6)\%$ and $\langle m_2\rangle = (2.0 \pm 1.3)\%$. For the following analysis we shall adapt the slightly modified calibration factor $c_{\rm cal} = 0.93^{-1}$, as the value derived from STEP1 ($c_{\rm cal} = 0.91^{-1}$) was based on a smaller data set. The difference between the two values agrees with the estimated $\sim 2\%$ accuracy.

We also test our STEP2 analysis for a possible dependence of the calibration bias on half-light-radius $r_{\rm h}$ (bottom left panel of Figure 4.16). As for STEP1, we detect a more negative bias for large galaxies, which, however, only sets in for $r_{\rm h} \gtrsim 4$ pixels for the STEP2 simulations. Hence, a more careful rejection of stars and poorly resolved galaxies with increased $r_{\rm h}$ cuts would not introduce selection bias for the STEP2 data.

In Figure 4.17 we revisit the dependence of calibration bias and PSF anisotropy residuals on galaxy magnitude and size for our KSB+ analysis. In contrast to the original M07 analysis we treat the two shear components seperately in order not to average out PSF residuals. Additionally, we apply the refinded calibration factor $c_{\rm cal} = 0.93^{-1}$. The left panel corresponds to the cut S/N > 4 applied in the original blind analysis, whereas we utilise the adapted cut $\mathrm{S/N} \gtrsim 7$ ($\mathrm{S/N}^{\rm true} \gtrsim 2.5$) in the right panel. This cut rejects 30% of the originally selected galaxies from the faint end, leading to the modified binning, see the S/N–magnitude correlation shown in Figure 4.18. Furthermore, we apply a cut in the measured magnitude `MAG_AUTO` < 24.4 to increase the homogeneity of the data, which however only leads to an additional rejection of 2.2% of the remaining galaxies. With these modifications the average calibration bias remains consistent with zero and the variation with magnitude is reduced to $m \sim +4\%$ at the bright end and $m \sim -4\%$ for the faintest magnitude bin.

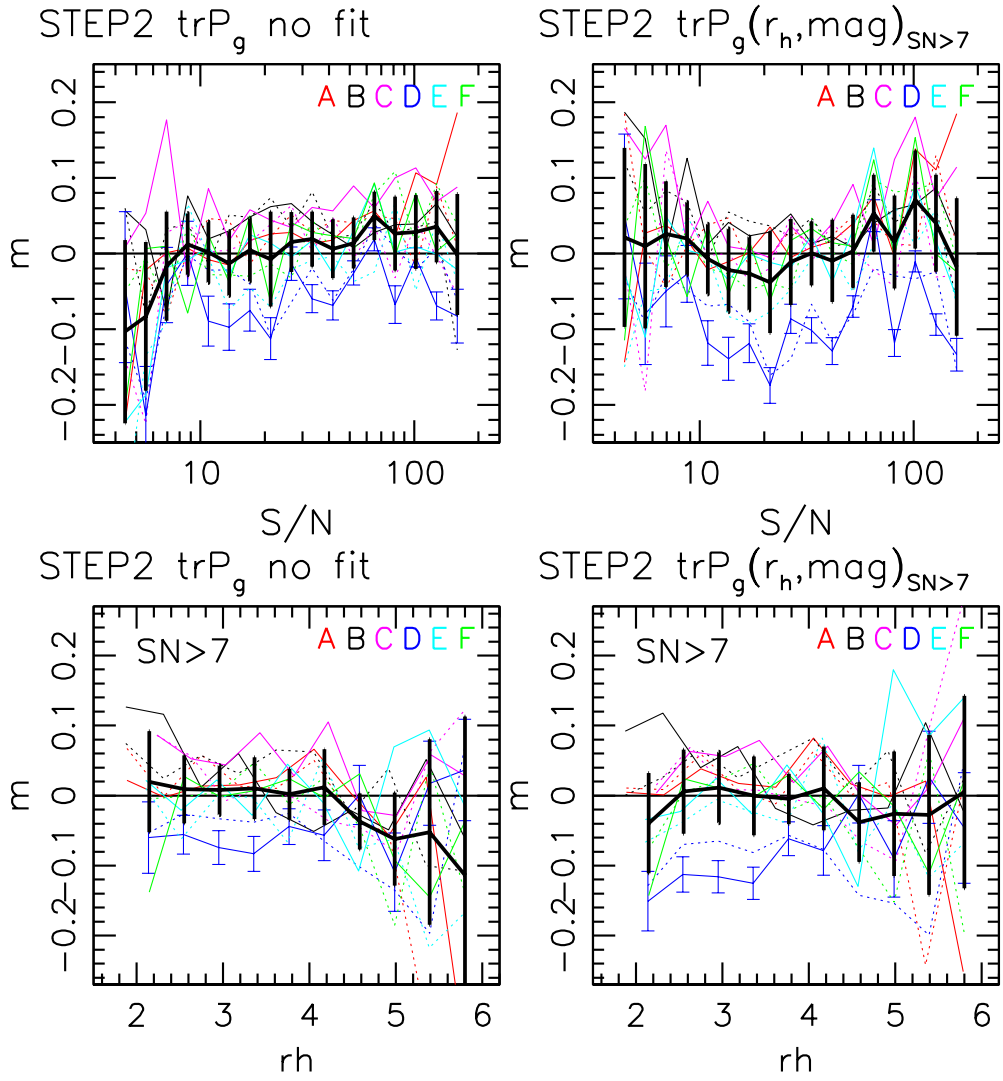


Figure 4.16: Calibration bias $m$ as a function of the uncorrected signal-to-noise S/N (*top*) and half-light-radius $r_\mathrm{h}$ (*bottom*) for the TS analysis of the STEP2 simulations. The *left* panels correspond to the default correction with $\mathrm{Tr}P^g/2$ from individual galaxies, whereas $\mathrm{Tr}P^g/2$ was fit as a function of $r_\mathrm{h}$ and observed magnitude using only galaxies with S/N > 7 for the *right* panels. For all plots an adapted calibration factor $c_\mathrm{cal} = 0.93^{-1}$ (original $0.91^{-1}$) was applied, and for the *bottom* panels additionally cuts S/N > 7 and `MAG_AUTO` < 24.4. Thin solid (dashed) lines show $\gamma_1$ ($\gamma_2$) estimates for individual PSFs, where we show individual errorbars only for one PSF for clarity. Bold solid lines and errorbars show the mean and standard deviation of the individual PSF estimates and shear components. Note the deterioration of the shear estimate for the STEP2 galaxies with S/N $\lesssim 7$ ($\mathrm{S/N}^\mathrm{true} \lesssim 2.5$) if no $\mathrm{Tr}P^g/2$ fitting is done.

For comparison we also repeat the analysis with an alternative cut $\mathrm{Tr}P^g/2 > 0.0$ instead of $\mathrm{Tr}P^g/2 > 0.1$. In this case the bias in the faintest magnitude bin is slightly enhanced ($m \sim 6\%$), but the calibration bias shows no more dependence on galaxy size.

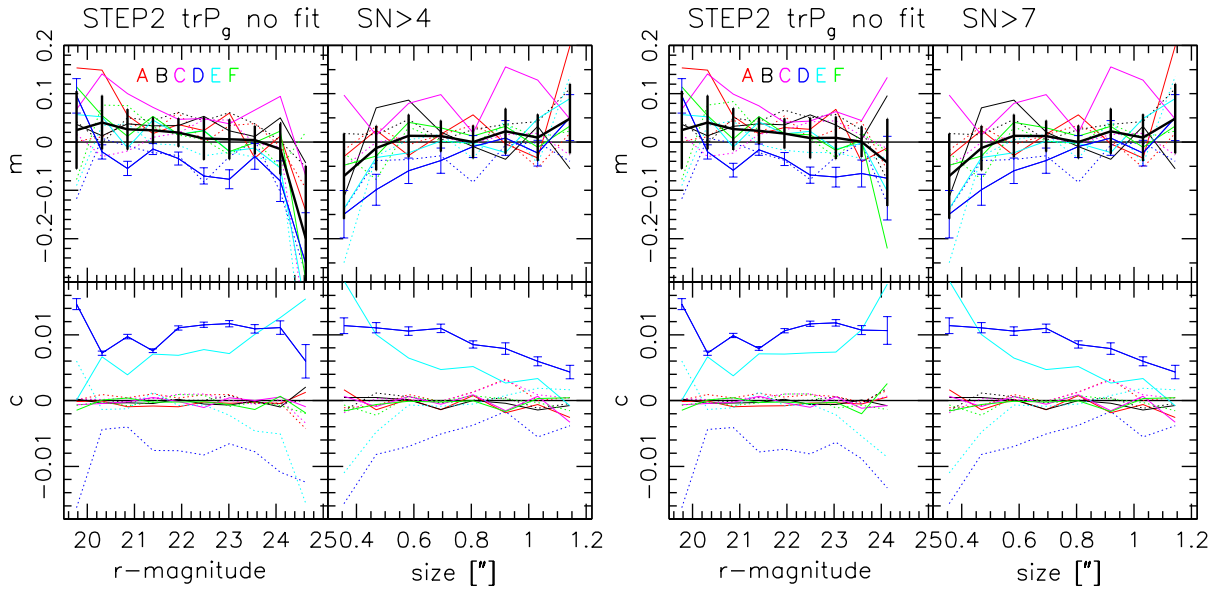


Figure 4.17: Calibration bias $m$ and PSF residuals $c$ as a function of input galaxy magnitude and size for our refined analysis of the STEP2 data. Thin solid (dashed) lines show $\gamma_1$ ($\gamma_2$) estimates for individual PSFs, where we include individual errorbars only for one PSF for clarity. Bold solid lines and errorbars show the mean and standard deviation of the individual PSF estimates and shear components. For the *left* panel all galaxies with $\mathrm{S/N} > 4$ are included, showing the strong deterioration at the faint magnitude end already seen in Figure 4.14. In the *right* panel only galaxies with $\mathrm{S/N} > 7$ ($\mathrm{S/N}^{\mathrm{true}} > 2.5$) and `MAG_AUTO` $< 24.4$ are taken into account, strongly reducing the deterioration. For both plots the default correction with $\mathrm{Tr}P^g/2$ from individual galaxies and an adapted calibration factor $c_{\mathrm{cal}} = 0.93^{-1}$ (original $0.91^{-1}$) were applied.

### 4.3.8 $P^g$–fitting

We also tested the impact of $\mathrm{Tr}P^g/2$–fitting as a function of less noisy observables for the STEP2 data.

Considering only the sample with $\mathrm{S/N} > 7$, fitting as a function of $r_{\mathrm{h}}$ and magnitude leads to a slightly flatter slope in the magnitude range $20 < r < 23.5$, but amplifies the bias at the faint end to $\sim -10\%$ (top right panel of Figure 4.19). Interestingly, a fit derived from the on average unbiased sample with $\mathrm{S/N} > 7$, which is then applied to all galaxies with $\mathrm{S/N} > 4$, leads to an almost flat slope down to $r \sim 24.2$, and only in the faintest magnitude bin a substantial calibration bias of $\sim -12\%$ occurs (top left panel of Figure 4.19). Hence, a fit of $\mathrm{Tr}P^g/2$ as a function of $r_{\mathrm{h}}$ and magnitude derived from sufficiently high signal-to-noise galaxies, but applied to a larger sample, might be a possibility to increase the number density of galaxies usable with KSB, if

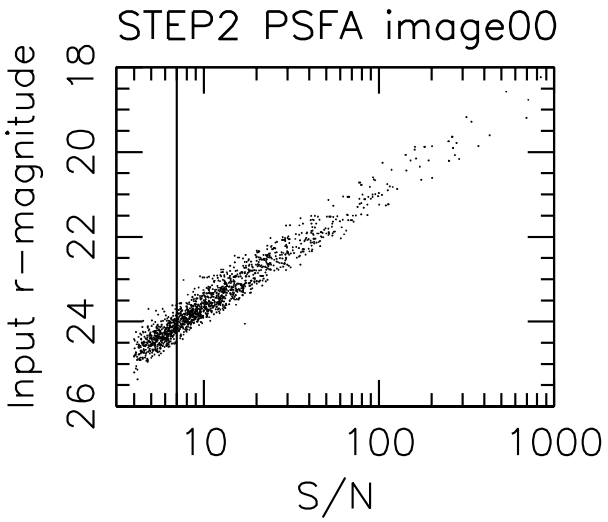


Figure 4.18: Distribution of galaxies in S/N–magnitude-space for a simulated STEP2 set A image. The line indicates the adjusted cut S/N > 7, corresponding to $S/N^{true} > 2.5$ when corrected for noise correlations. This cut rejects 30% of the galaxies originally selected with S/N > 4.

an additional magnitude cut is applied to reject objects in the faint magnitude tail. However, the actual behaviour in the faint magnitude bins depends significantly on the exact cut to select the fit sample, which is not surprising given that S/N and magnitude are not independent quantities. As a further side-effect, the described fitting scheme introduces a significant size dependence of the calibration bias, which might be similarly problematic as a magnitude dependence for a real cosmic shear survey. Furthermore, it slightly enhances the scatter in the calibration bias between the different PSF models. Therefore, we decided not to follow this approach in our cosmic shear pipeline.

On the other hand we found that $\mathrm{Tr}P^g/2$–fitting as a function of $r_\mathrm{h}$ and $|e|$ worsens the negative shear calibration bias for faint galaxies and introduces a strong dependence on size (bottom panels of Sect. 4.19). This is in contrast to the STEP1 results, where this fitting approach led to a higher shear estimate for faint galaxies (Sect. 4.2.7.2). Due to this apparent dependence on the exact image properties the approach seems to be little useful. Hence, we also do not include it in our cosmic shear pipeline.

### 4.3.9 Conclusions from STEP2

The shear calibration factor and improved selection criteria derived from the STEP1 analysis for our KSB+ implementation proved to be robust providing good results also for the STEP2 simulations. The resulting average calibration bias was consistent with zero at the two-percent level except for the highly elliptical ($e \sim 12\%$) PSFs D and E, which led to a significantly negative shear calibration bias of $(-3.8 \pm 2.5)\%$. For these PSFs significant PSF anisotropy leakage was detected for all KSB+ methods. Complex morphologies seem to increase the overall trend of

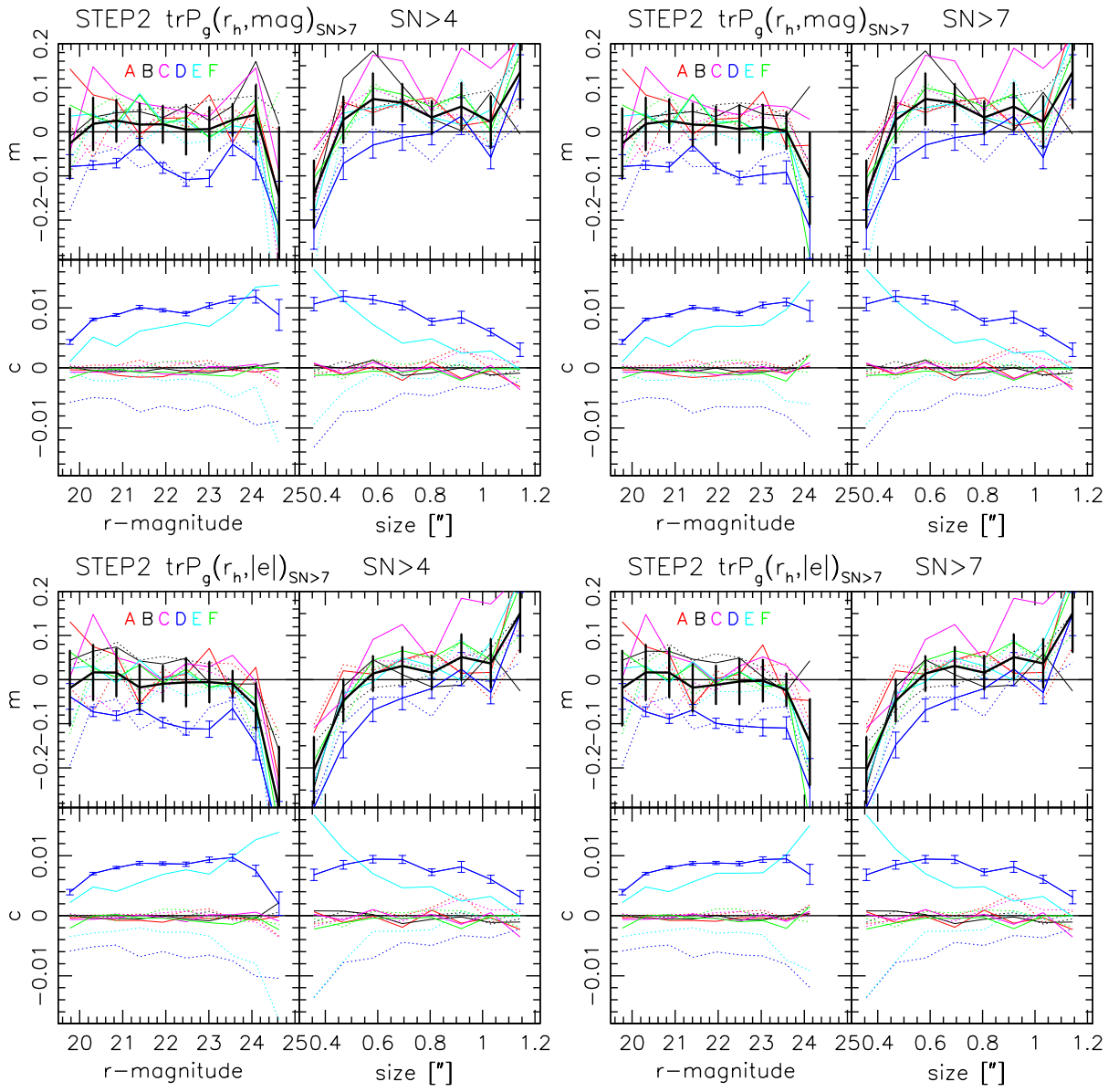


Figure 4.19: As Figure 4.17, but with $\mathrm{Tr}P^g/2$ fitted as a function of $r_\mathrm{h}$ and observed magnitude (*top*) or $r_\mathrm{h}$ and uncorrected ellipticity (*bottom*). For all panels the fit was derived using only galaxies with S/N > 7 ($\mathrm{S/N}^\mathrm{true} > 2.5$). It was then applied to all galaxies with S/N > 4 for the *left* panels. For the *right* panels only the brighter galaxies with S/N > 7 and `MAG_AUTO` < 24.4 are taken into account. In all cases fitting increases the calibration bias for the faintest magnitude bin and introduces a strong size dependence.

KSB+ implementations to under-estimate the shear. The STEP2 analysis also identified a trend for most tested shear measurement pipelines that the $\gamma_1$ component is typically measured with less bias than the $\gamma_2$ component, where the difference is probably caused by pixelisation.

All methods tested in STEP2 suffer from an under-estimation of the shear at the faint magnitude end. Tests conducted later suggest that for our method this deterioration originates from the negligence of noise correlations, which lead to an over-estimation of objects' signal-to-noise by a factor $\sim 2.8$. Adjusting the cut to $\mathrm{S/N} > 7$ ($\mathrm{S/N}^{\mathrm{true}} > 2.5$) cures the deterioration and reduces the overall bias, so that a slightly reduced calibration factor $1/0.93$ fits the data better, with a weaker dependence of the calibration bias on magnitude, ranging from $\sim +4\%$ for the brightest galaxies to $\sim -4\%$ at the faint end.

Our tests to fit $\mathrm{Tr}P^g/2$ as a function of half-light-radius and magnitude or half-light-radius and ellipticity did not help to reliably reduce the remaining magnitude-dependent calibration bias, without introducing a size dependence. Therefore we abstain from applying $\mathrm{Tr}P^g/2$ fits in our cosmic shear analysis.

## 4.4 STEP3: Simulated space-based images

In parallel to the STEP2 analysis a third STEP project was launched in 2005, STEP3, the blind analysis of shear simulations with properties of space-based data. Given that a large fraction of this data mimics the PSF and image properties of ACS, the analysis became a particularly valuable test for this thesis project. Before, it has been unclear how well KSB+ is able to correct for the PSF of the space-based instrument due to the fundamental limitations of the method. The results summarised here have not been published at the time of the write-up.

### 4.4.1 Simulations

The STEP3 simulations were created by William High and Richard Massey and are, similarly to the STEP2 data, based on the Massey et al. (2004) shapelet simulation package.

The different STEP3 data sets are summarised in Table 4.10. Sets A, B, and C resemble $3\farcm33 \times 3\farcm33$ 1 ks *i*–band exposures from the planned SNAP satellite, where the different sets correspond to different telescope apertures and pixel scales. Image sets D to L mimic the PSF properties of the ACS Wide-Field-Channel (WFC) Detector (see Sect. 5.1.2) with a $2\farcm67 \times 2\farcm67$ field-of-view and 2 ks exposure time, where the PSF was modelled using a modified version of the `TinyTim` package described in Rhodes et al. (2007) for different stellar positions within the ACS field-of-view . Whereas the true WFC features a pixel scale of $0\farcs05$, most simulated ACS data sets have a pixel scale of $0\farcs04$, which reflects the slightly improved sampling achievable for drizzled dithered data. On the other hand image sets E and G have coarse pixels sized $0\farcs10$ resembling the pixel scale of WFPC2, which is the major workhorse for HST since the failure of ACS. A small cutout from an ACS-type image of set D is shown in Figure 4.20.

In addition to the STEP3 image simulations five times oversampled PSF images were provided, which some methods used to derive a PSF model. The galaxies have been modelled including complex morphologies with shapelets using the *Hubble* Deep Field North as a training set, except for image sets F and G which contain simplified galaxies with exponential profiles. The images contain stars with surface densities predicted at the galactic poles. In additional, one stellar field with increased number density was provided, which can be used to characterise the PSF similarly to periodical observations of globular cluster fields in real WL surveys. The PSF does not change across the field-of-view or within one image set. This is a simplification compared to real data, which allows the separation of two important, but different problems, namely shape measurement as tested here, and second PSF interpolation and stability, which we test for ACS in detail in Sect. 6.2. In contrast to STEP2, the STEP3 data contain uncorrelated noise.

### 4.4.2 Shear estimation

The different methods tested in the STEP3 blind analysis are listed in Table 4.11.

We applied our KSB+ pipeline with some minor modifications compared to the STEP2 analysis, in order to keep it as similar to the analysis of real ACS images presented in Chapter 6 as possible. We apply different detection parameters for image sets with large pixels of

Table 4.10: Overview of the STEP3 image sets. The ACS-type PSFs H to L differ in the PSF model, which has been computed for different image positions but the same telescope focus using `TinyTim`.

| **Image set** | **Instrument** | **Pixel scale / ″** | **Galaxy model** | **Number of images** |
|---|---|---|---|---|
| A | 2.0m SNAP | 0.05 | Shapelet | 100 |
| B | 2.0m SNAP | 0.10 | Shapelet | 100 |
| C | 1.4m SNAP | 0.10 | Shapelet | 100 |
| D | ACS | 0.04 | Shapelet | 100 |
| E | ACS | 0.10 | Shapelet | 100 |
| F | ACS | 0.04 | Exponential | 100 |
| G | ACS | 0.10 | Exponential | 100 |
| H | ACS | 0.04 | Shapelet | 50 |
| I | ACS | 0.04 | Shapelet | 50 |
| J | ACS | 0.04 | Shapelet | 50 |
| K | ACS | 0.04 | Shapelet | 50 |
| L | ACS | 0.04 | Shapelet | 50 |

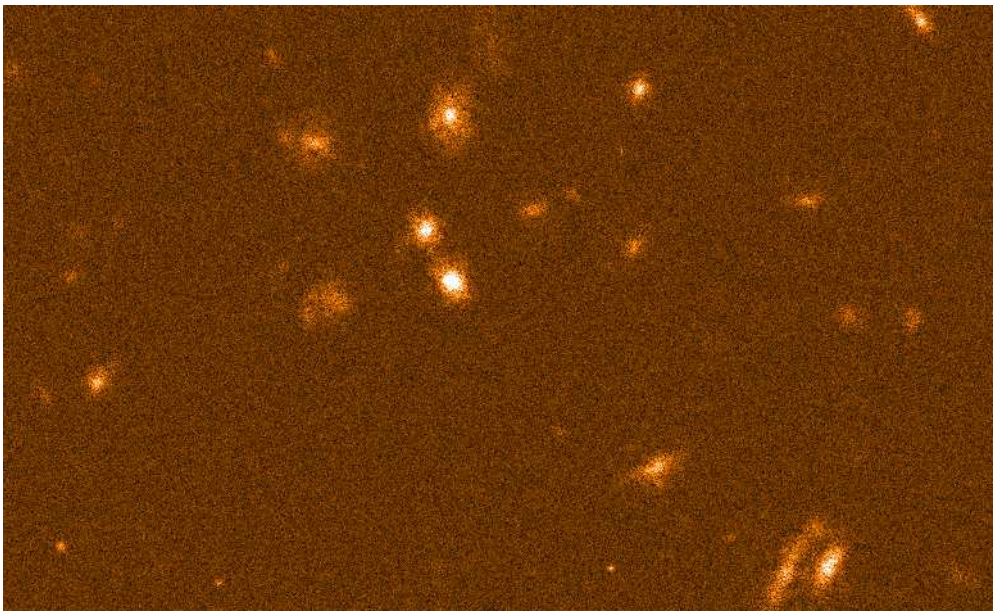

Figure 4.20: Cutout from one STEP3 image from set D with ACS-like properties (width 30″).

Table 4.11: Shear measurement methods and implementations tested in the analysis of the STEP3 image simulations.

| **Author** | **Key** | **Method** |
|---|---|---|
| Bergé | JB | Shapelets (Massey & Refregier 2005) |
| Heymans | CH | KSB+ |
| Mandelbaum | RM | Reglens (Hirata & Seljak 2003) |
| Nakajima | RN | Bernstein & Jarvis (2002) (Nakajima & Bernstein 2007) |
| Paulin-Henrikson | SP | KSB+ |
| Rhodes | JR | RRG (Rhodes et al. 2000) |
| Schrabback | TS | KSB+ |
| Schrabback | T2 | KSB+ (high resolution PSFs) |

size 0.″10 (`DETECT_MINAREA`=6, `DETECT_THRESH`=1.5, filter gauss_2.5_5x5.conv), and for image sets with pixel scales 0.″04 and 0.″05 (`DETECT_MINAREA`=8, `DETECT_THRESH`=1.4, filter gauss_3.0_7x7.conv). In the case of more than one detection within a radius of 1.″2 we only keep the brightest object in order to exclude possible contamination from galaxy substructures, as done for real ACS data. When measuring PSF quantities from stars we integrate to a radius of 4.5 stellar flux-radii in order to properly account for the extended wings of the ACS PSFs.

Our default PSF correction and analysis (TS) is based on the stars present in the simulated star field images. As an additional test we derive alternative PSF models from the over-sampled high-resolution PSF images. The ellipticity definition (3.85) is normalised and dimensionless, and hence does not depend on the coordinate system or pixel scale. The same is true for the $P^{\rm sh}$ tensor, as follows from (A.24). This is different for the $P^{\rm sm}$ tensor (A.18), which is not normalised and scales as (pixel scale)$^2$, as can be seen by comparing the definitions of $Q_{ij}$ (A.4) and $X_{\alpha\beta}$ (A.12). We therefore need to scale the estimates for the $P^{\rm sm}$ components derived from the high-resolution images by $5^2$, in order to correct the galaxies. This alternative correction scheme has the key T2. However, we expect that it will preform worse than the TS method as pixelisation effects can no longer cancel out between stars and galaxies.

For the TS analysis we list stellar flux-radii and ellipticities in Table 4.12. Note that the simulated STEP3 PSFs are only moderately elliptical with $|e^*| \lesssim 2.3\%$ for $r_{\rm g} = 0.''16$.

Given the flat $r_{\rm h}$ dependence of the shear calibration bias found in STEP2, we apply a more conservative rejection for stars and poorly resolved galaxies $r_{\rm h} > 1.15 r_{\rm h}^{*,\rm upper} \simeq 1.2 r_{\rm h}^*$. Furthermore, we select galaxies with cuts $|e^{\rm iso}| \leq 2.0$, $\mathrm{Tr}P^g/2 > 0.1$, and $\mathrm{S/N} > 4$. In order to take account for the overall calibration bias detected in STEP1, a constant shear calibration factor of $0.91^{-1}$ was applied in the blind analysis. We do not use a weighting scheme in our STEP3 analysis.

Table 4.12: PSF quantities estimated for the STEP3 simulations using the TS KSB+ pipeline, with PSF estimation from the low-resolution stars in the simulated stellar field. $r_f$ is the SExtractor FLUX_RADIUS. The ellipticities have been estimated using a Gaussian weight function with filter scale $r_g = 0.''16$.

| Image set | Pixel scale / '' | $r_f$ / '' | $\langle e_1 \rangle$/% | $\langle e_2 \rangle$/% |
|---|---|---|---|---|
| A | 0.05 | 0.0792 ± 0.0001 | 0.49 ± 0.03 | 0.51 ± 0.04 |
| B | 0.10 | 0.0934 ± 0.0002 | 0.54 ± 0.05 | 0.48 ± 0.03 |
| C | 0.10 | 0.1132 ± 0.0003 | 0.01 ± 0.03 | −0.04 ± 0.03 |
| D | 0.04 | 0.0721 ± 0.0001 | −0.07 ± 0.03 | −2.25 ± 0.03 |
| E | 0.10 | 0.0895 ± 0.0003 | 0.05 ± 0.14 | −1.57 ± 0.03 |
| F | 0.04 | 0.0721 ± 0.0001 | 0.00 ± 0.03 | −2.30 ± 0.02 |
| G | 0.10 | 0.0896 ± 0.0003 | 0.09 ± 0.14 | −1.60 ± 0.03 |
| H | 0.04 | 0.0721 ± 0.0001 | 2.31 ± 0.04 | −0.15 ± 0.04 |
| I | 0.04 | 0.0721 ± 0.0001 | 0.15 ± 0.03 | 2.29 ± 0.04 |
| J | 0.04 | 0.0721 ± 0.0001 | −2.27 ± 0.03 | 0.21 ± 0.04 |
| K | 0.04 | 0.0721 ± 0.0001 | −0.18 ± 0.03 | −2.22 ± 0.04 |
| L | 0.04 | 0.0721 ± 0.0001 | −0.01 ± 0.03 | 0.02 ± 0.04 |

### 4.4.3 Analysis

The analysis of the submitted shear catalogues was done by Catherine Heymans and Jason Rhodes. The estimates for calibration bias and PSF anisotropy residuals are summarised in Table 4.13, where our TS analysis yields the best results, followed by the CH analysis also using KSB+ and the JR implementation of RRG (Rhodes et al. 2000). These methods have all been used and optimised for space-based data before. On the other hand, methods not yet used for space-based data suffer from stronger calibration bias or PSF residuals.

Interestingly, all KSB+ implementations and the related RRG method yield higher shear estimates (less negative calibration bias) for the poorly sampled image sets than for the sets with pixel scale $0.''04$. This indicates that pixelisation in fact increases the shear estimate, in contrast to the effects seen in STEP2 (Sect. 4.3.4). The difference in the shear estimate is in fact lowest for the TS and T2 methods amounting to $\sim 1\%$, which is probably due to the interpolation scheme used. The trend of a higher shear estimate for the poorer sampled data is also seen for the RM reglens method and the JB implementation of shapelets.

The TS and T2 results for the individual image sets are shown in Figure 4.21. The T2 analysis yields a shear estimate which is lower than the TS estimate by $\sim 7\%$, consistently for the better and worse sampled image sets. This difference provides an approximate estimate for the impact of pixelisation effects, which largely cancel out for the TS but not T2 method. However, note that the high resolution PSF was not additionally convolved with the larger pixel size. Hence, it is effectively slightly narrower than the low resolution PSF, which will lead to lesser seeing correction and a smaller shear estimate, explaining at least parts of the difference between TS

Table 4.13: Number density of galaxies $N$, calibration bias $m_\alpha$ and PSF anisotropy residuals $c_\alpha$ for the methods tested in the STEP3 blind analysis. The first row for each author was computed from the simulations with pixel scale $0\farcs04$, whereas the second row corresponds to the sets with coarse sampling (analysis by CH).

| **Key** | $N$ | $\langle m_1 \rangle$ | $\langle c_1 \rangle$ | $\langle m_2 \rangle$ | $\langle c_2 \rangle$ |
|---|---|---|---|---|---|
| TS | 71 ± 3 | −0.01 ± 0.01 | 0.001 ± 0.000 | 0.01 ± 0.01 | 0.001 ± 0.000 |
| TS | 57 ± 13 | 0.01 ± 0.01 | 0.001 ± 0.001 | 0.02 ± 0.01 | 0.001 ± 0.000 |
| T2 | 71 ± 3 | −0.07 ± 0.01 | 0.001 ± 0.001 | −0.06 ± 0.01 | 0.001 ± 0.001 |
| T2 | 57 ± 13 | −0.06 ± 0.00 | 0.001 ± 0.000 | −0.05 ± 0.01 | 0.001 ± 0.000 |
| RM | 159 ± 3 | −0.10 ± 0.01 | −0.007 ± 0.001 | −0.10 ± 0.01 | 0.002 ± 0.001 |
| RM | 112 ± 25 | −0.04 ± 0.00 | 0.018 ± 0.009 | −0.02 ± 0.02 | 0.003 ± 0.002 |
| RN | 74 ± 7 | −0.06 ± 0.01 | 0.001 ± 0.001 | −0.03 ± 0.01 | 0.001 ± 0.001 |
| RN | 106 ± 25 | −0.09 ± 0.01 | 0.001 ± 0.000 | −0.09 ± 0.01 | 0.000 ± 0.000 |
| JR | 67 ± 0 | 0.03 ± 0.02 | 0.003 ± 0.000 | −0.02 ± 0.02 | −0.002 ± 0.001 |
| JR | 46 ± 9 | 0.07 ± 0.02 | 0.003 ± 0.001 | 0.00 ± 0.01 | 0.000 ± 0.000 |
| JB | 175 ± 7 | −0.22 ± 0.01 | −0.001 ± 0.001 | −0.23 ± 0.01 | −0.001 ± 0.001 |
| JB | 132 ± 28 | −0.11 ± 0.03 | 0.000 ± 0.000 | −0.10 ± 0.04 | −0.001 ± 0.001 |
| CH | 105 ± 4 | −0.05 ± 0.01 | 0.001 ± 0.000 | −0.06 ± 0.01 | 0.000 ± 0.000 |
| CH | 101 ± 24 | −0.02 ± 0.01 | 0.000 ± 0.000 | −0.03 ± 0.01 | 0.000 ± 0.000 |
| SP | 64 ± 2 | −0.19 ± 0.01 | 0.001 ± 0.000 | −0.17 ± 0.01 | −0.002 ± 0.001 |
| SP | 46 ± 7 | −0.10 ± 0.01 | 0.000 ± 0.001 | −0.11 ± 0.01 | 0.000 ± 0.000 |

and T2. In any case we would expect a larger difference for the PSFs with $0\farcs10$ pixel scale, being more strongly affected by pixelisation, but maybe this is compensated by the interpolation scheme.

### 4.4.4 Subtraction of the intrinsic ellipticity

After receiving the results for the mean calibration bias and PSF residuals in the blind analysis, I conducted a more detailed analysis to study their behaviour as a function of galaxy parameters similarly to STEP2. Here I relaxed the signal-to-noise cut to $\mathrm{S/N} > 3$ and adapted the calibration factor to $1/0.93$ due to the conclusions from STEP2. Due to the lacking rotated image pairs in STEP3, the derived constraints for a magnitude or size dependence were however weak compared to the STEP2 results. In order to decrease the disturbing shape noise, we therefore decided to subtract the intrinsic ellipticity

$$\epsilon^{\mathrm{int}} = \frac{\epsilon^{\mathrm{input}} - \gamma}{1 - \gamma^* \epsilon^{\mathrm{input}}}\,, \tag{4.13}$$

which we estimate from the shear $\gamma$ and input ellipticity

$$\epsilon^{\mathrm{input}} = \frac{a-b}{a+b} \mathrm{e}^{2\mathrm{i}\phi}\,, \tag{4.14}$$

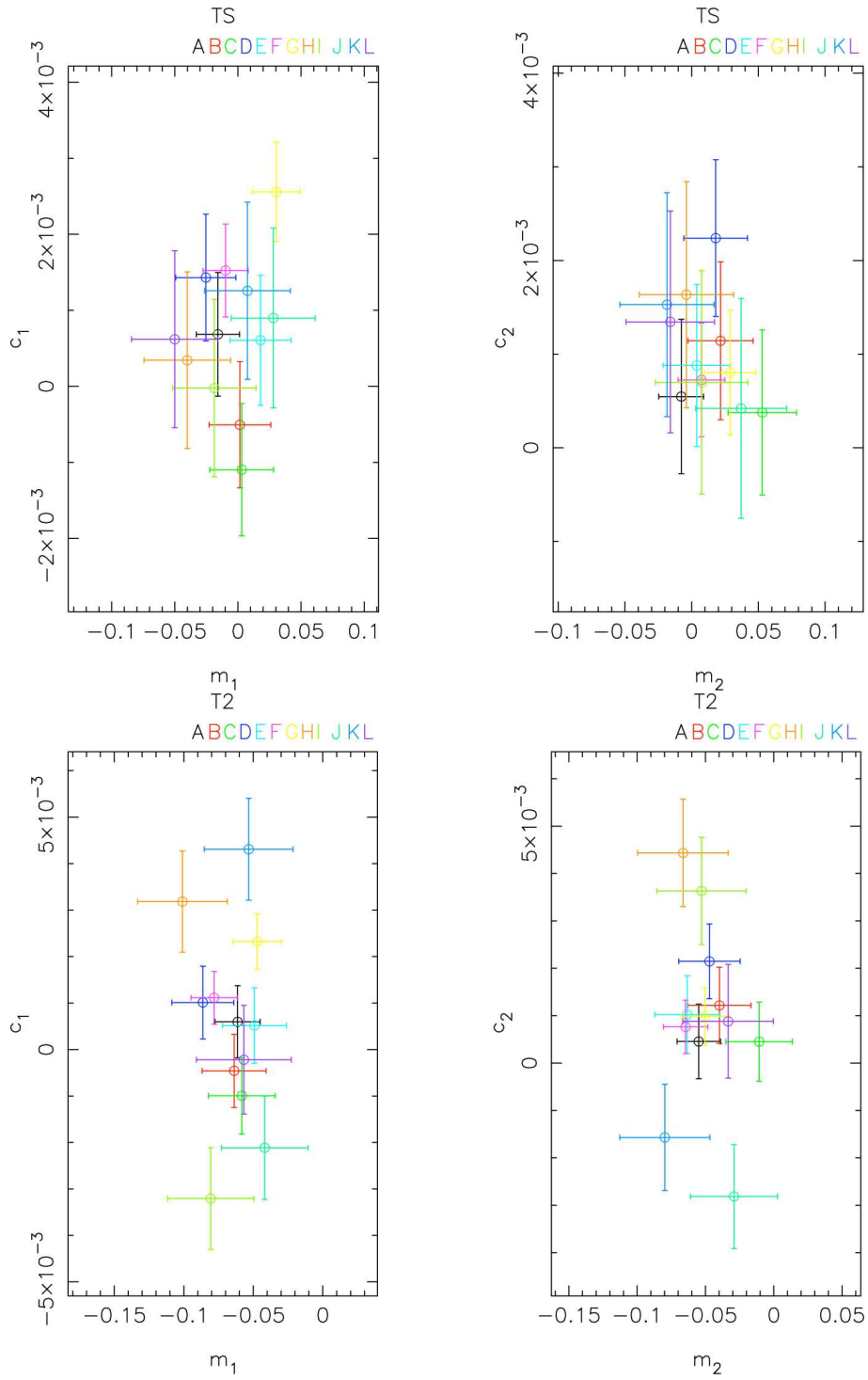


Figure 4.21: STEP3 calibration bias $m_\alpha$ and PSF anisotropy residuals $c_\alpha$ for the standard TS analysis (*top*) and the T2 analysis (*bottom*), in which the PSF model was determined from a five times oversampled PSF images. The *left* panels correspond to the $\gamma_1$ component, whereas the analysis for $\gamma_2$ is shown in the *right* panels. Biases in the KSB+ estimates due to pixelisation largely cancel out for stars and poorly resolved galaxies, if measured from the same pixel scale (TS). If only the stars are measured with high sampling the effects can no longer cancel, which explains the poor performance of the T2 method (plot by CH).

Table 4.14: Estimates for calibration bias $m_\alpha$ and PSF anisotropy residuals $c_\alpha$ for the different image sets using the TS method with a modified cut S/N > 3, a calibration factor 1/0.93, and the intrinsic ellipticity subtracted shear estimator $\hat{\gamma}$.

| Image set | $\langle m_1\rangle$/% | $\langle c_1\rangle \cdot 10^4$ | $\langle m_2\rangle$/% | $\langle c_2\rangle \cdot 10^4$ |
|---|---|---|---|---|
| A | $-1.9 \pm 1.0$ | $-5.3 \pm 4.8$ | $-0.7 \pm 1.0$ | $-3.7 \pm 4.9$ |
| B | $-1.0 \pm 1.4$ | $0.8 \pm 5.0$ | $0.7 \pm 1.5$ | $8.5 \pm 5.0$ |
| C | $-0.4 \pm 1.6$ | $-6.4 \pm 5.4$ | $0.0 \pm 1.6$ | $8.3 \pm 5.4$ |
| D | $0.1 \pm 1.5$ | $7.9 \pm 5.3$ | $0.3 \pm 1.6$ | $2.3 \pm 5.4$ |
| E | $1.9 \pm 1.6$ | $6.6 \pm 5.5$ | $0.4 \pm 1.6$ | $8.5 \pm 5.6$ |
| F | $0.9 \pm 1.1$ | $12.8 \pm 3.8$ | $0.7 \pm 1.1$ | $11.3 \pm 3.9$ |
| G | $6.4 \pm 1.2$ | $12.6 \pm 4.2$ | $4.2 \pm 1.2$ | $3.8 \pm 4.2$ |
| H | $-1.0 \pm 2.2$ | $-1.8 \pm 7.4$ | $1.6 \pm 2.2$ | $0.0 \pm 7.6$ |
| I | $-0.4 \pm 2.1$ | $-7.8 \pm 7.4$ | $3.2 \pm 2.2$ | $-9.5 \pm 7.6$ |
| J | $1.1 \pm 2.1$ | $4.0 \pm 7.4$ | $2.8 \pm 2.2$ | $-11.0 \pm 7.6$ |
| K | $-0.6 \pm 2.2$ | $10.3 \pm 7.5$ | $-2.5 \pm 2.2$ | $-1.9 \pm 7.6$ |
| L | $-1.4 \pm 2.2$ | $2.5 \pm 7.4$ | $-1.8 \pm 2.1$ | $-3.0 \pm 7.6$ |

where the galaxy major axis $a$, minor axis $b$, and position angle $\phi$ are computed from the shapelet coefficients and included in the input catalogues. We then use the shape noise reduced shear estimator

$$\hat{\gamma} = c_{\rm cal}\, e^{\rm iso} - \epsilon^{\rm int}\,. \tag{4.15}$$

We list the global estimates for calibration bias and PSF anisotropy residuals derived from $\hat{\gamma}$ in Table 4.14. On average the uncertainties in the estimated calibration bias for the different image sets shrink by 39% when using the shape noise reduced shear estimator. For the ACS-type simulations only, we then compute the overall calibration bias and anisotropy residuals

$$\langle m_1, m_2\rangle_{\rm ACS} = (-0.1 \pm 1.1,\ 0.6 \pm 2.0)\,\%\,, \tag{4.16}$$

$$\langle c_1, c_2\rangle_{\rm ACS} = (3.1 \pm 5.7,\ -2.1 \pm 6.2)\cdot 10^{-4}\,, \tag{4.17}$$

where the errors correspond to the $1\sigma$–scatter between the different image sets. If all image sets are considered, these values become

$$\langle m_1, m_2\rangle_{\rm ACS+SNAP} = (0.3 \pm 2.1,\ 0.8 \pm 1.9)\,\%\,, \tag{4.18}$$

$$\langle c_1, c_2\rangle_{\rm ACS+SNAP} = (3.0 \pm 7.0,\ 1.1 \pm 7.0)\cdot 10^{-4}\,. \tag{4.19}$$

### 4.4.5 Dependence on galaxy properties

In the STEP3 simulations we detect no degradation of the shear signal down to S/N = 3 (top panels of Figure 4.22), similarly to the behaviour for the true signal-to-noise in STEP2. The

strong dependence of the shear estimate on $r_h$ seen in STEP1 does not occur for our STEP3 analysis (bottom panels of Figure 4.22), as it was the case for STEP2. We therefore consider this behaviour to probably be a peculiarity of the STEP1 simulations and conclude that more conservative cuts in $r_h$ used to exclude poorly resolved galaxies should not introduce a strong selection bias in the analysis of the ACS images.

The signal-to-noise cut S/N $> 3$ roughly corresponds to a magnitude cut $i \lesssim 26.5$ (Figure 4.23). Down to this limit we detect no significant magnitude-dependent calibration bias in our shear estimate (Figure 4.24), but only a large increase in the noise for the faintest bin. For the ACS-type simulations there seems to be a slight trend to over-estimate shear by $\sim 6\%$ in the brightest bin, but the scatter is too large to be conclusive.

The simulations with a coarse pixel grid show a trend to systematically over-estimate the shear for intrinsically small galaxies. This agrees with the interpretation of more positive average calibration bias being caused by pixelisation issues (see Sect. 4.4.3), which will have the strongest influence for small galaxies.

PSF anisotropy residuals are generally small. The ACS-type simulations appear to have a slight deterioration in the faintest magnitude bin, but again the scatter is too large to be conclusive.

### 4.4.6 Conclusions from STEP3

For the ACS cosmic shear project the most important conclusion from STEP3 is that our KSB+ implementation performs very well for simulated ACS data. The calibration correction $1/0.93$ derived from STEP2 leads to a calibration bias consistent with zero, which shows a $1\sigma$–scatter of 2% (4.16) between all ACS and SNAP type simulated images. PSF anisotropy residuals are also consistent with zero, with a scatter of $7 \times 10^{-4}$ (4.17). Although the ACS-type simulations do not exactly resemble all possible configurations of the spatially and temporarily variable ACS PSF (e.g. simulated ellipticities $\lesssim 2.3\%$), the inclusion of the SNAP-type simulations should provide a fair estimate of the expected scatter for real ACS data. Hence, we conclude that the average shear calibration should be accurate to 2% in the analysis of the ACS data. For a proper PSF interpolation scheme PSF anisotropy residuals should be suppressed to a level well below the statistical accuracy of the ACS data.

We do not detect a significant dependence of the shear estimate on half-light-radius $r_h$. Hence, conservative cuts to reject poorly resolved galaxies should not lead to a significant selection bias. The magnitude and size dependence of the shear calibration is flat except for a slight trend to over-estimate the shear at the bright end by $\sim 6\%$, but the statistical accuracy is too low to be conclusive.

Additionally, in the simulations with pixel scale $0\farcs10$ we significantly over-estimate the shear for intrinsically small galaxies. This agrees with the general trend of all KSB+ implementations and the related RRG method to obtain a higher shear estimate for the poorly sampled data than the $0\farcs04$ ACS simulations. This indicates that pixelisation, which has most impact for poorly sampled data and small galaxies, in fact leads to an over-estimation of the shear, an effect which partially cancels with the under-estimation due to the $\mathrm{Tr}P^g/2$ approximation. The comparison of the TS and T2 analysis, where the latter one uses super-sampled high-resolution PSFs, indicates

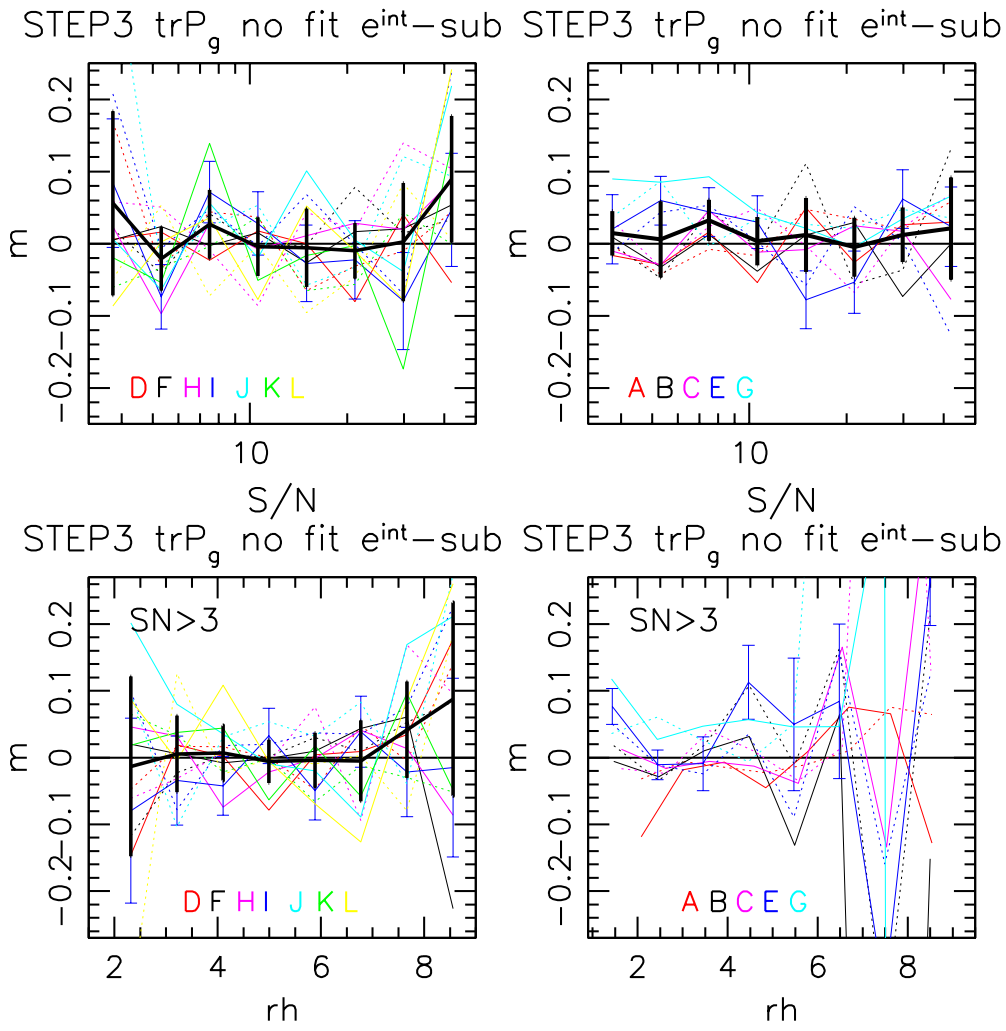


Figure 4.22: Calibration bias $m$ as a function of (true) signal-to-noise S/N (*top*) and half-light-radius $r_\mathrm{h}$ (*bottom*) for the TS analysis of the STEP3 simulations, computed from the intrinsic ellipticity subtracted shear estimator $\hat{\gamma}$. The *left* panels show the ACS–type image sets with pixel scale $0\farcs04$, whereas the *right* panels correspond to the larger pixel scales. For all plots $\mathrm{Tr}P^g/2$ was computed from individual galaxies and an adapted calibration factor $c_\mathrm{cal} = 0.93^{-1}$ (original $0.91^{-1}$) was applied. Galaxies were selected with cuts S/N $>$ 3, $|e^\mathrm{iso}| < 1.4$, and $\mathrm{Tr}P^g/2 > 0.1$. Thin solid (dashed) lines show $\gamma_1$ ($\gamma_2$) estimates for individual PSFs, where we show individual error-bars only for one PSF for clarity. Bold solid lines and error-bars show the mean and standard deviation of the individual PSF estimates and shear components. In the *bottom right* panel the errors increase for large $r_\mathrm{h}$ due to the low number of remaining galaxies.

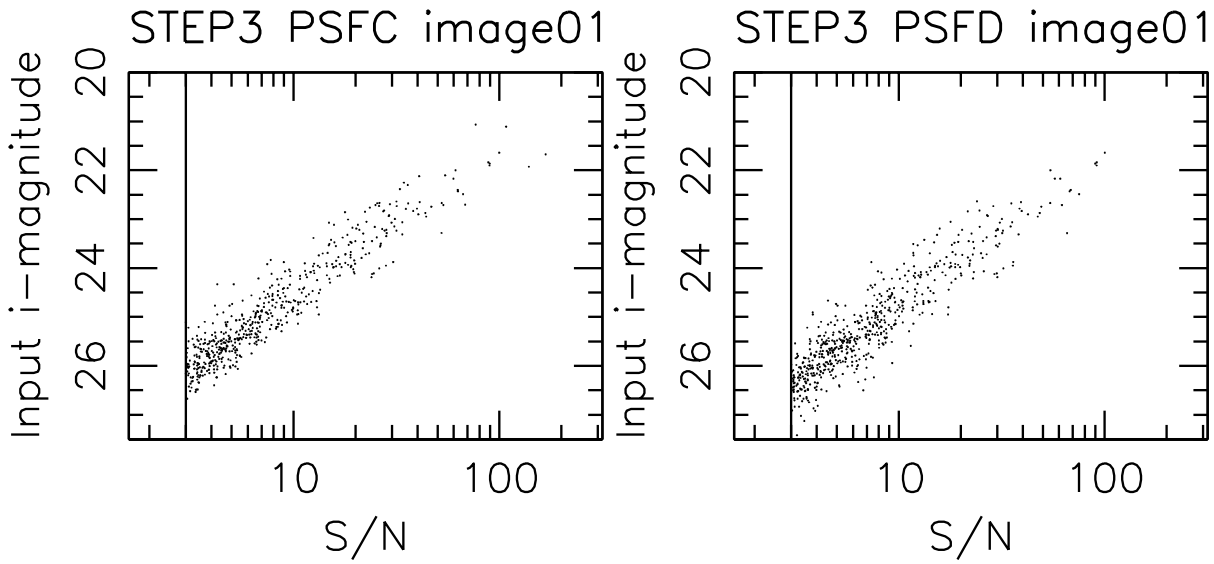


Figure 4.23: Distribution of galaxies in S/N–magnitude-space for simulated STEP3 images from set C (1.4m SNAP-like, *left*) and D (ACS-like, *right*).

that pixelisation has an impact on the shear estimate of order $\sim$ 7%, which however largely cancels out if both the galaxies and stars are measured from the same images.

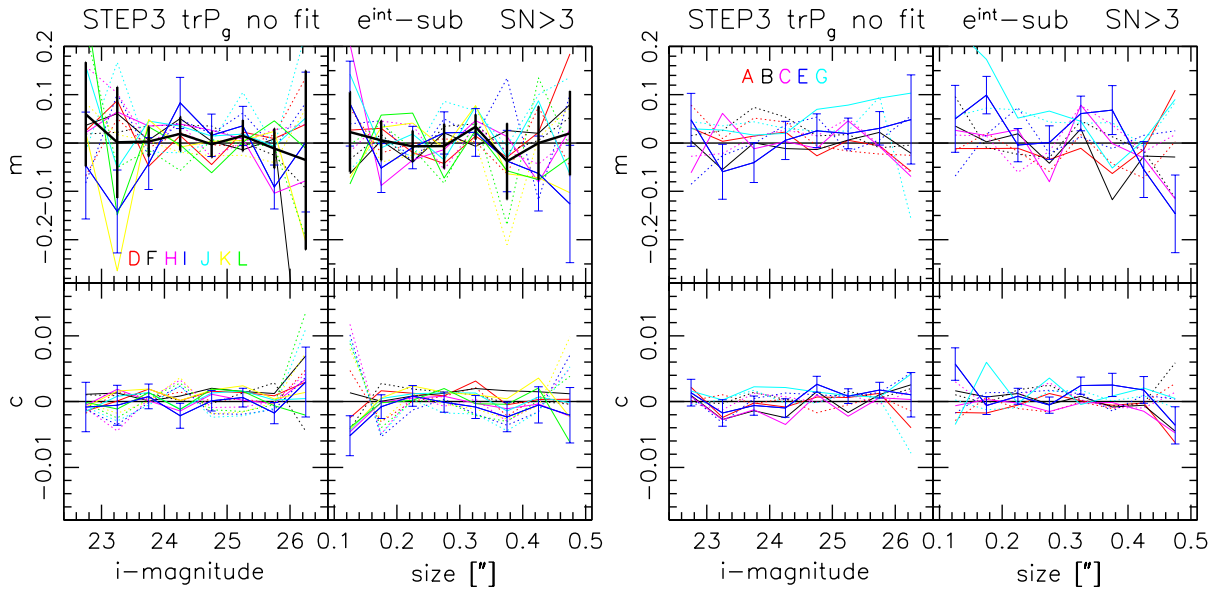


Figure 4.24: Calibration bias $m$ and PSF residuals $c$ as a function of input galaxy magnitude and size for the TS analysis of the STEP3 simulations, computed from the intrinsic ellipticity subtracted shear estimator $\hat{\gamma}$. The *left* panel shows the ACS-type image sets with pixel scale $0\farcs04$, whereas the *right* panel corresponds to the larger pixel scales. For all plots $\mathrm{Tr}P^g/2$ was computed from individual galaxies and an adapted calibration factor $c_{\mathrm{cal}} = 0.93^{-1}$ (original $0.91^{-1}$) was applied. Galaxies were selected with cuts S/N $> 3$, $|e^{\mathrm{iso}}| < 1.4$, and $\mathrm{Tr}P^g/2 > 0.1$. Thin solid (dashed) lines show $\gamma_1$ ($\gamma_2$) estimates for individual PSFs, where we show individual errorbars only for one PSF for clarity. Bold solid lines and errorbars show the mean and standard deviation of the individual PSF estimates and shear components. Note the significantly more stable correction for the space-based data shown here compared to the simulated ground-based STEP data shown in Figure 4.17.

## 4.5 Conclusions

The Shear TEsting Programme has demonstrated that nowadays several shear measurement pipelines reach an accuarcy at the 2% level, whereas tests prior to STEP yielded 10 – 15% only. Within the subsequent projects of STEP we identified the origin of biases which originally affected our analysis. After elliminating biases introduced by object selection and our weighting scheme for the case of a constant shear, our KSB+ implementation suffers from a remaining bias at the 7% (STEP2, STEP3) to 9% (STEP1) level, which seems to mostly originate from the approximate trace-inversion of the $P^g$ tensor required for noise minimisation. Similarly, all other tested KSB+ implementations which apply a trace-inversion show a tendency to under-estimate shear, if calibration corrections boosting the shear signal are ignored.

For our method the bias is stable at the $\sim$ 2% level between the different simulation sets, justifying the use of a calibration correction. However, the derived correction cannot directly be applied to independent KSB+ implementations, as details of the coding modify the bias shown by the scatter of the different KSB+ results. In particular, we identify a significant dependency on the choice of the scale factor for the Gaussian filter function. Hence, we urge independent methods to verify their accuracy, e.g. on the public STEP simulations. In addition, we identify a moderate increase of the bias for highly elliptical PSFs as given by image sets D and E for STEP2. However, real cosmic shear surveys will most likely discard images taken under such poor conditions.

Although the KSB+ method is based on assumptions which are strictly fullfilled only for certain simple PSF types, the analysis of the STEP3 simulations has revealed that our modified KSB+ implementation also yields 2% accuracy for simulated space-based data. Within the statistical accuracy of the simulations we detect no significant dependence of the shear estimate on magnitude or size. For the analysis of the ACS data we therefore conclude that systematic errors due to shape measurement will be well within the statistical errors.

Finally, we want to highlight the importance to apply proper signal-to-noise cuts. For our pipeline we found that galaxies selected with $S/N > 3$ show only a weak dependence of the calibration bias on magnitude. Possibly, this cut can even be relaxed to $S/N > 2.5$, where the additional galaxies are, however, very noisy, so that a weighting scheme should probably be applied. These signal-to-noise cuts refer to the case of uncorrelated noise. Correlated noise, introduced for example by drizzling, leads to an under-estimation of the background noise, which must be taken into account for the computation of a meaning-full signal-to-noise estimate. In the case of the STEP2 simulations this modifies the $S/N$ estimate by a factor $\sim 2.8$.

The reachable 2% accuracy of shear measurements with KSB+, which has been demonstrated for the CH, HH, and our implementation, is reassuring concerning its use on current and upcoming surveys. Nonetheless, KSB+ suffers from fundamental shortcomings, namely it's assumptions regarding the image PSF and the lack of proper treatment both of noise and pixelisation. We therefore regard it unlikely that KSB+ will be tuneable to serve as tool for precision cosmology with sub-percent accuracy, underlining the urgent need to develop and improve more sophisticated methods.

# Chapter 5

# Instrument and data reduction

In this chapter I will first summarise relevant properties of the *Hubble Space Telescope* and its *Advanced Camera for Surveys*, which are relevant for weak lensing analyses. I will then describe our data reduction pipeline, which has been upgraded throughout the course of this project. For the data used in the cosmic shear study, we distinguish between two different development stages named Mark-I and Mark-II reduction. During the development of the Mark-II reduction we joined forces with the HAGGLeS[1] project, which aims at the detection of galaxy-scale strong lenses in the ACS archive.

In this chapter I describe the general scheme of the data reduction. The particular data sets are then described in the following chapters.

## 5.1 The Advanced Camera for Surveys on-board the Hubble Space Telescope

### 5.1.1 The Hubble Space Telescope

The *Hubble Space Telescope*[2] (HST) is a 2.4 meter $f/24$ Ritchey–Chretien Cassegrain telescope deployed in April 1990 into a low Earth orbit with a period of 96 minutes. Being unaffected by Earth's atmosphere, it provides high-resolution imaging in UV, optical, and near-infrared wave bands. In addition, space-based observations have a lower sky background, which in combination with the high resolution enables very deep observations. For weak lensing measurements it provides the great advantage of a high number density of resolved galaxies, allowing accurate weak lensing measurements at small angular scales.

[1] `http://www.slac.stanford.edu/~pjm/HAGGLeS/`

[2] The HST is a joint programme of the National Aeronautics and Space Administration (NASA) and the European Space Agency (ESA).

### 5.1.2 The Advanced Camera for Surveys

The *Advanced Camera for Surveys* (ACS) was installed on board the *Hubble Space Telescope* during Servicing Mission 3B on March 7, 2002. ACS consists of three independent detectors:

- The **Wide Field Channel** detector, called ACS/WFC, consists of two $2048 \times 4096$ pixel thinned, backside-illuminated CCDs, with $\sim 0.05$ arcseconds per pixel, thus covering a nominal field-of-view of $202 \times 202$ arcseconds. ACS/WFC is sensitive in the spectral range from $\sim 3700$Å to $11,000$Å.

- The **High Resolution Channel** detector, called ACS/HRC, is a $1024 \times 1024$ pixel thinned, backside-illuminated CCD, with $\sim 0.028 \times 0.025$ arcseconds per pixel, covering a nominal $29 \times 26$ arcsecond field-of-view, with a spectral response from $\sim 2000$Å to $11,000$Å.

- The **Solar Blind Channel** detector, called ACS/SBC, is a solar-blind CsI Multi-Anode Micro-channel Array (MAMA), with $1024 \times 1024$ pixels. With one pixel corresponding to $\sim 0.034 \times 0.030$ arcseconds, ACS/SBC has a nominal $35 \times 31$ arcsecond field-of-view, with a far-UV spectral response from 1150Å to 1700Å.

For weak lensing measurements the ACS Wide Field Channel detector is the instrument of choice, as it provides the largest field-of-view and highest sensitivity in optical bands of all HST cameras, in combination with relatively good sampling enabling accurate shape measurements. I will hence limit the discussion to the Wide Field Channel in the following subsections. For a detailed description of ACS, the reader is referred to the *ACS Instrument Handbook* (Pavlovsky et al. 2006b).

### 5.1.3 Instrument design of the ACS Wide Field Channel

The Wide Field Channel was designed to increase the survey capabilities and therefore the discovery efficiency of HST. On one hand this is achieved by a field-of-view ($202'' \times 202''$) which is larger than the field of any other HST camera. Furthermore, the quantum efficiency of the WFC (48% at maximum including the optical telescope assembly) is about a factor of three to four higher at optical and near-infrared wavelengths than for STIS and WFPC2 (see Fig. 5.1).

The high throughput is possible due to the use of very sensitive thinned, backside-illuminated CCD chips with anti-reflection coatings optimised for red wavelengths. Additionally, the number of optical elements is minimised, since only three mirrors with silver coating are used inside the camera. The design of the ACS/WFC is sketched in Fig. 5.2: Light coming from the HST secondary mirror is reflected by these three mirrors through two filter wheels onto the WFC CCD chips. The mirrors are also used to correct for the spherical aberration of the HST primary mirror and field dependent astigmatism.

The two filter wheels are shared by the WFC and the HRC and allow the use of the following filters for the WFC: F435W, F475W, F502N, F550M, F555W, F606W, F625W, F658N, F660N, F775W, F814W, F850LP, and the grism G800L. The throughput of the different broad-band filters is compared in Figure 5.3.

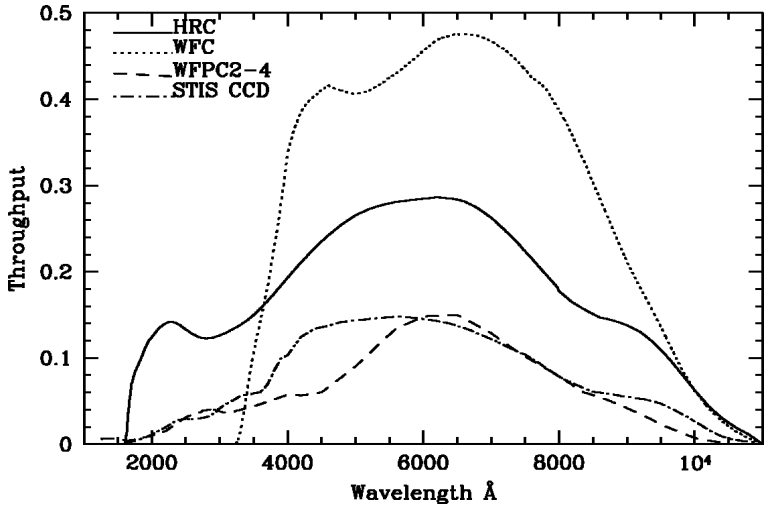


Figure 5.1: The total throughput for the CCD systems of ACS/WFC, ACS/HRC, WFPC2–4, and STIS. For optical and near-infrared observations ACS/WFC has by far the highest sensitivity (Fig. 5.7 from Pavlovsky et al. 2006b).

The two CCD chips are usually denoted WFC1 and WFC2, where WFC1 is located at higher Y positions in the composite image. Both have $2048 \times 4096$ pixels with a nominal pixel size of 0.050 arcseconds per pixel. The WFC PSF has a FWHM of $\sim$ 2.3 pixels for the F775W filter. The CCDs are read-out by four read-out amplifiers in the corners of the camera. For gain = 1, which is the default value, the number of photons which can be accumulated without saturation in a single exposure is limited by the 16 bit-per-pixel internal buffer, which corresponds to 65,535 counts. For higher gains (2, 4, 8 possible), the dynamical range is limited by the depth of the potential well (84,700 $e^-$). The read-out noise amounts to 5.0 $e^-$. The nominal dark current is 0.002 $e^-$/s. For further details the reader is referred to Pavlovsky et al. (2006b).

### 5.1.4 Geometric distortion of the WFC

The two chips of the WFC are located about 200 to 500 arcseconds from the optical axis of the telescope. This results in a tilted focal surface with respect to the optical axis, creating a strong geometric distortion. As a result the pixel scale is smaller along the radial direction from the optical axis than along the tangential direction. Thus, the square pixels are projected onto trapezoids of varying area across the field. In Fig. 5.4, the projected position of the WFC field-of-view relative to the optical axis and the other cameras is shown. Similarly to the single pixels, the whole WFC field-of-view is stretched along the direction tangential to the optical axis relative to the radial direction, which approximately coincides with the diagonal from the upper left corner of WFC1 to the lower right corner of WFC2. This leads to a projected angle of the *x*-/*y*-detector axes on the sky of $\sim$ 85 degrees.

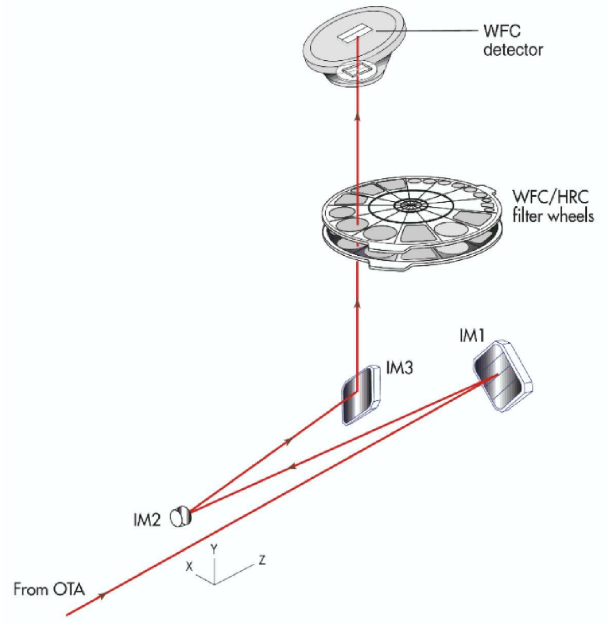


Figure 5.2: Design of the ACS Wide Field Channel. Light coming from the HST secondary mirror is imaged by a spherical mirror (IM1) onto mirror IM2, which is an anamorphic asphere designed to correct for the spherical aberration in the HST primary mirror and the field dependent astigmatism of the HST at the centre of the WFC field-of-view. The light is then reflected by a Schmidt-like plate (IM3) through the two filter wheels onto the WFC CCD chips (Fig. 3.2 from Pavlovsky et al. 2006b).

Meurer et al. (2003) measure the field-dependent distortion of the WFC from dithered, i.e. relatively shifted observations of 47 Tucanae taken with the F475W filter (Sloan g′). Fitting the measured distortions with polynomials they find that fourth-order fits characterise the distortion to an accuracy of better than 0.2 pixel over the entire field, with an rms of $\sim 0.04$ pixels in $x$ and $y$. The largest offset is required for pixels in the upper left corner of WFC1, which are shifted by $\sim 82$ pixels. An updated distortion model including a look-up table for filter-dependent residual distortions was found by Anderson (2006). The derived distortion coefficients are provided by the Space Telescope Science Institute (STScI) as so-called IDCTAB tables, which are used for the distortion correction with `MultiDrizzle` (Sect. 5.2.4).

Proper correction for camera distortion is essential for a weak lensing analysis due to various reasons: First, dithered images can only be co-added if they are mapped to a distortion-free coordinate system. Otherwise local residual shifts lead to a degradation of the image PSF. Second, the varying pixel scale across the field-of-view influences the flux measurement of compact sources. Finally geometric distortions influence the shape and position of objects leading to wrong shear measurements.

Note that Anderson (2007) recently reported on detected temporal variations of the distortion solution, similar to our findings from the ACS GOODS observations detailed in Sect. 6.1.2. Such

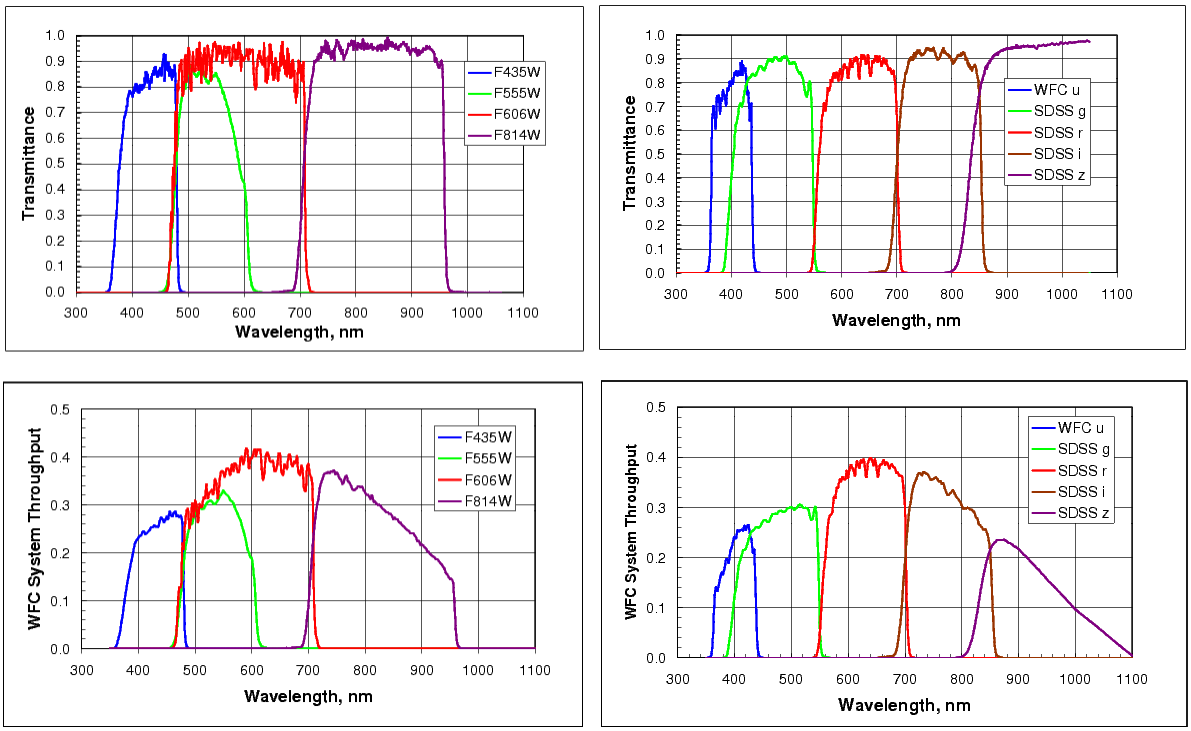


Figure 5.3: Transmission curves for the ACS broad-band filters (*left*) and the ACS SDSS filter set (*right*). The *top* panels show the filter transmittance, whereas the *bottom* panels refer to the total system throughput. The Sloan filters are also named: $g'$ = F475W, $r'$ = F625W, $i'$ = F775W, $z'$ = F850LP (from http://acs.pha.jhu.edu/instrument/filters/).

changes are not taken into account in the data reduction. We discuss possible implications for the shear measurement in Sect. 7.8.

### 5.1.5 Parallel observations

The HST scientific instruments are located at fixed positions in the focal plane of the telescope. Therefore it is possible to use one or more instruments in addition to the primary instrument. In these *parallel observations*, regions in the sky close to the primary pointing are observed, where the offset can be read off from Fig. 5.4.

Since parallel observations must not interfere with the primary observation, the choice of exposure time and, in case of shared filter wheels, also the choice of the filter is restricted by the primary instrument. Additionally, the dither pattern (relative shifts between the different exposures) is determined by the primary observation.

Parallel observations are possible for the ACS/WFC and the ACS/HRC in combination with any other instrument on-board HST. One distinguishes between *ACS coordinated parallels*, which are coordinated observations with another HST instrument of specific targets, *ACS auto-parallels*,

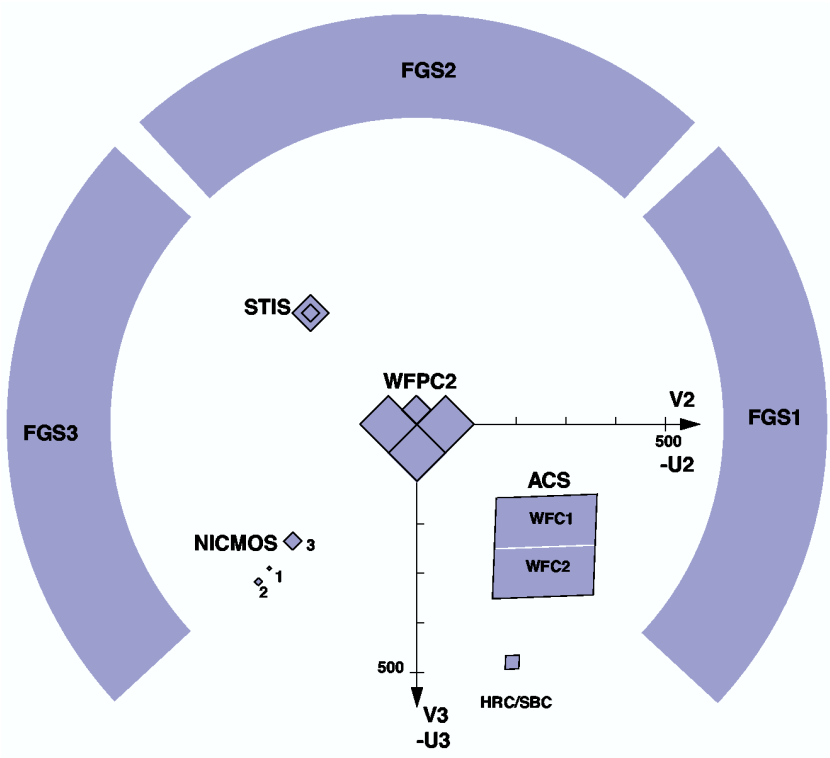


Figure 5.4: The HST field-of-view after Servicing Mission 3B. The positions of the cameras mounted in the HST focal plane and the Fine Guidance Sensors (FGS) are shown. The offsets from the optical axis in the V2 and V3 direction are given in arcseconds. The stretched shape of the ACS/WFC CCDs is due to the strong geometric distortion (Fig. 3.3 from Pavlovsky et al. 2003).

where two ACS channels are used simultaneously, and *ACS pure parallels*, which are taken completely independent of the observation of the primary instrument.

Especially in the early phase of ACS many observations were still conducted with the HST cameras WFPC2 and STIS, so that ACS parallel observations could be executed on many occasions, leading to a relatively quickly growing data set. Pure parallels additionally have the advantage that the data becomes publicly available immediately, whereas other HST observations are protected (proprietary) for one year. Cosmic shear studies benefit from the relatively large data volume available for parallel observations. In addition, parallel observations are separated by several arcminutes from the primary target (e.g. $\sim 6'$ for WFPC2) providing nearly random pointings for most classes of primary targets.

### 5.1.6 Cosmic rays, hot pixels, and other image defects

As in the case of any other CCD camera, ACS/WFC images are affected by image defects like hot and cold pixels or bad columns. In contrast to ground-based CCDs, cosmic rays (cosmics) are of

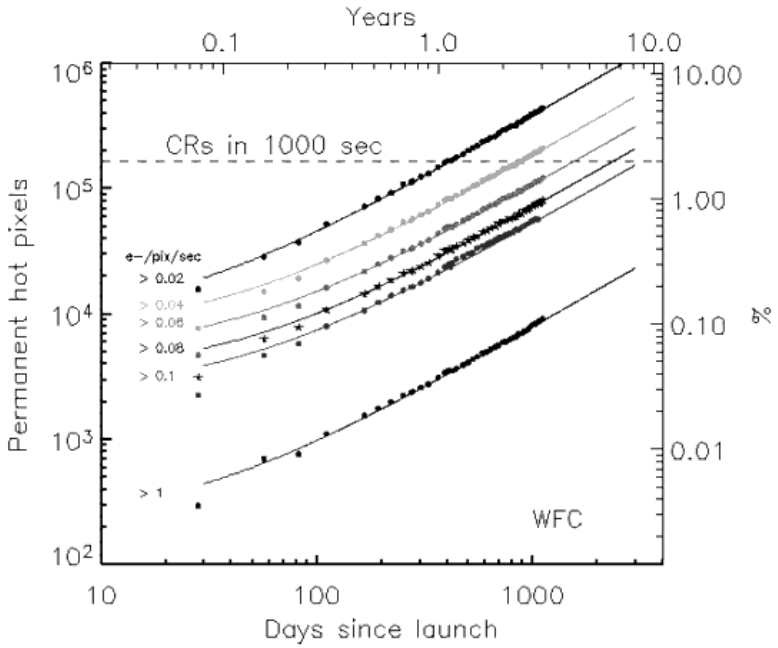


Figure 5.5: Number of permanent hot pixels in the ACS/WFC as a function of time, for different dark current thresholds (Fig. 4.9 from Pavlovsky et al. 2006b).

special concern for space-based cameras. These are highly energetic particles of extraterrestrial origin, which deposit energy while passing through the CCD leading to pixels with very high signal. Depending on the angle under which a cosmic passes through the chip, its signature in the image can range from only very few neighbouring pixels to long traces of affected pixels. As can be seen in Fig. 5.6, the number of cosmics in a typical 500 sec ACS/WFC image is much larger than the number of galaxies in the field. Also, many galaxies are affected by cosmic rays, making any reliable brightness and shape measurement impossible. However, since cosmic rays occur at random positions, they can be rejected if several separate exposures are combined.

Another concern is the steadily increasing number of hot pixels in the ACS/WFC (~ 1200 new hot pixels per day), which are largely created by the strong bombardment of the camera with cosmic rays. As for the other HST CCD cameras, a fraction of these new hot pixels can be annealed by heating the camera, which is usually done once per month by pointing HST at Earth. However, the rate of successful annealing is with ~60-65% significantly lower than for the other HST CCDs (~80-85%). Figure 5.5 shows the number of persistent hot pixels as function of time for different thresholds. Due to the rapid increase dithering becomes particularly important for later observing cycles. Unfortunately, a large fraction of the GO (guest observer) observations were taken without proper dithering, also affecting simultaneous parallel observations.

Furthermore, the ACS/WFC includes a significant number of bad or variable columns (see Sect. 5.3.5) and cold pixels with very low response, which can only be corrected using dithered data.

### 5.1.7 Charge-transfer efficiency

For space-based cameras a degradation of the charge-transfer efficiency (CTE) can significantly influence weak lensing shape measurements. The continuous cosmic ray bombardment in space creates chip defects acting as charge traps. If the image of an object moves across such a trap during parallel read-out transfers, a fraction of its charge will first be trapped and then statistically released during the following read-out steps. This effectively creates charge-trails behind objects in the readout direction.

The ACS/WFC has two read-out amplifiers per chip, which are located in the four corners of the instrument. During parallel transfer charges are moved along their column towards the top of the upper chip (WFC1) or bottom of the lower chip (WFC2) respectively. Also in the distortion corrected drizzled images (Sect. 5.2.4) the read-out direction is approximately parallel to the $y-$direction. The created charge trails lead to an average alignment of objects in the $y-$direction, corresponding to a negative average $e_1$ ellipticity component. CTE degradation is increasing with time due to the continued cosmic ray bombardment. As the depth of charge traps is limited, faint objects loose a larger fraction of their charges than bright ones, leading to a signal-to-noise and shape dependence of the effect. Therefore PSF models derived from high signal-to-noise stars do not provide a sufficient CTE correction for faint and more extended galaxies. In addition, the effect depends on the number of transfers (position) and sky background, where high sky values fill the traps continuously, reducing the effect of charge trails.

For the photometric loss due to CTE degradation empirical corrections have been found (Riess & Mack 2004; Riess 2004; Mutchler & Sirianni 2005). The non-linear influence of CTE degradation on object shape has however not been modelled in detail yet. For the GEMS and early parallel data we detect no significant CTE signature from the galaxy ellipticity (Sect. 6.4.1.2). However, from the galaxies in the COSMOS data, which have been taken later in time, we measure a highly significant CTE signal manifesting in a negative mean $e_1$ ellipticity (Sect. 7.2.5).

### 5.1.8 Tracking precision and velocity aberration

Pointing and tracking of the HST is done with the Fine Guide Sensors (FGS) system, which uses stars of the Guide Star Catalog as reference. The accuracy of the absolute pointing is typically precise to $\lesssim 2''$, except for a low number of exposures where we detected substantial offsets in the world coordinate system (WCS) defined in the image header, of up to $\sim 1'$. Such WCS errors complicate proper image registration, but do not affect the final weak lensing analysis.

For weak lensing analyses the tracking precision is of larger concern, because deviations from the nominal position broaden the image PSF within an exposure, and in case of non-isotropic pointing errors also introduce an additional anisotropy of the PSF. Random pointing errors can be created by various effects, such as jumps due to thermal expansion of telescope material or impacts of cosmic dust particles. The tracking quality is usually good if two guide stars are available. Then one star is used to control the pitch of the telescope and the other one to stabilise the roll-angle. In this case the tracking precision typically scatters between $0\farcs005$ and $0\farcs03$ during a single visit, if the same guide stars can be used continuously. If only one or no guide star is available, the HST gyros are used for tracking. Here substantially larger drifts and rotations

can occur. In this work we therefore only use exposures taken with two guide-stars.

Another concern is differential velocity aberration, both *between* different HST cameras, but also *across the field-of-view* of the WFC CCDs: Due to the orbital motion, velocity aberration shifts the apparent positions of objects. If the HST would track onto a guide star *exactly*, the positions of all other points in the HST focal plane would slowly change due to differential velocity aberration. However, this effect is taken into account and the HST always tracks correctly for the image centre of the primary instrument. Nevertheless, differential velocity aberration leads to imperfect tracking for a secondary (parallel) instrument. The strength of this effect of course depends on the geometrical alignment of the source position and the HST orbit, as well as the separation of the primary and the secondary instrument.

For a typical separation of 600″ between a primary and a secondary camera (compare Fig. 5.4), drifts introduced by differential velocity aberration during 1/2 orbit (∼48 min) do not exceed 0.″023 (0.46 WFC pixels) according to the *HST Observation Logs Documentation*[3]. Since individual exposures are much shorter (∼400-600 sec), the un-corrected drift during one exposure will typically be smaller than ∼ 0.″01 (0.2 WFC pixels). We investigate the tracking accuracy for the early parallel data in Sect. 6.1.1.

Resulting from the relatively large field-of-view, also differential velocity aberration *across the field-of-view* plays a role for ACS/WCS. Cox & Gilliland (2002) found that differential velocity aberration can create a shift of 0.3 pixels across a diagonal of the ACS/WFC during one full orbit. Due to the movement of the Earth relative to the Sun, images taken six months apart can even have misregistrations up to 1.4 pixels. This effect is corrected in the data reduction with `MultiDrizzle` (Sect. 5.2.4).

### 5.1.9 ACS status

After suffering malfunctions in the primary electronics ACS was operated using the backup side-two electronics since June 30th, 2006. On January 27th, 2007 a serious failure of the side-two electronics led to the loss of the ACS WFC and HRC. Since then, the *Wide Field Planetary Camera 2* (WFPC2) became the major workhorse for optical observations with HST. However, due to its smaller field-of-view, poorer resolution, lower sensitivity, and worse CTE degradation it provides only limited capabilities for weak lensing measurements.

Currently Servicing Mission 4 is scheduled for autumn 2008. During the mission WFPC2 will be replaced by the *Wide Field Camera 3* (WFC3), which has a slightly reduced area and optical sensitivity compared to ACS, but adds UV and infrared sensitivity. In addition plans for a possible repair of ACS are being considered at the moment. However, due to the strongly degraded ACS CTE, WFC3 will probably become the instrument of choice for most weak lensing studies.

[3] http://www.stsci.edu/hst/observatory/pointing/obslog/OL_1.html

## 5.2 Mark-I reduction

In this section I will detail on our "Mark-I" data reduction pipeline, which was used for the pilot study (Chapter 6). Later upgrades ("Mark-II") are then described in Sect. 5.3.

### 5.2.1 On-the-fly re-processing by the archive

The data archives at the Space Telescope Science Institute (STScI) and the Space Telescope European Coordinating Facility (ST-ECF) usually provide data products for different reduction stages. Hence, users can choose which of the automatically performed reduction steps are sufficient for their science goals, and which they have to redo with refined parameters. This is possible as the basic reduction packages used by the archives, `CALACS` and `MultiDrizzle`, are publicly available. The data products provided are automatically reprocessed *on-the-fly* using the most up-to-date calibration files, once data is requested by users.

We decided to base our Mark-I reduction on the flat-fielded *FLT* (*_flt.fits) images provided by the archives. These files have been pre-processed with the ACS Calibration Pipeline `CALACS`. The reduction steps are fairly straightforward and critical steps regarding the weak lensing analysis should only occur afterwards. For the ACS/WFC `CALACS` performs the following tasks:

1. Creation of a simple noise map by calculating a noise model for each pixel as $\sigma = \sqrt{|signal - bias|/(gain) + (readnoise/gain)^2}$, where the first addend in the square root is an estimate for the Poisson noise, while the second one accounts for the readout noise;

2. Creation of a static bad pixel mask by flagging known bad and saturated pixels;

3. Bias subtraction from bias images and the over-scan regions;

4. Subtraction of a dark image, which was scaled with the exposure time;

5. Division by a flat field image;

6. Calculation of photometry header keywords and some image statistics;

7. Trimming of the over-scan regions.

The calibrated science frames of the two chips are then saved together with the corresponding static bad pixel masks and noise maps in a multi-extension *FLT* fits file. An example for a science frame and the associated bad pixel mask is given in Fig. 5.6.

Additionally to the *FLT*-images we also use the so-called jitter files containing information about the tracking accuracy. In this work I denote all files belonging to a single exposure as a *dataset*. For a detailed description of the ACS Calibration Pipeline the reader is referred to the *ACS Data Handbook* (Pavlovsky et al. 2006a).

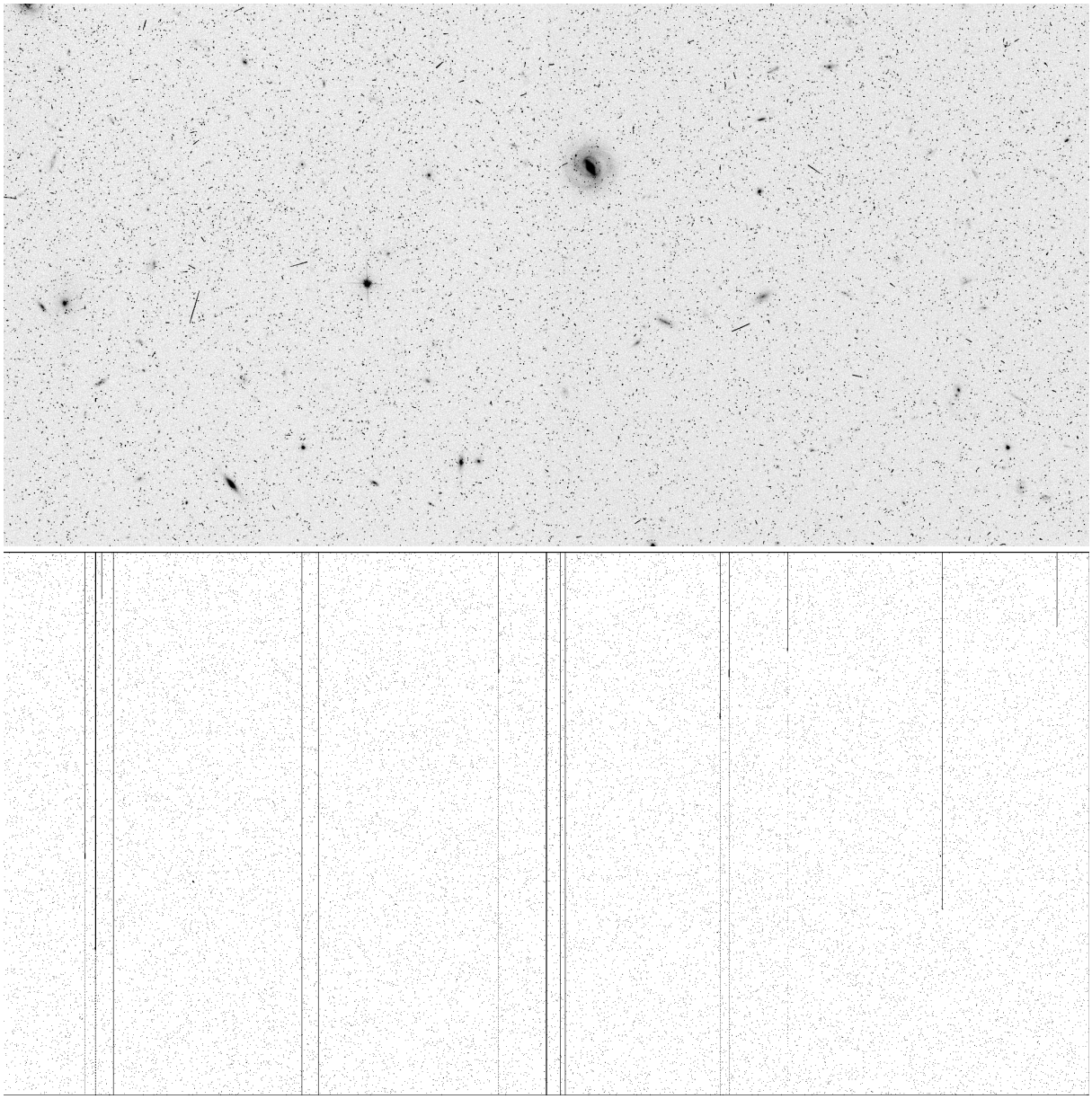

Figure 5.6: The pre-calibrated science frame (*top*) and static bad pixel mask (*bottom*) in the file j8hodtkiq_flt.fits, created with the `CALACS` pipeline for the ACS/WFC2 chip. Note the large number of cosmic rays present in the science frame. The exposure time of this image is 500 seconds.

### 5.2.2 Association identification

From the individual datasets we define associations containing all exposures which shall later be co-added. Here we allow for a maximal dither of $50''$ corresponding to $1/4$ of the field-of-view. For the parallel fields in the pilot study we aimed at a maximal stability of the observing conditions, keeping datasets from different visits separate (Sect. 6.1.1). Due to the good results achieved for the combination of two GOODS epochs of the CDFS (Sect. 6.1.2), we however later abandoned this limitation in order to obtain deeper data.

### 5.2.3 Drizzling and distortion correction

#### 5.2.3.1 Drizzling

"Drizzling" denotes a technique to map the pixels of an input image onto another output pixel grid. It was originally developed by Fruchter & Hook (2002) to reconstruct a higher resolution image from the under-sampled WFPC2 data of the HDF–North. Drizzling is implemented into the dither package of STSDAS (`drizzle`). The reconstruction of a higher resolution image requires that the individual exposures are dithered by non-integer shifts, so that different exposures sample the PSF- and pixel-convolved light-distribution at different positions. For this application, the output pixel grid also has to be finer than the input grid, which is controlled by the factor `scale` in `drizzle`. All individual exposures are then mapped and added onto the same output grid.

In the simplest approach, the flux of one input pixel is simply distributed to the output pixels it covers after the mapping, according to the fraction of the overlapping area. However, this will lead to a final image which is still convolved with the window function of one input pixel. Furthermore, in this case the additional sampling leads to an effective further broadening of the PSF. This can be avoided by shrinking the input pixels by a factor `pixfrac` $\in [0, 1]$. Drizzling is schematically illustrated in Fig. 5.7. In this sketch, the original input pixels are drawn in red, whereas the shrunken pixels are depicted in blue. For the configuration plotted, the central pixel of the output grid receives no flux from this input image. This illustrates that the `pixfrac` parameter should significantly be reduced below 1 only if the data is properly dithered, so that gaps are filled by other input frames. Additionally, one has to be aware of the fact that drizzling produces correlated noise in the output image, since flux from one input pixel is distributed over several output pixels. Here the degree of correlation depends on the relative size of the shrunken input pixels to the output pixels.

The properties of the output image strongly depend on the drizzle `kernel`, the function describing how the flux of each input pixel is distributed across the output image. In the description above this has always been the *square* kernel, with variable `pixfrac`. Other kernels which are often used are *gaussian*, which leads to smooth object profiles but strong noise correlations, and *lanczos3*, which is a 3rd-order polynomial approximation of the sinc–function. In principle the latter yields an optimal reconstruction with minimal noise correlations. For space-based data it however has the disadvantage to introduce "ringing" around the large number of masked pixels. Hence, it should only be used if a large number of exposures is stacked.

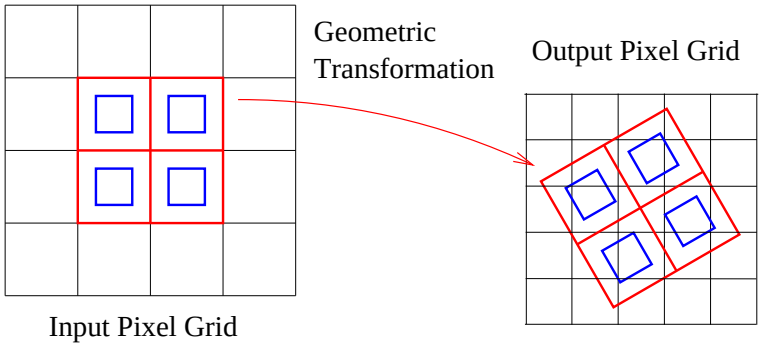


Figure 5.7: Schematic illustration of drizzling: The input pixel grid (*left*) is mapped onto a finer output grid (*right*). In the mapping a shift, rotation and geometric distortion can be taken into account. The input pixels can be "shrunken" to smaller pixels, which are called drops (the inner blue squares). Output pixels only receive flux from overlying drops. In the depicted situation the central pixel in the output grid receives no flux from any shrunken input pixel.

In principle, the mapping carried out by `drizzle` can be any geometric transformation. Besides accounting for relative shifts and rotations, it can therefore be used to correction for geometric field distortion. However, if strong field distortions are present, as it is the case for ACS, half-pixel shifts commanded for the image centre translate into different shifts for different camera positions. For very deep observations the best strategy is then often given by large dither steps, which are necessary to correct for bad pixels or fill gaps between chips, in combination with random sub-pixel shifts.

For a detailed introduction into the drizzling method the reader is referred to the *HST Dither Handbook* (Koekemoer et al. 2002).

#### 5.2.3.2 Motivation for drizzling ACS/WFC images

The ACS/WFC suffers from strong geometric distortions (see Sect. 5.1.4). Hence, drizzling is required for the co-addition of separate exposures. Furthermore, accurate point source photometry requires distortion correction: Owing to the distortion, the area of sky one pixel covers varies between 0.89 and 1.08 times the central value. Correcting for this effect with simple flat-fielding will artificially brighten or respectively dim poorly resolved objects with steep brightness profiles in the centre. In contrast, drizzling by construction conserves surface brightness and enables us to perform correct point source photometry.

The issue of reconstructing a higher resolution image is less important than for WFPC2, since the ACS/WFC pixels sample the HST PSF better by a factor of two than the pixels of the Wide Field chips of WFPC2. In addition, due to the strong field distortion of ACS, complex dither patterns are required for a uniform reconstruction with higher resolution across the whole field-of-view (Sect. 5.2.3.1). Additionally, the WFC PSF is significantly broadened by charge diffusion, which cannot be recovered by dithering.

#### 5.2.3.3 PyDrizzle

`PyDrizzle` was developed by STScI to automatise the usage of `drizzle` for ACS. It combines the flat-fielded frames of the two WFC CCDs onto one output grid taking the camera distortion stored in the IDCTABs (see Sect. 5.1.4) into account. In addition, it includes a correction for differential velocity aberration across the field-of-view (Sect. 5.1.8). `PyDrizzle` is able to process any number of input images, where their relative shifts and rotations have to be specified in an association table. The input images are then drizzled onto the same output grid taking these transformations into account.

`PyDrizzle` also takes bad pixel masks into account, so that flagged pixels do not contribute to the output image. In principle each input pixel can be assigned a specific weight. As default option the different exposures are weighted according to their exposure time, which performs reasonably well in the case of sky-limited images if sky conditions are stable. Given that all the data used for weak lensing are taken in broad-band filters with relatively long exposure times, they are sky-limited. In addition, the co-added exposures have usually been taken closely in time with similar sky background. We therefore use this simple weighting scheme for the Mark-I reduction. Then the created output weight image gives the cumulative exposure time contributing for each output pixel, scaled with the relative area of output to input pixels.

In the actual drizzling process, `PyDrizzle` allows the user to choose between different kernels. Besides the already mentioned *square*, *gaussian*, and *lanczos3* kernels, further options are *point* (as *square* with `pix_frac` = 0), *turbo* (square kernel ignoring rotations), and *tophat* (top hat). Concerning units it converts electrons as given in the *FLT*-images to electrons per second for the drizzled output science image (*DRZ*-image). `PyDrizzle` does not reject cosmic rays and previously unknown bad pixels, a task performed by `MultiDrizzle`, as detailed in the next section.

### 5.2.4 Cosmic ray rejection and co-addition with MultiDrizzle

To automatise the rejection of cosmic rays and the co-addition of several input images, Koekemoer et al. (2002) developed the python based package `MultiDrizzle`[4], which uses `PyDrizzle` and several task of the STSDAS dither package. Here I will summarise the main steps performed by the software. For a more detailed description the reader is referred to the *ACS Data Handbook* (Pavlovsky et al. 2006a) and the MultiDrizzle Homepage[5].

First `MultiDrizzle` creates an association table for the provided *FLT*-files, computing relative shifts and rotations from the image WCS possibly updated by user-provided absolute or residual ("delta") shifts (see Sect. 5.2.5). Next, the static bad pixel masks of the input images are updated for pixels which are more than $5\sigma$ below the median value. Also, the median sky background in the field is subtracted. The following major steps are also illustrated in Fig. 5.8:

1. The sky-subtracted *FLT*-images are drizzled separately but onto the same output coordinate system, i.e. relative shifts and rotations are taken into account.

[4] In the Mark-I reduction we use `MultiDrizzle` version 2.7.0.

[5] `http://stsdas.stsci.edu/multidrizzle/`

2. The median image of the separately drizzled images is calculated taking their pixel masks and weights into account. This median image provides a first estimate for the cosmic ray-cleaned image. However, double- and triple-incidences of cosmic rays can lead to remaining artifacts, especially if the number of combined images is small. To make the rejection more efficient, the `combine_nhigh` pixels with the highest values are generally rejected, where `combine_nhigh` = 1 by default.

3. The median image is transformed back to the coordinates of each input image. This inverse drizzling is called *blotting*.

4. For each exposure the blotted median image is compared to the corresponding *FLT*-image in order to identify cosmic rays in this image. Pixels for which the absolute difference of these images is larger than expected by noise statistics, or the flattening effect of taking the median, are flagged as cosmic rays.

5. Finally, all sky-subtracted *FLT*-images are drizzled onto the same output grid taking both relative shifts and a combined mask of bad pixels and cosmic rays into account. The result is a cosmic ray-cleaned and distortion-corrected image with a weighted mean co-addition.

Compared to a pure median image this approach provides cleaner cosmic ray rejection and better statistics.

`MultiDrizzle` also provides an alternative rejection mechanism for the median image called *minmed*, which further improves the cosmic ray rejection in the case of few input images. In this algorithm, first the median is calculated, again with rejecting the `combine_nhigh` highest pixels. If this median is more than *n* sigma above the minimum pixel value, it is replaced by the minimum, where *n* is by default 6 and sigma is approximated as the square-root of the median counts. In case the minimum is taken for a certain pixel, the procedure is repeated for all pixels in a radius of `combine_grow` (default 1.0 pixel) around this particular pixel, but now with a lower threshold (3 sigma by default). The latter is done to properly reject the "halos" around cosmic rays. Similarly, lower thresholds are used for neighbours of already masked pixels in the comparison of the blotted median image to the *FLT*-image.

Note that the cosmic ray rejection carried out by `MultiDrizzle` also removes previously un-flagged hot pixels, if the data are well dithered.

### 5.2.5 Shift refinement

Usually the image WCS is not accurate enough to provide proper alignment of the single frames. If datasets have been taken at different visits their astrometry may be misaligned by several arcseconds. Even for data taken within one orbit sub-pixel shifts may occur which would significantly degrade the image PSF if the data was simply co-added. We therefore refine relative shifts and rotations by matching `SExtractor` (Bertin & Arnouts 1996) positions of compact sources detected in the separately drizzled frames. Here we use `SExtractor` positions measured with a Gaussian window function which are more accurate than simple first moments. The rotations and shifts between the separate frames are then computed using the IRAF task `geomap`. The

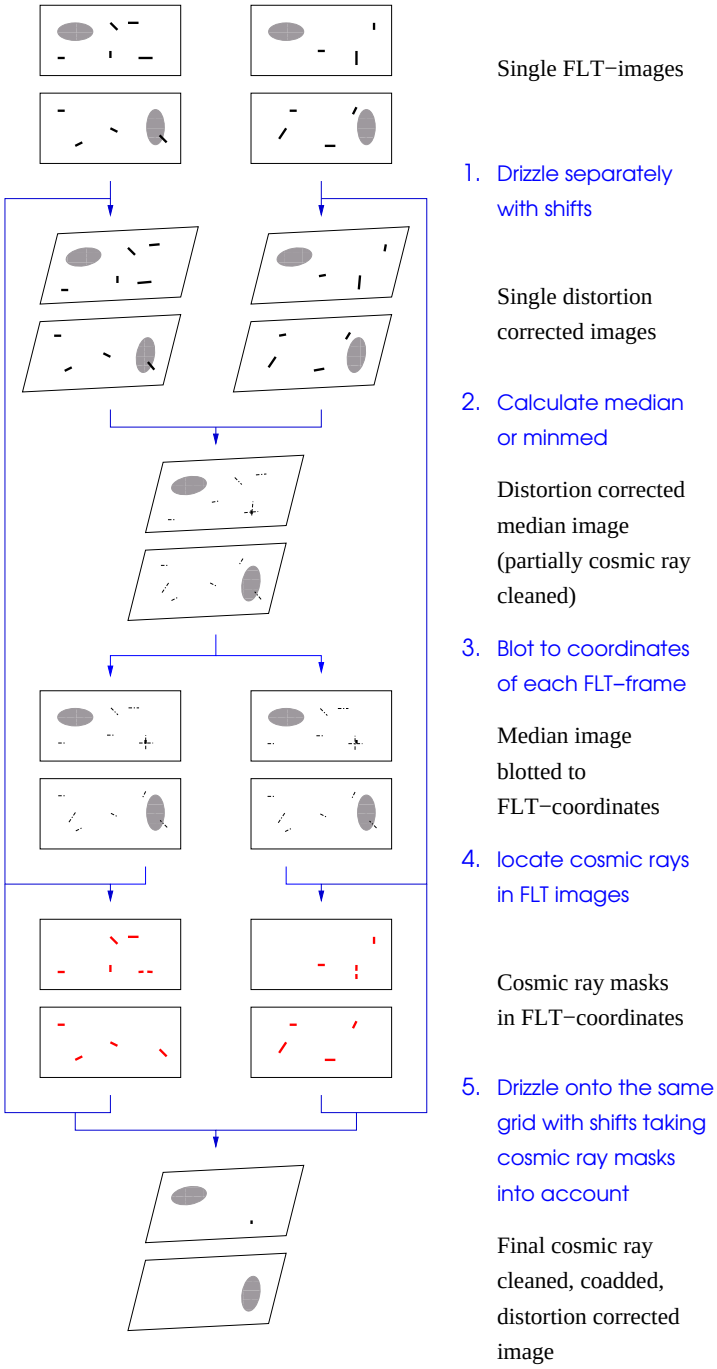


Figure 5.8: Flow chart for the main steps `MultiDrizzle` performs to create cosmic ray-cleaned, distortion-corrected, co-added images. Whereas the rectangles indicate un-drizzled images, the rhomboids correspond to drizzled, distortion-corrected images. The grey ellipses represent real objects (galaxies), whereas the solid black lines correspond to cosmic rays and the dashed-dotted black lines to cosmic ray artifacts. The red lines represent flagged pixels in the cosmic ray masks. The sketch only shows two input images. A higher number is processed completely analogously. The depicted situation corresponds to small (in the sketch unnoticeable) shifts between the two exposures. Note that there is a chance alignment (double-incidence) of two cosmic rays in the upper chip, which therefore cannot be rejected completely.

derived transformations are then passed to `MultiDrizzle` as "delta"-shifts. For not yet understood reasons the frames usually do not line up perfectly after the first correction. We therefore iteratively repeat the procedure adding derived residual shifts and rotations until they converge to residuals < 0.04 pixels. For the early parallel data we quantify the derived shifts and rotations in Sect. 6.1.1.1.

For the alignment of multi-epoch GOODS observations (Sect. 6.1.2) we determined significant residual rotations ($\sim 0.1^\circ$). When we passed these "delta" rotations to `MultiDrizzle`, we found that it falsely introduces a significant change in the applied image scale, which would lead to a significant misalignment in the outer regions of the field-of-view. As a work-around we correct the *FLT* image header for the derived rotation, which seems to work fine.

Note that we do not align multi-colour data in the Mark-I reduction.

### 5.2.6 Parameters for the data reduction

Deviating from the default parameters, we use the `minmed` algorithm during the creation of the median image as it is more efficient to reject cosmic rays for a low number of co-added exposures. For the cosmic ray masks we let rejected regions grow by one pixel in each direction (`driz_cr_grow`=3) in order to improve the rejection of neighbouring pixels affected due to charge diffusion and pixels with cosmic ray co-incidences in different exposures.

In the final drizzle step we use a finer pixel `scale` of $0\farcs03$ per pixel in combination with the `square` kernel in order to increase the resolution in the co-added image and reduce the impact of aliasing. For the default pixel scale ($0\farcs05$ per pixel) resampling adds a strong artifical noise component to the shapes of un- and poorly resolved objects (aliasing), which depends on the position of the object centre relative to the pixel grid and most strongly affects the $e_1$-ellipticity component. According to our testing with stellar field images, the `gaussian` kernel leads to even lower shape noise caused by aliasing. However, as it leads to stronger noise correlations between neighbouring pixels, we decided to use the `square` kernel for the analysis. In the Mark-I analysis we use `pixfrac` = 1.0.

Aliasing most strongly affects unresolved stars, which is critical if one aims to derive PSF models from a low number of stars in drizzled frames. However, since we determine our PSF model from un-drizzled images (see Sect. 6.2.4), this does not affect our analysis. Consistent with the results from Rhodes et al. (2005, 2007) we find that a further reduction of the pixel scale does not further reduce the impact of aliasing significantly, while unnecessarily increasing the image file size.

In the subsequent chapters the term *pixel* refers to the scale of the drizzled images ($0\farcs03$ per pixel) when dealing with ACS data, unless we explicitly allude to *WFC pixels*. An example for a fully processed single filter image is shown in Fig. 5.9.

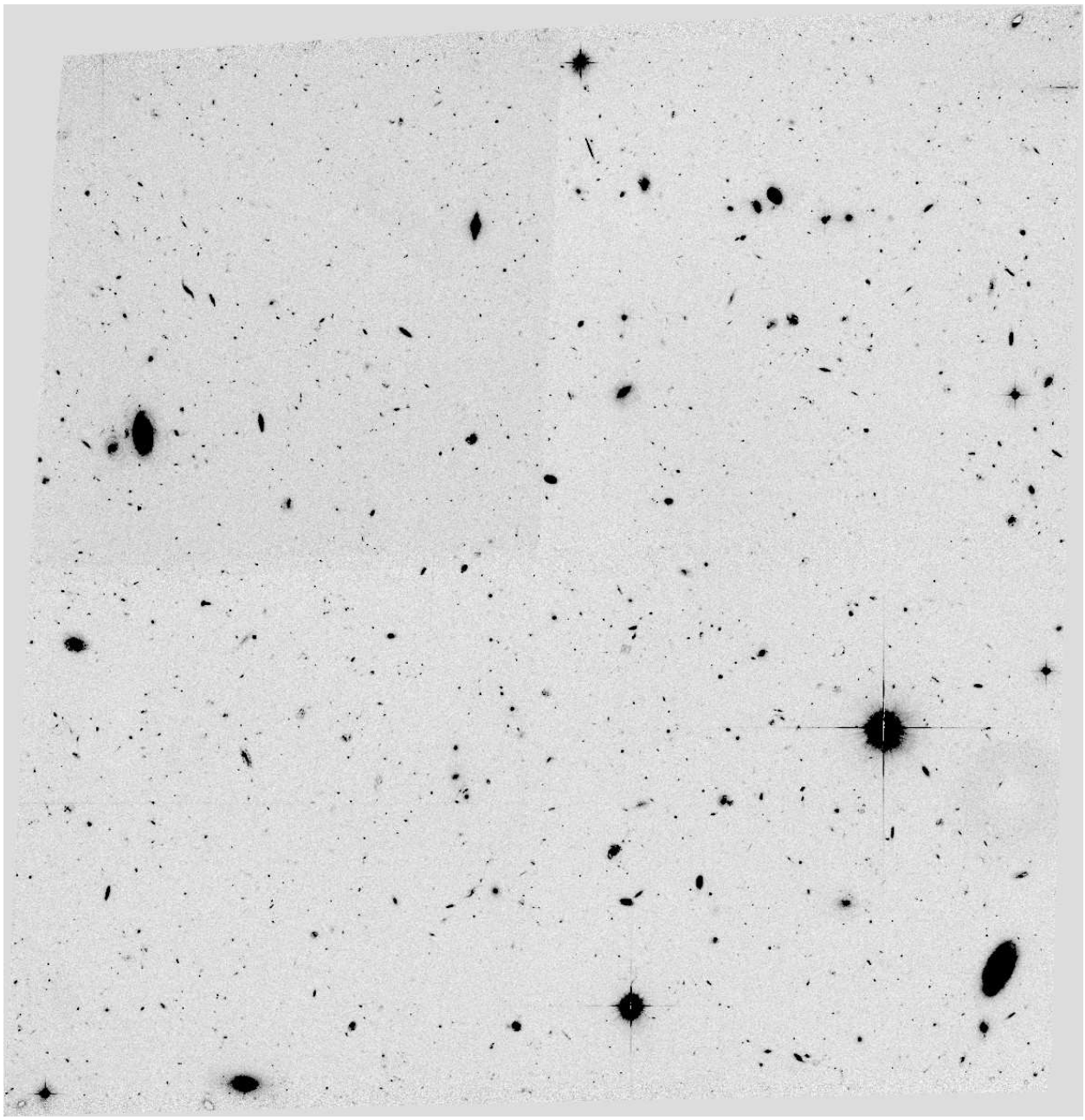

Figure 5.9: Example for a cosmic ray-cleaned, distortion-corrected, co-added ACS/WFC image, which was processed with `MultiDrizzle` and our Mark-I pipeline. For this GEMS F606W field three exposures with a total exposure time of 2160 seconds were co-added. The dither pattern was selected in order to cover the gap between the two WFC CCDs. Note the slightly higher background level in the upper left image quadrant, which is due to a residual bias level. We correct for this blemish in the Mark-II version of our pipeline. Near the upper and lower image border objects have falsely been rejected as cosmic rays by `MultiDrizzle`, because only one input exposure contributes to these regions. They are excluded from the shear analysis by our manual masks.

## 5.3 Mark-II reduction and the HAGGLeS pipeline

In our analysis of the early ACS parallel data we detect a significant mean alignment of the galaxies with the image y–axis for poorly dithered data (Sect. 6.4.1.3). We interpret this effect to be caused by galaxies whose images are affected by artifacts of insufficiently rejected bad columns and pixels. In order to properly reject affected galaxies, accurate knowledge of problematic pixels is required. Unfortunately not all affected pixels are flagged in the static bad pixel masks. After finishing this pilot study it was therefore one of the primary goals to upgrade our reduction pipeline by introducing improved bad pixel masks and optimised weighting of pixels.

At this point Phil Marshall (KIPAC, UC Santa Barbara), who is leading the HAGGLeS Project, the *HST Archive Galaxy-scale Gravitational Lens Survey*, and I decided to join forces as we independently planned to reduce a large fraction of the ACS archive, where HAGGLeS aims at the detection of galaxy-scale strong lenses. Together with Chris Fassnacht (UC Davis), Eric Morganson (KIPAC), and Marusa Bradač (KIPAC, UC Santa Barbara) he had already set up a `MultiDrizzle`-based pipeline for ACS data reduction at the computing farm of the Stanford Linear Accelerator Center (SLAC). After adding some of my scripts we developed several upgrades and additional functions for this joint pipeline.

I will give an overview about the pipeline in Sect. 5.3.1 and then detail on my major contributions to the code being improved pixel masks, background subtraction and weighting, but also optimised shift refinement and the development of efficient tools for masking and image inspection in Sections 5.3.2 to 5.3.7. In the following chapters I will refer to this improved reduction as “Mark-II” reduction.

A paper on details of the HAGGLeS data reduction and first results from the lens search is currently been written (Marshall et al. in prep.). The data processed in the frame of HAGGLeS will be made publicly available through the *HST Legacy Archive*[6] starting with multi-colour observations used for the strong lens search around the end of 2007. The weak lensing fields used for the cosmic shear analysis (see Sect. 8.3) will be added in 2008 after completion of the shear analysis.

### 5.3.1 HAGGLeS pipeline overview

The HAGGLeS pipeline performs the following tasks:

1. **Work space set up**: The raw image files are identified and moved to a temporary directory tree.

2. **CALACS**: The ACS calibration pipeline processes the raw exposures using the adequate reference files to create flat-fielded *FLT* frames.

3. **Background subtraction**: The sky background is subtracted as detailed in Sect. 5.3.2.

[6] `http://hla.stsci.edu/hlaview.html`

4. **Manual inspection of *FLT*-images**: Using the web inspection tool detailed in Sect. 5.3.3, we mark *FLT* frames affected by satellite trails or variable scattered light. In a second step we manually create masks for the affected frames (see Sect. 5.3.4).

5. **Improving the bad pixel masks**: We update the static bad pixel masks using the manual masks from the last step plus automatically created masks for hot pixels, bad or variable columns, and other persistent defects (Sect. 5.3.5).

6. **Computation of an accurate noise model**: We compute accurate noise estimates for each input pixel as detailed in Sect. 5.3.6, from which we derive optimal weights for the image co-addition.

7. **Shift refinement**: All exposures from all filters belonging to one field are drizzled together but without co-addition using `MultiDrizzle`[7]. We iteratively refine their relative shifts and rotations until the frames are optimally aligned (Sect. 5.3.7).

8. **MultiDrizzle**: Using `MultiDrizzle` we create cosmic ray masks and co-add the single exposures as generally described in Sect. 5.2.4. Here we treat different filters separately. Deviations from the default `MultiDrizzle` parameters are detailed in Sect. 5.3.8.

9. **Computation of an output RMS image**: We transform the inverse-variance map computed by `MultiDrizzle` into a RMS map, which can directly be used by `SExtractor` as weight image if `WEIGHT_TYPE` = MAP_RMS is specified. Then the `SExtractor` detection parameters do not require a correction for noise correlation.

10. **WCS correction**: In order to correct for the astrometric uncertainty of the Guide Star Catalog we match the positions of bright objects to their USNO-B counterparts and correct the image header for the average shift.

11. **Colour JPG**: In case observations in multiple filters are available a colour JPG is created, otherwise a grey-scale JPG.

12. **Catalogue creation**: Automatically a `SExtractor` catalogue is created, which is used as input for the strong lens search. However, due to the different detection requirements this catalogue is not used for the weak lensing analysis.

**The HAGGLeS pipeline in Bonn** For the reduction of the COSMOS (Chapter 7), STAGES (Sect. 8.4), and RXJ1347 data (Sect. 8.2) in Bonn I used a slightly modified version of the HAGGLeS reduction pipeline which starts with the *FLT*-images provided by the archives. This approach is not followed at SLAC to save disk space on the cost of more CPU time. In addition, the Bonn version concludes with the WCS correction, for which I replaced the originally used IDL routines by an self-written Perl script. These differences will have no impact on the weak lensing analysis. As an example for a Mark-II-reduced image see Figure 3.4.

[7] In the Mark-II reduction we use `MultiDrizzle` version 2.7.2

Table 5.1: Keywords added to *FLT* headers during the background subtraction.

| **Keyword** | **Possible value** | **Description** |
|---|---|---|
| BG_MODEL | MEDIAN\|MODE | Statistic used for subtraction |
| BG_MODUL | 1\|0 | Request residual modulation with flat-field |
| BG_MFLAT | String | Name of modulation flat-field |
| BGMED_*ij* | Float | Sky median in chip *i* and amplifier *j* |
| BGMOD_*ij* | Float | Sky mode in chip *i* and amplifier *j* |
| SKY_SHAG | Float | Mean subtracted sky estimate |
| BG_FLAGS | Flag | First bit: residual modulation done<br>Second bit: Background difference above threshold |

### 5.3.2 Improved background subtraction

Sometimes ACS *FLT*-images show a moderate jump in the background level between different image quadrants, which is caused by uncorrected residual bias offsets (Anton Koekemoer, private communication). These jumps are typically in the order of a few tenths of an electron, but can amount to $\sim 2e^-$ and more. Although such residuals are usually not critical given that most science applications apply their own background subtraction, we still aim at removing this blemish.

For this we first run `SExtractor` on each *FLT*-image to detect and mask all kinds of objects including cosmic rays. The created mask is then combined with the static bad pixel mask. From the unmasked pixels we next estimate the background value separately for each chip, where we by default use the median and optionally the mode statistics. In the next step we subtract the mean background estimate from all chips. The difference between the individual and mean estimate is then modulated with the inverse flat-field variation in the quadrant, normalised to 1. This difference is then subtracted from the corresponding image quadrant. The modulation is necessary as the *FLT*-images have been divided by a flat-field image after the imperfect bias subtraction.

We found that for crowded fields or fields containing very bright and extended objects, the background estimates can be significantly disturbed. In order to ensure that our method does not lead to an erroneous over-correction of the background jump for such cases, we adopt a maximal accepted difference in the background estimates (by default $4e^-$). If this is exceeded we only subtract the minimal background estimate for all quadrants. Our pipeline also adds a number of header keywords, which are listed in Table 5.1.

### 5.3.3 Web inspection tool

In the HAGGLeS project a huge amount of data is centrally stored at SLAC, with several remote users processing and analysing the data. Hence, soon the need arose for an efficient tool to quickly browse and inspect large numbers of images using limited band-width. This was necessary for the pre-selection of *FLT*-images which require manual masking (Sect. 5.3.4), but

also the inspection and classification of strong lens candidates identified by a lens robot, and the verification of automatically created masks for the stacked images (Sect. 7.2.1).

To fulfil these needs I wrote a perl/cgi-based web interface which displays compressed JPG versions of the images requiring inspection, in combination with form elements allowing efficient image selection and annotation. The entered data are stored in asci-tables with user- and time-stamps, and are automatically parsed by subsequent scripts. Screen-shots of the interface are shown in Figure 5.10.

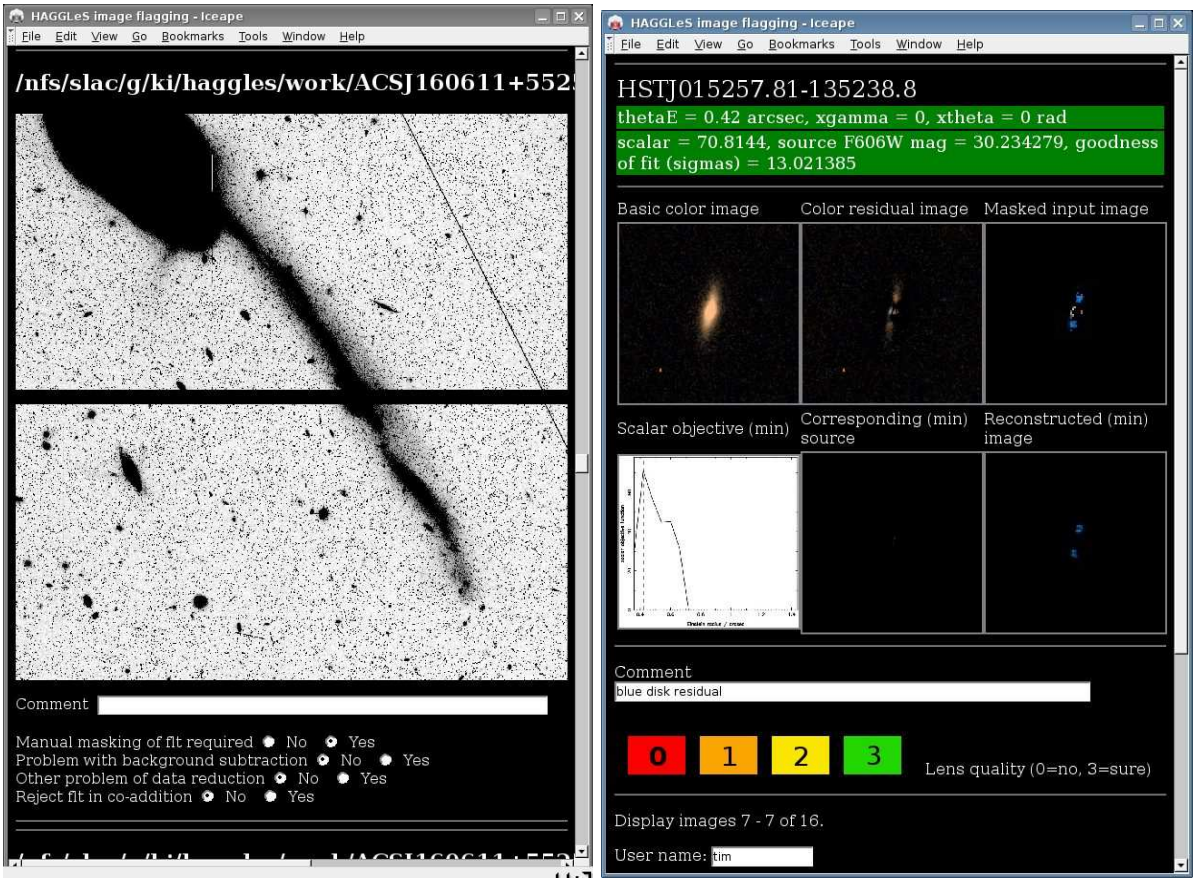


Figure 5.10: Screen-shots of the perl/cgi-based web interface for efficient image inspection via the Internet. The *left* panel shows the *FLT*-inspection mode, in which *FLT* frames can quickly be scanned visually by scrolling a web browser window. In the example shown the image has been selected for manual masking due to the satellite trail present. The *right* panel shows an example for the lens inspection mode, in which strong lens candidates identified by a robot are visually inspected and classified one-by-one. Here a static web page produced as output from the robot is converted into dynamic cgi-output.

### 5.3.4 Efficient masking of FLT frames

Using the web inspection tool (Sect. 5.3.3) we visually inspected all *FLT*-images processed with the HAGGLeS pipeline, amounting to more than 12,000 files at the time of the write-up. About 20% of these files were marked for manual masking, as they either showed satellite trails or scattered light which moves between dithered observations (see Figure 5.11). These features are only incompletely masked by the cosmic ray rejection in `MultiDrizzle`, as they have less sharp edges than cosmic rays. Hence, we mask them manually in order to achieve optimal data quality and maximal usable area in the co-added frames.

To make this tedious work most efficient I wrote a further script which is run on the user's local computer. It automatically transfers the inspection file lists from the cgi server and downloads the JPG images of marked *FLT*s. These are locally converted to low resolution fits files and automatically displayed using `ds9`. Here the user manually creates polygonal region files to mask the disturbing objects. These files are automatically renamed and scaled to the correct *FLT* scale. Then they are checked into a repository making sure that no file is unnecessarily inspected twice.

For a survey of this size manual masking is still feasible, if it is combined with efficient image display tools. However, this will be impossible for dedicated future weak lensing surveys, which will require the development of fully automated masking routines.

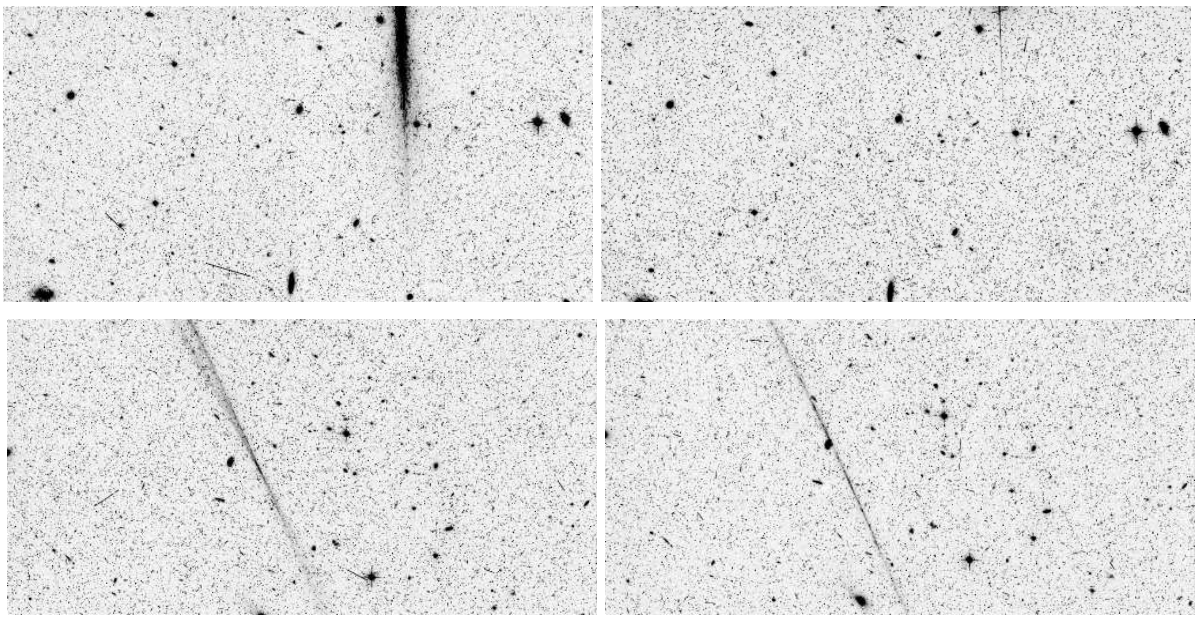

Figure 5.11: For dithered data scattered light often changes its appearance and position relative to the locations of stars and galaxies, which can be seen by comparing the *left* and *right* panels showing dithered data from the COSMOS survey. By masking these features in the *FLT*-frames we increase the usable sky area in the co-added frames. Note that the chips displayed in the *top* and *bottom* do not belong to the same pointing.

### 5.3.5 Improved bad pixel masks

Due to the results from the early parallel data (Sect. 6.4.1.3) we invested a considerable effort into optimising the bad pixel masks in the Mark-II pipeline. To fulfil the lensing requirements we follow a philosophy to aggressively reject problematic pixels, possibly excluding a fraction of pixels which might still be usable for other applications.

#### 5.3.5.1 Mask creation

For each *FLT*-image we combine the existing static bad pixel mask with the following new time-dependent masks:

1. **Updated hot pixel mask**: We reject all pixels with dark current $> 0.04e^-$/sec in the associated dark reference file. By default pixels with dark current $> 0.08e^-$/sec are rejected as hot pixels in the static bad pixel mask, whereas pixels with dark current $> 0.02e^-$/sec are only marked as warm pixels.

2. **Bias variance mask**: The ACS/WFC shows different bias structures, most prominently columns with high bias values. If this bias value is time-dependent, high or low column values will occur in the science frames after subtraction of a bias reference file. To identify variable columns we use all available bias reference frames. For each one we compute the variance from itself and the four bias reference frames taken closest in time, providing a good estimate for the degree of variability in a time-window of $\sim 2$ months. An example for such a variance image is shown in Figure 5.12. From this variance image we create masks using `ccdmask` as detailed in Sect. 5.3.5.2.

3. **Median image mask**: The other masks are usually able to identify most of the problematic pixels and columns. Yet, a small number of culprits still tends to efficiently resist capture. As a solution we found that a median image mask in most cases does the job: Here we compute the median image from the *FLT*-frames of 50 different pointings observed closely in time, after sky-subtraction and masking of objects detected with `SExtractor`. In order to exclude domination of few very deep pointings we limit the maximal number of *FLT*s from one pointing to six. An example for such a median image, which is similar to what is usually called a *super-flat*, is shown in Figure 5.13. From these median images we create masks using `ccdmask` as detailed in Sect. 5.3.5.2.

4. **Manual masks**: The manual masks for satellite trails and scattered light, which have been described in Sect. 5.3.4, are also included at this stage.

All of these masks are time-dependent. Hence, a science *FLT*-image is always corrected with the proper mask for the time of observation. The names of the applied mask files are stored in the *FLT* image header.

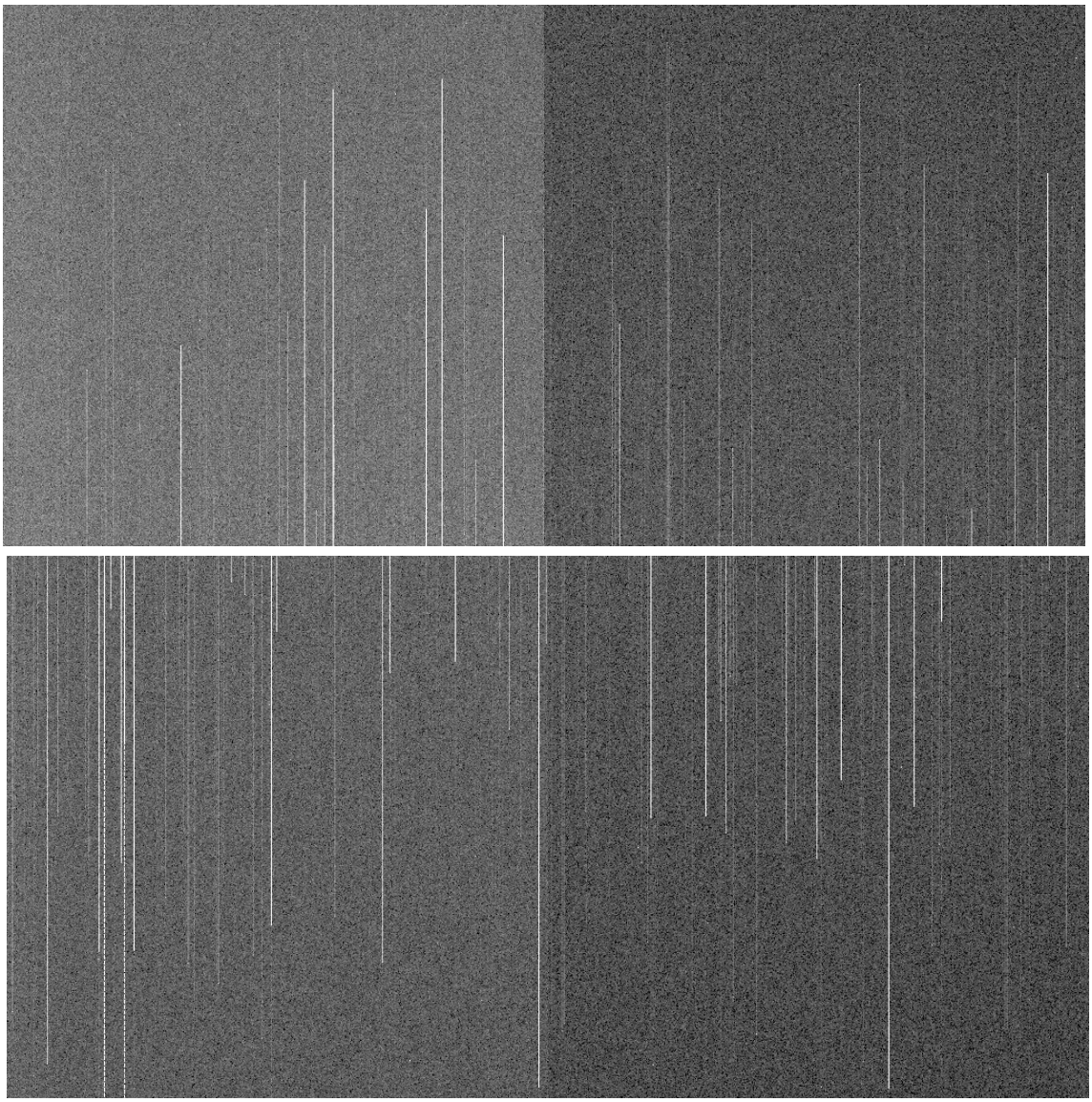

Figure 5.12: Variance image computed from five ACS/WFC super-bias frames for gain=1, which combine bias frames taken in December 2004 and January 2005. After the $5 \times 5$ binning (average), the dynamic range is 0.5 $\mathrm{COUNTS}^2$ (black) to 4.5 $\mathrm{COUNTS}^2$ (white).

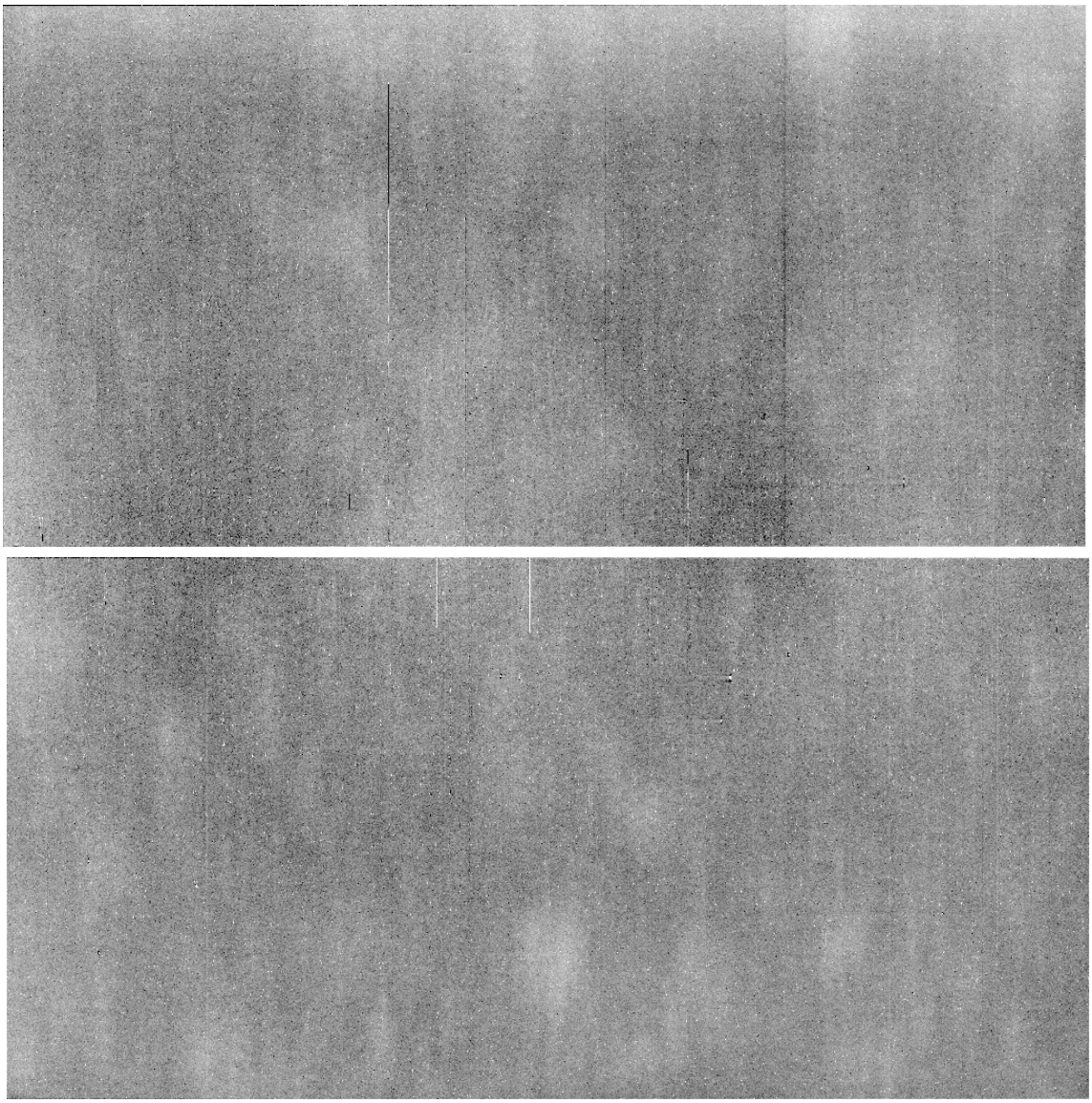

Figure 5.13: Median image computed from the background-subtracted *FLT*-frames of 40 COSMOS pointings observed in May 2005. Besides some remaining large-scale variation and hot pixels a number of bright and dark columns are visible, where the latter usually represent overcorrections in the bias subtraction. After the $5 \times 5$ binning (average), the dynamic range is $-1\,\mathrm{e}^-$ (black) to $4\,\mathrm{e}^-$ (white).

Table 5.2: Lower and upper $\sigma$ thresholds for pixel masking using the `ccdmask` task for the bias variance and median images.

| **Image type** | **lsigma** | **hsigma** |
|---|---|---|
| Bias variance | 100 | 25, +5 if more than 2.5% masked |
| Median, gain=1 | 13 | 11 |
| Median, gain=2 | 15 | 15 |

#### 5.3.5.2 Column masking with ccdmask

In order to create masks from the bias variance and median images described in the previous subsection, we realised that simple thresholding is not well suited for the noisy images with large-scale variation, as it either leads to fragmented bad column masks or falsely rejected noisy pixels. We achieve better results using the `IRAF` task `ccdmask`, which is part of the NOAO `imred` package. It computes the local median signal and rms variation in moving rectangles. A pixel is then masked if its values is either `lsigma` below or `hsigma` above the local median value. This is done for individual pixels and sums of pixels in column sections, where in the latter case the background dispersion is scaled by the square root of the number of pixels in the section. In the end each column is scanned for short segments of un-flagged pixels between bad pixels. We additionally mask these segments if their length is less than 15 pixels.

The selection of proper thresholds `lsigma` and `hsigma` strongly depends on the image noise properties. Therefore we had to manually tune these thresholds for the different image types investigated, where we summarise the derived parameters in Table 5.2. Note that sometimes even between images of one type significant variations in the noise properties occur, e.g. due to the growing number of hot pixels. Therefore the performance was not optimal in all cases. This was particularly troublesome for a number of bias variance images, where the parameters listed in Table 5.2 lead to a false flagging of a significant fraction of good pixels. As a solution we iteratively increase `hsigma` by 5 until the fraction of flagged pixels drops below 2.5%, yielding acceptable results.

### 5.3.6 Computation of an accurate noise model

We compute a noise image for each input *FLT*, which is used for inverse-variance weighting in the co-addition yielding optimal signal-to-noise in the stacked frame. Here we do not use the simple noise model computed by `CALACS` (Sect. 5.2.1), as it includes photon shot-noise, which would lead to a subtile bias towards an under-estimation of object flux[8].

The *FLT* science frames are in units of electrons. This is also handy for the computation of a noise image given that electrons are the relevant unit for the Poisson noise from sky background

[8]Including photon noise would down-weight exposures with positive deviations from the expectation value and up-weight exposures with negative deviations, leading to an effective bias.

and dark current. Hence, we compute the rms noise image for the flat-fielded science frame as

$$ERR = F^{-1}\sqrt{sF + tD + \sigma_{\rm r}^2 + \gamma^2 V}\,, \tag{5.1}$$

with the normalised flat-field reference image $F$. The sky background $s$ was estimated in Sect. 5.3.2 and is given in $e^-$. For the error contribution from dark current, the corresponding dark reference image $D$, which is given in $e^-/s$, has to be scaled with the exposure time $t$. A further contribution comes from the read-noise $\sigma_{\rm r}$, which is about $5\,e^-$. Finally, we also take the bias variance image $V$ into account, which was described in Sect. 5.3.5. As the ACS bias frames are given in counts instead of electrons, a conversion using the gain $\gamma$ (expressed in $e^-$/count) is required. We store the computed noise image in the *ERR*-extension of the *FLT* image. An example noise image is shown in Figure 5.14.

### 5.3.7 Robust shift refinement

Similarly to the Mark-I reduction (Sect. 5.2.5) we iteratively refine relative shifts and rotations by drizzling the frames separately but onto the same output pixel grid. We match windowed `SExtractor` positions of compact sources, which we select with filter-dependent size and magnitude cuts. "Delta" shifts and rotations are then computed using the `IRAF` task `geomap` with a rejection at the $2\sigma$-level.

In this step we include the exposures from all filters, leading to stacks for different filters which are aligned on the same pixel grid. However, due to the sometimes relatively large WCS errors, the dominance of cosmic rays, various different dither patterns, and differences in depth and object morphology between the different filters, proper catalogue matching turned out to be challenging for a large fraction of the HAGGLeS data.

We ended up with a complex combination of scripts to catch various special cases. One of the central procedures is a pixelised catalogue cross-correlation, which was the best methods to find initial off-sets in the case of large WCS errors. Fortunately, the HST role-angle is usually well constrained ($\lesssim 0.1°$), so that delta rotations do not need to be considered in the initial matching. Another challenging task was the robust automatic detection of matching failures, with merged catalogues based on chance alignments mostly of cosmic rays. We found that these could be well identified by their rms shift residuals after applying the `geomap` transformation to the catalogues, in combination with the number of positive matches.

Using only exposures from one of the broad-band lensing filters, matched catalogues typically consist of order $\gtrsim 100$ compact sources for typical extra-galactic fields. When aligning exposures from different filters typically 30 – 60 pairs of matched positions are available, which is still sufficient to constrain relative shifts and rotations with high accuracy. The iterative alignment is continued until shifts and rotations change by less then 0.05 WFC pixels and 0.0004° respectively, where the latter corresponds to a maximal displacement of 0.02 WFC pixels in the corners of the FOV.

We apply the same work-around for "delta" rotations as used in Sect. 5.2.5, since the reported problem also occurs for `MultiDrizzle` version 2.7.2, as used in the Mark-II reduction.

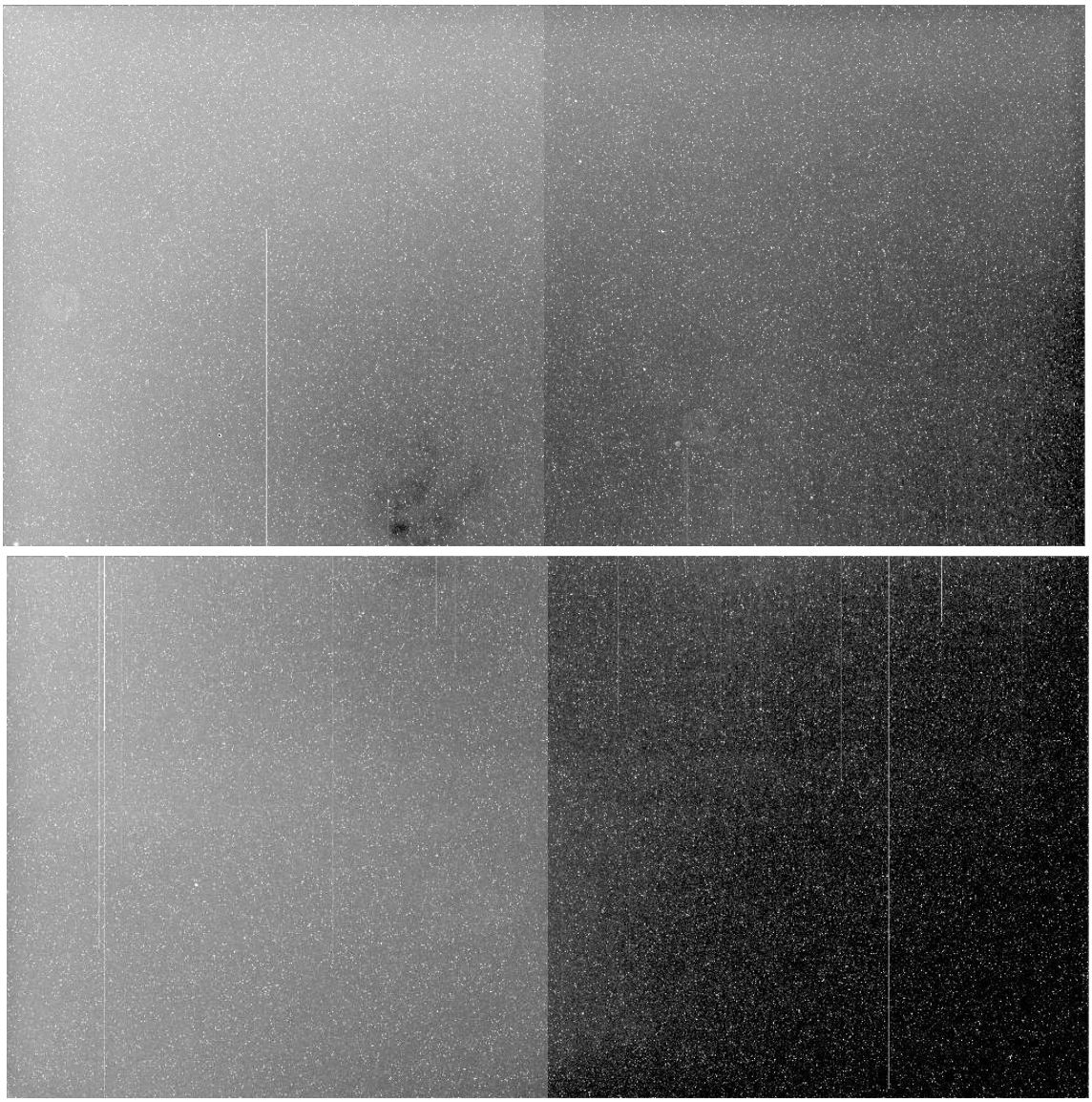

Figure 5.14: This image shows the rms noise model computed for the COSMOS *FLT*-image j8xi24lx (stored in the updated *ERR*-image extension). After the $5 \times 5$ binning (average), the dynamic range is $9\,e^-$ (black) to $11\,e^-$ (white).

### 5.3.8 MultiDrizzle parameters and output RMS image

As for the Mark-I reduction (Sect. 5.2.6) we use a finer output pixel scale of $0\farcs03$, in combination with the `square` drizzle kernel. Here we choose to slightly shrink the pixels (`pix_frac` = 0.9), to reduce the degree of noise correlation. We found that a further reduction of `pix_frac` leads to significantly enhanced aliasing. Further pixel shrinkage therefore only seems useful for deep stacks of well dithered data. As done for the Mark-I reduction, we use the `minmed` algorithm in the computation of the median image, and grow cosmic ray masks by one pixel in all directions (`driz_cr_grow` = 3) in order to reliably reject charge diffusion halos of cosmic rays.

As weighting scheme we specify `final_weight_type` = ERR, so that `MultiDrizzle` uses the *ERR*-extension image of the *FLT*-file to perform inverse-variance weighting. Note that we over-write the original *ERR*-image with a noise image including all noise sources *except* photon noise, as detailed in Sect. 5.3.6. In this way we exclude a possible bias in the co-addition due to the photon shot-noise. Furthermore, using our noise scheme the final weight image computed by `MultiDrizzle` provides an accurately scaled inverse variance noise map. We save its inverse square root image using the "rms.fits" extension (*RMS*-image). This *RMS*-image can directly be specifies as noise map to `SExtractor` (`WEIGHT_TYPE` = MAP_RMS). For proper photometry, `SExtractor` requires an rms image, which includes all noise sources except photon noise, exactly as provided by the pipeline.

# Chapter 6

# Analysis of the GEMS and early ACS parallel data

In this chapter I present results from a pilot study testing the capabilities of ACS for cosmic shear measurements with early parallel observations and the combined GEMS and GOODS data of the *Chandra* Deep Field South (CDFS). The results of this study have been published in Schrabback, Erben, Simon, Miralles, Schneider, Heymans, Eifler, Fosbury, Freudling, Hetterscheidt, Hildebrandt, & Pirzkal 2007, A&A, 468, 823–847.

In this work we developed a new correction scheme for the time-dependent ACS point-spread-function (PSF) based on observations of stellar fields. At the time the paper was submitted this represented the only technique which takes the full time variation of the PSF between individual ACS exposures into account and can be applied for arbitrary dither patterns and rotations. We estimate that our PSF correction scheme reduces the systematic contribution to the shear correlation functions due to PSF distortions to $< 2 \times 10^{-6}$ for galaxy fields containing at least 10 stars, which corresponds to $\lesssim 5\%$ of the cosmological signal expected on scales of a single ACS field. We perform a number of diagnostic tests indicating that the remaining level of systematics is consistent with zero for the GEMS and GOODS data confirming the success of our PSF correction scheme. For the parallel data we detect a low level of remaining systematics which we interpret to be caused by a lack of sufficient dithering of the data. Combining the shear estimate of the GEMS and GOODS observations using 96 galaxies arcmin$^{-2}$ with the photometric redshift catalogue of the GOODS-MUSIC sample, we determine a *local single field estimate* for the mass power spectrum normalisation $\sigma_{8,\mathrm{CDFS}} = 0.52^{+0.11}_{-0.15}(\mathrm{stat}) \pm 0.07(\mathrm{sys})$ (68% confidence assuming Gaussian cosmic variance) at a fixed matter density $\Omega_\mathrm{m} = 0.3$ for a $\Lambda$CDM cosmology marginalising over the uncertainty of the Hubble parameter and the redshift distribution. We interpret this exceptionally low estimate to be due to a local under-density of the foreground structures in the CDFS.

This chapter is organised as follows: After describing the data and data reduction in Sect. 6.1, we present our analysis of the ACS PSF and the correction scheme in Sect. 6.2. Next we elaborate on the galaxy selection and determined redshift distribution (Sect. 6.3), and compute several estimators for the shear and systematics in Sect. 6.4. After presenting the results of the cosmological re-analysis of the GEMS and GOODS data in Sect. 6.5, we conclude in Sect. 6.6.

## 6.1 Data

In this pilot project we use pure parallel ACS/WFC F775W observations from HST proposal 9480 (PI J. Rhodes), denoted as the "parallel data" for the rest of this chapter.

For comparison we also apply our data reduction and analysis pipeline to the combined F606W ACS/WFC observations of the GEMS field (Rix et al. 2004) and the GOODS observations of the *Chandra* Deep Field South (CDFS, Giavalisco et al. 2004). A cosmic shear analysis of this $\sim 28' \times 28'$ mosaic has already been presented by Heymans et al. (2005) (H05 henceforth), allowing us to compare the different correction schemes applied.

Both datasets were taken within the first operational year of ACS (August 2002 to March 2003 for the parallel data; July 2002 to February 2003 for the GEMS and GOODS observations). Therefore these data enable us to test the feasibility of cosmic shear measurements with ACS at an early stage, when the charge-transfer-efficiency (CTE) had degraded only slightly (Riess & Mack 2004; Riess 2004; Mutchler & Sirianni 2005).

### 6.1.1 The ACS parallel data

The data analysed consist of 860 WFC exposures, which we associate to fields by joining exposures dithered by less than a quarter of the field-of-view observed with the guiding mode `FINE_LOCK`. In order to permit cosmic ray rejection we only process associations containing at least two exposures. Furthermore, in this pilot study we only combine exposures observed within one visit and with the same role-angle in order to achieve maximal stability of the observing conditions. With these limitations, which are similar to those used by Pirzkal et al. (2001) for the STIS Parallel Survey, we identify 208 associated fields (including re-observations of the same field at different epochs), combining 835 exposures.

For a weak lensing analysis, accurate guiding stability is desired in order to minimise variations of the PSF. In case of parallel observations, differential velocity aberration between the primary and secondary instrument can lead to additional drifts during observations with the secondary instrument (Cox 1997). In order to verify the guiding stability for each exposure we determine the size of the telemetry jitter-ball, which describes the deviation of the pointing from the nominal position. While the jitter-balls typically have shapes of moderately elliptical ($\langle b/a \rangle = 0.68$) distributions with $\langle \mathrm{FHWM} \rangle = 9.8$ mas (0.196 WFC pixel), we have verified that FHWM $< 20$ mas (0.4 WFC pixel) and $b/a > 0.4$ for all selected exposures. Therefore the tracking accuracy is sufficiently good and expected to affect the image PSF only slightly. Any residual impact on the PSF will be compensated by our PSF correction scheme, which explicitly allows for an additional ellipticity contribution due to jitter (see Sect. 6.2.4).

#### 6.1.1.1 Data reduction

For this pilot study we used the Mark-I reduction detailed in Sect. 5.2. When refining shifts for the star and galaxy fields selected for the analysis (see Sect. 6.1.1.2), we find a median "delta" shift relative to the first exposure of an association of 0.17 WFC pixels, with 7.3% of the exposures requiring shifts larger than 0.5 WFC pixels. Refinements of rotations were in most

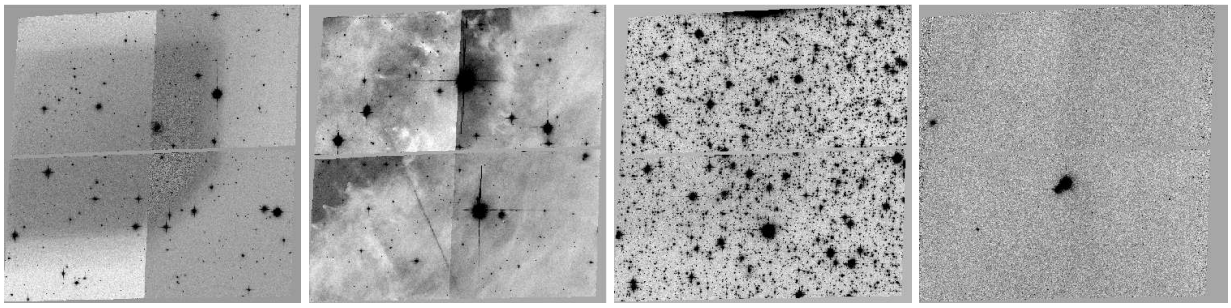

Figure 6.1: Examples for fields which were rejected by visual inspection for the following reasons (panels *left* to *right*): erroneous calibration, galactic nebula, many saturated stars, almost empty field.

cases negligible with a median of $1.6 \times 10^{-4}$ degrees corresponding to a displacement of $\simeq 0.008$ WFC pixels near the edges of the FOV. Only in 1.5% of the exposures rotation refinements exceeded $3 \times 10^{-3}$ degrees, corresponding to displacements of $\simeq 0.15$ WFC pixels.

#### 6.1.1.2 Field selection

The 208 associations were all visually inspected. We discard in total 31 fields for the following reasons:

- Fields which show a strong variation of the background in the pre-processed exposures (4 fields).
- Fields containing galactic nebulae (10 fields).
- Fields of significantly poorer image quality (6 fields).
- Fields which contain a high number of saturated stars with extended diffraction spikes (5 fields).
- Fields in M31 and M33 with a very high number density of stars, resulting in a strong crowding of the field, which makes them even unsuitable for star fields (4 fields).
- Almost empty galactic fields affected by strong extinction (2 fields).

Examples of the discarded fields are shown in Fig. 6.1.

After this pre-selection, fields fulfilling the following criteria are selected as galaxy fields for the cosmic shear analysis:

- Fields have to be located at galactic latitudes $|b| \geq 25^\circ$ in order to be affected only weakly by galactic extinction.
- Only fields co-added from at least three individual exposures are used, facilitating sufficiently good cosmic ray rejection.

Table 6.1: Observation dates and position angles (`ORIENTAT`) of the ACS/WFC F606W GOODS/CDFS observations.

| Epoch | Observation dates | Position angle |
|---|---|---|
| 1 | 2002-07-31–2002-08-04 | $-112^\circ$ |
| 2 | 2002-09-19–2002-09-22 | $-67^\circ$ |
| 3 | 2002-10-31–2002-11-03 | $-22^\circ$ |
| 4 | 2002-12-19–2002-12-22 | $23^\circ$ |
| 5 | 2003-02-01–2003-02-05 | $68^\circ$ |

- Fields are required not to be dominated by a single object or stars resolved in a local group galaxy.
- In the case of re-observations of the same field at different visits, the observation with the longest exposure time is used.

55 independent fields fulfil these selection criteria. Additionally four fields with $20^\circ < |b| < 25^\circ$ are included, which contain a high number density of galaxies indicating rather low extinction, making a total of 59 galaxy fields. This corresponds to 28.4% of the fields and 36.2% of the co-added exposures.

All fields passing the preselection and containing at least 300 stars are used as star fields for the PSF analysis (see Sect. 6.2). These 61 fields consisting of 205 exposures amount to 29.3% of the fields and 24.5% of the co-added exposures.

### 6.1.2 The GEMS+GOODS data

The GEMS F606W data consist of 63 ACS/WFC tiles imaged with three exposures of 720 to 762 seconds each. They are arranged around the ACS GOODS/CDFS observations, which have been imaged in five epochs with different position angles (see Tab. 6.1) consisting of two exposures per tile and epoch with 480 to 520 seconds per exposure.

In total the ACS GOODS/CDFS field is covered with 15 tiles during epochs 1, 3, and 5, whereas 16 tiles were used for epochs 2 and 4. H05 limit their analysis to the epoch 1 data. In order to reach a similar depth for the used GOODS and GEMS data we decided to combine the data of epoch 1 with either epoch 3 or 5 as they have an optimal overlap. The combination of epoch 1 and epoch 5 exposures is unproblematic. In contrast we find significant, FOV dependent residual shifts between matched object positions in exposures from epochs 1 and 3 after applying refined image shifts and rotations (Fig. 6.2). Possible interpretations for these remaining shifts are slight medium-term temporal changes in the ACS geometric distortion or a slightly imperfect treatment of the distortion correction in the `MultiDrizzle` version used. Pirzkal et al. (2005) report similar effects for two epochs of *Hubble* Ultra Deep Field (UDF) data. As remaining shifts also occur for UDF images observed with position angles that are $\sim 90^\circ$ apart, the `MultiDrizzle` interpretation might be more plausible. The largest residual shifts have a comparable magnitude

of $\sim 0.5$ pixels for both the GOODS and UDF data. A combination of exposures with remaining shifts would in any case degrade the PSF of the combined image. Additionally central pixels of some stellar images could falsely be flagged as cosmic rays by `MultiDrizzle`. Therefore we only use the combined epoch 1 and 5 exposures for the cosmic shear analysis that follows.

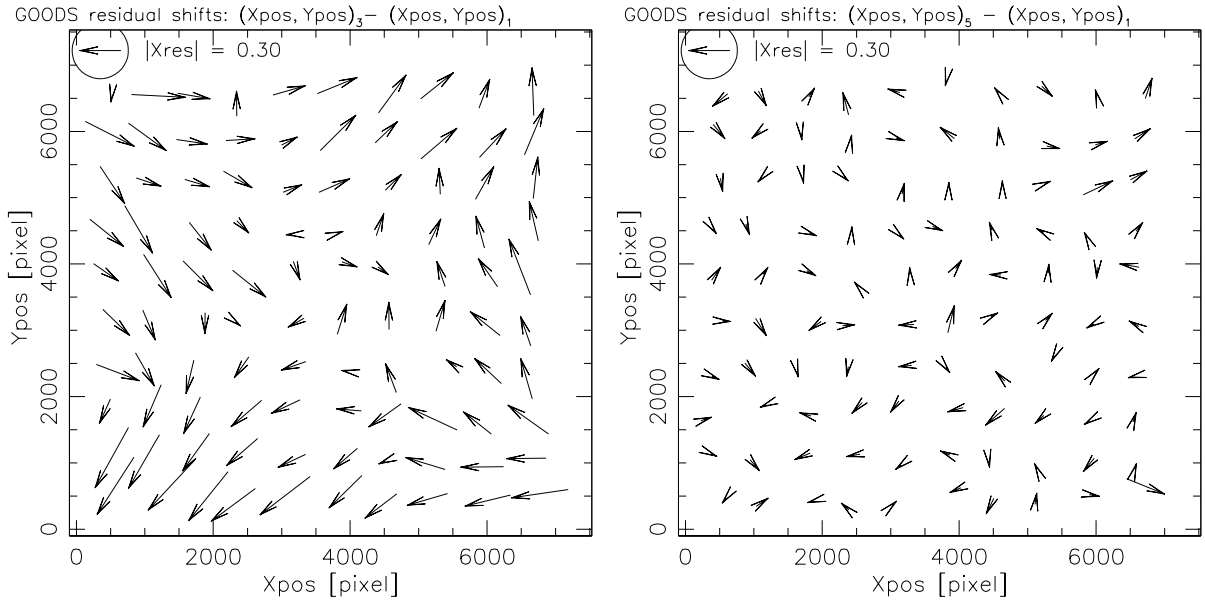


Figure 6.2: Residual shifts [pixel] computed from windowed SExtractor positions of compact sources between epochs 3 and 1 (*left*) and between epoch 5 and 1 (*right*) of the F606W ACS GOODS/CDFS observations. For these plots compact objects from all 15 tiles are used, and residual shifts are averaged in bins of $700^2$ pixels. For each tile the exposures of each epoch were drizzled onto one output pixel grid, with a common WCS per tile defined by epoch 1. Possible interpretations for the residual shifts in the left panel are slight temporal changes in the ACS geometric distortion or a slightly imperfect treatment of the distortion correction in the `MultiDrizzle` version used.

In order to investigate the ACS F606W PSF, we additionally analysed 184 archival F606W exposures of dense stellar fields containing at least 300 stars, which were observed between July 2002 and July 2003.

### 6.1.3 Catalogue creation

We use `SExtractor` (Bertin & Arnouts 1996) for the detection of objects and the Erben et al. (2001) implementation of the KSB formalism for shape measurements. The pipeline version is the same as the one used for the original STEP2 analysis (Sect. 4.3), i.e. we apply a shear calibration factor $c_{\rm cal} = 1/0.91$ and uniform weights $w_i = 1$.

We analyse the images of galaxies in the combined drizzled images. However, for the time-dependent PSF correction described in Sect. 6.2.4, we additionally perform stellar shape mea-

Table 6.2: Relevant parameters for the object detection with `SExtractor` for the galaxy fields and the star fields. Note that the number of pixels for a detection `DETECT_MINAREA` corresponds to the sub-pixel of the drizzled images except for the values in brackets, which are used for object detection in the un-drizzled *COR*-images.

| **Parameter** | **Galaxy fields** | **Star fields** |
|---|---|---|
| `BACK_TYPE` | AUTO | MANUAL |
| `BACK_SIZE` | 100 | – |
| `BACK_FILTERSIZE` | 5 | – |
| `BACK_VALUE` | – | 0.0 |
| `DETECT_MINAREA` | 16 | 16 (5) |
| `DETECT_THRESH` | 1.5 | 3 (4) |
| `DEBLEND_NTHRESH` | 16 | 32 |
| `DEBLEND_MINCONT` | 0.05 | 0.1 |
| `FILTER_NAME` | gauss_2.5_5x5 (gauss_2.0_3x3) | |

surements in the un-drizzled but cosmic ray-cleaned *COR*-images, which are also created by `MultiDrizzle`, and the drizzled un-combined frames (*DRZ*-images).

The `SExtractor` object detection and deblending parameters are summarised in Table 6.2. We use a rather low detection threshold for the galaxies in order to minimise the impact of PSF-based selection bias (Kaiser 2000; Bernstein & Jarvis 2002). Spurious detections are later rejected with cuts in the signal-to-noise ratio. We find that the deblending parameters applied perform well except for the case of spiral galaxies extended by several arcseconds, for which substructure components are in some cases detected as separate objects. Thus, we mask these galaxies manually. If more than one object is detected within $1\farcs2$, only the brighter component is kept. We furthermore reject galaxies containing pixels with low values in the `MultiDrizzle` weight image ($w_{\rm min} = 100\,{\rm s}$)[1] within their `SExtractor` isophotal area and also semi-automatically create masks to reject bright stars with diffraction spikes and extended image artifacts like ghost-images.

We use different detection parameters for the star fields (see Table 6.2). Due to the increased detection threshold `DETECT_THRESH`, the object detection becomes less sensitive to the faint and extended stellar diffraction spikes, reducing the time needed for masking.

We use the `SExtractor` `FLUX_RADIUS` parameter as Gaussian filter scale $r_{\rm g}$ for the shape measurements of the galaxies. Here the integration is carried out to a radius of $3r_{\rm g}$ from the centroid. This truncation was introduced to speed up the algorithm and is justified due to the strong down-weighting of the outer regions in KSB. We also verified from the data that it does not bias the shape measurement. For the stellar *DRZ*-images we repeat the shape measurements for 18 different filter scales ranging from 2.0 to 15 pixels, which are later matched to the filter scales of the galaxies. For larger filter scales we find that it is essential to continue the integration

[1]The weight image pixel value corresponds to the effective exposure time contributing for the pixel, scaled with the relative area of output and input pixels.

out to sufficiently large radii due to the wide diffraction wings of the PSF. Therefore, we employ a stellar integration limit of $4.5 \times$ `FLUX_RADIUS`$^* \simeq 9$ pixels. For the stellar shape measurements in the *COR*-images we use a fixed Gaussian filter scale $r_g = 1.5$ WFC pixels, which according to our testing roughly maximises the signal-to-noise of the stellar ellipticity measurement for most of the occurring PSF anisotropy patterns (see Sect. 6.2).

For object selection we use the signal-to-noise definition given in (3.93). In the computation of S/N we do not take the correlation of noise in adjacent pixels into account, which is created by drizzling. However, Casertano et al. (2000) estimate a correction for the noise in a large area (e.g. the extent of a galaxy), given by their Eq. A19

$$\frac{\sigma_N}{\sigma_1} = m\frac{p}{s}\left[1 - \frac{p}{3ms}\right]\left[1 - \frac{s}{3p}\right]^{-1} , \tag{6.1}$$

where $\sigma_1 = \sigma_{\rm sky}$ is the single pixel background dispersion, while $\sigma_N$ denotes the dispersion computed from areas of size $N = m^2$ (drizzled) pixels. The variables $p$ and $s$ denote the drizzle parameters `pix_frac` and `scale`, both given in input pixels. Inserting the applied values $p = 1.0$ and $s = 0.6$ yields

$$\frac{\sigma_N}{\sigma_1} = m\left[\frac{25}{12}\left(1 - \frac{5}{9m}\right)\right] . \tag{6.2}$$

The expression in squared brackets gives the correction factor to the area scaling expected for uncorrelated noise. Using the effective area of the Gaussian weight function $A = 2\pi r_g^2$ and $m = \sqrt{A}$ we estimate a noise correction factor which increases from 1.86 for unresolved sources ($r_g \simeq 2.1$ pixels) to 2.05 for the largest galaxies considered. For $m \to \infty$ (6.2) yields a correction factor of 2.08. The true S/N will be lower than the directly computed value by this factor. The cuts applied to the data refer to the directly computed value.

## 6.2 PSF analysis and correction

Due to the low number of stars ($\sim 10 - 30$) present in galaxy fields at high galactic latitudes we examined the ACS PSF from stellar fields (see Section 6.1.1.2) containing $\sim 300 - 20000$ stars. We do this analysis on the basis of single exposures instead of combined images, in order to optimally investigate possible temporal PSF variations. We investigate the PSF both in the undrizzled, but cosmic ray cleansed *COR*-images created by `MultiDrizzle`, and also the drizzled and cosmic ray cleansed single exposures (*DRZ*). Here we limit the discussion to the F775W data. Our analysis of the F606W PSF was performed in an identical fashion with only minor differences in the resulting PSF models. A detailed KSB+ analysis of the F606W PSF can be found in H05.

### 6.2.1 Star selection

In the *DRZ*-images (*COR*-images) we select stars with 0.6 pixel (0.45 WFC pixel) wide cuts in half-light radius $r_{\rm h}$ (Erben et al. 2001) and cuts in the signal-to-noise ratio S/N > 40 (S/N > 30).

We furthermore reject stars with saturated pixels using magnitude cuts, and, in the case of crowed fields, stars with a neighbour closer than 20 (10) pixels, which would otherwise affect the shape measurements for large $r_g$.

### 6.2.2 PSF anisotropy variation

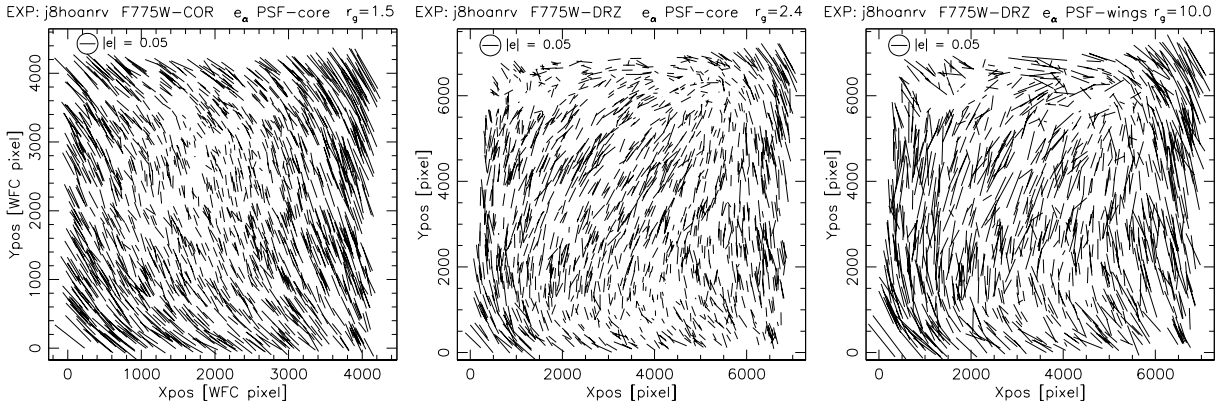


Figure 6.3: Stellar "whisker plots" for an example F775W stellar field exposure. Each whisker represents a stellar ellipticity. The *left* panel shows $e^*_\alpha$ in the un-drizzled *COR*-image measured with $r_g$ = 1.5 WFC pixels (PSF core). The *middle* and *right* panels correspond to the drizzled *DRZ*-image showing the PSF core ($r_g$ = 2.4 pixels, *middle*) and the PSF wings ($r_g$ = 10.0 pixels, *right*). The fit to the ellipticities in the middle panel is shown in the lower right panel of Fig. 6.5.

Investigating stellar fields we find that the stellar ellipticity $e^*_\alpha$ and anisotropy kernel $q^*_\alpha$ vary smoothly across each WFC chip and can well be fit with third-order polynomials. Fig. 6.3 shows the FOV variation of $e^*_\alpha$ for a 400 second stellar field exposure both for the un-drizzled *COR*-image (left panel) and the drizzled and thus distortion corrected *DRZ*-image, where the middle panel corresponds to the PSF core measured with $r_g$ = 2.4 pixels, whereas the right panel shows the PSF wings ($r_g$ = 10.0 pixels). The observed differences between the PSF core and wings, which mainly constitute in a stronger ellipticity for larger $r_g$, underline the importance to measure stellar quantities as a function of filter scale $r_g$ (see also Hoekstra et al. 1998; H05).

In Fig. 6.4 we compare the stellar ellipticity distribution in the *COR*-image and the *DRZ*-image for similar Gaussian filter scales of $r_g$ = 1.5 WFC pixels and $r_g$ = 2.4 pixels, both uncorrected and after the subtraction of a third-order polynomial model for each chip. Here drizzling with the `SQUARE` kernel increases the corrected ellipticity dispersion $\sigma(e_1^{\rm ani*})$ by $\simeq$ 24% and thus decreases the accuracy of the ellipticity estimate. For the galaxy fields we therefore determine the PSF model from the un-drizzled *COR*-images (see Sect. 6.2.4). Note that the stellar ellipticities in the *COR*-images (left panels in Fig. 6.3 and 6.4) are created by the combined image PSF and geometric camera distortion, whereas the *DRZ*-image ellipticities correspond to pure image PSF. However, since the resulting pattern can in both cases well be fit with third-order polynomials, the corrected ellipticity dispersions are directly comparable.

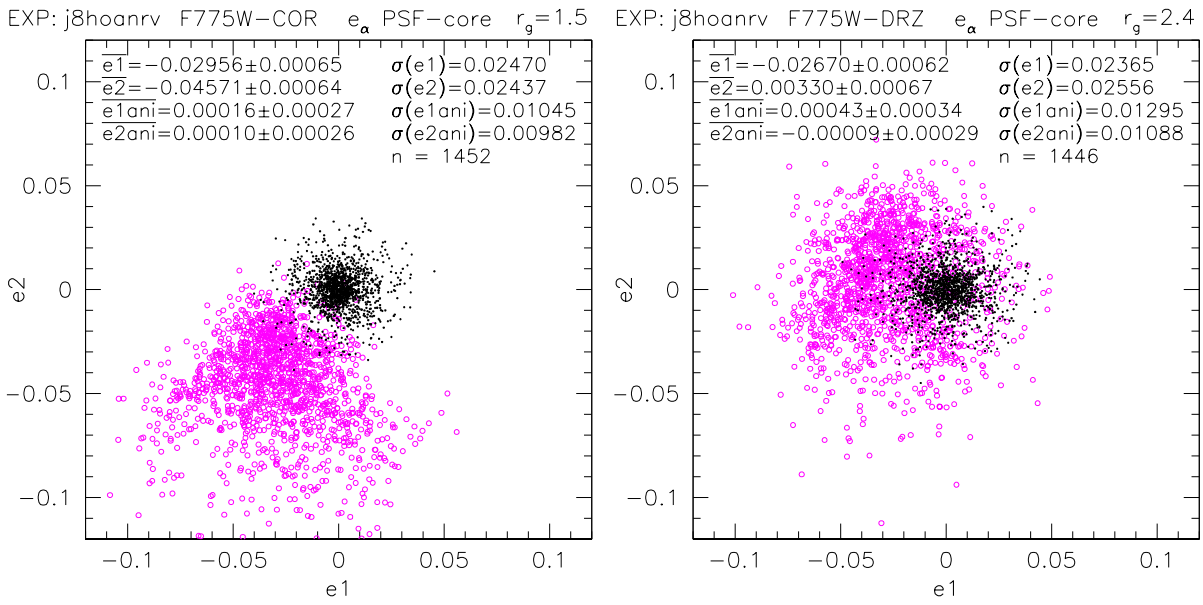


Figure 6.4: Stellar ellipticity distribution (PSF core) for an example F775W stellar field exposure measured in the un-drizzled *COR*-image (*left*) and the drizzled *DRZ*-image (*right*). The open circles represent the uncorrected ellipticities $e^*_\alpha$, whereas the black points show the ellipticities $e^{\mathrm{ani}*}_\alpha$ corrected with a third-order polynomial for each chip. In the right panel $\sigma(e^{\mathrm{ani}*}_1)$ is significantly increased, which is a result of the re-sampling in the drizzle algorithm. In these plots outliers have been rejected at the $3\sigma$ level.

Note that we always plot the FOV variation in terms of $e^*_\alpha$ in order to simplify the comparison to other publications. However, for the actual correction scheme we employ fits of $q^*_\alpha$ defined in (3.88) due to a slight PSF width variation leading to a variation of $P^{\mathrm{sm}*}_{\alpha\beta}$ (see Sect. 6.2.3).

Comparing stellar field exposures observed at different epochs, we detect significant temporal variations of the PSF anisotropy already within one orbit. Time variations of the ACS PSF were also reported by Krist (2003); Jee et al. (2005a,b, 2006); H05; Rhodes et al. (2005, 2007) and Anderson & King (2006), and are expected to be caused by focus changes due to thermal breathing of the telescope. Krist (2003) illustrates the variation of PSF ellipticity induced by astigmatism, which increases for larger focus offsets and changes orientation by 90° when passing from negative to positive offsets. This behaviour is approximately reproduced in Fig. 6.5 showing polynomial fits to stellar ellipticities in two series of subsequent exposures.

### 6.2.3 PSF width variation

Additional to the PSF ellipticity variation we also detect time and FOV variations of the PSF width. Fig. 6.6 shows the FOV dependence of the stellar half-light radius $r_\mathrm{h}$ for three different exposures. Among all F775W stellar field exposures the average half-light radius varied between $1.89 \leq \overline{r_\mathrm{h}} \leq 2.07$, with an average FOV variation $\overline{\sigma(r_\mathrm{h})} = 0.085$. We find that the variation of the stellar quantity $T^*$ needed for the PSF correction of the galaxy ellipticities (3.96) closely follows

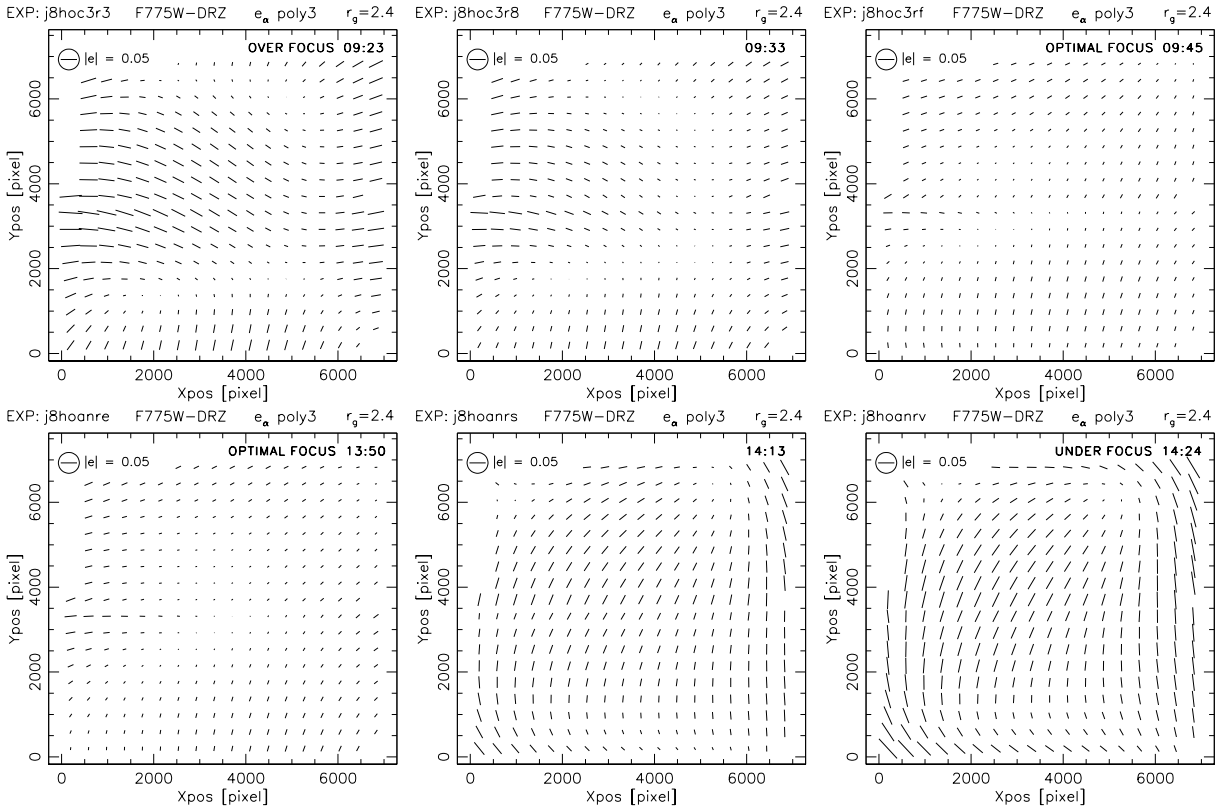


Figure 6.5: Third-order polynomial fits to stellar ellipticities in the *DRZ*-images of two series of subsequent exposures. The 400 second exposures were taken on 2002-08-28 (*upper* panels) and 2002-08-17 (*lower* panels), where the time indicated corresponds to the middle of the exposure (UT). The variations are interpreted as thermal breathing of the telescope. The *upper right* and *lower left* plots are near the optimal focus position, whereas the other exposures represent positive focus offsets (*upper left* panel) or negative focus offsets (*lower right* panel).

the variation of $r_h$ and can well be fitted with fifth-order polynomials in each chip. For a further discussion of the PSF width variation see Krist (2003).

### 6.2.4 PSF correction scheme

In order to correct for the detected temporal PSF variations using the low number of stars present in most galaxy fields (see Fig. 6.7), we apply a new correction scheme, in which we determine the best-fitting stellar field PSF model for each galaxy field exposure separately.

#### 6.2.4.1 Description of the algorithm

Due to the low number of stars present in galaxy fields, we require a PSF fitting method with as few free parameters as possible, excluding the possibility to use for example a direct polynomial interpolation. As the main PSF determining factor is the focus position, we expect a nearly

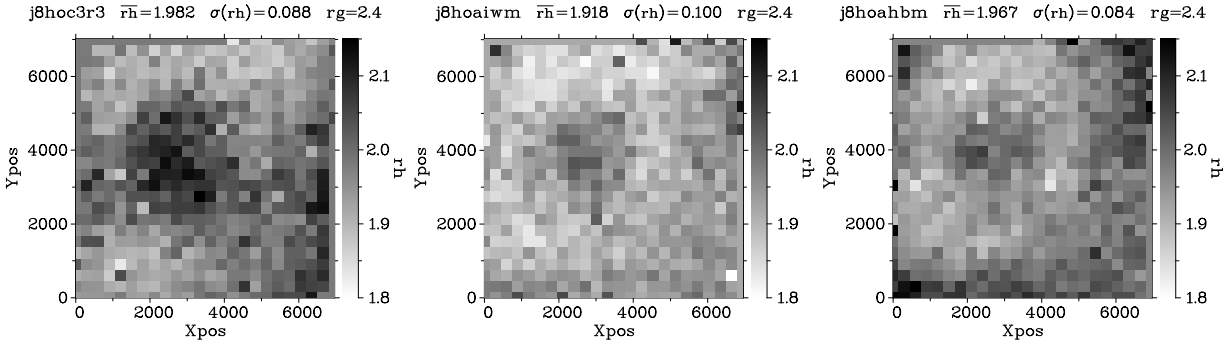


Figure 6.6: Field-of-view variation of the stellar half-light radius $r_\mathrm{h}$ in the *DRZ*-images of three F775W stellar field exposures with positive focus offset (*left*), near optimal focus (*middle*) and negative focus offset (*right*). For these plots $r_\mathrm{h}$ was averaged within bins of $300 \times 300$ pixels. Bins without any stars show the average value.

1-parameter family of PSF patterns. With the high number of stellar field exposures analysed $N_\mathrm{sf} = 205$ for F775W and $N_\mathrm{sf} = 184$ for F606W, we have a nearly continuous database of the varying PSF patterns. This database consists of well-constrained third- or fifth-order polynomial fits to $q_\alpha(x, y, r_\mathrm{g})$ and $T(x, y, r_\mathrm{g})$ for numerous values of $r_\mathrm{g}$, both for the *COR*- and *DRZ*-images. In this section we omit the asterisk when we refer to these polynomial fits derived from the stellar fields in order to allow for a clear distinction to $q^*_\alpha$ measured from the stars in the galaxy fields.

Given the noisier $e^*_\alpha$ and $q^*_\alpha$ measurement in drizzled images (see Sect. 6.2.2), we estimate the PSF correction for a galaxy field from the stellar images in each *COR*-exposure of the galaxy field. However, we apply the corresponding *DRZ*-image PSF model as galaxy shapes are also measured on the drizzled co-added image.

In order to determine the correction for a co-added galaxy field, we fit the measured $q^{*,\mathrm{COR}}_\alpha(r_\mathrm{g} = 1.5)$ of the $N_{\mathrm{stars},k}$ stars present in galaxy field exposure $k$ with the stellar field PSF models $q^{\mathrm{COR}}_{\alpha,j}(x, y, r_\mathrm{g})$, with $j \in 1, ..., N_\mathrm{sf}$ and identify the best fitting stellar field exposure $j_k$ with minimal

$$\chi^2_{k,j} = \sum_{i=1}^{N_{\mathrm{stars},k}} \left[ q^{*,\mathrm{COR}}_{\alpha,i}(r_\mathrm{g} = 1.5) - q^{\mathrm{COR}}_{\alpha,j}(x_i, y_i, 1.5) \right]^2 . \tag{6.3}$$

Here we choose the Gaussian window scale $r_\mathrm{g} = 1.5$ WFC pixels to maximise the signal-to-noise in the shape measurement (see Sect. 6.1.3). In this fit we reject outliers at the $2.5\sigma$ level to ensure that stars in the galaxy field with noisy ellipticity estimates do not dominate the fit.

Having found the "most similar" (best-fitting) *COR*-PSF model $j_k$ for each galaxy field exposure, we next have to match the coordinate systems of the corresponding *DRZ*-image and the co-added galaxy field. This is necessary, as the single *DRZ*-images used to create the PSF models are always drizzled without extra shifts in the default orientation of the camera, whereas the galaxy field exposures are aligned by `MultiDrizzle` according to their dither position. For this we trace the position of each object in the co-added galaxy field back to the position it would

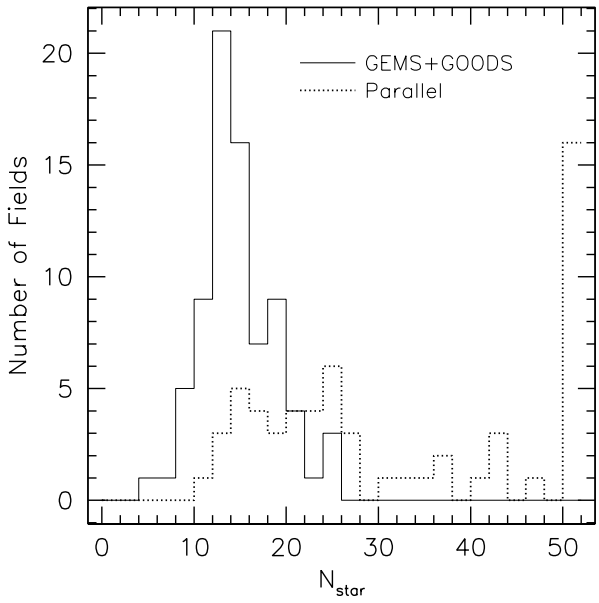


Figure 6.7: Histogram of the number of galaxy fields with $N_{\rm star}$ selected stars in the co-added images for the Parallel Survey (dashed line) and the GEMS+GOODS data (solid line).

have in the single drizzled exposure $k$ without shift and rotation. Let $\phi_k$ and $(x_0, y_0)_k$ denote the rotation and shift applied by `MultiDrizzle` for exposure $k$. For a galaxy with coordinates $(x, y)$ in the co-added image we then compute the "single *DRZ*"-coordinates

$$\begin{pmatrix} \tilde{x} \\ \tilde{y} \end{pmatrix}_k = \begin{pmatrix} \cos\phi_k & \sin\phi_k \\ -\sin\phi_k & \cos\phi_k \end{pmatrix} \begin{pmatrix} x - x_{0,k} \\ y - y_{0,k} \end{pmatrix} \tag{6.4}$$

and the PSF model

$$q_k^{\rm DRZ}(x, y, r_{\rm g}) = q_{j_k}^{\rm DRZ}(\tilde{x}, \tilde{y}, r_{\rm g})\, {\rm e}^{2{\rm i}\phi_k} \tag{6.5}$$

$$T_k^{\rm DRZ}(x, y, r_{\rm g}) = T_{j_k}^{\rm DRZ}(\tilde{x}, \tilde{y}, r_{\rm g})\,, \tag{6.6}$$

where we denote the components of $q_k^{\rm DRZ}$ as $q_{\alpha,k}^{\rm DRZ}$.

In order to estimate the combined PSF model for the co-added galaxy image, we then compute the exposure time $t_k$-weighted average

$$q_{\alpha,{\rm comb}}^{\rm DRZ}(x, y, r_{\rm g}) = \left( \sum_k t_k q_{\alpha,k}^{\rm DRZ}(x, y, r_{\rm g}) \Delta_k \right) / \sum_k t_k \Delta_k \tag{6.7}$$

$$T_{\rm comb}^{\rm DRZ}(x, y, r_{\rm g}) = \left( \sum_k t_k T_k^{\rm DRZ}(x, y, r_{\rm g}) \Delta_k \right) / \sum_k t_k \Delta_k \tag{6.8}$$

of all shifted and rotated single exposure models, with $\Delta_k = 1$ if the galaxy is located within the chip boundaries for exposure $k$ and $\Delta_k = 0$ otherwise.

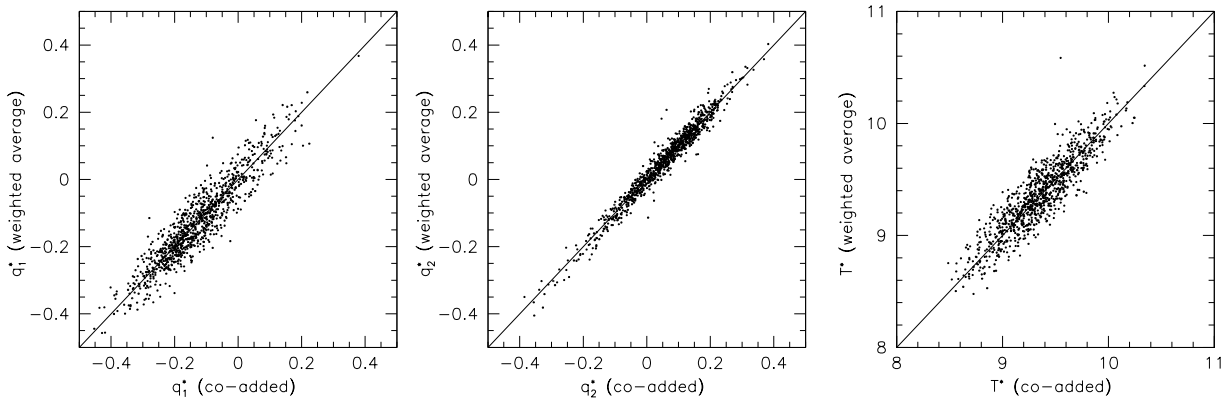


Figure 6.8: Comparison of the stellar quantities $q^*_\alpha$ and $T^*$ measured from a co-added stellar field to the same quantities computed as an exposure time-weighted average of the estimates in the single *DRZ*-images. In both cases a fixed Gaussian filter scale $r_g = 2.4$ pixels was used. The good and unbiased agreement justifies the direct use of these quantities in the PSF correction scheme without the need to work on individual moments. For these plots the three stellar field exposures shown in the bottom of Fig. 6.5 have been used. Note the larger scatter for $q^*_1$ compared to $q^*_2$ which is mainly due to the noise created by re-sampling (compare Sect. 6.2.2).

Another factor which is expected to influence the image PSF besides focus changes are jitter variations created by tracking inaccuracies (Sect. 6.1). To take those into account we fit an additional, position-independent jitter term $q^0_\alpha(r_g)$. We already take this constant into account while fitting the galaxy field stars with the stellar field models to ensure that a large jitter term does not bias the identification of the best-fitting star field. Yet, as the number of stars with sufficient signal-to-noise is higher in the co-added image and since only the combined jitter effect averaged over all exposures is relevant for the analysis, we re-determine the jitter term in the co-added drizzled image after subtraction of the combined PSF model $q^{\rm DRZ}_{\alpha,\rm comb}(x,y,r_g)$. The final PSF model used for the correction of the galaxies is then given by

$$q^{\rm DRZ}_{\alpha,\rm total}(x,y,r_g) = q^{\rm DRZ}_{\alpha,\rm comb}(x,y,r_g) + q^0_\alpha(r_g) \tag{6.9}$$

and $T^{\rm DRZ}_{\rm comb}(x,y,r_g)$.

Note that this correction scheme assumes that the PSF model quantities $q^{\rm DRZ}_{\alpha,k}(x,y,r_g)$ and $T^{\rm DRZ}_k(x,y,r_g)$ determined for each galaxy field exposure can directly be averaged to determine the correction for the co-added image. While only brightness moments add exactly linearly, this computation-simplifying approach is still justified, as both the PSF size variation and the absolute value of the stellar ellipticities are small (see Sections 6.2.2 and 6.2.3). Computing the flux-normalised trace of the stellar second brightness moments

$$\hat{Q} \equiv \frac{Q_{11} + Q_{22}}{\rm FLUX^*} \tag{6.10}$$

for all stars in the F775W stellar field exposures with fixed $r_g = 2.4$ pixels, we find that $\hat{Q}$ has a relative variation of 3% only ($1\sigma$). Therefore we can well neglect non-linear terms induced by the

denominator in (3.85). The same holds for non-linear contributions of $P^{\mathrm{sm}*}$ and $T^*$, which show $1\sigma$-variations of only 6% ($\mathrm{Tr}\,[P^{\mathrm{sm}*}]$) and 5% ($T^*$). As a (very good) first-order approximation we can therefore simply average $q^{\mathrm{DRZ}}_{\alpha,k}(x,y,r_{\mathrm{g}})$ and $T^{\mathrm{DRZ}}_{k}(x,y,r_{\mathrm{g}})$ linearly, as also demonstrated in Fig. 6.8, where we compare the exposure time-weighted average of the quantities measured from stars in individual drizzled frames to the value measured in the co-added image.

#### 6.2.4.2 Test with star fields

In order to estimate the accuracy of our fitting scheme we test it on all co-added stellar field images. For each stellar field we randomly select subsets of $N_{\mathrm{star}}$ stars from the *COR*-images and the co-added image, in order to simulate the low number of stars present in galaxy fields. This subset of stars is used to derive the PSF model as described in Sect. 6.2.4.1 which we then apply to the entirety of stars in the co-added image. For the fitting of a particular stellar field exposure, we ignore its own entry in the PSF model database and only consider the remaining models. The strength of any coherent pattern left in the stellar ellipticities after model subtraction provides an estimate of the method's accuracy. In order to determine the actual impact of the remaining PSF anisotropy on the cosmic shear estimate, one has to consider that although galaxy ellipticities are less affected by PSF anisotropy than stars, they are additionally scaled with the $P^g$ correction (3.89, 3.90). We thus "transform" the remaining stellar ellipticity into a corrected galaxy ellipticity (see e.g. Hoekstra 2004)

$$e^{*,\mathrm{iso}}_{\alpha} = \frac{2c_{\mathrm{cal}}}{\mathrm{Tr}P^{g}_{\mathrm{gal}}}\left[\frac{\mathrm{Tr}P^{\mathrm{sm}}_{\mathrm{gal}}}{\mathrm{Tr}P^{\mathrm{sm}*}(r_{\mathrm{g}})}e^{*}_{\alpha}(r_{\mathrm{g}}) - P^{\mathrm{sm}}_{\alpha\beta,\mathrm{gal}}\,q^{\mathrm{DRZ}}_{\beta,\mathrm{total}}(x,y,r_{\mathrm{g}})\right], \tag{6.11}$$

where we randomly assign to each star the value of $P^g_{\mathrm{gal}}$, $P^{\mathrm{sm}}_{\mathrm{gal}}$, and $r_{\mathrm{g}}$ from one of the parallel data galaxies used for the cosmic shear analysis (see Sect. 6.4). Fig. 6.9 shows the estimate of the two-point correlation functions of $e^{*,\mathrm{iso}}_{\alpha}$ averaged over all star fields and 30 randomisations for different numbers of random stars $N_{\mathrm{star}}$. This plot indicates that already for $N_{\mathrm{star}} = 10$ stars present in a galaxy field the contribution of remaining PSF anisotropy is expected to be reduced to a level $\langle e^{*,\mathrm{iso}}_{t/\times} e^{*,\mathrm{iso}}_{t/\times}\rangle < 2\times10^{-6}$ corresponding to $\simeq 1-5\%$ of the cosmological shear correlation function expected on scales probed by a single ACS field. Since all of the examined parallel fields and the large majority of the GEMS+GOODS fields contain more than 10 stars (see Fig. 6.7), we are confident that the systematic accuracy of this fitting technique will be sufficient also for the complete ACS parallel data.

The further reduction of the remaining systematic signal for larger $N_{\mathrm{star}}$ shows that the accuracy is mainly limited by the number of available stars and not by a too narrow coverage of our PSF database or the linear averaging of $q^{\mathrm{DRZ}}_{\alpha,k}(x,y,r_{\mathrm{g}})$.

For comparison we also plot in Fig. 6.9 the correlation functions calculated from the $P^g$-scaled, but *not* anisotropy corrected stellar ellipticity, which for larger scales is of the same order of magnitude as the expected shear signal. Note that the plotted values depend on the selection criteria for the galaxies (see Sect. 6.3.1). Particularly, the inclusion of smaller, less resolved galaxies would increase both the corrected and uncorrected signal. Additionally, it is assumed that the distribution of PSFs occurring is the same for the star and galaxy fields. For

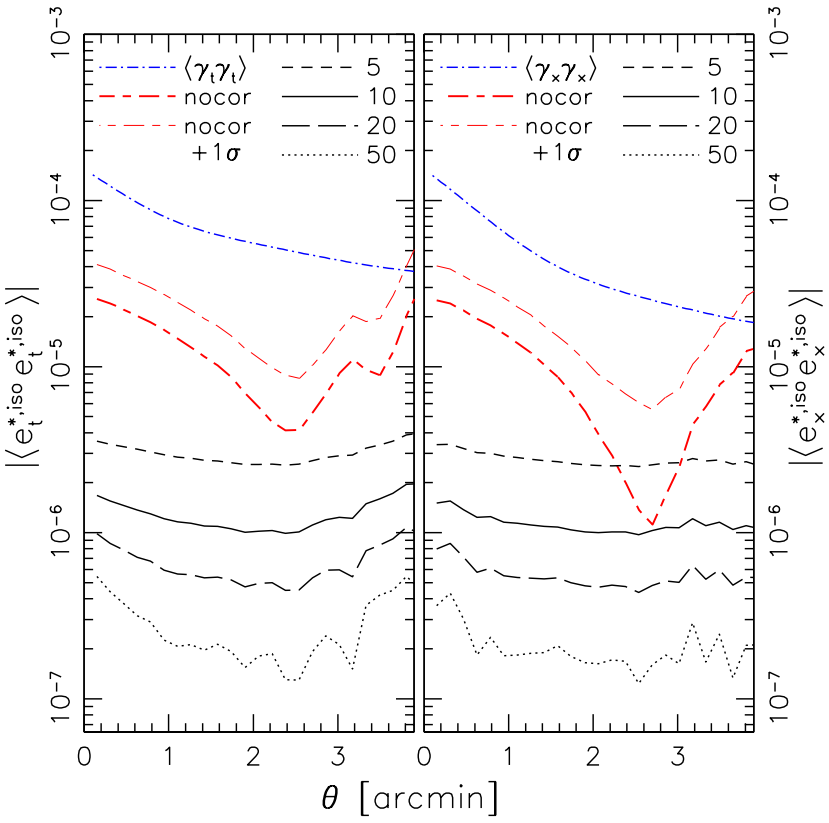


Figure 6.9: Estimate for the PSF fitting accuracy: In order to simulate the low number of stars in galaxy fields, the PSF correction technique was applied to the 61 parallel data star fields, from which only small random subsets of $N_{\rm star}$ stars were used to determine the fit. We plot the correlation functions $\langle e_{\rm t}^{*,{\rm iso}} e_{\rm t}^{*,{\rm iso}}\rangle$ (*left*) and $\langle e_\times^{*,{\rm iso}} e_\times^{*,{\rm iso}}\rangle$ (*right*) of the "transformed" and corrected stellar ellipticity $e_\alpha^{*,{\rm iso}}$ (6.11), which accounts for the different susceptibility of stars and galaxies to PSF effects. The numbers $N_{\rm star} = (5, 10, 20, 50)$ indicate the number of random stars used in each subset. Note that the uncorrected PSF signal computed from the transformed but *not* anisotropy corrected ellipticity (nocor) and its $1\sigma$ upper limit (nocor+$1\sigma$) are only slightly lower than $\Lambda$CDM predictions for the cosmological lensing signal shown by the dashed-dotted curves for $\sigma_8 = 0.7$, $z_{\rm m} = 1.34$.

more homogeneous surveys (e.g. the GEMS+GOODS data) one might expect that more similar PSFs occur more frequently than for the quasi random parallel star fields, for which the stellar correlation function is expected to partially cancel out. Thus, we also plot the one sigma upper limit of the uncorrected correlation function in Fig. 6.9, which might be a more realistic estimate for the uncorrected systematic signal for such surveys.

#### 6.2.4.3 Discussion of the algorithm

The applicability of the proposed algorithm relies on the assumption that the stellar fields densely cover the parameter space of PSF patterns occurring in the galaxy fields. This is likely to be the case if

1. both datasets roughly cover the same time span,
2. the number of star field exposures is sufficiently large,
3. and no significant additional random component occurs besides the constant jitter offset that we have considered.

For both the F606W and F775W data (1.) is fulfilled and from the ensemble of observed stellar field PSFs we are confident that (2.) and (3.) are also well satisfied. This is also confirmed by the test presented in Sect. 6.2.4.2. Yet, the reader should note that datasets might exist for which conditions (1.) to (3.) are not well fulfilled, e.g. due to observations in a rarely used filter with only a low number of observed stellar fields. In such a case the algorithm described might be adjusted using a principal component analysis (Jarvis & Jain 2004, see also Sect. 7.7) or theoretical PSF models (Rhodes et al. 2005, 2007). Note that the differences in the observed PSFs are interpreted to be mainly driven by different focus offsets. However, the suggested algorithm will work just as well if further factors play a role, as long as sufficient stellar field exposures are available.

#### 6.2.4.4 Advantages of our PSF correction scheme

Finally we want to summarise the advantages our method provides for the high demands of a cosmological weak lensing analysis on accurate PSF correction:

1. Our technique deals very well with the low number of stars present in typical high galactic latitude fields, which inhibits direct interpolation across the field-of-view.
2. The ACS PSF shows substantial variation already between consecutive exposures (see Fig. 6.5), which is adequately taken into account in our technique. When exposures from different focus positions are combined, a single-focus PSF model, as e.g. used by Rhodes et al. (2007), is no longer guaranteed to be a good description for the co-added image.
3. Our PSF models are based on actually observed stellar fields and are thus not affected by possible limitations of a theoretical PSF model.
4. We determine the PSF fits in the un-drizzled *COR*-images, which excludes any impact from additional shape noise introduced by re-sampling.
5. The algorithm is applicable for arbitrary dither patterns and rotations, and can easily be adapted for other weak lensing techniques (e.g. Nakajima et al. in prep.).

#### 6.2.4.5 Comparison to independent correction schemes

H05 use a PSF correction scheme, in which they combine the stars within each of the two GEMS observation epochs. Although this approach is expected to correct for longer term trends in the average focus position, it does not take short-term PSF variations into account. Hence, it is likely that some residual PSF residuals are present in their analysis. Although the tests for systematics presented by H05 indicate zero contamination for the GEMS data, remaining systematics are indeed measured at small scales if the GOODS data are included.

Rhodes et al. (2005, 2007) propose a correction scheme, in which they fit co-added frames with theoretical single-focus PSF models created with a modified version of `TinyTim`[2]. Although this approach will probably yield a better time-dependent correction than the H05 method, it also fails to capture inter-exposure variations. Also there are residual discrepancies between their `TinyTim`-model and actual stars in the COSMOS field (Fig. 6.10). The discrepancies are neither symmetric between the two chips, nor vanish at the top or bottom of the field, as would be expected for CTE effects. Hence, they cannot be mainly explained by CTE degradation as argued by the authors.

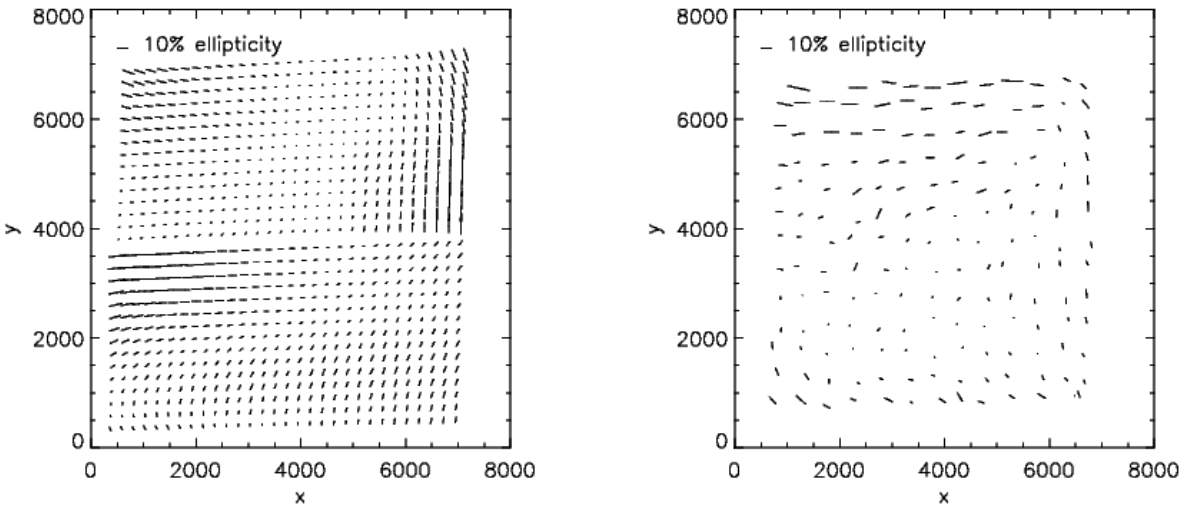


Figure 6.10: Rhodes et al. (2007) `TinyTim` PSF model (*left*) for a focus value of $-2\mu$m and the average of many observed stars (*right*) from COSMOS fields with a similar estimated focus value. The discrepancies are neither symmetric between the two chips, nor vanish at the top or bottom of the field. Hence, they cannot be mainly explained by CTE degradation (Fig. 8 from Rhodes et al. 2007).

[2] `http://www.stsci.edu/software/tinytim/tinytim.html`

## 6.3 Galaxy catalogue and redshift distribution

### 6.3.1 Galaxy selection

We select galaxies with cuts in the signal-to-noise ratio S/N > 4, half-light radius $2.8 < r_h < 15$ pixels, corrected galaxy ellipticity $|e^{iso}| < 2.0$, and $\mathrm{Tr}P^g/2 > 0.1$. From the analysis of the STEP1 image simulations (Heymans et al. 2006b) we find no indications for a significant bias in the shear estimate introduced by these conservative cuts for $|e^{iso}|$ and $\mathrm{Tr}P^g$. However, due to a detected correlation of the shear estimate both with $r_h$ and the `SExtractor FLUX_RADIUS`, cuts in the latter quantities may introduce a significant selection bias. For the analysis of the STEP2 image simulations we therefore chose $r_h$-cuts closely above the stellar sequence (Massey et al. 2007a). Yet, as the magnitude-size relation is very different for ground- and space-based images, we

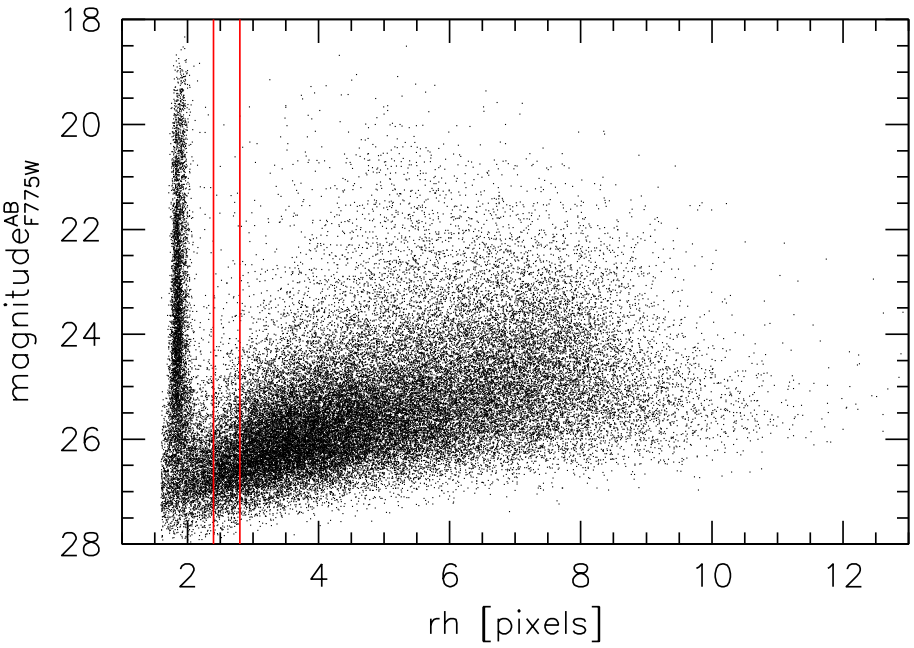


Figure 6.11: $r_h$–magnitude distribution of the Parallel data F775W objects after applying a cut S/N > 4. The vertical lines indicate two different cuts for the galaxy selection: Although a cut $r_h > 2.4$ pixels is sufficient to reliably exclude stars, we additionally reject very small galaxies (2.4 pixels $< r_h <$ 2.8 pixels), which are most strongly affected by the PSF.

expect that a cut at larger $r_h$ will introduce a smaller shear selection bias for space-based images. In Fig. 6.11 we plot the $r_h$–magnitude distribution of the objects in the F775W galaxy fields after a cut S/N > 4 was applied. Considering the PSF size variation (Sect. 6.2.3) and increased noise in the $r_h$ measurement for faint objects, stars can reliably be rejected with a cut $r_h \gtrsim 2.4$ pixels. With the cuts in $|e^{iso}|$, and $\mathrm{Tr}P^g$ applied, increasing the size cut to $r_h > 2.8$ pixels rejects only 6.1% of the remaining galaxies. As these galaxies are most affected by the PSF, and considering the possible limitations for the application of the KSB formalism for a diffraction limited PSF (Sect. 3.4.2), we decided to use the more resolved galaxies with $r_h > 2.8$ pixels. At the time

the Schrabback et al. (2007) paper was submitted, it was still unclear if this conservative cut might introduce significant selection bias, as it was the case for STEP1. However, the recent STEP3 results indicate that no significant selection bias should be introduced by the cut in $r_\mathrm{h}$ (Sect. 4.4.5).

In total we select 39898 (77749) galaxies corresponding to an average galaxy number density of 63 arcmin$^{-2}$ (96 arcmin$^{-2}$) for the parallel F775W fields (GEMS+GOODS F606W tiles) with a corrected ellipticity dispersion $\sigma(c_\mathrm{cal} e_\alpha^\mathrm{iso}) = 0.32$ (0.33) for each component.

H05 found that the faintest galaxies in their catalogue were very noisy, diluting the shear signal. Therefore they use a conservative rejection of faint galaxies ($m_{606} < 27.0$, significance $\nu > 15$) leading to a lower galaxy number density of $\sim$ 60 arcmin$^{-2}$ for the GEMS and GOODS F606W data. For our primary analysis we use a rather low cut S/N > 4 (see above). In order to assess the impact of the faintest galaxies and ease the comparison to H05, we repeat the cosmological parameter estimation in Sect. 6.5 with more conservative cuts S/N > 5, $m_{606} < 27.0$ leading to a number density of 72 arcmin$^{-2}$, which is roughly comparable to the value found by H05 given the deeper combined GOODS images in our analysis. Note that the primary cut S/N > 4, corresponding to S/N$^\mathrm{true} \gtrsim 2$ if (6.2) is taken into account, is in fact relatively low given the recent results from the STEP2 and STEP3 simulations. Therefore, the more conservative cut should yield more reliable results, which however was not yet clear at the time the cosmic shear paper was finalized.

We plot the average galaxy number density as a function of exposure time for the different datasets in Fig. 6.12, indicating that F606W is more efficient than F775W in terms of the average galaxy number density. However one should keep in mind that the parallel fields are subject to varying extinction, sky background, and less homogeneous data quality.

For the GEMS+GOODS tiles we rotate the galaxy ellipticities to a common coordinate system and reject double detections in overlapping regions which leaves 71682 galaxies for S/N > 4 and 53447 galaxies for S/N > 5, $m_{606} < 27.0$.

### 6.3.2 Comparison of shear catalogues

In regions where different GEMS and GOODS tiles overlap, we have two independent shear estimates from the same galaxies with different noise realisations corrected for different PSF patterns. This provides us with a good consistency check for our shear pipeline. We compare the two shear estimates in the left panel of Fig. 6.13. Although there is a large scatter created by the faint galaxies, which are strongly affected by noise, the shear estimates agree very well on average confirming the reliability of the pipeline.

Additionally, we match our shear catalogue to the H05 catalogue, which stems from an independent data reduction and weak lensing pipeline, and compare the two shear estimates in the right panel of Fig. 6.13. Overall there is good agreement between the two pipelines with a slight difference in the shear calibration, where our shear estimate is in average larger by 3.3%. This is also consistent with results of the STEP project given a 3% under-estimation of the shear for the Heymans pipeline in STEP1 (Heymans et al. 2006b) and an error of the average shear calibration consistent with zero for the Schrabback pipeline in STEP2 (Massey et al. 2007a). The slightly different results for the two KSB+ pipelines are likely to be caused by the shear calibration factor

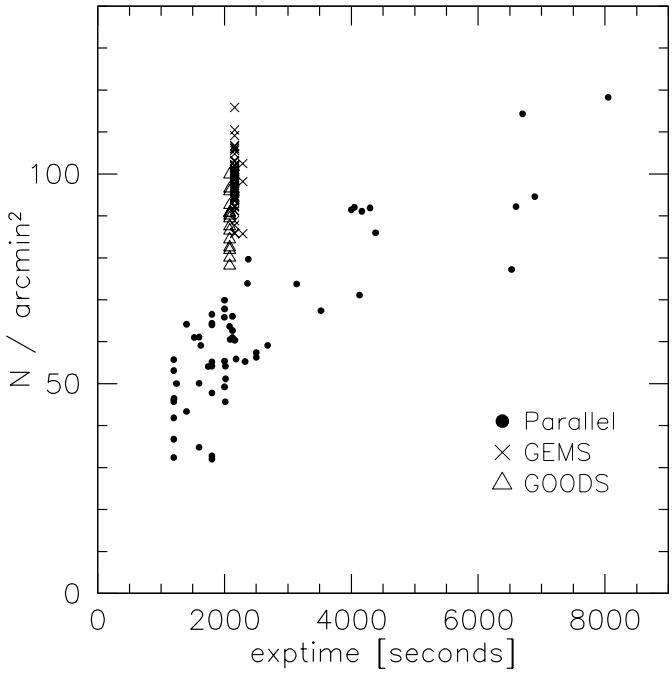


Figure 6.12: Number density of selected galaxies (S/N > 4) for the parallel data F775W fields and the GEMS/GOODS F606W tiles as a function of exposure time.

used in our pipeline and the different treatment of measuring shapes from pixelised data, where we interpolate across pixels while H05 evaluate the integrals at the pixel centres. See Sect. 4.2.6 for a further comparison of the two KSB+ pipelines. For the GEMS and GOODS data a shear calibration error of $\sim 3\%$ is well within the statistical noise.

### 6.3.3 Redshift distribution

In order to estimate cosmological parameters from cosmic shear data, accurate knowledge of the source redshift distribution is required. This is of particular concern if the redshift distribution is constrained from external fields (see e.g. van Waerbeke et al. 2006; Huterer et al. 2006). However, as the *Chandra* Deep Field South has been observed with several instruments including infrared observations, accurate photometric redshifts can directly be obtained for a significant fraction of the galaxies without the need for external calibration. In this work we use the photometric redshift catalogue of the GOODS-MUSIC sample presented by Grazian et al. (2006). This catalogue combines the F435W, F606W, F775W, and F850LP ACS GOODS/CDFS images (Giavalisco et al. 2004), the *JHK*s VLT data (Vandame et al. in prep.), the Spitzer data provided by the IRAC instrument at 3.6, 4.5, 5.8, and 8.0 $\mu$m (Dickinson et al. in prep.), and *U*–band data from the MPG/ESO 2.2m and VLT-VIMOS. Additionally the GOODS-MUSIC catalogue contains spectroscopic data from several surveys (Cristiani et al. 2000; Croom et al. 2001; Wolf et al. 2001; Bunker et al. 2003; Dickinson et al. 2004; Le Fèvre et al. 2004; Szokoly et al. 2004; Stanway et al. 2004; Strolger et al. 2004; van der Wel et al. 2004; Mignoli et al. 2005; Vanzella et al.

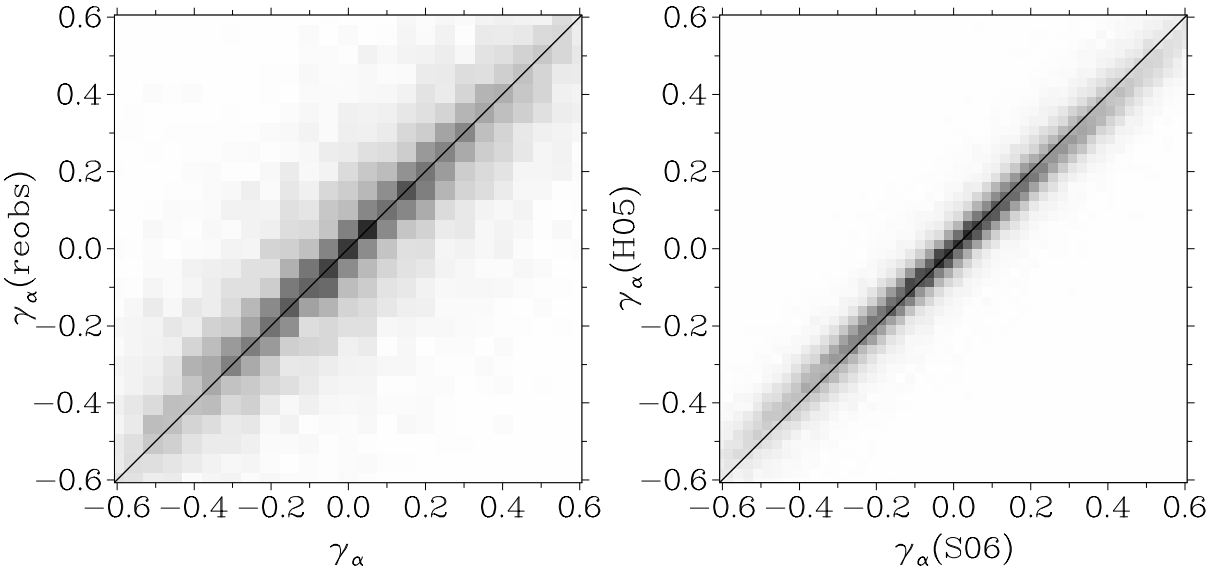


Figure 6.13: Comparison of the shear estimates between overlapping ACS tiles (*left*) and between the H05 and our catalogue (*right*). The grey-scale indicates the number of galaxies. Note the slight difference in the shear calibration between the two pipelines ($\sim$ 3.3%). In the *left* panel galaxies from different noise realisations are compared, leading to the larger scatter. The solid line shows a 1:1 relation.

2005), which are also compiled in a Master[3] catalogue by the ESO-GOODS team. We match the GOODS-MUSIC catalogue to our filtered galaxy shear catalogue, yielding in total 8469 galaxies with a photometric redshift estimate, including 408 galaxies with additional spectroscopic redshifts and a redshift quality flag $qz \leq 2$. In the area covered by the GOODS-MUSIC catalogue 95.0% of the galaxies in our shear catalogue with $m_{606} < 26.25$ have a redshift estimate, and only for fainter magnitudes substantial redshift incompleteness occurs (Fig. 6.14). Grazian et al. (2006) estimate the photometric redshifts errors from the absolute scatter between photometric and spectroscopic redshifts to be $\langle|\Delta z/(1+z)|\rangle = 0.045$.

In cosmic shear studies the redshift distribution is often parametrised as

$$p(z) = \frac{\beta}{z_0 \Gamma\left(\frac{1+\alpha}{\beta}\right)} \left(\frac{z}{z_0}\right)^\alpha \exp\left[-\left(\frac{z}{z_0}\right)^\beta\right] \tag{6.12}$$

(e.g. Brainerd et al. 1996; Semboloni et al. 2006; Hoekstra et al. 2006). In order to extrapolate the redshift distribution for the faint galaxies with redshift-incomplete magnitudes we consider $p(z) = p(z, m_{606})$ and assume a linear relation between the magnitude $m_{606}$ and the median redshift $z_\mathrm{m}$ of an ensemble of galaxies with this magnitude

$$z_\mathrm{m} = r z_0 = a(m_{606} - 22) + b\,, \tag{6.13}$$

where $r(\alpha,\beta)$ is calculated from numerical integration of (6.12). For a single galaxy of magnitude $m_{606}$, (6.12) corresponds to the redshift probability distribution given the parameter set

[3] `http://www.eso.org/science/goods/spectroscopy/CDFS_Mastercat/`

$(\alpha, \beta, a, b)$. Thus, we can constrain these parameters via a maximum likelihood analysis, for which we marginalise over the photometric redshift errors $\Delta z$. The total redshift distribution of the survey with $N$ galaxies is then constructed as

$$\phi(z) = \frac{\sum_{i=1}^{i=N} p(z, m_{606}(i))}{N} . \tag{6.14}$$

Note that this approach is similar to the one used by H05, but does not require magnitude or redshift binning.

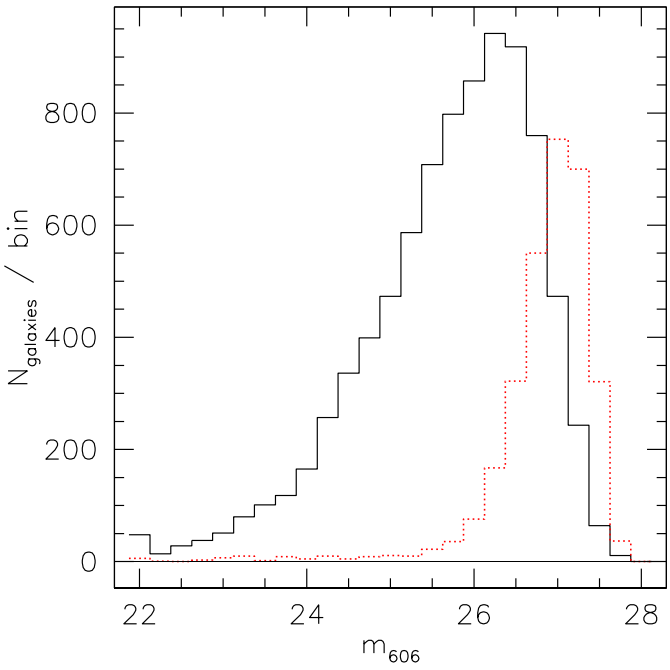


Figure 6.14: Number of selected GOODS-CDFS galaxies as a function of $m_{606}$. The solid line corresponds to galaxies for which spectroscopic or photometric redshift are available from the GOODS-MUSIC sample (Grazian et al. 2006), whereas the dotted line shows galaxies in the shear catalogue without redshift estimate located in the same area.

For the maximum likelihood analysis we apply the CERN Program Library `MINUIT`[4] and use all galaxies with redshift estimates in the magnitude range $21.75 < m_{606} < 26.25$. Varying all four parameters $(\alpha, \beta, a, b)$ we find the best fitting parameter combination $(\alpha, \beta, a, b) = (0.563, 1.716, 0.299, 0.310)$, for which $z_m = 0.7477 z_0$. In order to estimate the fit accuracy, we fix $\alpha$ and $\beta$ to the best fitting values and identify the 68% (95%) confidence intervals for $a$ and $b$: $a = 0.299^{+0.006(0.013)}_{-0.007(0.014)}$, $b = 0.310^{+0.018(0.037)}_{-0.017(0.033)}$.

Using these parameter estimates, we reconstruct the redshift distribution of the galaxies used for the fitting (Fig. 6.15). The reconstruction fits the actual redshift distribution very well except for a prominent galaxy over-density at $z \simeq 0.7$ and an under-density at $z \gtrsim 1.5$, which are known

[4] `http://wwwasdoc.web.cern.ch/wwwasdoc/minuit/`

large-scale structure features of the field (Gilli et al. 2003, 2005; Szokoly et al. 2004; Le Fèvre et al. 2004; Adami et al. 2005; Vanzella et al. 2006; Grazian et al. 2006). Yet, given that the reconstruction and the photometric redshift distribution have almost identical average redshifts $\langle z_{\rm recon}(\text{fit sample})\rangle = 1.39$, $\langle z_{\rm photo}(\text{fit sample})\rangle = 1.41$, we estimate that the impact of the large-scale structure on the cosmic shear estimate via the source redshift distribution will be small. Also, we find that $P_\kappa(\ell)$ computed for the two distributions differs by $< 1\%$ for $200 < \ell < 10000$ assuming a flat WMAP-3 ΛCDM cosmology. However, the large-scale structure significantly influences the estimate of the median redshift $z_{\rm m,recon}(\text{fit sample}) = 1.23$, $z_{\rm m,photo}(\text{fit sample}) = 1.10$. Thus, a redshift distribution determined from the computed median redshift of the galaxies would most likely be biased to too low redshifts. Note that in Fig. 6.15 the reconstruction falls off slower for high $z$ than the actual distribution of the data. To exclude a possible bias we thus always truncate the high redshift tail for $z > 4.5$.

For comparison we also determine a reconstruction from the best fitting values for $(a, b)$ with fixed values $(\alpha, \beta) = (2, 1.5)$, which are sometimes used in the literature (e.g. Baugh & Efstathiou 1994; H05). While they seem to provide a good parametrisation for shallower surveys (see e.g. Brown et al. 2003), they lead to a distribution that is too narrowly peaked with a maximum at too high redshifts for the deep GEMS and GOODS data (Fig. 6.15).

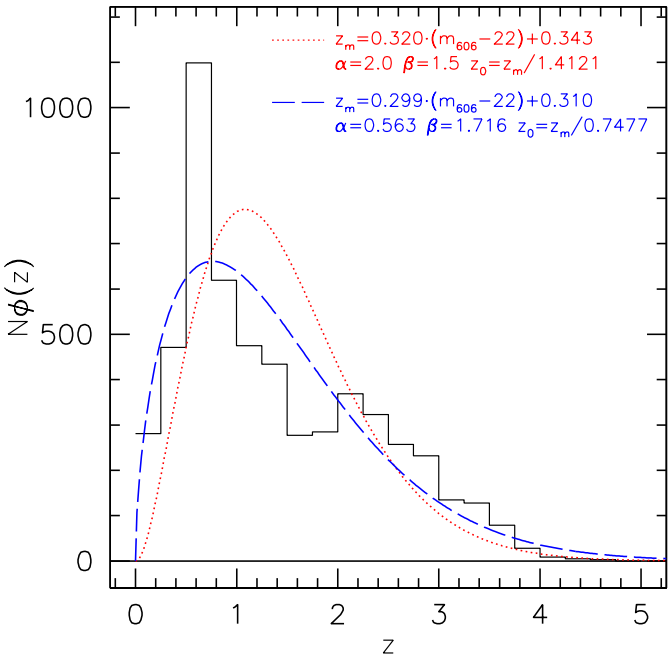


Figure 6.15: Redshift distribution for the matched shear catalogue galaxies with redshift estimate from the GOODS-MUSIC sample in the magnitude range $21.75 < m_{606} < 26.25$ (solid line histogram). The dashed curve shows the reconstructed redshift distribution $N\phi(z)$ for these galaxies using the best fitting values for $(\alpha, \beta, a, b) = (0.563, 1.716, 0.299, 0.310)$. The dotted curve was computed for fixed $(\alpha, \beta) = (2, 1.5)$.

A maximum likelihood analysis can only yield reasonable parameter constraints if the model

is a good description of the data. To test our assumption of a linear behaviour in (6.13), we bin the matched galaxies in redshift magnitude bins and determine a single $z_m$ for each bin using an additional likelihood fit with fixed $(\alpha, \beta) = (0.563, 1.716)$, see Fig. 6.16. A linear $z_m(m_{606})$ description is indeed in excellent agreement with the data in the magnitude range used for the joint fit. Only at the bright end the large-scale structure peak at $z \simeq 0.7$ induces an increased scatter. However, the likelihood fit is much less affected by large-scale structure than the directly computed median redshift, which in contrast under-estimates the slope of the $z_m(m_{606})$ relation for $z_m \lesssim 24.7$ (see Fig. 6.16). This is the reason why H05, who use the median redshift computed from spectroscopic data in the magnitude range $21.8 < m_{606} < 24.4$, derive a significantly flatter $z_m(m_{606})$ relation

$$z_m^{H05} = -3.132 + 0.164\, m_{606} \quad (21.8 < m_{606} < 24.4) \tag{6.15}$$

leading to an estimate of $z_m = 1.0 \pm 0.1$ for their shear catalogue.

In order to verify the applicability of (6.13) for our fainter shear galaxies, we also plot $z_m(m_{606})$ in Fig. 6.16 computed from photometric redshifts for the HUDF (Coe et al. 2006), finding a very good agreement.

Using the parameters $(\alpha, \beta, a, b)$ we construct the redshift distribution for all GEMS and GOODS galaxies in our shear catalogue from (6.14). The resulting redshift distribution has a median redshift $z_m(\text{GEMS + GOODS}) = 1.46 \pm 0.02(0.05)$, where the statistical errors stem from the uncertainty of $a$ and $b$. Systematic uncertainties might arise from applying (6.13) for galaxies up to 1.5 magnitudes fainter than the magnitude range used to determine the fit. Additionally, the photometric redshift errors used in the maximum likelihood analysis do not take catastrophic outliers or systematic biases into account, but see Grazian et al. (2006) for a comparison to the spectroscopic subsample. Furthermore the impact of the large-scale structure on the source redshift distribution will be slightly different for the whole GEMS field compared to the GOODS region. We estimate the resulting systematic uncertainty as $\Delta z \simeq 0.1$, yielding $z_m(\text{GEMS + GOODS}) = 1.46 \pm 0.02(0.05) \pm 0.10$. The constructed redshift distribution is well fit with a magnitude independent distribution (6.12) with $(\alpha, \beta, z_0) = (0.537, 1.454, 1.832)$.

Given that we derive the redshift parametrisation from the matched GOODS-MUSIC galaxies in the magnitude range $21.75 < m_{606} < 26.25$, while a low level of redshift incompleteness already occurs for $m_{606} \gtrsim 25.75$ (see Fig. 6.14), we repeat our analysis as a consistency check using only galaxies with $21.75 < m_{606} < 25.75$ yielding a very similar redshift distribution with $z_m = 1.44$. We thus conclude that the low level of incompleteness does not significantly affect our analysis.

For the brighter galaxies in our shear catalogue with $S/N > 5, m_{606} < 27.0$, the constructed redshift distribution is shallower as expected with $z_m = 1.37 \pm 0.02(0.05) \pm 0.08$. It can well be fit with a magnitude-independent distribution (6.12) with $(\alpha, \beta, z_0) = (0.529, 1.470, 1.717)$. Using our redshift parametrisation we also estimate the median redshift for the H05 shear catalogue yielding $z_m = 1.25 \pm 0.02 \pm 0.08$. Here we estimate slightly lower systematic errors due to the lesser extrapolation to fainter magnitudes.

In Sect. 6.5 we will use our derived redshift distribution to constrain cosmological parameters marginalising over the statistical plus systematic error in $z_m$. Furthermore we will use this redshift distribution when we compare cosmic shear estimates for the GEMS and GOODS data

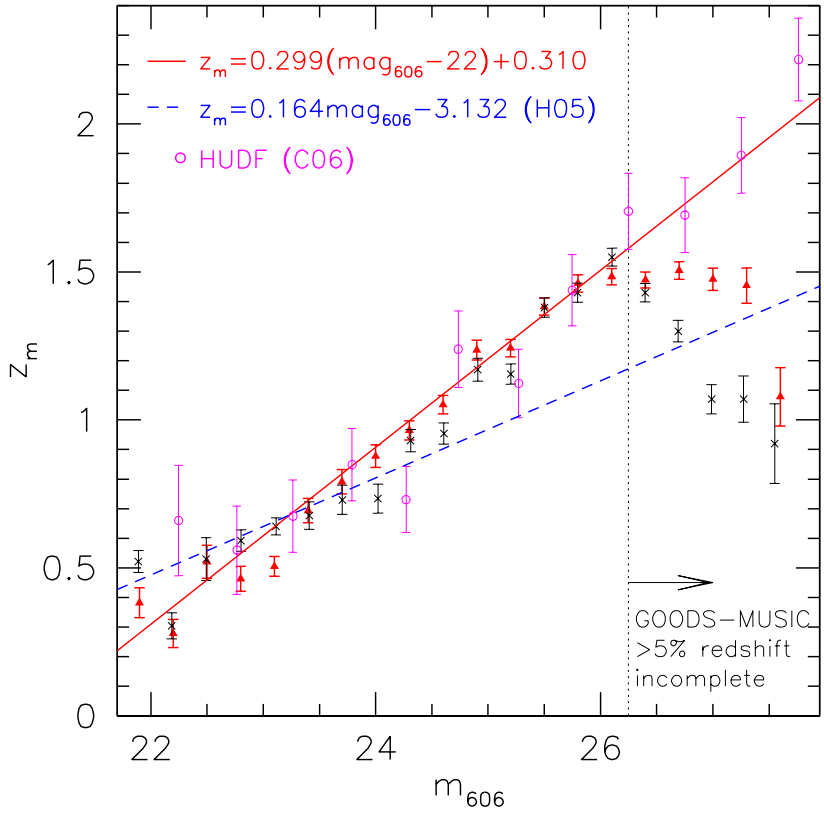


Figure 6.16: Median redshift of the galaxies in the matched shear-photo-$z$ catalogue computed in $m_{606}$ bins. The median has been estimated directly from the data (thin crosses) and determined from a maximum likelihood fit for $z_{\rm m}$ with fixed $(\alpha, \beta) = (0.563, 1.716)$ (triangles), with errors-bars indicating the error of the mean or the $1\sigma$ confidence region, respectively. The solid line corresponds to the best fitting parameters of the joint likelihood fit, whereas the dashed line shows the fit determined by H05 for the magnitude range $21.8 < m_{606} < 24.4$. Note that a large-scale structure peak at $z \simeq 0.7$ induces both the flatter slope for the directly computed $z_{\rm m}$ for $m_{606} \lesssim 24.7$ and the increased spread for the fitted points for $m_{606} \lesssim 23.3$. For $m_{606} \gtrsim 26.25$ substantial redshift incompleteness occurs. For comparison we also plot the directly computed median photometric redshift from the HUDF (open circles, Coe et al. 2006).

with theoretical models. The theoretical cosmic shear predictions shown in this chapter are calculated for a flat ΛCDM cosmology according to the three year WMAP-only best-fitting values for $(\Omega_\Lambda, \Omega_m, \Omega_b, h, n_s) = (0.76, 0.24, 0.042, 0.73, 0.95)$ (Spergel et al. 2007) for different power spectrum normalisations $\sigma_8$ calculated using the non-linear correction to the power spectrum from Smith et al. (2003).

At this stage we use the parallel data to test our pipeline and search for remaining systematics, while presenting a cosmological parameter estimation in a future paper based on a larger data set. Given the inhomogeneous depth and data quality of the parallel data, this cosmological parameter estimation will require a thoroughly estimated, field-dependent redshift distribution. For the purpose of comparing the different estimators for shear and systematics to the expected shear signal in the current work, we apply a simplified global redshift distribution estimated from the F775W magnitudes in GOODS-MUSIC catalogue. Similarly to the F606W data we apply our likelihood analysis to all GOODS-MUSIC galaxies with $22.0 < m_{775} < 26.0$ yielding best fitting parameters $(\alpha, \beta, a, b) = (0.723, 1.402, 0.309, 0.395)$, for which $z_m = 0.9395 z_0$. The upper magnitude limit was chosen due to a similar turn-off point of $z_m(m_{775})$ as in Fig. 6.16 indicating redshift incompleteness. To account for the different extinction in the parallel fields and the CDFS ($A_{775}^{CDFS} = 0.017$ mag), we apply an extinction correction based on the maps by Schlegel et al. (1998).

Using the extinction-corrected magnitudes of all F775W galaxies in the parallel data shear catalogue, we construct a redshift distribution with $z_m = 1.34$, which can be fit with a magnitude-independent distribution with $(\alpha, \beta, z_0) = (0.746, 1.163, 1.191)$.

## 6.4 Cosmic shear estimates and tests for systematics

In this section we compute different cosmic shear statistics and perform a number of diagnostic tests to check for the presence of remaining systematics. For the GEMS and GOODS data the plots in this section correspond to the larger galaxy set with S/N > 4 including the faint galaxies which are stronger affected by the PSF.

### 6.4.1 Average galaxy ellipticity

For data uncontaminated by systematics the average galaxy ellipticity is expected to be consistent with zero[5]. Any significant deviation from zero indicates an average alignment of the galaxies relative to the pixel grid. We plot the average corrected but not rotated (see Sect. 6.3.1) galaxy ellipticity $\langle e_\alpha^{iso} \rangle$ for each field in Fig. 6.21. Whereas the global average is essentially consistent with zero for the GEMS and GOODS data ($\langle e_1^{iso} \rangle = -0.0004 \pm 0.0011$, $\langle e_2^{iso} \rangle = 0.0012 \pm 0.0011$), the average $e_1^{iso}$-component is significantly negative for the parallel data ($\langle e_1^{iso} \rangle = -0.0084 \pm 0.0015$, $\langle e_2^{iso} \rangle = 0.0020 \pm 0.0015$) corresponding to an average orientation in the direction of the *y*-axis.

[5]Note that for a single field the average galaxy ellipticity may significantly deviate from zero due to a net mean gravitational shear in the field. For GEMS, however, we combine tiles observed under different role-angles. Thus, we expect that the average corrected but not rotated galaxy ellipticity should vanish with good accuracy.

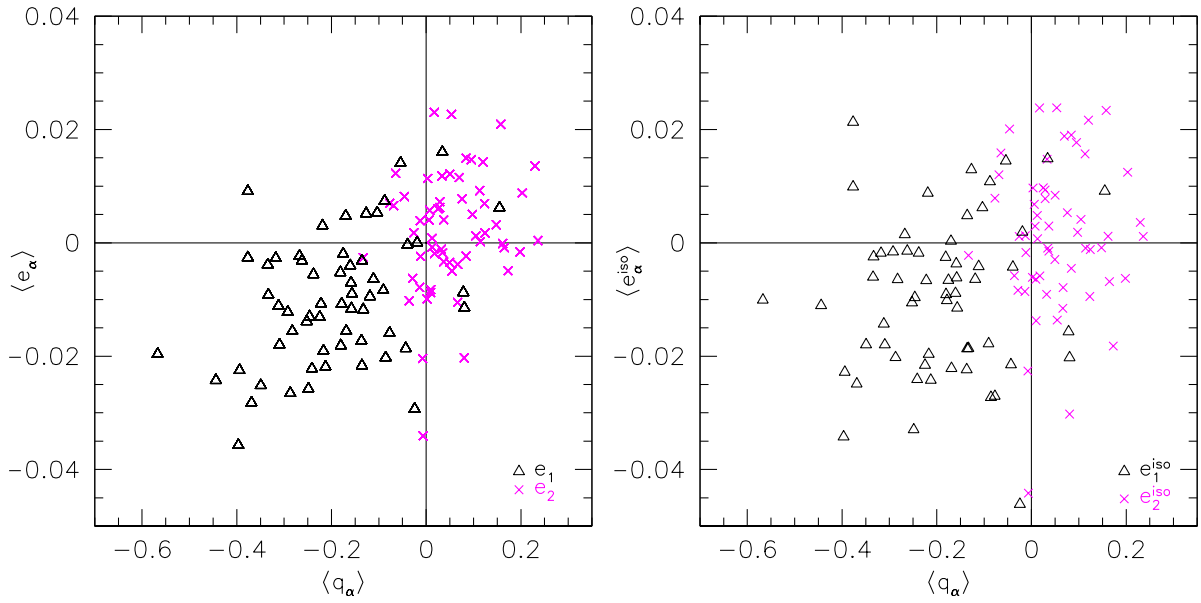


Figure 6.17: Mean galaxy ellipticity before ($\langle e_\alpha \rangle$, *left*) and after ($\langle e_\alpha^{\rm iso} \rangle$, *right*) PSF correction as a function of the mean PSF anisotropy kernel averaged over all galaxies in a field $\langle q_\alpha \rangle$, computed on a *field-by-field* basis for the F775W parallel fields. The lack of a correlation after PSF correction (correlation cor = 0.08) is a clear indication that PSF anisotropy residuals cannot be the origin for the negative average ellipticity $\langle e_1^{\rm iso} \rangle$.

#### 6.4.1.1 Could it be residual PSF contamination?

There are different effects which could in principle cause such an average alignment: For example one could speculate that our PSF fitting technique fails for the parallel data or that our implementation of the KSB+ formalism under-estimates the PSF anisotropy correction, e.g. due to neglected higher-order moments. Yet, the average corrected galaxy ellipticity is consistent with zero for the GEMS and GOODS data, while the average uncorrected ellipticity is significantly non-zero for both datasets (parallel: $\langle e_1 \rangle = -0.0102 \pm 0.0012$, $\langle e_2 \rangle = 0.0028 \pm 0.0012$; GEMS+GOODS: $\langle e_1 \rangle = -0.0090 \pm 0.0009$, $\langle e_2 \rangle = 0.0045 \pm 0.0009$). Therefore this explanation becomes quite implausible, particularly as the average number of stars usable to derive the fit is higher for the parallel data (Fig. 6.7).

To further test whether imperfect PSF correction could be the cause, we plot the mean galaxy ellipticity as a function of the mean PSF anisotropy kernel on a *field-by-field* basis for parallel data in Fig. 6.17. While there is a substantial correlation between $\langle q_\alpha \rangle$ and the mean uncorrected ellipticity $\langle e_\alpha \rangle$ (correlation cor = $\mathrm{cov}[\langle q_\alpha \rangle, \langle e_\alpha \rangle]/(\sigma_{\langle q_\alpha \rangle} \sigma_{\langle e_\alpha \rangle}) = 0.38$), the mean PSF corrected ellipticity $\langle e_\alpha^{\rm iso} \rangle$ is basically uncorrelated with $\langle q_\alpha \rangle$ (cor = 0.08), clearly indicating that imperfect PSF correction is not the culprit here.

We also plot the mean corrected galaxy ellipticity $\langle e_\alpha^{\rm iso} \rangle$ computed in $q_\alpha$-bins in Fig. 6.18. The absence of a correlation both for the GEMS+GOODS data and additionally $\langle e_2^{\rm iso} \rangle$ in the parallel data again confirms the success of the PSF correction. For the parallel data a moderate correlation

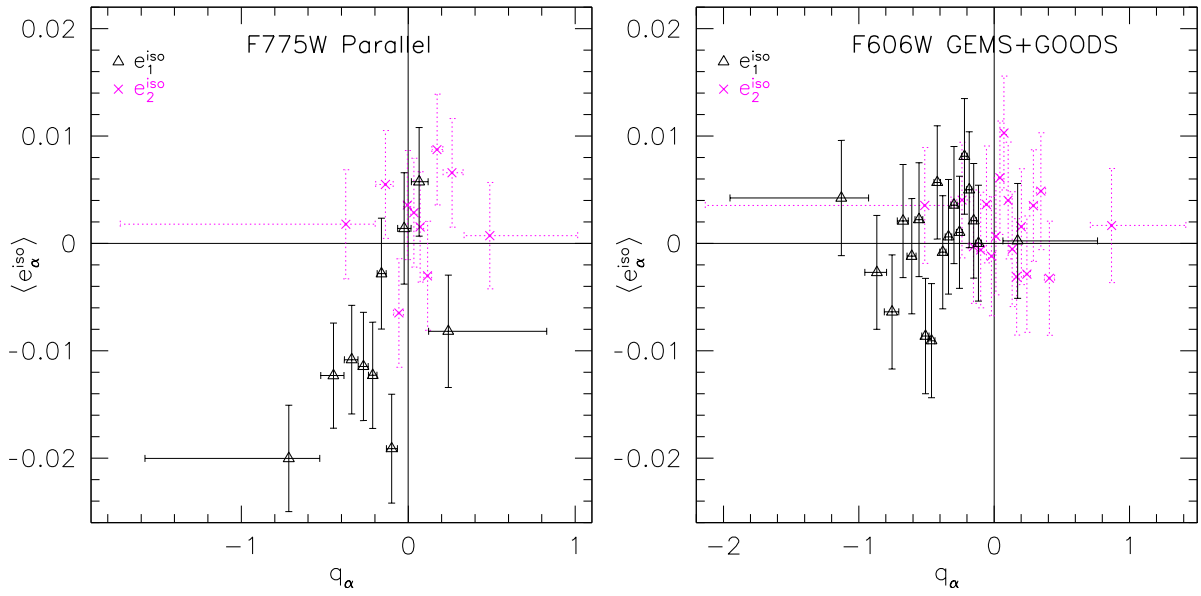


Figure 6.18: Mean PSF-corrected galaxy ellipticity $\langle e_\alpha^{\rm iso} \rangle$ binned as a function of the PSF anisotropy kernel $q_\alpha$ for the parallel data (*left*) and the GEMS+GOODS data (*right*). The binning (indicated by the horizontal error-bars) was chosen such that all bins contain an equal number of galaxies. The lack of a correlation for the GEMS+GOODS data and $\langle e_2^{\rm iso} \rangle$ for the parallel data confirms the success of the PSF correction. The interpretation of the moderate correlation detected for $\langle e_1^{\rm iso} \rangle$ in the parallel data is ambiguous as it can also be caused by a position dependence of $\langle e_1^{\rm iso} \rangle$.

is observed between $\langle e_1^{\rm iso} \rangle$ and $q_1$, which at first sight might be interpreted as an indication for imperfect PSF anisotropy correction. However, it is important to keep in mind that $q_\alpha$ is position dependent. Hence, if a different position dependent effect causes the non-zero $\langle e_1^{\rm iso} \rangle$ it will also mimic a dependence on $q_\alpha$. From Fig. 6.5 we find for example that highly negative values for $q_1$ appear mainly near medial $y$-positions close to the gap between the two chips. Thus, the apparent correlation between $\langle e_1^{\rm iso} \rangle$ and $q_1$ shown in Fig. 6.18 could also be caused by a different effect which acts most strongly near the chip gap, such as CTE degradation (see Sect. 6.4.1.2) or artefacts due to bad columns (see Sect. 6.4.1.3). In this sense the *field-by-field* comparison shown in Fig. 6.17 is a better test for imperfect PSF anisotropy correction, as it is independent of a possible position dependence. Given the fact that this test does not show a significant indication for imperfect PSF anisotropy correction, we conclude that it is most likely not the explanation for the non-zero $\langle e_1^{\rm iso} \rangle$. We investigate the position dependence further in Sect. 6.4.1.2 and compute the star-galaxy cross-correlation as an additional test for PSF anisotropy residuals in Sect. 6.4.3.

### 6.4.1.2 Impact of CTE degradation

Another possible explanation is a degradation of the charge-transfer efficiency (CTE), which can lead to a spurious negative $e_1$ ellipticity component, as described in Sect. 5.1.7.

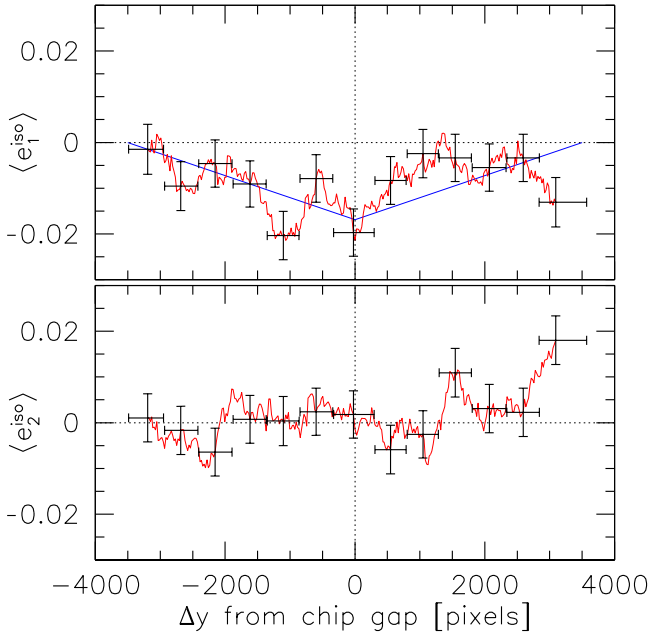


Figure 6.19: Average corrected galaxy ellipticity $\langle e_\alpha^{\rm iso} \rangle$ for the parallel F775W galaxy fields as a function of $\Delta y$, the $y$-position relative to the gap between the two camera chips. The curve shows $\langle e_\alpha^{\rm iso} \rangle(\Delta y)$ box-averaged over 3000 galaxies. For certain $\Delta y$ the error-bars indicate the width of the averaging in $\Delta y$ and the error of the estimate. The straight lines indicate the expected dependence if the negative $\langle e_1^{\rm iso} \rangle$ was purely caused by CTE degradation assuming a linear dependence of the mean ellipticity on the CTE charge loss.

For a uniform distribution of charge traps, the impact of CTE degradation depends linearly on the number of parallel transfers, so that objects located near the gap between the two chips will be affected the most. Mutchler & Sirianni (2005) find no significant difference in the parallel CTE for the two chips, indicating that also any impact on the weak lensing measurement should be symmetric between the two chips. In Fig. 6.19 we plot $\langle e^{\rm iso} \rangle$ as a function of $\Delta y$, the $y$-position relative to the gap between the two camera chips. Although for the lower chip ($\Delta y < 0$) $\langle e^{\rm iso} \rangle(\Delta y)$ roughly agrees with the linear trend expected for a CTE degradation, there are significant deviations for the upper chip ($\Delta y > 0$).

Furthermore the ACS/WFC CTE decreases nearly linearly with time (Riess & Mack 2004; Riess 2004; Mutchler & Sirianni 2005) so that one would also expect a linear decrease of $\langle e_1^{\rm iso} \rangle$ with time, which is not in agreement with the data (Fig. 6.20). In addition, again, the discrepancy does not occur for the GEMS and GOODS data, which were taken nearly in the same time period as the parallel data. We thus conclude that CTE degradation is not the dominant source for the observed negative $\langle e_1^{\rm iso} \rangle$.

As a further test we also split the data shown in Figures 6.19 and 6.20 into a low and a high signal-to-noise subset. Here the observed dependencies are qualitatively unchanged, but at a lower significance, with a slightly larger absolute values of the negative $\langle e_1^{\rm iso} \rangle$ for the fainter sample: $\langle e_1^{\rm iso} \rangle({\rm S/N} < 7.5) = -0.0092 \pm 0.0022$, $\langle e_1^{\rm iso} \rangle({\rm S/N} > 7.5) = -0.0077 \pm 0.0018$. If the effect

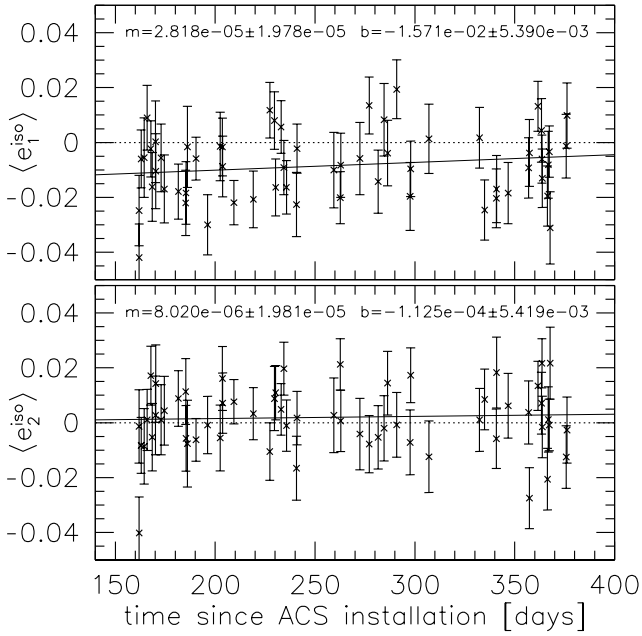


Figure 6.20: Average corrected galaxy ellipticity $\langle e_\alpha^{\rm iso}\rangle$ for the parallel F775W galaxy fields as a function of time since the installation of ACS on March 7, 2002. The solid line shows a linear fit. If the negative $\langle e_1^{\rm iso}\rangle$ would be created by degradation of CTE an increase of the effect with time would be expected, which is not supported by the data.

was caused by CTE, one would probably expect a stronger dependence on the signal-to-noise ratio.

Note that we do detect a signature of CTE degradation in the COSMOS data (Sect. 7.2.5), similarly to Rhodes et al. (2007). This is not in contradiction with the results presented here, as the COSMOS data were taken at later epochs with significantly increased CTE degradation.

#### 6.4.1.3 Impact of dithering

In order to understand the origin of the negative $\langle e_1^{\rm iso}\rangle$ for the F775W parallel data it is helpful to consider the differences between the two surveys, as the problem does not occur for the F606W GEMS and GOODS images. Besides the different filters and more homogeneous depth of the GEMS and GOODS tiles there are only two effects which can significantly affect the image quality: Firstly the F775W fields are taken in parallel in contrast to the F606W data. Although this could have some impact on the image PSF (Sect. 6.1.1), it is taken into account in our PSF correction scheme (Sect. 6.2.4). Secondly the GEMS and GOODS data are well dithered, whereas most of the parallel fields were observed with no or only small dithering as defined by the primary observations. To test the impact on the galaxy shape measurement we split the parallel fields in Fig. 6.21 into three sets according to the maximal shift $\Delta X$ between the exposures in $x-$direction. Indeed $\langle e_1^{\rm iso}\rangle$ is almost consistent with zero for the well-dithered fields with $\Delta X > 10$ pixels (6 WFC pixels), whereas it is significantly negative for the less dithered fields.

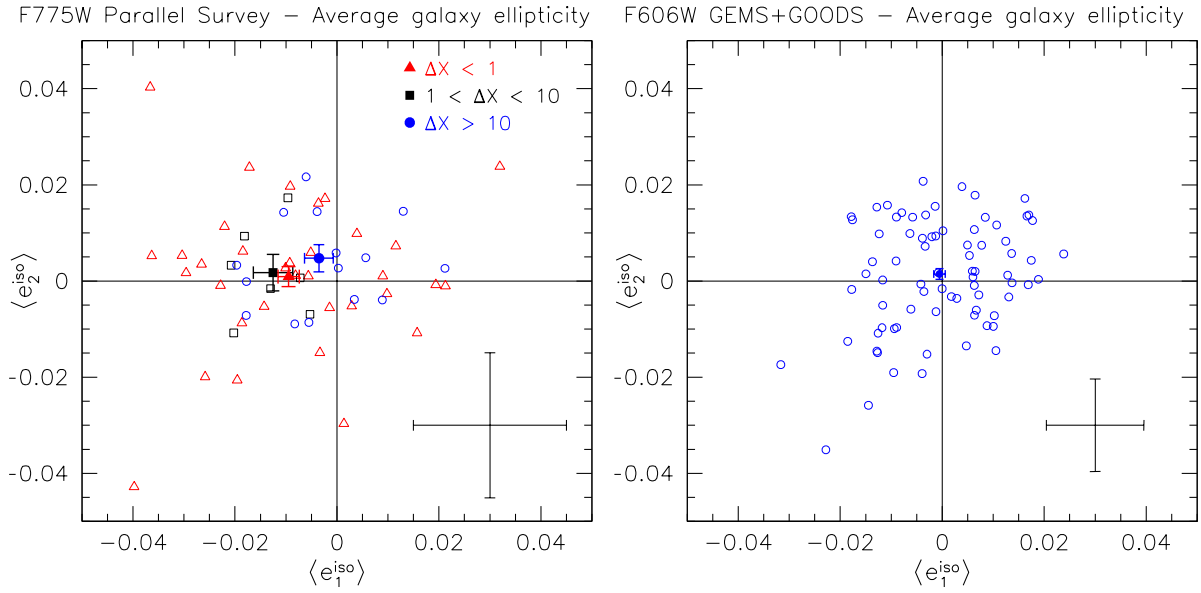


Figure 6.21: Average corrected galaxy ellipticity $e_\alpha^{\rm iso}$ for the parallel data (*left*) and the GEMS+GOODS data (*right*). The open symbols represent single field averages, whereas the bold symbols with error-bars ($1\sigma$) show global averages. The large error-bars in the lower right corner correspond to the average single field $1\sigma$ error, where the GEMS+GOODS error-bar is smaller compared to the parallel data error-bar due to the higher average galaxy number density (Fig. 6.12). The parallel data was split according to the maximal dither between the exposures in the $x-$direction $\Delta X$ [pixels], as the $x-$dithering determines the possibilities to correct for bad columns.

Proper dithering is important to correct for bad or hot pixels, which otherwise create artifacts in the co-added frame. Without dithering, known bad pixels lead to output pixels receiving zero weight, which we set to zero pixel value, while unknown bad pixels such as spontaneously hot pixels or variable bias structures directly contribute with their bad pixel value.

Bad pixels are not completely randomly distributed on the CCD chips, but sometimes occur as bad columns or clusters of bad pixels, which are preferentially aligned in the readout direction and therefore the $y-$direction. Thus, without proper dithering the shapes of faint objects containing bad columns or pixel clusters could possibly be influenced such that a slight average alignment in the $y$-direction is created and a negative $\langle e_1^{\rm iso}\rangle$ is measured. We expect that faint galaxies are more strongly, and due to their size more likely, affected than compact high signal-to-noise stars, which additionally might be rejected as noisy outliers during the PSF fitting, explaining why this effect is not taken into account by the PSF correction.

We try to minimise the impact of known bad pixels by rejecting galaxies containing low weight pixels within their `SExtractor` isophotal area (see Sect. 6.1.3). However, also a bad column located near the edge of a galaxy image might bias the shape estimate without being rejected in this way. Note that bad column segments appear with a higher density near the chip gap, which might qualitatively explain the $\Delta y$ dependence plotted in Fig. 6.19.

Although the comparison shown in Fig. 6.21 supports our interpretation that the negative $\langle e_1^{\rm iso}\rangle$ is caused by a lack of dithering, we will need to further investigate this effect on the basis of the complete ACS Parallel Survey for a final judgement, as it extends over a much larger time span allowing a clearer distinction from CTE effects.

So far we co-add parallel data observed within one visit to maximise the stability of the image conditions. Due to the successful PSF correction for the two-epoch GOODS data (see also Sections 6.4.3 and 6.4.4) we are confident that a combination of different visits will also be possible for parallel data with re-observations, which will reduce the number of fields with poor dithering. Additionally we are working on an improved search algorithm for galaxies which are affected by bad columns.

## 6.4.2 Error estimates

In the following subsections we compute several estimators for the cosmic shear signal and remaining systematics. The statistical errors of these estimates are always computed in a similar way.

### 6.4.2.1 Parallel data

**Bootstrapping on galaxy basis.** To derive statistical weights for $\xi_\pm$ and $\langle M_{\rm ap}^2\rangle$, we generate for each field $i$ 200 bootstrap samples of the galaxy catalogue and compute $\xi_{\pm,ij}$ and $\langle M_{\rm ap}^2\rangle_{ij}$ for each angular bin $j$. The weight $w_{ij}$ for this field and bin is then given as the inverse bootstrapping variance $w_{ij} = 1/\sigma_{ij}^2$, yielding the combined estimates

$$\xi_{\pm,j} = \frac{\sum_{i=1}^{N_{fields}} \xi_{\pm,ij} w_{ij}}{\sum_{i=1}^{N_{fields}} w_{ij}}\,, \quad \langle M_{\rm ap}^2\rangle_j = \frac{\sum_{i=1}^{N_{fields}} \langle M_{\rm ap}^2\rangle_{ij} w_{ij}}{\sum_{i=1}^{N_{fields}} w_{ij}}\,. \tag{6.16}$$

The estimate for the galaxy-star cross-correlation (see Sect. 6.4.3) is calculated accordingly, with bootstrapping of the galaxy catalogue and a fixed stellar catalogue.

**Bootstrapping on field basis.** We determine the measurement error of the field combined estimates for $\xi_{\pm,j}$ and $\langle M_{\rm ap}^2\rangle_j$ from 300 bootstrap samples of our fields, combining the estimates for each realisation according to (6.16). The error of the combined signal in each angular bin $j$ is then given by the bootstrap variance $\sigma_j^2$. This error estimate accounts both for the shape noise and cosmic variance.

### 6.4.2.2 GEMS and GOODS

**Bootstrapping on galaxy basis.** For the combined GEMS and GOODS mosaic catalogue we analogously perform bootstrapping on galaxy basis to derive the shape noise error. The errors plotted for the galaxy-star cross-correlation and the E-/B-mode decomposition within Sections 6.4.3 and 6.4.4 correspond to this bootstrap variance.

For the cosmological parameter estimation in Sect. 6.5 covariances are required, which additionally take sampling variance into account. We compare covariances estimated directly from the data using a jackknife method with estimates from Gaussian realisations of the cosmic shear field.

**Jackknife method.** We use the modified jackknife method applied by H05 to estimate the covariance matrix of the cosmic shear estimators. In contrast to the bootstrapping on galaxy basis, the jackknife method includes an estimate for small-scale cosmic variance. However, it must under-estimate cosmic variance on scales of the order of the field size. We describe the algorithm in terms of the correlation functions $\xi_\pm$: We first compute the correlation function $\xi_{\pm,j}$ in the angular bin $j$ from the complete galaxy catalogue. Next, we divide the whole survey into $N$ separate sub-regions on the sky, where for convenience we use the $N = 78$ individual ACS tiles. Then, the correlation function $\xi_{\pm,ij}$ is computed omitting the $i$-th subregion for $i = 1, ..., N$. With

$$\xi^*_{\pm,ij} = N\xi_{\pm,j} - (N-1)\xi_{\pm,ij}\,, \tag{6.17}$$

the jackknife estimate for $\xi_{\pm,j}$ is given by the average $\hat{\xi}_{\pm,j} = \langle\xi^*_{\pm,ij}\rangle$, and the jackknife estimate of the covariance between bins $j$ and $k$ can be computed as

$$\langle\Delta\xi_{\pm,j}\Delta\xi_{\pm,k}\rangle = \frac{1}{N(N-1)}\sum_{i=1}^{i=N}\left(\xi^*_{\pm,ij} - \hat{\xi}_{\pm,j}\right)\left(\xi^*_{\pm,ik} - \hat{\xi}_{\pm,k}\right)\,. \tag{6.18}$$

Note that this jackknife method is expected to slightly underestimate the error even on scales much smaller than the field size due to the mixing of power between different scales in the non-linear regime.

**Sampling variance from Gaussian random fields.** Given that the GEMS and GOODS mosaic samples only one particular field in the sky, the large scale sampling variance errors cannot be determined from the data itself. In order to derive a theoretical error estimate we have created 2000 $1^\circ \times 1^\circ$ Gaussian realisations of the shear field for a $\Lambda$CDM cosmology with $\sigma_8 = 0.7$ and the GEMS redshift distribution, which we populate with 96 galaxies arcmin$^{-2}$ with ellipticities randomly drawn from our shear catalogue. We then select a $\sim 28' \times 28'$ subregion representing the actual masked geometry of the mosaic. From the sheared ellipticities we then compute the covariance matrix of the correlation functions from the different realisations (see Simon et al. 2004). This provides us with a robust estimate of the error covariance in the Gaussian limit also including the shape and shot noise contribution. Note, however, that the Gaussian assumption strongly under-estimates the sampling variance for $\theta \lesssim 10'$ (Kilbinger & Schneider 2005; Semboloni et al. 2007), which we further discuss in Sect. 6.5.

### 6.4.3 Star-galaxy cross-correlation

An important diagnostic test for the effectiveness of the PSF anisotropy correction is given by the cross-correlation between uncorrected stellar ellipticities $e^*$ and PSF and calibration corrected galaxy ellipticities $\gamma$, which can be used as an estimate for residual PSF contamination.

Following Bacon et al. (2003) we compute

$$C^{\rm sys}(\theta) = \frac{\langle \gamma e^* \rangle(\theta) |\langle \gamma e^* \rangle(\theta)|}{\langle e^* e^* \rangle(\theta)} \,. \tag{6.19}$$

For the parallel data we substitute $e^*$ with the smearing corrected PSF model ellipticity

$$e^*_{{\rm mod},\alpha} \equiv \frac{2c_{\rm cal}}{{\rm Tr}P^g_{\rm gal}} P^{\rm sm}_{\alpha\beta,{\rm gal}}\, q^{\rm DRZ}_{\beta,{\rm total}}(x,y,r_{\rm g}) \,, \tag{6.20}$$

(see Eq. 6.11), at all galaxy positions, which is necessary as $\langle e^* e^* \rangle$ is very noisy and undetermined in many bins due to the few stars present in most of the single parallel fields.

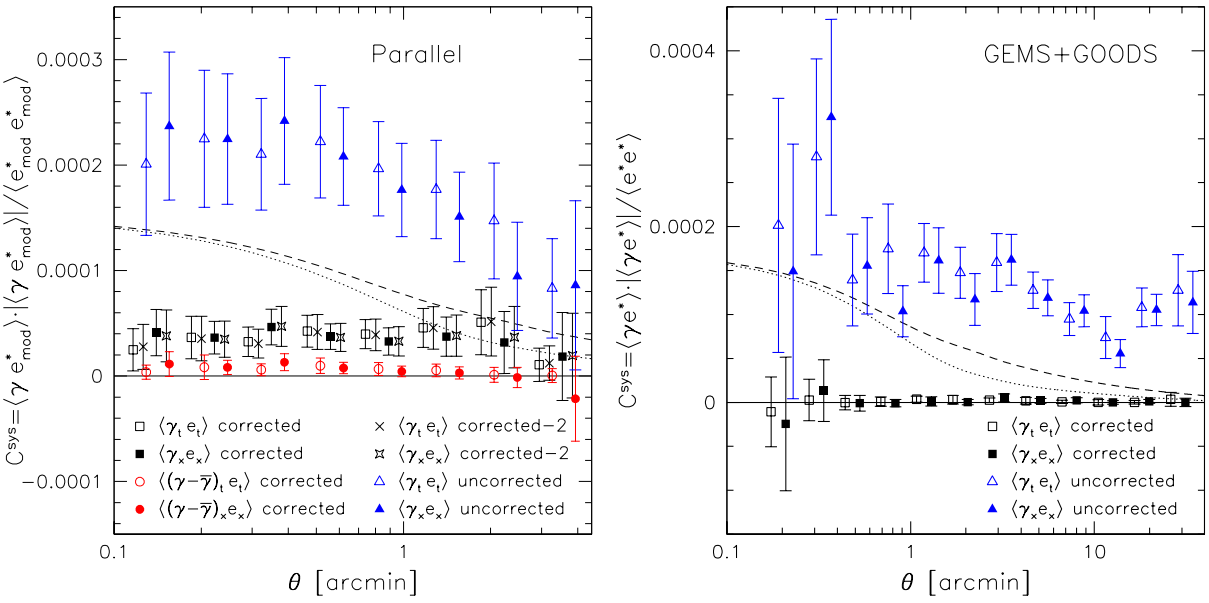


Figure 6.22: Star-galaxy cross-correlation $C^{\rm sys}$ for the parallel data (*left*) and the GEMS and GOODS data (*right*), where $C^{\rm sys}$ is calculated from the uncorrected stellar ellipticities $e^*$ for the GEMS and GOODS data and the PSF anisotropy model $e^*_{\rm mod}$ for the parallel data. The squares show $C^{\rm sys}$ computed from the corrected galaxy ellipticities. For the parallel data this can be compared to the crosses (stars), where the PSF correction was derived using the second-best fit PSF models. The negligible difference between the two indicates that the F775W stellar field exposures sample the PSF variations sufficiently well. For comparison we also plot $C^{\rm sys}$ determined from the smearing but not anisotropy corrected galaxy ellipticities (triangles), and in case of the parallel data also computed from corrected galaxy ellipticities after subtraction of the mean corrected ellipticity (circles). The different data sets are displayed with different $\theta$-offsets for clarity. The dashed (dotted) line shows $\Lambda$CDM predictions for $\langle \gamma_t \gamma_t \rangle$ ($\langle \gamma_\times \gamma_\times \rangle$) for $\sigma_8 = 0.7$.

As can be seen from Fig. 6.22, $C^{\rm sys}$ is consistent with zero for the GEMS and GOODS data for all $\theta$ indicating that the PSF correction works very well for this dataset. For comparison we also plot $C^{\rm sys}$ computed from the smearing but not anisotropy corrected galaxy ellipticities,

which exceeds the theoretically expected cosmic shear signal, emphasising the need for proper PSF correction.

In contrast, $C^{\rm sys}$ is non-zero for the parallel data for most $\theta$. Considering the results from Sect. 6.4.1.3 we interpret this remaining systematic signal as cross-correlation between the (average) PSF pattern and the mean ellipticity component induced by the lack of dithering. This interpretation is supported by the fact that $C^{\rm sys}$ is almost consistent with zero when computed from the corrected galaxy ellipticities minus the mean ellipticity (Fig. 6.22), suggesting that the PSF correction also performs well for the parallel data.

The underlying assumption of our PSF correction algorithm is that the stellar fields sample the parameter space of PSF variations in the galaxy fields sufficiently well (see Sect. 6.2.4.3). To test this assumption we repeat the analysis always using the *second*-best fit PSF model instead of the best fitting model. If the sampling of the PSF variations was not sufficient, we would expect a significant impact on the PSF corrected ellipticities and particularly $C^{\rm sys}$ when switching to the *second*-best fit PSF model. However, as the observed impact is negligible both for $C^{\rm sys}$ (left panel of Fig. 6.22) and the mean corrected galaxy ellipticity ($\langle e_1^{\rm iso,mod2}\rangle = -0.0085 \pm 0.0014$, $\langle e_2^{\rm iso,mod2}\rangle = 0.0018 \pm 0.0014$, compare to Sect. 6.4.1), the sampling of the PSF parameter space indeed seems to suffice.

## 6.4.4 E-/B-mode decomposition

As a further test for contamination of the data with systematics we decompose the shear signal into E- and B-modes using the shear correlation functions $\xi^E(\theta)$, $\xi^B(\theta)$ (Fig. 6.23) and the aperture mass dispersion (Fig. 6.24). For this we first calculate $\xi_+(\theta)$ and $\xi_-(\theta)$ in 300 (1800) finite linear bins of width $\Delta\theta = 0\farcs83$ ($1\farcs17$) from $1''$to $4\farcs2$ ($35'$) for the parallel (GEMS and GOODS) data. $\xi^{E,B}(\theta)$ and $\langle M^2_{\rm ap,\perp}\rangle(\theta)$ are then computed according to equations (3.77, 3.81) and logarithmically re-binned to reduce noise.

### 6.4.4.1 $\xi^E/\xi^B$ decomposition

As the computation of $\xi^{E,B}(\theta)$ requires knowledge of $\xi_-$ also for $\theta$ larger than the field size (see Sect. 3.3.3), we substitute the measured $\xi_-$ for $\theta > 4'$ in the case of the parallel data and $\theta > 35'$ for the GEMS and GOODS data with theoretical predictions for a fiducial $\Lambda$CDM cosmology with $\sigma_8 = 0.7$. The impact of the fiducial cosmology on the E-/B-mode decomposition can be estimated by comparing $\xi^{E,B}(\theta)$ computed for $\sigma_8 = 0.6$ and $\sigma_8 = 1.0$ (dotted lines in Fig. 6.23). While the difference is small for the GEMS and GOODS data ($\sim 2 \times 10^{-5}$), the small size of the single ACS fields leads to a stronger cosmology dependence ($\sim 1.5 \times 10^{-4}$) for the parallel data. The B-mode component $\xi^B$ is consistent with zero for both datasets indicating that we are not subject to major contaminations with systematics. The only exception is the slightly negative $\xi^B$ for the GEMS and GOODS data at large scales, which is an artefact of the discontinuity between the fiducial cosmological model and the low shear signal measured at large scales (see the E-mode signal and Sect. 6.4.5.1) in combination with the bootstrap errors, which do not take cosmic variance into account.

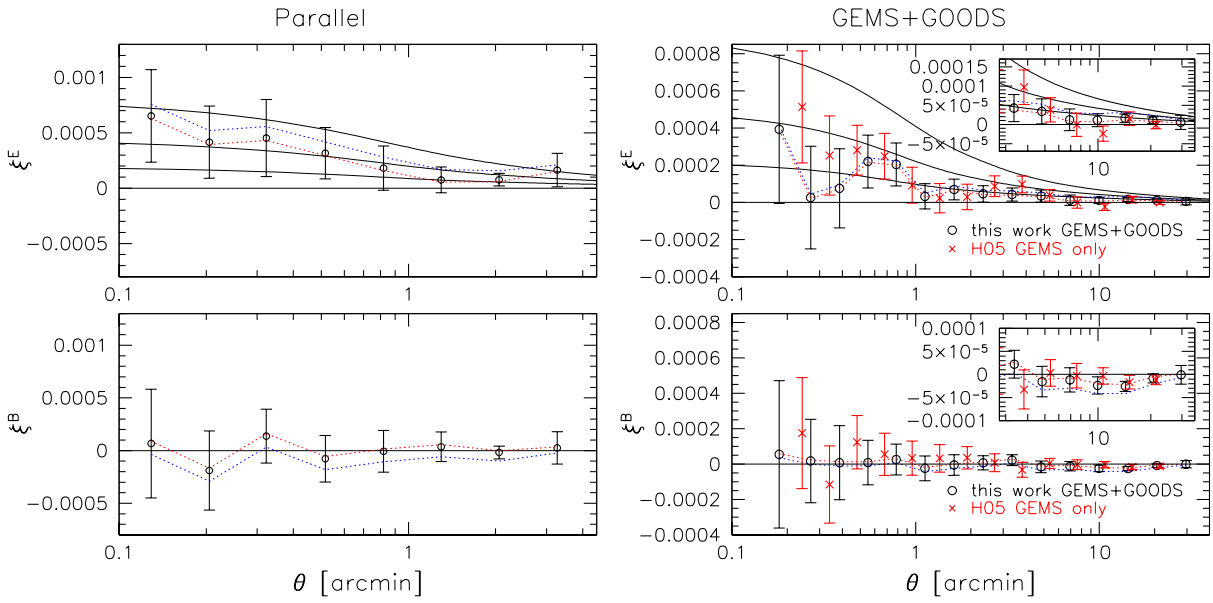


Figure 6.23: E-/B-mode decomposition of the correlation functions for the parallel data (*left*) and the combined GEMS and GOODS data (*right*). The open circles show $\xi^E$ and $\xi^B$ computed using a fiducial ΛCDM model with $\sigma_8 = 0.7$ for the extrapolation in Eq. (3.78), whereas the dotted lines correspond to $\sigma_8 = 1.0$ (upper line for $\xi^E$, lower line for $\xi^B$) and $\sigma_8 = 0.6$ (lower line for $\xi^E$, upper line for $\xi^B$). The thin solid lines show ΛCDM predictions for $\sigma_8 = (0.6, 0.8, 1.0)$. In the right panels we also plot the H05 GEMS only estimate for $\xi^E$ and $\xi^B$ for $\sigma_8 = 0.7$ (crosses). Note that the H05 catalogue is slightly shallower.

#### 6.4.4.2 $\langle M_{\rm ap}^2\rangle/\langle M_\perp^2\rangle$ decomposition

We also compute the B-mode component of the aperture mass dispersion $\langle M_\perp^2\rangle(\theta)$, which is consistent with zero for both datasets indicating the success of our PSF correction scheme (Fig. 6.24). Note that the E-/B-mode mixing due to incomplete knowledge of $\xi_\pm(\theta)$ for small $\theta$, which was recently discussed by Kilbinger et al. (2006), only leads to minor effects for the $\theta$ range considered here, since we truncate $\xi_\pm(\theta)$ only for $\theta < \theta_{\rm min} = 2''$. See Schneider & Kilbinger (2007) for a E-/B-mode decomposition which can also be used for larger $\theta_{\rm min}$.

### 6.4.5 Shear correlation functions

We plot our estimate for the logarithmically binned shear two-point correlation functions $\langle\gamma_t\gamma_t\rangle(\theta)$ and $\langle\gamma_\times\gamma_\times\rangle(\theta)$ in Fig. 6.25. Note that we use $\xi_\pm(\theta)$ for the cosmological parameter estimation in Sect. 6.5, but plot the equivalent data vectors $\langle\gamma_t\gamma_t\rangle(\theta)$ and $\langle\gamma_\times\gamma_\times\rangle(\theta)$ in order to enable the comparison with H05.

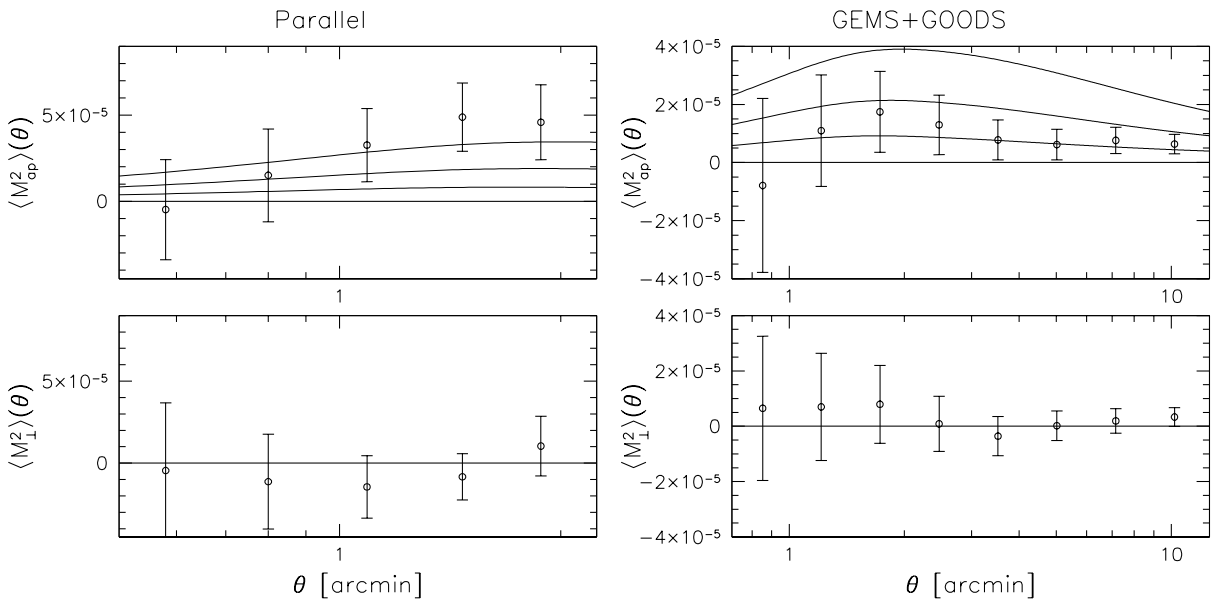


Figure 6.24: E-/B-mode decomposition of the aperture mass dispersion for the parallel data (*left*) and the combined GEMS and GOODS data (*right*). The thin solid lines show ΛCDM predictions for $\sigma_8 = (0.6, 0.8, 1.0)$.

#### 6.4.5.1 GEMS and GOODS data

As we have shown in the previous sections, the GEMS and GOODS data are not contaminated with significant non-lensing signals. We are therefore confident that the measured shear signal (right panel of Fig. 6.25) is of cosmological origin. While we detect significant shear correlations at small angular scales consistent with predictions for $\sigma_8 \sim 0.6$, both $\langle \gamma_t \gamma_t \rangle(\theta)$ and $\langle \gamma_\times \gamma_\times \rangle(\theta)$ are consistent with zero for $\theta \gtrsim 5'$, which we interpret as caused by a large-scale under-density of the foreground structures in the CDFS.

There is good agreement between the error-bars determined from the jackknife method and from Gaussian realisations. Only for scales of the order of the field size the jackknife method significantly under-estimates the modelled errors as it does not account for large-scale cosmic variance. Note the good agreement of the data with the results from H05.

#### 6.4.5.2 Parallel data

While the measured shear correlation functions are roughly consistent with the plotted ΛCDM predictions for $\sigma_8 \sim 0.8$ (left panel of Fig. 6.25), one must be careful with its interpretation due to the detected indications for remaining systematics (Sect. 6.4.1 and 6.4.3), even if they do not show up as B-modes. We thus postpone the cosmological interpretation of the parallel data shear signal to a future analysis based on a larger data set with further corrections for the remaining systematics.

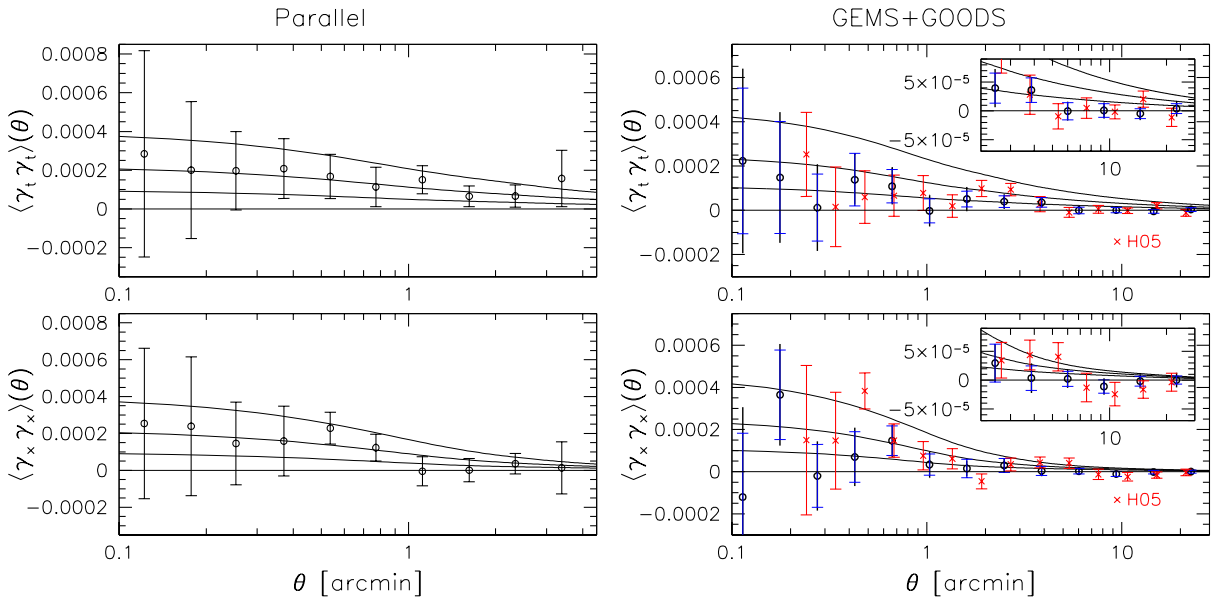


Figure 6.25: Two-point correlation functions $\langle\gamma_t\gamma_t\rangle$ and $\langle\gamma_\times\gamma_\times\rangle$ for the parallel data (*left*) and the combined GEMS and GOODS data (*right*). In the right panels we plot our estimate (open circles) both with the errors determined from Gaussian realisations (bold error-bars) and the Jackknife errors (thin caps), and for comparison also the H05 results (crosses). The thin solid lines show ΛCDM predictions for $\sigma_8 = (0.6, 0.8, 1.0)$. Note the very low cosmic shear signal measured from the GEMS and GOODS data for large $\theta$.

## 6.5 Cosmological parameter estimation from the GEMS and GOODS data

In the last section we have shown that our GEMS and GOODS shear catalogue is not subject to significant non-lensing systematics. We therefore use our estimate of the shear correlation functions, binned in 14 logarithmic bins for $0.'058 < \theta < 28.'1$, in combination with the redshift distribution determined in Sect. 6.3.3, for a cosmological parameter estimation. Here we apply a Monte Carlo Markov Chain (MCMC) technique (see e.g. Tereno et al. 2005) as detailed in Hetterscheidt et al. (2007) and utilise the covariance matrix derived from the Gaussian realisations. This is motivated by the good agreement with the errors determined from the jackknife method at small scales indicating rather low impact of non-Gaussianity. However, using ray-tracing simulations Kilbinger & Schneider (2005) and Semboloni et al. (2007) found that Gaussian statistics strongly under-estimate the covariances also for GEMS like surveys, which we further discuss below.

For the parameter estimation we consider two simple ΛCDM cosmological models:

**A**: a Λ-universe with $\Omega_m, \Omega_\Lambda \in [0, 1.5]$,

**B**: a flat universe: $\Omega_m + \Omega_\Lambda = 1$ with $\Omega_m > 0$,

both with fixed $(w, \Omega_b, n_s) = (-1, 0.042, 0.95)$. We assume a strong constraint $h = 0.70 \pm 0.07$ for the Hubble parameter, as supported by the HST key project (Freedman et al. 2001) and compute the non-linear power spectrum using `halofit` (Smith et al. 2003), with the shape parameter calculated according to Sugiyama (1995): $\Gamma = \Omega_m h \exp[-\Omega_b(1 + \sqrt{2h}/\Omega_m)]$, and the transfer function as given in Efstathiou et al. (1992). In the likelihood analysis we marginalise over the uncertainty in both $h$ and our redshift distribution.

We plot the derived likelihood contours for $\sigma_8, \Omega_m$, and $\Omega_\Lambda$ in Fig. 6.26, where we use all galaxies with S/N > 4 ($N_{gal} = 96\,\mathrm{arcmin}^{-2}$) corresponding to a median redshift $z_m = 1.46 \pm 0.12$. For the more general model **A** the data only weakly constrain $\Omega_\Lambda(\Omega_m = 0.3) = 0.64^{+0.49}_{-0.41}$, whereas more stringent constraints are found for $\sigma_8(\Omega_m = 0.3) = 0.52^{+0.11}_{-0.15}$, or respectively, $\Omega_m(\sigma_8 = 0.6) = 0.26^{+0.07}_{-0.09}$, reflecting the marginalised 68% confidence regions with strong priors on $\Omega_m$ or $\sigma_8$ respectively. Assuming flatness (model **B**) changes the estimates only marginally to $\sigma_8(\Omega_m = 0.3) = 0.51^{+0.09}_{-0.13}$ and $\Omega_m(\sigma_8 = 0.6) = 0.25^{+0.07}_{-0.08}$, respectively.

Using the more conservative sample selection with S/N > 5, $m_{606} < 27.0$, $N_{gal} = 72\,\mathrm{arcmin}^{-2}$, $z_m = 1.37 \pm 0.10$ leads to a higher estimate of $\sigma_8(\Omega_m = 0.3) = 0.59^{+0.11}_{-0.14}$ or $\Omega_m(\sigma_8 = 0.6) = 0.30^{+0.08}_{-0.08}$ for model **A** without significantly affecting the error. In principle, one would expect that the inclusion of the faint galaxies increases the signal-to-noise of the shear measurement as both the galaxy number density and the lensing efficiency increase. However, we can confirm the trend seen by H05 that the faintest galaxies appear to mainly add noise, possibly leading to a slight under-estimation of the shear. This is also consistent with the results from the STEP2 image simulations, where we find that the shear calibration of our KSB+ implementation is on average accurate to $\sim 3\%$, but shows a significant dependence on magnitude, with a slight over-estimation at the bright end and a $\sim 20\%$ under-estimation of the shear for the faintest galaxies (Massey et al. 2007a). Given the on average good calibration found for our analysis of the STEP2 simulations, which incorporate a cut S/N > 4, we consider the estimate of $\sigma_8$ for the same cut to be more robust. Yet, as the magnitude and size distribution, and additionally also the noise correlations are somewhat different for the STEP2 simulations and our data, we expect a slight remaining systematic error also for the average shear calibration[6]. Therefore, we use the difference of the two estimates for $\sigma_8$ as a conservative estimate of this uncertainty and take it into account as additional systematic error, yielding $\sigma_8(\Omega_m = 0.3) = 0.52^{+0.11}_{-0.15}(\mathrm{stat}) \pm 0.07(\mathrm{sys})$. For a future shear tomography analysis this issue will need to be revisited, as it does not only require accurate shear calibration on average, but also over the whole magnitude range.

The constrained value for $\sigma_8$ is significantly lower than the estimates from other recent lensing surveys, e.g. $\sigma_8 = 0.86 \pm 0.05$ (Semboloni et al. 2006) and $\sigma_8 = 0.85 \pm 0.06$ (Hoekstra et al. 2006), both from the CFHTLS for $\Omega_m = 0.3$; see Hetterscheidt et al. (2007) for a compilation of recent estimates. Our results are consistent with $\sigma_8 = 0.8, \Omega_m = 0.3$ only at the $3\sigma$-level assuming Gaussian cosmic variance, which we interpret as a substantial local under-density of the foreground structures in the CDFS. In order to allow a clear comparison to the H05 results, who determine $\sigma_8(\Omega_m/0.3)^{0.65} = 0.68 \pm 0.13$, we recompute our redshift distribution using their $z_m$(mag) relation (6.15), yielding a median redshift $z_m = 1.12$ ($z_m = 1.07$) for the galaxies with

[6]Note that we conducted the detailed analysis of the STEP2 noise correlations (Sect. 4.3.7) after the cosmic shear paper was accepted. Hence, the results are not taken into account at this point.

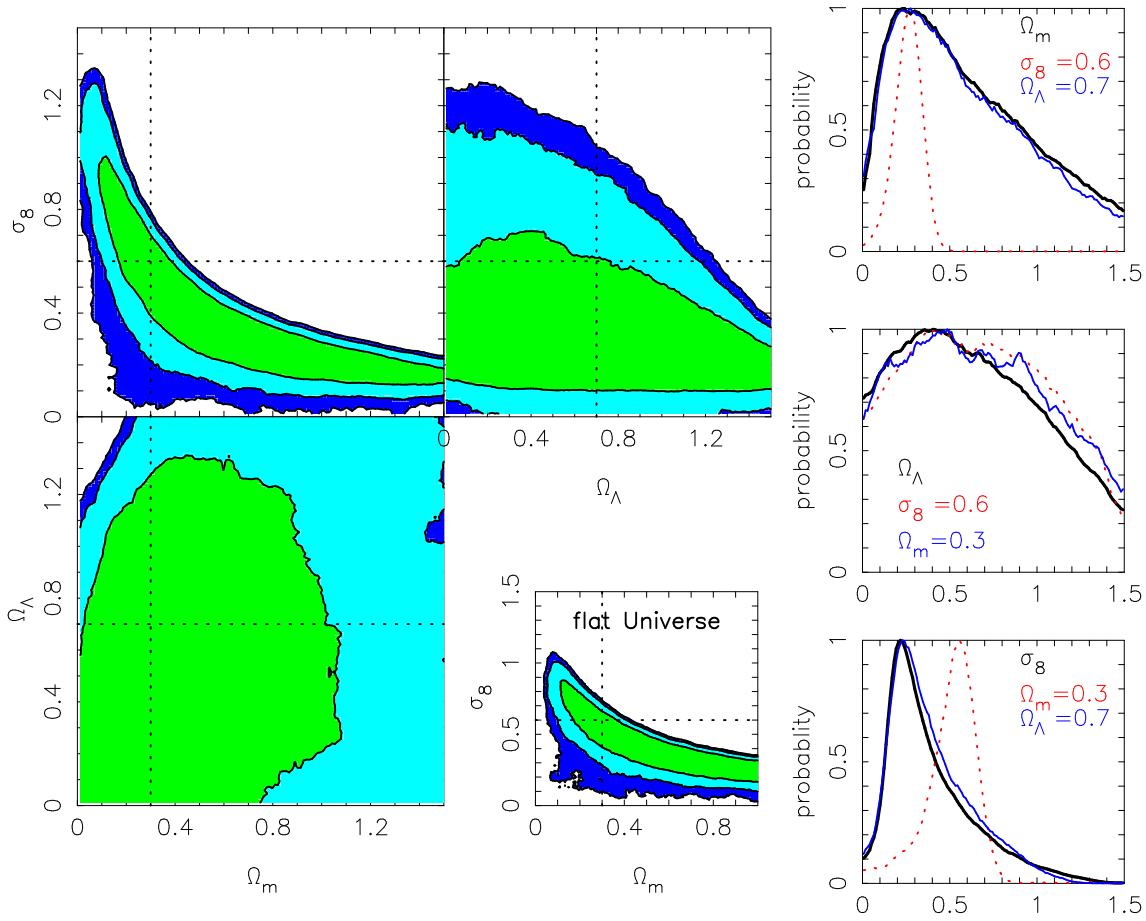


Figure 6.26: Constraints on $\sigma_8, \Omega_m$, and $\Omega_\Lambda$ from the GEMS and GOODS data using all galaxies with S/N > 4. The three large contour plots show marginalised joint 2-dimensional $1, 2$, and $3\sigma$ likelihood contours for model **A**, whereas the small one was computed assuming flatness (model **B**). For model **A** the marginalised probability is plotted on the right for $\Omega_m$ (top), $\Omega_\Lambda$ (middle), and $\sigma_8$ (bottom), where the thick solid curves correspond to the total marginalised values, while the thin solid (dotted) lines correspond, from top to bottom, to fixed $\Omega_\Lambda = 0.7$ ($\sigma_8 = 0.6$), $\Omega_m = 0.3$ ($\sigma_8 = 0.6$), $\Omega_\Lambda = 0.7$ ($\Omega_m = 0.3$).

S/N > 4 (S/N > 5, $m_{606} < 27.0$). Then we repeat the cosmological parameter estimation assuming a redshift uncertainty $\Delta z_m = 0.1$ to be consistent with H05. For this redshift distribution we find $\sigma_8(\Omega_m = 0.3) = 0.62^{+0.12}_{-0.16}$ ($\sigma_8(\Omega_m = 0.3) = 0.66^{+0.11}_{-0.14}$) in excellent agreement with the H05 results. We thus conclude that our lower $\sigma_8$ estimate compared to H05 is mainly a result of our new redshift distribution based on the GOODS-MUSIC sample, and that the two independent shear pipelines yield consistent results (see also Sect. 6.3.2).

Our estimate of the statistical error includes the shape noise contribution, the estimated uncertainty of the redshift distribution, and a Gaussian estimate for cosmic variance. Although there is good agreement of the errors from the jackknife method and Gaussian realisations at small scales, we expect to under-estimate cosmic variance due to non-linear evolution. Kilbinger & Schneider (2005) and Semboloni et al. (2007) found that the Gaussian approximation can lead to a substantial under-estimation for the correlation function covariance matrix in the non-linear regime. Using a fitting formula found by Semboloni et al. (2007) we estimate that the diagonal elements of the $\xi_+$ covariance matrix will be under-predicted by a factor of $\sim 2.9$ for a single source redshift plane at $z = 1.4$ and $\theta \sim 2'$. As this corresponds to the median redshift of our galaxies and since our shear signal has the highest significance for $0\farcm6 \lesssim \theta \lesssim 5'$ (see Fig. 6.25), which (logarithmically averaged) roughly corresponds to a scale $\theta \sim 2'$, we estimate very broadly that we on average under-estimate the cosmic variance contribution to the covariance matrix by a factor of $\sim 2.9$ leading to an error of $\sigma_8$ which is actually larger by $\sim \sqrt{2.9} \approx 1.7$. Note that this is probably a conservative estimate, given that the correlation function for $\theta > 5'$, which shows a rather low signal, still influences the parameter estimation significantly. However, at larger scales the corrections due to non-Gaussianity become less important.

Apart from the shear calibration uncertainty considered above, further systematic errors might be introduced by intrinsic alignment of sources (Brown et al. 2002; King & Schneider 2002; Heymans & Heavens 2003; Heymans et al. 2004, 2006c; Mandelbaum et al. 2006) or a correlation between the intrinsic ellipticities of galaxies and the density field responsible for gravitational lensing shear, detected by Mandelbaum et al. (2006). Given the depth of the data analysed here, we however expect that the impact of these two effects will be small compared to the statistical uncertainties (see Heymans et al. 2006c). Further uncertainties arise from the limited accuracy of the predictions for the non-linear power spectrum. Yet, given that the measured shear signal is particularly low for large $\theta$ (see Sect. 6.4.5.1), which are less affected by non-linear evolution, this cannot explain the low estimate of $\sigma_8$ for the GEMS and GOODS data.

## 6.6 Conclusions

We have presented a cosmic shear analysis of a first set of HST/ACS pure parallel observations and the combined GEMS and GOODS data of the CDFS. We estimate that our new correction scheme for the temporally variable ACS PSF reduces the systematic contribution to the shear correlation functions due to PSF distortions to $< 2 \times 10^{-6}$ for galaxy fields containing at least 10 stars. This is currently the only technique taking the full time variation of the PSF between individual ACS exposures into account. In the GEMS and GOODS data the success of the PSF correction is confirmed by a number of diagnostic tests indicating that the remaining level of

systematics is consistent with zero. For the parallel data we detect a low level of remaining systematics manifesting in a slight average alignment of the measured galaxy ellipticities in the $y-$direction, which we interpret to be due to a lack of proper dithering. This has led to the implementation of improved bad pixel masks in the Mark-II pipeline (Sect. 5.3). Although the degradation of the ACS charge-transfer-efficiency has not been found to be a problem for the early data analysed in this work, an in-depth analysis and correction will be required for later datasets. Furthermore the parallel data are rather inhomogeneous regarding depth and extinction, raising the need for a well calibrated field-dependent redshift distribution. It will also be necessary to carefully exclude any selection bias which might arise for certain classes of primary targets, particularly galaxy clusters. Once these remaining obstacles are overcome, it will be possible to measure cosmic shear at small angular scales with unprecedented accuracy from the complete ACS Parallel Survey, with a strong reduction both of the shape noise and cosmic variance error due to many independent pointings. The main limitation of the cosmological interpretation of the data might then arise from the current accuracy of theoretical predictions for the non-linear power spectrum at small scales. An interesting comparison will be possible with the ACS COSMOS data (Massey et al. 2007c, Chapter 7), from which cosmic shear can be measured on a wide range of angular scales.

Given the high demands concerning the control over systematics for cosmic shear measurements with ACS, the derived technical expertise (see also H05; Jee et al. 2005a; Rhodes et al. 2005; Rhodes et al. 2007; Leauthaud et al. 2007) will also be of benefit for other weak lensing studies with the instrument, and possibly also other research fields requiring accurate PSF modelling.

Due to the weakness of the shear signal on the one hand, and the strong impact of poorly understood systematics on the other hand, an analysis of identical datasets with more than one independent pipeline is of great value to check the reliability of the algorithms employed. In this work we have independently re-analysed the ACS observations of the GEMS and GOODS fields. If we assume the same redshift parametrisation, our shear estimates are in excellent agreement with the earlier results found by H05 indicating the reliability of both lensing pipelines. Such an independent comparison will also be highly desired both for the complete ACS Parallel Survey (Rhodes et al. in prep.) and the ACS COSMOS field (Massey et al. 2007c). These comparisons, together with the results from the STEP project, will aid the preparations of future space-based cosmic shear survey such as DUNE or SNAP, which will reach a very high statistical accuracy (Refregier et al. 2004) requiring the continued advancement of improved algorithms such as shapelets (Bernstein & Jarvis 2002; Refregier & Bacon 2003; Massey & Refregier 2005; Kuijken 2006; Nakajima & Bernstein 2007).

Finally, we want to stress the possible impact of the field selection on a cosmic shear analysis: The *Chandra* Deep Field South was originally selected in a patch of the sky characterised by a low Galactic neutral hydrogen column density ($N_{\rm H} = 8 \times 10^{19} {\rm cm}^{-2}$) and a lack of bright stars (Giacconi et al. 2001). Additionally, it neither contained known relevant extragalactic foreground sources nor X-ray sources from the ROSAT ALL-Sky Survey Catalogue[7] excluding e.g. the presence of a low redshift galaxy cluster. Adami et al. (2005) present a detailed analysis of

[7] see `http://www.mpe.mpg.de/~mainieri/cdfs_pub/index.html`

compact structures in the CDFS showing the presence of a chain-like structure at $z = 0.66$, a massive group at $z = 0.735$ embedded into a galaxy wall extending beyond the $21' \times 21'$ field covered by the Vimos VLT Deep Survey (Le Fèvre et al. 2004), and a further massive group at $z = 1.098$ (see also Gilli et al. 2003; Szokoly et al. 2004; Vanzella et al. 2006). Wolf et al. (2004) identify a strong galaxy over-density at $z \sim 0.15$, which is too close to produce a significant lensing signal. Given the lack of massive structures at lower redshifts $0.3 \lesssim z \lesssim 0.6$ with high lensing efficiency, one would expect to measure a shear signal biased to lower values in this field as a result of strong sampling variance. Therefore it is not surprising that our local single field estimate of $\sigma_{8,\mathrm{CDFS}}(\Omega_\mathrm{m} = 0.3) = 0.52^{+0.11}_{-0.15}(\mathrm{stat}) \pm 0.07(\mathrm{sys})$ based on a source redshift distribution derived from the GOODS-MUSIC sample (Grazian et al. 2006), is incompatible at the $\sim 3\sigma$-level assuming Gaussian cosmic variance with recent results of other weak lensing studies (e.g. Hoekstra et al. 2006; Semboloni et al. 2006), which probe much larger regions on the sky. Kilbinger & Schneider (2005) and Semboloni et al. (2007) investigate the impact of non-Gaussianity on cosmic shear covariances. From their results we broadly determine an under-estimation of the cosmic variance contribution to our error on $\sigma_8$ by a factor $\approx 1.7$, indicating that the CDFS is still an exceptionally under-dense field, but with a lower significance ($\sim 2\sigma$) than under the Gaussian assumption. Our $\sigma_8$ estimate is also significantly lower than the H05 results of $\sigma_8(\Omega_\mathrm{m}/0.3)^{0.65} = 0.68 \pm 0.13$ due to the deeper redshift distribution found in our analysis with a median source redshift $z_\mathrm{m} = 1.46 \pm 0.12$. Recently Phleps et al. (2007) found a strong deficiency of faint red galaxies in the CDFS for the redshift range $0.25 \lesssim z \lesssim 0.4$ indicating a substantial under-density, which is in excellent agreement with the low shear signal found in our analysis.

We believe that the CDFS represents a somewhat extreme case. However, also other cosmic shear studies which observe a low number of small "empty fields" could be slightly biased just due to this prior selection. Such a bias can of course be eliminated either with the observation of sufficiently large fields or truly random pointings, which are realized in good approximation for a large fraction of the fields in the ACS Parallel Survey.

We plan to further investigate the peculiarity of the CDFS based on a shear tomography analysis with photometric redshifts derived for the full GEMS field, also using deep ground-based optical images from the MPG/ESO 2.2m telescope (Hildebrandt et al. 2006) in combination with infrared images from the ESO 3.5m NTT (Olsen et al. 2006b,a). If the low estimate for $\sigma_{8,\mathrm{CDFS}}$ indeed stems from an under-density of foreground structures we would expect an increased shear signal for a high-redshift sample of source galaxies due to the spectroscopically confirmed structures at $z = 0.735$ and $z = 1.098$. Comparing the results with ray-tracing through N-body simulations we aim to further quantify the rarity of such an under-dense foreground field.

# Chapter 7

# Preliminary analysis of the ACS COSMOS Survey

The COSMOS Survey is the largest continuous field ever imaged by the Hubble Space Telescope, spanning a total area of 1.64 deg$^2$. In combination with accurate photometric redshift catalogues derived from deep multi-colour ground-based observations, COSMOS provides a unique dataset for weak lensing measurements. It is particularly well suited for dark matter mapping, galaxy-galaxy lensing, and cosmological weak lensing studies at small and intermediate scales. Although the cosmic shear signal can be measured out to relatively large scales in the COSMOS Survey, large-scale constraints are subject to strong sampling variance.

I conducted an analysis of the COSMOS data in the last five months of this thesis project. Because of the special requirements our weak lensing pipeline places on the data reduction, such as the creation of the cosmic ray cleaned, un-drizzled *COR*-images, we independently reduced the COSMOS data and did not use the public reduced images. Given that the data volume is huge, COSMOS provides a substantial increase in statistical accuracy compared to the seven times smaller sky area of the GEMS Survey analysed in Chapter 6. This revealed previously undetectable residual systematic errors indicated by a significant B-mode signal, whose origin could not be identified unambiguously in the short time remaining. Therefore, the analysis presented here is still preliminary, leaving room for further development in the time after the PhD project. The analysis has been carried out in collaboration with Patrick Simon and Jan Hartlap.

A cosmological weak lensing analysis of COSMOS has already been presented by Massey et al. (2007c), as well as dark matter maps of the field (Massey et al. 2007b), allowing for independent tests of the analysis. Interestingly, a similar signal for remaining systematic errors has been reported by Massey et al. (2007c).

This chapter is organised as followed: In Sect. 7.1 I will summarise important properties of the data and data reduction. I will then detail on the creation of the shear catalogue in Sect. 7.2 and our estimate of the redshift distribution in Sect. 7.3. We compute dark matter maps of the field as described in Sect. 7.4. After summarising tests for remaining systematics in Sect. 7.5, the cosmic shear analysis is presented in Sect. 7.6. In order to further investigate the origin of the detected B-mode I performed a PCA analysis of the ACS PSF, as described in Sect. 7.7. Finally, I will draw preliminary conclusions and discuss planed future projects based on COSMOS in

Sect. 7.8.

## 7.1 Data and data reduction

The ACS/WFC COSMOS data consist of 583 pointings observed with the F814W filter ("broad I"), each consisting of four 507 second exposures. The mosaic is centred at R.A. = $10^{\rm h}00^{\rm m}28.6^{\rm s}$, decl. = $+02^\circ12'21\farcs0$ (J2000.0) and covers a total area of 1.64 deg$^2$, with approximately $77'$ along each side. In addition, the central $3 \times 3$ tiles have also been imaged using the blue F475W filter. However, due to the relative size we do not use these additional data for the shear analysis. The exposures are well dithered to cover the chip gap and allow for proper correction of bad columns. In addition, half-pixel shifts have been applied to improve the sampling of the PSF, see Koekemoer et al. (2007) for further details on the dither pattern.

For the data reduction we use our "Mark-II" reduction pipeline as set-up in Bonn (see Sect. 5.3). Here we match the astrometry of the co-added frames to the USNO-B1 catalogue. However, due to the small field size of ACS, several pointings end-up with only one or no USNO source, raising the need for an additional registration of neighbouring tiles, as detailed in Sect. 7.2.3.

The correctly scaled RMS maps created in the Mark-II reduction allow us to test the approximate correction for noise correlations given by (6.1), which yields a correction factor of $f^{\rm predict} = 1.93$ for the Mark-II drizzle parameters $s = 0.6$, $p = 0.9$ and $m \to \infty$. Figure 7.1 shows the RMS map for a typical COSMOS tile. The median value of this map is $0.00565 e^-/\mathrm{sec}$. Compared to the `SExtractor` estimate for the median single pixel RMS $\sigma_1^{\rm measure} = 0.00299 e^-/\mathrm{sec}$ computed from the science frame, we find a measured correction factor $f^{\rm measure} = 1.89$, in good agreement with the predicted value.

## 7.2 Catalogue creation

We create catalogues similarly to our analysis of the GEMS and early parallel data described in Sect. 6.1.3. Here we therefore only describe updates included after this earlier analysis.

### 7.2.1 Automated masking in co-added images

The huge COSMOS data volume rose the need for a further automatisation of the image masking process. In the mask creation we consider the following steps, which are included as different bits in the final flag image:

1. We detect bright stars with diffraction spikes using SExtractor (`DETECT_MINAREA` = 50, `DETECT_MINTHESH` = 50, uncorrected RMS from the science frame) and select them according to their location in size–magnitude space. We create magnitude dependent polygonal regions, which cover the diffraction spikes and extended halos of the selected stars, and which are converted into masks using `WeightWatcher`.

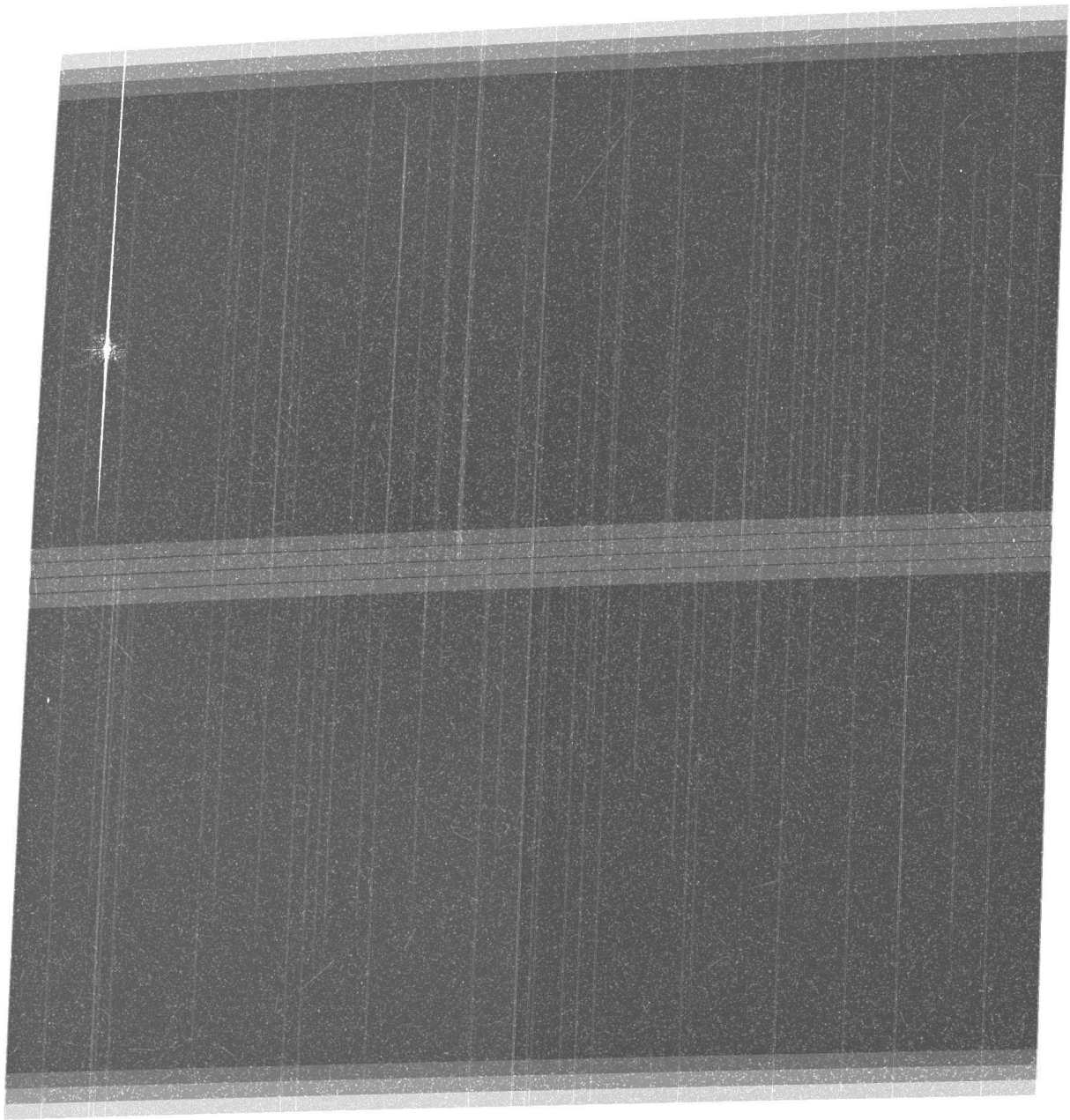

Figure 7.1: RMS map of a typical co-added COSMOS tile, centred at R.A. = $09^{h}58^{m}50^{s}$, decl. = +02°39′20″. The grey-scale ranges from 0.0045$e^{-}$/sec (black) to 0.014$e^{-}$/sec (white). The median value 0.00565$e^{-}$/sec agrees well with the `SExtractor` RMS estimate 0.00299$e^{-}$/sec from the science frame, if scaled with the noise correlation correction factor $f = 1.93$, yielding 0.00577$e^{-}$/sec. The feature near the left end of the upper chip is caused by a saturated star with substantial blooming.

2. We also create masks using SExtractor with a very low detection threshold but large detection area (DETECT_MINAREA = 5000, DETECT_MINTHESH = 0.5, uncorrected RMS from the science frame). Then the SExtractor "OBJECTS" check image provides masks for all detected large objects including extended galaxies, but also bright stars and stellar "ghost" images if present. We furthermore grow these masks by 10 pixels using the IRAF task noao.imred.crutil.crgrow. Our usual detection parameters are tuned to include the faint and typically small galaxies relevant for the shear analysis. Therefore, large galaxies are sometimes falsely de-blended into multiple objects. Their exclusion from the lensing analysis using our masks is unproblematic as they anyway carry very little shear information.

3. Our properly scaled RMS maps allow us to robustly flag objects containing problematic pixels in the co-added image. Here we distinguish between pixels containing basically no more information (RMS $> 10\,\mathrm{e}^-$) and poorly constrained pixels with high noise. To define the threshold for the latter we first compute the mean RMS of all pixels with RMS $< 0.05\,\mathrm{e}^-$. Pixels are then flagged if their RMS exceeds $\sqrt{N - 0.5}\,\langle\mathrm{RMS}\rangle$, where $N$ is the number of combined exposures (four in case of COSMOS). The subtracted value of 0.5 has been tuned such that an output pixel is accepted if two or more input exposures contribute to it with reasonably good pixels.

4. We reject pixels near the image boundaries by creating a mask of all science frame pixels which are exactly equals 0 and growing this mask by 15 pixels. This procedure also performs well for most dither patterns in the Extended ACS Parallel Survey (Sect. 8.3.2). As all the COSMOS tiles have been dithered exactly in the same way, we additionally include a manually created static region file to precisely define the image boundaries used.

The automatically created masks are then inspected using the web tool (Sect. 5.3.3). Here we create a JPG image with green markings for the masked sections and red markings for the detected objects (Sect. 7.2.2). This enables us to quickly check if manual corrections to the automatically created masks are required. Minor corrections, which are usually done within less then one minute, are necessary for about half of the images. An example for a marked JPG image is shown in Figure 7.2.

### 7.2.2 Object detection and shape measurement

Object detection and shape measurement are done similarly to our analysis of the GEMS and early parallel data (Sect. 6.1.3). As a modification we now utilise our properly scaled RMS maps as input weight images for SExtractor, leading to adjusted detection parameters DETECT_MINAREA = 16 and DETECT_MINTHESH = 0.8.

### 7.2.3 Astrometric registration of neighbouring tiles

The astrometric accuracy of our images matched to USNO-B1 is not sufficient to directly identify double detections in neighbouring tiles. We therefore cross-correlate the galaxy catalogues

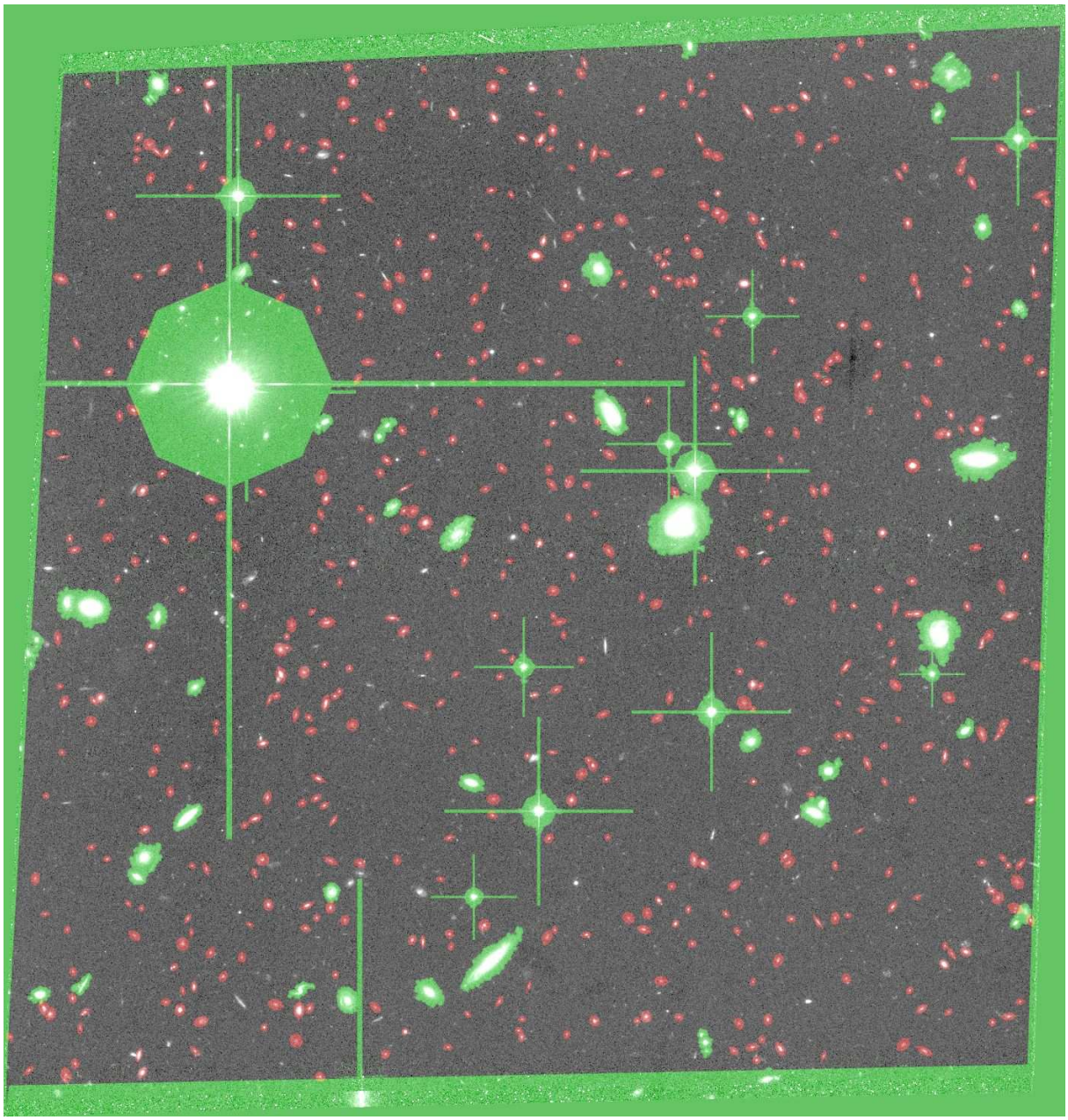

Figure 7.2: Example for a mask inspection image computed for a typical co-added COSMOS tile, centred at R.A. = $10^{h}01^{m}16^{s}$, decl. = $+02°06'59''$. Masked regions are shown in green, whereas included objects are highlighted in red.

starting from the central pointing and then adding neighbouring tiles in a spiral pattern. As a last step we subtract the mean shift from the matched positions. In the properly matched overlapping regions we keep the detection with the higher signal-to-noise estimate.

### 7.2.4 PSF correction and galaxy selection

For COSMOS we again utilise our new PSF correction scheme as detailed in Sect. 6.2.4, with a PSF library built from a total of 577 stellar field F814W exposures. We select galaxies with cuts $\mathrm{Tr}P^g/2 > 0.1$, $|e^{\mathrm{iso}}| < 2.0$, $2.8 < r_{\mathrm{h}} < 10.0$, and $\mathrm{S/N} > 5.5$ corresponding to $\mathrm{S/N}^{\mathrm{true}} > 2.9$ using the measured correction factor $f^{\mathrm{measure}} = 1.89$ (Sect. 7.1). For the final shear catalogue we also apply a cut `MAG_AUTO` $< 26.1$, which rejects 4.8% of the galaxies, to minimise calibration bias introduced by the faintest galaxies and make the sample more homogeneous. We use a shear calibration correction of $0.93^{-1}$ as supported for example by the ACS-type STEP3 simulations (Sect. 4.4). Our final shear catalogue consists of 251057 galaxies, corresponding to a number density of $43/\mathrm{arcmin}^2$. In the analysis presented here we do not apply a weighting scheme.

### 7.2.5 CTE correction

The ACS COSMOS images were taken between October 2003 and November 2005, significantly later than the early parallel or GEMS data analysed in Chapter 6. Therefore we expect a much stronger impact of CTE degradation for COSMOS. Indeed, Rhodes et al. (2007) clearly show that CTE degradation significantly affects the $e_1$ ellipticity component of galaxies in their COSMOS analysis. They apply a parametric correction for their shear catalogue, which is based on similar assumptions as our investigation for CTE degradation in Sect. 6.4.1.2. Rhodes et al. (2007) assume a linear dependence of the spurious $\gamma_1$ signal on the number of parallel $y-$transfers, time, and inverse S/N. They optionally also include a size dependent term, which leads to similar results if the power of the S/N term is also adjusted.

Here we follow their approach, but additionally vary the power law exponents of the different contributing terms and check for a dependence on sky background, which would be expected given that high sky values lead to a higher fraction of already filled charge traps. Dependencies on S/N and sky background might be somewhat degenerate, because higher sky values lead to stronger noise. Therefore we alternatively fit for a dependence on flux and sky background. Hence, our general CTE model is given as

$$e_1^{\mathrm{cte}} = e_0 \left(\frac{y^{\mathrm{CTE}}}{\langle y^{\mathrm{CTE}}\rangle}\right)^A \left(\frac{\mathrm{FLUX}}{\langle \mathrm{FLUX}\rangle}\right)^B \left(\frac{\mathrm{S/N}}{\langle \mathrm{S/N}\rangle}\right)^C \left(\frac{r_{\mathrm{f}}}{\langle r_{\mathrm{f}}\rangle}\right)^D \left(\frac{\mathrm{SKY}}{\langle \mathrm{SKY}\rangle}\right)^E \left(\frac{t_{\mathrm{ACS}}}{\langle t_{\mathrm{ACS}}\rangle}\right)^F , \tag{7.1}$$

where $t_{\mathrm{ACS}}$ denotes the time since the installation of ACS, and $r_{\mathrm{f}}$ is the flux radius from `SExtractor`. For the y-distance the charge of an object is transfered during read-out

$$y^{\mathrm{CTE}} = y^{\mathrm{gap}}(x) - |y - y^{\mathrm{gap}}(x)| \tag{7.2}$$

we approximate $y^{\mathrm{gap}}(x)$ as a straight line along the middle of the chip gap, neglecting minor effects from the dither pattern. We constrain the fit parameters in (7.1) by minimising $\chi^2 =$

Table 7.1: Coefficients for three tested parametric CTE models, based on (7.1). In the first data row the fitted value for the CTE amplitude $e_0$ is given. In the other data rows the first column specifies the considered parameter, for which the fitted power law exponent (A, B, C, D, E, or F, respectively) is given in columns 2 to 4. The mean value of the corresponding parameter, which is used for normalisation, is listed in column 5. Note that the sky value has been averaged between the co-added exposures. The errors refer to the diagonal covariance matrix elements computed by `MINUIT` from the Hessian, and thus only provide a rough estimate of the true uncertainty. If exponents have been fixed for a certain model their values are given without errors.

| $X$ | **Exp. model 1** | **Exp. model 2** | **Exp. model 3** | $\langle X \rangle$ |
|---|---|---|---|---|
| $e_0$ | $-0.00306 \pm 0.00085$ | $-0.00341 \pm 0.00093$ | $-0.00321 \pm 0.00095$ | |
| $y^{\mathrm{CTE}}$ | 1 | 1 | $1.193 \pm 0.453$ | 2008 pixels |
| FLUX | $-0.134 \pm 0.228$ | $-0.039 \pm 0.221$ | 0 | $4.423\,\mathrm{e}^-/\mathrm{s}$ |
| S/N | 0 | 0 | $-0.072 \pm 0.254$ | 16.51 |
| $r_{\mathrm{f}}$ | 0 | $-0.264 \pm 0.487$ | $-0.317 \pm 0.451$ | 6.226 pixels |
| SKY | $-1.355 \pm 0.781$ | $-1.274 \pm 0.778$ | $-1.265 \pm 0.774$ | $57.81\,\mathrm{e}^-$ |
| $t_{\mathrm{ACS}}$ | 1 | $0.449 \pm 0.448$ | $0.443 \pm 0.449$ | 836.4 days |

$\sum[(e_1^{\mathrm{ani}} - e_1^{\mathrm{cte}})/\sigma_e]^2$ using `MINUIT`. Note that we determine the CTE model from the anisotropy but not isotropy corrected galaxy ellipticity. This is done as CTE effects occur *after* PSF convolution and should therefore in principle be corrected first. However, for our parametric correction the data first has to be corrected for PSF anisotropy, as it also influences the diagnostic $e_1$ ellipticity component. Estimating the CTE correction from the fully corrected galaxy ellipticity (as done by Rhodes et al. 2007) would introduce a mixing with the $P^g$ correction, probably leading to a different size dependence of the CTE model.

We have tested several combinations of varied and fixed exponents and summarise the results for three models in Table 7.1. In order to better constrain the time dependence, we use both our COSMOS and GEMS catalogues for the fit, where GEMS has been observed at a significantly earlier epoch. Interestingly, the time dependence seems to be weaker than the linear trend expected from photometric losses due to CTE degradation (e.g. Riess 2004). However, the estimates for the dependence on time and sky background are somewhat degenerate due to the different sky conditions in GEMS and COSMOS. Therefore the observed trend is not really conclusive. Furthermore, we measure a strong dependence of the CTE signature on sky background, which is not taken into account in the Rhodes et al. (2007) model. The dependencies on FLUX, S/N, and $r_{\mathrm{f}}$ seem to be rather weak, so that the choice which of the quantities are considered is probably of minor importance. With model 3 we verify that the dependence on $y^{\mathrm{CTE}}$ and hence the number of parallel transfers is in good agreement with the expected linear trend.

We base our primary cosmic shear analysis on CTE model 1, with fixed linear dependencies on time and $y^{\mathrm{CTE}}$, and fitted dependencies on sky background and total object flux. We verified that the choice which of the three CTE models is applied, has only minor impact on the shear correlation functions and residual B-mode component reported in Sect. 7.5. Hence, we conclude

that the CTE correction should be sufficient for the preliminary 2D shear analysis presented here. For a future tomographic analysis further testing might however be required to ensure a good correction as a function of magnitude and size.

The correction for field distortion leads to a mean rotation of the original $y$-axis and hence readout direction by $\phi \sim -2.5°$. Thus, CTE degradation also has a minor effect on the $e_2$ ellipticity component, which we also correct in our analysis as

$$e_2^{\rm cte} = \tan(2\phi)\, e_1^{\rm cte} \simeq -0.088\, e_1^{\rm cte} \,. \tag{7.3}$$

## 7.3 Redshift distribution

In our analysis we make use of the public photometric redshift catalogue by Mobasher et al. (2007) which covers the full ACS mosaic. It is based on SuprimeCam/SUBARU data taken in B$g$V$ri$$z$ and the NB815 narrow band filter, $u^*$ and $i$ band data from CFHT, $K_{\rm s}$ near-Infrared imaging (Flamingos/CTIO and Kitt Peak) and F814W HST/ACS images. Mobasher et al. (2007) estimate the accuracy of the redshift catalogue via the comparison to 868 spectroscopic redshifts of galaxies with $z < 1.2$, where they find a very low rms scatter of

$$\sigma_z/(1+z) = 0.031 \,. \tag{7.4}$$

In order to match our shear catalogue containing 251057 galaxies to their photo-$z$ catalogue we subtract a residual astrometric shift of $\Delta\alpha = 1.134 \times 10^{-4}$deg, $\Delta\delta = 0.344 \times 10^{-4}$deg from our catalogue and match sources in a radius of $0\farcs8$, providing a total of 142569 unique matches. The magnitude distribution of matched and unmatched galaxies in our shear catalogue is shown in Figure 7.3. 95.3% of the shear catalogue galaxies with $m_{814} < 24.7$ have a redshift estimate, whereas significant redshift incompleteness occurs for fainter magnitudes.

As done in Sect. 6.3.3, we use a maximum likelihood analysis to estimate the redshift distribution parameters $(\alpha, \beta, a, b)$ from the galaxies with $m_{814} < 24.7$, where we now assume a linear dependence between the F814W $I$-band magnitude and the median redshift

$$z_{\rm m} = r z_0 = a(m_{814} - 21) + b \,. \tag{7.5}$$

In order to include the uncertainties on the redshift estimate, we marginalise over the $1\sigma$ redshift confidence interval using the rms scatter (7.4). From the best fitting parameters $(\alpha, \beta, a, b) = (1.228, 1.484, 0.199, 0.345)$, for which $z_{\rm m} = 1.120\, z_0$, we reconstruct the redshift distribution of the matched galaxies with $m_{814} < 24.7$. It agrees well with the input distribution as shown in Figure 7.4, with similar median redshifts $z_{\rm m,input} = 0.88$ and $z_{\rm m,recon} = 0.89$.

We test the assumed linear relation between magnitude and median redshift by binning the matched galaxies as a function of magnitude and fitting $z_{\rm m}$ for fixed $(\alpha, \beta) = (1.228, 1.484)$. As can be seen in Figure 7.5, the linear relation fits the data very well in the redshift complete magnitude range $21.5 < m_{814} < 24.7$, justifying the approach. Note that the derived slope $a$ is significantly flatter than the value found from the GOODS/CDFS data (Figure 6.16). The main reason for this difference is probably given by the different filters, but also the detected foreground under-density in the CDFS will likely lead to a steeper slope.

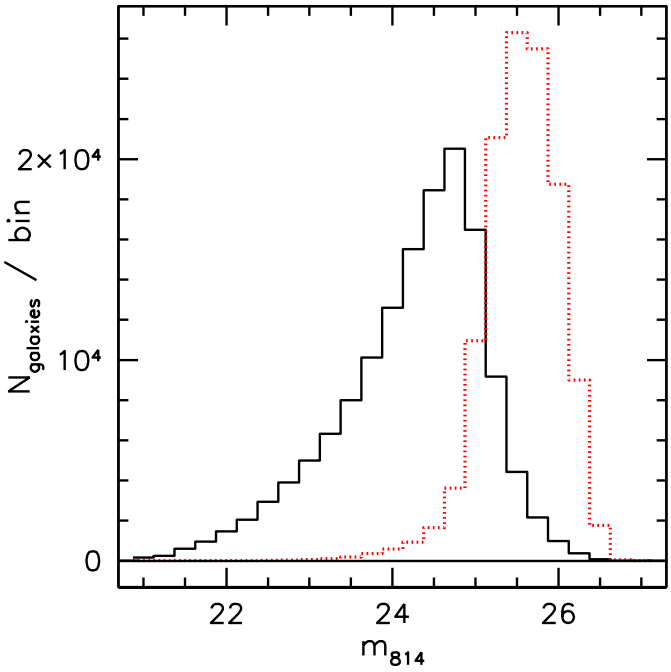


Figure 7.3: Number of selected COSMOS galaxies as a function of $m_{814}$. The solid line corresponds to galaxies for which photometric redshift are available from the public catalogue by Mobasher et al. (2007), whereas the dotted line shows galaxies in the shear catalogue without redshift estimate.

We construct the redshift distribution for our complete shear catalogue with $m_{814} < 26.1$ yielding a median redshift $z_{\rm m} = 1.07$. The constructed distribution can well be fit with a magnitude independent distribution with $(\alpha, \beta, z_0) = (1.251, 1.279, 0.807)$. To account for the magnitude extrapolation we consider a 8% error in the derived median redshift.

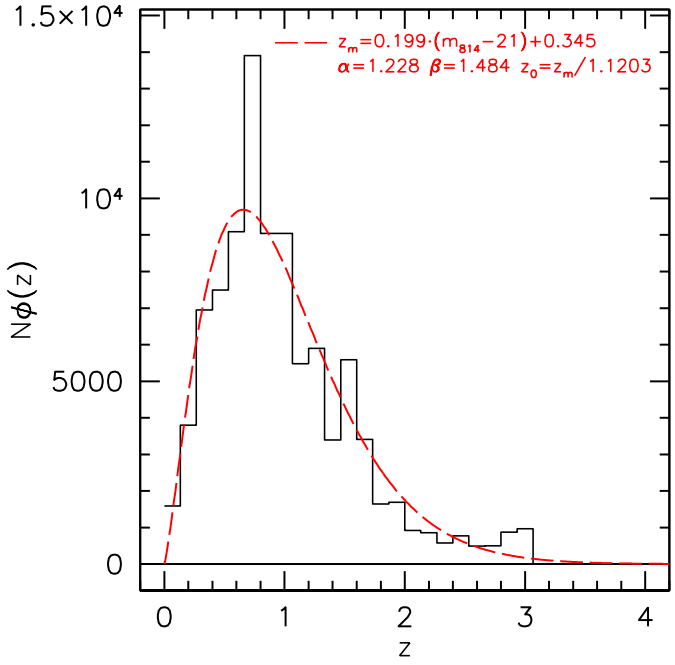


Figure 7.4: Redshift distribution of the matched COSMOS galaxies with $m_{814} < 24.7$ (black histogram), and reconstruction using the best fitting parameters $(\alpha, \beta, a, b) = (1.228, 1.484, 0.199, 0.345)$ (red curve). The peak at $z \sim 0.7$ is caused by a large-scale-structure concentration.

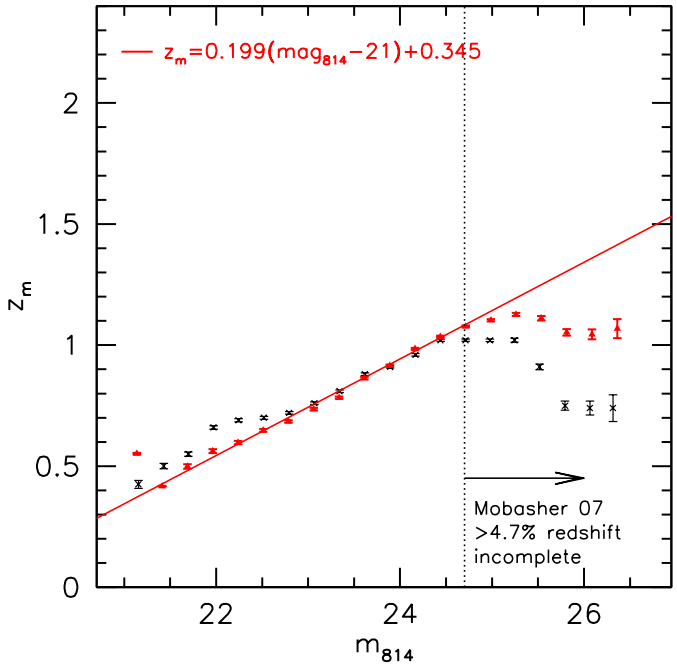


Figure 7.5: Median redshift of the matched COSMOS galaxies computed in F814W magnitude bins. Black crosses show the directly computed value, where error-bars indicate the error of the mean. Red triangles show the results for a likelihood fit with fixed $(\alpha, \beta) = (1.228, 1.484)$. They show a nearly linear trend in the redshift complete magnitude range $21.5 < m_{814} < 24.7$. For fainter magnitudes redshift incompleteness leads to significant deviations. The directly computed median redshift shows significant deviations for $m_{814} \lesssim 22.5$ due to the large-scale-structure peak at $z \sim 0.7$. The much higher number of galaxies leads to strongly reduced error-bars compared to the GOODS/CDFS data shown in Figure 6.16.

## 7.4 Dark matter mapping

We use our mosaic weak lensing catalogue to reconstruct the 2D-projected foreground mass in the COSMOS field. The algorithm is based on the Kaiser & Squires (1993) formalism detailed in Sect. 3.2.2, but includes noise propagation and Wiener filtering as proposed by Hu & Keeton (2002) to derive a maximum likelihood $\kappa$-reconstruction. The algorithm has been implemented and applied by Patrick Simon, and is further detailed in Hetterscheidt et al. (in prep.). In Figure 7.4 we compare our reconstruction to the earlier work by Massey et al. (2007b), who apply a wavelet transform to efficiently reduce noise and combine information from different scales as detailed in Starck et al. (2006). The two analyses make use of different shape measurement and PSF correction schemes, apply different selection criteria, and utilise different mass reconstruction techniques. Therefore it is not surprising that the maps show differences in details, especially at low $\kappa$ values. Nonetheless the prominent features are in good agreement, like the clusters in the left and upper image regions. Note the low signal in the lower right quadrant, where obviously several voids are aligned along the line-of-sight. Also note the good agreement with the baryonic tracers shown in the Massey et al. (2007b) map, confirming that baryons do trace the underlying dark matter distribution well. We postpone the detailed quantitative comparison to a future analysis based on an improved, ideally B-mode free catalogue.

## 7.5 Shear statistics and tests for systematics

We compute the shear two-point correlation functions, as well as the star-galaxy cross-correlation in 4800 linearly spaced angular bins between $1''$ and $75'$, from which we compute further shear statistics. The logarithmically re-binned correlation functions $\xi_\pm$ and the normalised star-galaxy cross-correlation functions $C^{\rm sys}$ are compared in Figure 7.7: We find that the shear correlation functions yield a significant signal almost over the entire $\theta-$range probed. For $1' \lesssim \theta \lesssim 20'$ we also detect a marginally significant signal in $C^{\rm sys}$, which indicates remaining systematics possibly related to the PSF anisotropy or CTE correction. However, in this $\theta-$range the signal is smaller than the expected cosmological signal by factors of about 100 to 10, so that we expect only a minor impact. As $C^{\rm sys}$ extends to relatively large scales, a residual CTE signature seems to be the more likely explanation. CTE degradation creates a large coherent saw-tooth pattern across the whole mosaic, whereas PSF effects should mainly be present on scales of single tiles.

As further tests we perform E/B-mode decompositions using the correlation function (Figure 7.8) and the aperture mass dispersion (Figure 7.9). Both statistics show a significant B-mode signal at small scales, indicating that remaining systematics are present. The affected scales are $\theta \lesssim 0\farcm7$ for $\xi_{\rm B}$ and $\theta \lesssim 5'$ for $\langle M_\perp^2 \rangle$, which is consistent given that the latter measures the power spectrum at smaller scales (see Sect. 3.3.2). For comparison see the E/B-mode estimates from Massey et al. (2007c) in Figure 7.8 and Figure 7.9, who detect a similar B-mode signal at small scales using $\langle M_\perp^2 \rangle$. Their B-mode estimate using $\xi_{\rm B}$ is consistent with zero. However, at small scales their error-bars highly exceed ours, which we currently do not understand as both analysis utilise similar galaxy number densities.

Until the time of the write-up we have not been able to identify the origin of the B-mode

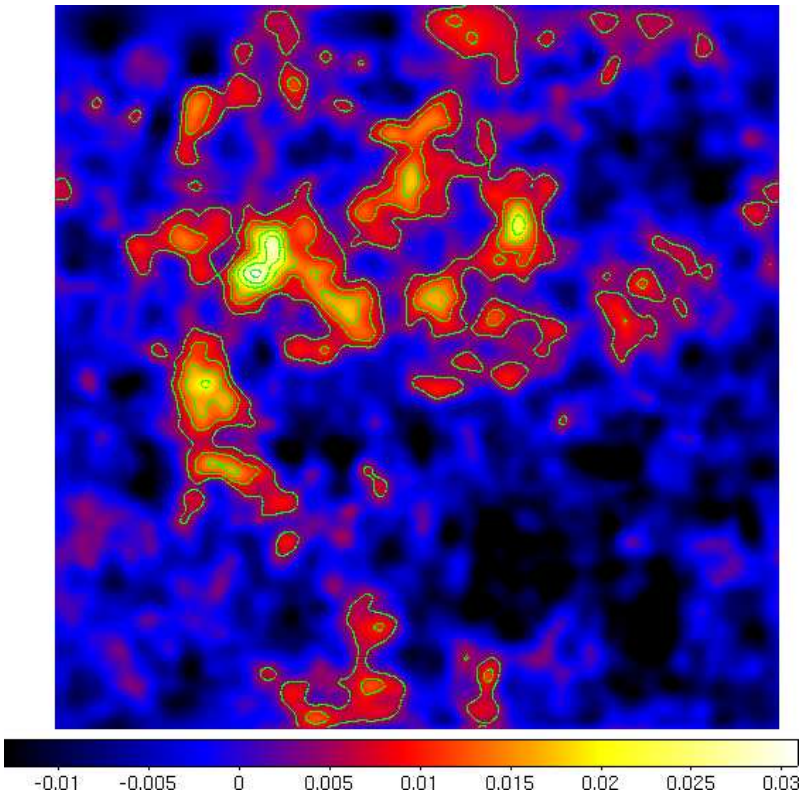


Figure 7.6: Reconstruction of the convergence (projected mass) in the COSMOS field. *Top:* Maximum likelihood reconstruction from our shear catalogue applying noise propagation and Wiener filtering as suggested by Hu & Keeton (2002). The algorithm has been implemented by Patrick Simon and is further described in Hetterscheidt et al. (in prep.). The absolute scale has been set such that the mean $\kappa$ vanishes. *Bottom:* Figure 3 from Massey et al. (2007b): The contours show a wavelet $\kappa$–reconstruction, while the colour coding indicates baryonic tracers (blue: stellar mass; yellow: galaxy number density; red: X-ray gas). For both maps the contours start at and are spaced in steps of $\kappa = 0.005$. Note that we use less galaxies due to our more stringent selection criteria ($43/\mathrm{arcmin}^2$ versus $71/\mathrm{arcmin}^2$). This leads to a larger effective smoothing scale for our Wiener filtered reconstruction compared to the wavelet reconstruction. Also note that the two maps are based on independent data reduction pipelines, shape measurement techniques, PSF correction schemes, and mass reconstruction codes.

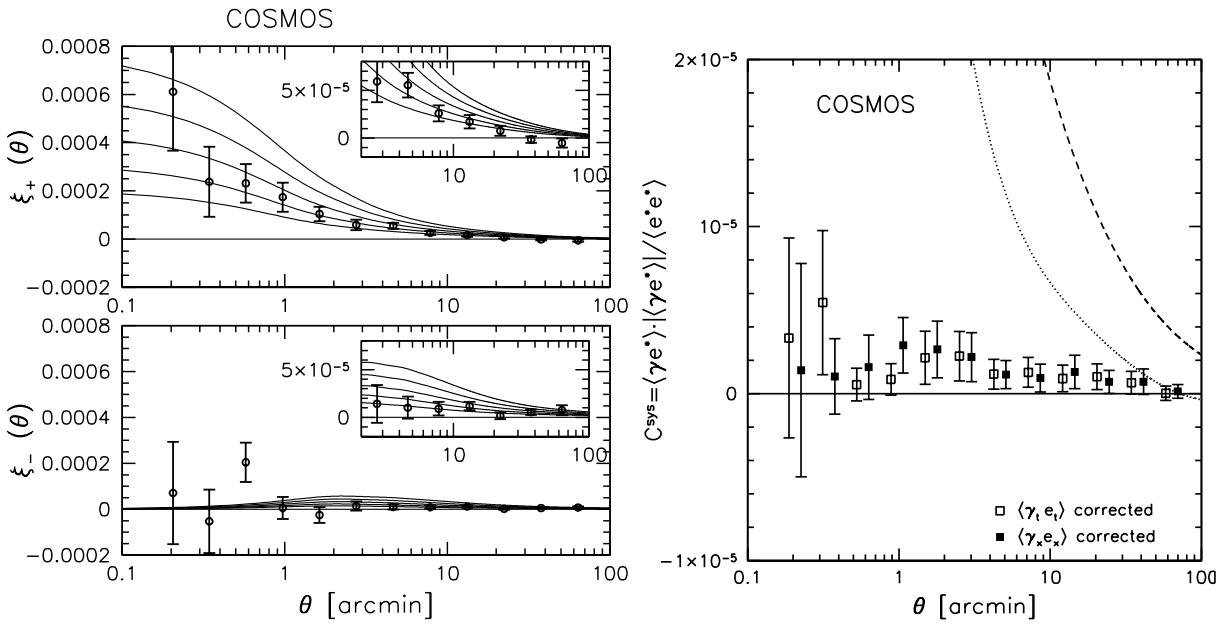


Figure 7.7: *Left:* Shear two-point correlation functions $\xi_\pm$ computed from our COSMOS catalogue. The curves show predictions for a flat ΛCDM cosmology with $\Omega_m = 0.3$ and $\sigma_8 = (0.6, 0.7, 0.8, 0.9, 1.0)$. *Right:* Star-galaxy cross-correlation functions $C^{sys}$ normalised by the star auto-correlation function. The dashed (dotted) curve shows predictions for $\langle \gamma_t \gamma_t \rangle$ ($\langle \gamma_\times \gamma_\times \rangle$) assuming $\Omega_m = 0.3$ and $\sigma_8 = 0.7$. In both panels the error-bars have been computed using bootstrapping. They include the uncertainty due to shape noise but not cosmic variance.

signal. For the parameter estimation presented in Sect. 7.6 we therefore only consider B-mode free scales.

## 7.6 Cosmological parameter estimation

For the cosmological parameter estimation we closely follow Sect. 6.5 using a MCMC technique. We assume a flat ΛCDM cosmology and marginalise over the uncertainty of the Hubble parameter $h = 0.70 \pm 0.07$. The non-linear power spectrum is estimated using `halofit` (Smith et al. 2003), with the shape parameter calculated according to Sugiyama (1995). In order to exclude the B-mode affected scales we base the parameter estimation on the correlation function measured in 20 logarithmic bins between 1′ and 80′. The B-mode affected scales $\theta < 1'$ are anyway problematic given that theoretical predictions are poor at such small scales due to the neglected influence of baryons on the power spectrum. We utilise a covariance matrix estimated from Gaussian shear field realisations and the redshift distribution derived in Sect. 7.3, where we marginalise over the redshift uncertainty. The estimated correlation between the angular bins of the covariance matrix is shown in Figure 7.10.

In Figure 7.11 we plot the estimated likelihood distribution for $\sigma_8$ for fixed values of $\Omega_m$,

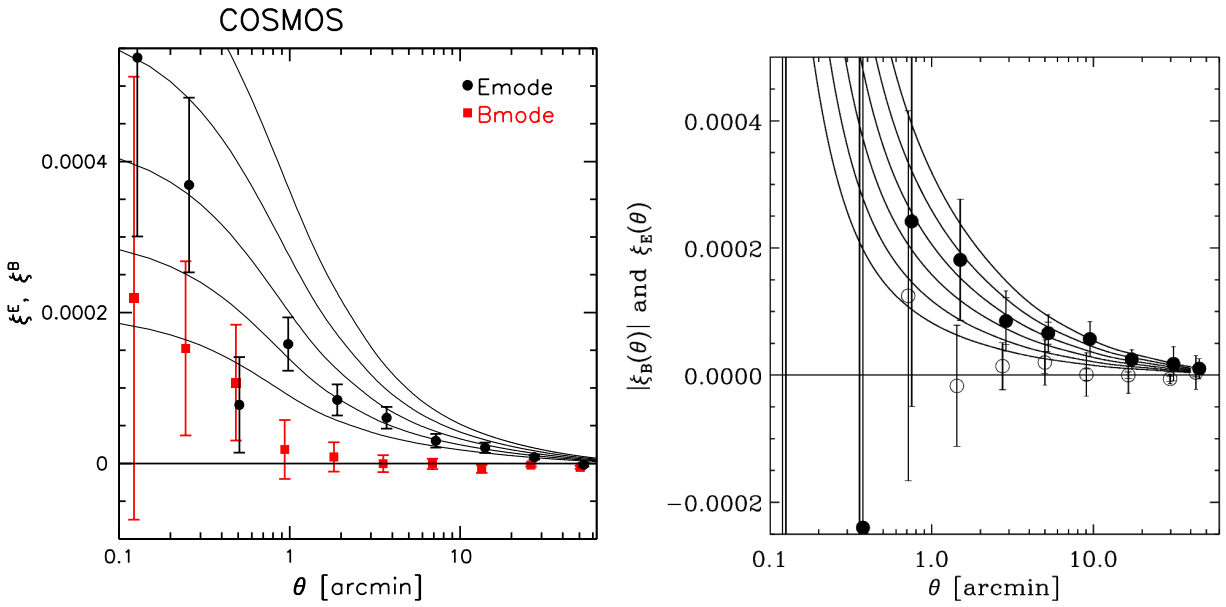


Figure 7.8: E/B-mode decomposition of the COSMOS data using the shear correlation functions. *Left:* Analysis based on our shear catalogue. The curves indicate ΛCDM predictions as in Figure 7.7. For the required extrapolation of the shear signal to infinity $\sigma_8 = 0.7$ was assumed. The error-bars include the uncertainty due to shape noise but not cosmic variance. *Right:* Analysis by Massey et al. (2007c), where the inner error-bars are statistical without cosmic variance, whereas the outer error-bars (without caps) include an estimate for cosmic variance. The solid points show the E-mode, whereas the open circles refer to the B-mode signal. The curves show theoretical predictions for a flat ΛCDM cosmology with $\Omega_m = 0.3$ and $\sigma_8$ varying from 0.7 (bottom) to 1.2 (top) (Figure 6 from Massey et al. 2007c).

where we both test the default lensing reference value $\Omega_m = 0.3$ and $\Omega_m = 0.24$ as suggested e.g. by WMAP3. From these we find the median estimates

$$\sigma_8 = 0.60 \pm 0.08 \quad \text{for} \quad \Omega_m = 0.30\,, \tag{7.6}$$

$$\sigma_8 = 0.71 \pm 0.09 \quad \text{for} \quad \Omega_m = 0.24\,, \tag{7.7}$$

where the $1\sigma$-error includes the statistical uncertainty assuming Gaussian cosmic variance, the uncertainty in the redshift distribution and the Hubble parameter, and a 2% error in the shear calibration as estimated from the STEP3 simulations (Sect. 4.4). Note that the neglected influence of non-Gaussian cosmic variance is expected to lead to an under-estimation of the true uncertainty. However, the effect should be smaller than for the GEMS data due to the much larger area of COSMOS, and hence stronger contribution of quasi-linear scales. For comparison we also estimate $\sigma_8$ using $\langle M_{ap}^2 \rangle$ computed in 20 linear bins between 5′ and 40′, which allows for a more stringent E/B-mode separation than the correlation function. From this we find a very similar estimate of $\sigma_8 = 0.71^{+0.08}_{-0.09}$ for $\Omega_m = 0.24$.

Our estimate for $\sigma_8$ is in good agreement with the WMAP3 result of $\sigma_8 = 0.761^{+0.049}_{-0.048}$ (Spergel et al. 2007), if we assume $\Omega_m = 0.24$ as suggested both by WMAP3 and the SDSS

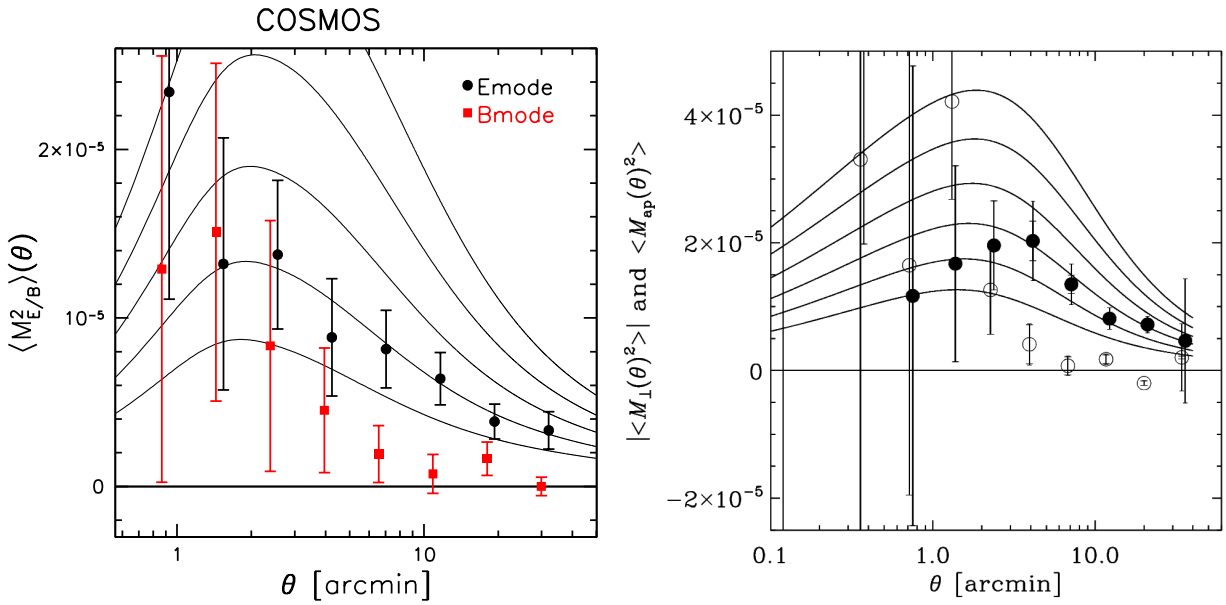


Figure 7.9: E/B-mode decomposition of the COSMOS data using $\langle M^2_{\rm ap}\rangle$. *Left:* Analysis based on our shear catalogue, with error-bars including the uncertainty due to shape noise but not cosmic variance. *Right:* Analysis by Massey et al. (2007c), where the inner error-bars are statistical without cosmic variance, whereas the outer error-bars (without caps) include an estimate for cosmic variance. The solid points show the E-mode, whereas the open circles refer to the B-mode signal. The curves show theoretical predictions as in Figure 7.8 (Figure 6 from Massey et al. 2007c).

baryonic acoustic oscillation measurements (see Sect. 2.3). Recently Benjamin et al. (2007) presented a joint cosmic shear analysis of several large ground-based surveys (CFHTLS-Wide, RCS, VIRMOS-DESCART, and GaBoDS) with a total area of approximately 100 deg$^2$ yielding $\sigma_8(\Omega_{\rm m}/0.24)^{0.59} = 0.84 \pm 0.05$. Together with the WMAP3 results this suggests that our $\sigma_8$ estimate is rather low, but within the errors the results are consistent. In fact, given that for example no extra-ordinarily massive galaxy cluster is present in the COSMOS field at redshifts with high lensing efficiency, one might expect a rather low $\sigma_8$ estimate from the field.

Surprisingly, Massey et al. (2007c) derive a significantly higher value for $\sigma_8$ from their cosmic shear analysis of the COSMOS field. Using a similar 2D analysis they find $\sigma_8\left(\frac{\Omega_{\rm m}}{0.3}\right)^{0.44} = 0.81 \pm 0.075\,({\rm stat.}) \pm 0.094\,({\rm syst.})$, corresponding to $\sigma_8 = 0.90 \pm 0.083\,({\rm stat.}) \pm 0.104\,({\rm syst.})$ for $\Omega_{\rm m} = 0.24$, which is still consistent with our results if all error sources are considered. Additionally, they perform a 3D analysis by splitting the galaxies into three redshift bins yielding tighter constraints $\sigma_8\left(\frac{\Omega_{\rm m}}{0.3}\right)^{0.44} = 0.866 \pm 0.033\,({\rm stat.})^{+0.052}_{-0.035}\,({\rm syst.})$, corresponding to $\sigma_8 = 0.96 \pm 0.037\,({\rm stat.})^{+0.058}_{-0.039}\,({\rm syst.})$ for $\Omega_{\rm m} = 0.24$. This result is no longer consistent with our estimate. However, note that they do not include the correction for covariance matrices estimated from data, which was described by Hartlap et al. (2007). This could lead to a significant underestimation of the statistical error.

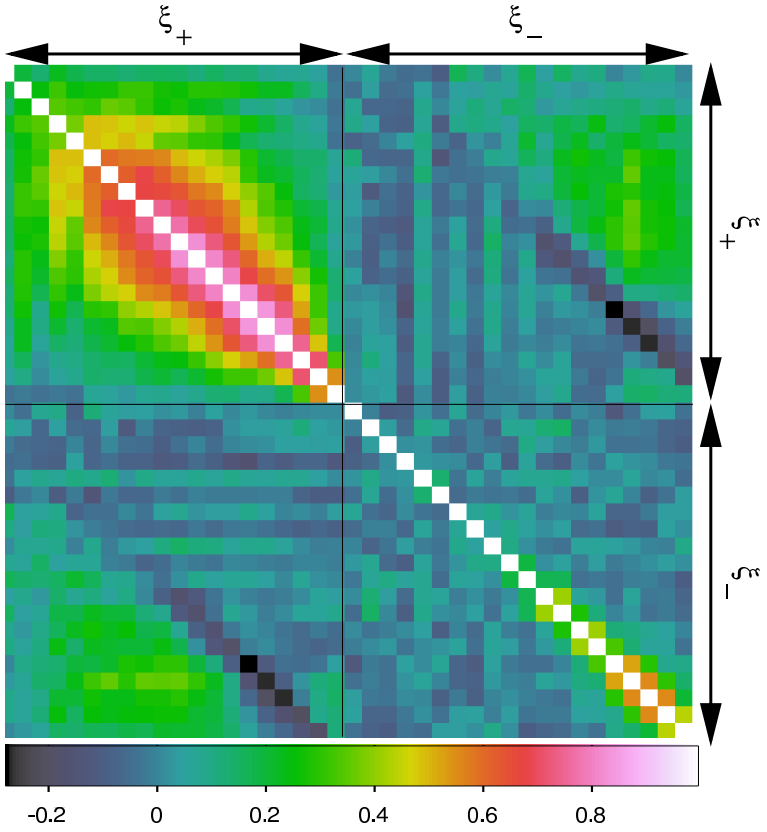


Figure 7.10: Correlation matrix derived from Gaussian shear field realisations for our COSMOS analysis, in which we use the correlation function computed in 20 logarithmic bins between 1′ (top left of each quadrant) and 80′ (bottom right of each quadrant).

In any case the fact that two analyses of the same data set yield at most marginally consistent results is somewhat disconcerting. However, both analysis are based on independent data reduction, shear measurement, and PSF correction methods. In particular, different galaxy selection criteria are applied, so that differences within both the statistical and systematical errors are not unexpected.

For GEMS the difference between the Heymans et al. (2005) and our estimate of $\sigma_8$ could be explained due to the different estimates of the redshift distribution, while the shear estimates were consistent (Sect. 6.5). For COSMOS the contrary effect seems to be the case: Both analyses are based on the photometric redshifts estimated by Mobasher et al. (2007), where Massey et al. (2007c) make use of an internal catalogue of the COSMOS collaboration, while we use the public catalogue, which is based on slightly fewer bands and only includes objects with $I < 25$. We therefore need to include an extrapolation for the redshift distribution. This difference might be responsible for some deviation within the systematic errors, but cannot explain the total effect. Note also that the median redshifts of the estimated distributions agree well, where we find $z_\mathrm{m} = 1.07$ while Massey et al. (2007c) estimate $z_\mathrm{m} = 1.11$ including their weighting scheme. However, Massey et al. (2007c) seem to measure a significantly higher shear signal, which can be

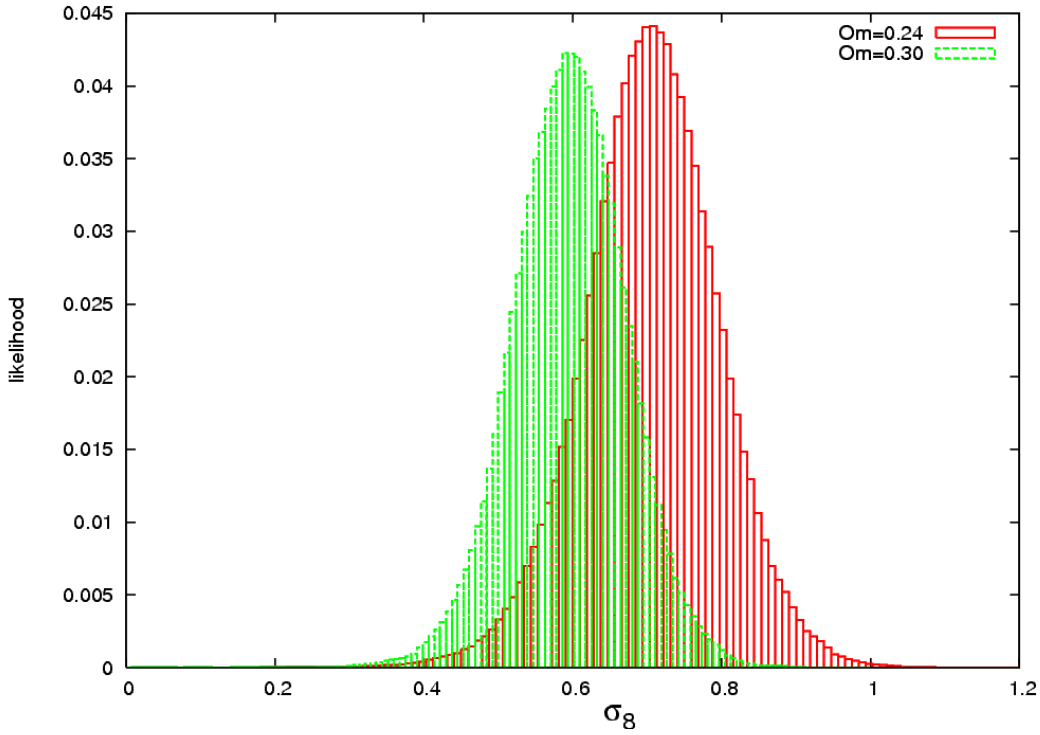


Figure 7.11: Histogram showing the likelihood distribution for $\sigma_8$ estimated from our COSMOS data assuming a flat ΛCDM cosmology. The green histogram corresponds to the default $\Omega_m = 0.3$, whereas the red histogram has been computed for $\Omega_m = 0.24$, as suggested e.g. by WMAP3. The likelihood has been marginalised over the uncertainties of $h$ and the redshift distribution.

seen from Figure 7.8 and Figure 7.9. Of course different selection criteria can yield significantly different shear estimates, but given the similar median redshifts we would expect more coinciding signal levels.

One reason for the different shear estimates could be given by a shear calibration bias of one of the methods, but due to the low bias estimated for both pipelines in STEP3, where the Massey et al. (2007c) analysis corresponds to the JR implementation of RRG, this explanation becomes rather implausible. The differences could also originate from the different PSF and CTE correction schemes, which could be related to the remaining B-modes detected at small scales for both analyses. Within the short time available for the COSMOS analysis we have not been able to unambiguously identify the reason for the different shear signal and postpone this task for a later stage, when we hopefully have a B-mode free catalogue at hand.

## 7.7 Principal component analysis of the ACS PSF

Earlier tests of our PSF correction scheme indicate that its accuracy should be sufficient for the statistical accuracy of the ACS data (Sect. 6.2.4.2). However, these tests were based on a limited sample of stellar fields, all taken with the F775W filter. Central assumptions of our correction scheme are that the PSF variation mainly occurs in a one-dimensional parameter space, and that the stellar fields sample this variation well. We decided to further test these assumptions given that we detect a significant small-scale B-mode in COSMOS (Sect. 7.5), which could be related to PSF residuals. For this test we perform a principal component analysis (PCA) of the ACS PSF variation.

A principal component analysis, which is often also referred to as Karhunen-Loève transform, is a linear transformation of the coordinate system providing new basis vectors pointing in the direction of the principal axes of data variation. Here we perform a PCA of the stellar field PSF patterns in coefficient space. This allows us to verify if the observed PSF variation is dominated by focus changes.

### 7.7.1 General description

As described in Sect. 6.2, we fit each of the two anisotropy kernel components in the stellar fields with third-order polynomials for each chip, resulting in a total of $M = 40$ coefficients for each field. For the $j$th field, we arrange these coefficients in a $M$-dimensional data vector $\boldsymbol{d_j}$, where we denote the $i$th component of the vector as $d_{ij}$. Computing the mean and standard deviation of the $i$th coefficient from all vectors

$$m_i = \frac{1}{N}\sum_{j=1}^{j=N} d_{ij}\,, \quad \sigma_i = \sqrt{\frac{1}{N}\sum_{j=1}^{j=N}\left(d_{ij} - m_i\right)^2}\,, \tag{7.8}$$

where $N$ denotes the number of fields, we define the mean-subtracted and standard deviation-normalised vector $\boldsymbol{x_j}$ for each field with components

$$x_{ij} = \frac{d_{ij} - m_i}{\sigma_i}\,, \tag{7.9}$$

which we arrange in a $M \times N$ dimensional data matrix

$$\boldsymbol{X} = \{\boldsymbol{x_1}, ..., \boldsymbol{x_j}, ..., \boldsymbol{x_N}\}\,. \tag{7.10}$$

The central step of the PCA is a singular value decomposition of $\boldsymbol{X}$

$$\boldsymbol{X} = \boldsymbol{W}\boldsymbol{\Sigma}\boldsymbol{V}^T\,, \tag{7.11}$$

where the orthonormal matrix $\boldsymbol{W}$ consists of the singular vectors of $\boldsymbol{X}$ and the diagonal matrix $\boldsymbol{\Sigma} = \{\boldsymbol{s_i}\}$ contains the ordered singular values of $\boldsymbol{X}$ as diagonal elements. Here the $k$th largest singular value corresponds to the $k$th singular vector, which is also named the $k$th principal

component. The first singular vector points in the direction of the strongest variation (largest scatter) of the data vectors $\boldsymbol{x_j}$ from the subtracted mean vector. Then the higher singular vectors define orthogonal directions along which the data vary less and less.

In the coordinate system spanned by the singular vectors, the correlation matrix of the data vectors $\boldsymbol{C}$ becomes diagonal

$$\boldsymbol{C} = \boldsymbol{X}\boldsymbol{X}^T = \boldsymbol{W}\boldsymbol{\Sigma}\boldsymbol{V}^T\boldsymbol{V}\boldsymbol{\Sigma}^T\boldsymbol{W}^T = \boldsymbol{W}\boldsymbol{\Sigma}\boldsymbol{\Sigma}^T\boldsymbol{W}^T = \boldsymbol{W}\boldsymbol{\Lambda}\boldsymbol{W}^T \,. \tag{7.12}$$

Hence, the singular vectors of $\boldsymbol{X}$ can be computed as the eigenvectors of $\boldsymbol{C}$. The eigenvalues $\lambda_i = s_{ii}^2$ of the diagonal matrix $\boldsymbol{\Lambda}$ are equal to the variance of the vectors $\boldsymbol{x_j}$ along the direction of the $i$th principal component.

Due to the normalisation applied in (7.9), the variance of the $i$th coefficient computed from all $N$ fields becomes

$$v_i = \frac{1}{N}\sum_{j=1}^{j=N}\Big(x_{ij} - 0\Big)^2 = \frac{1}{N\sigma_i^2}\sum_{j=1}^{j=N}\Big(d_{ij} - m_i\Big)^2 = 1 \,. \tag{7.13}$$

Using the invariance of the trace under orthonormal transformations we then find that

$$\mathrm{Tr}\,\boldsymbol{\Lambda} = \mathrm{Tr}\,\boldsymbol{C} = \sum_{i=1}^{i=M} v_i = M \,. \tag{7.14}$$

Hence, $\lambda_i/M$ gives the relative fraction of the total variation of the data along the direction of the $i$th principal component.

Again, the variation of the vectors $\boldsymbol{x_j}$ is largest in the direction of the (most important) first principal component, which we name "focus position" (in an arbitrary unit) in our case. The higher principal components are getting less and less important, as the data show less variation in these directions. Depending on the accuracy sought, one might therefore choose to only keep the first $L$ principal components and neglect the data variation along all higher ones. In some applications this is used for data compression. Yet, for a PSF analysis it is the main aim to describe the PSF variation with a low number of parameters.

Dropping the higher principal components corresponds to a projection of $\boldsymbol{X}$ onto the reduced space spanned by the first $L$ singular vectors

$$\boldsymbol{Y_L} = \boldsymbol{W_L}^T\boldsymbol{X} \,, \tag{7.15}$$

where we denote the components of $\boldsymbol{Y_L}$ as $y_{lj}$ and $\boldsymbol{W_L}^T$ has been formed out of $\boldsymbol{W}^T$ by filling rows $L+1, ..., M$ with 0. The data points projected onto the reduced space can then be transformed back to the original coordinates as

$$\boldsymbol{X_L} = \boldsymbol{W}\boldsymbol{Y_L} \,. \tag{7.16}$$

Note that a PCA is sometimes performed without the standard deviation-normalisation in (7.9), which yields the covariance matrix instead of the correlation matrix in (7.12), and a different normalisation with the $\lambda_i$ being *absolute* variances. The analysis presented here is partially based on public PCA code by F. Murtagh[1].

[1] `http://astro.u-strasbg.fr/~fmurtagh/mda-sw/pca.c`

### 7.7.2 Application to the PSF models

In this subsection we apply the PCA formalism described in Sect. 7.7.1 to the stellar field *DRZ*-PSF models. Here we limit most of the discussion and detailed plots to the F814W PSF models being the relevant filter for COSMOS and a specific Gaussian filter scale of $r_g = 2.8$ pixels. The derived results and conclusions are in qualitative agreement with those for other filters and Gaussian filter scales (e.g. similar eigenvalues, see Fig. 7.14) differing in details such as the higher singular vectors.

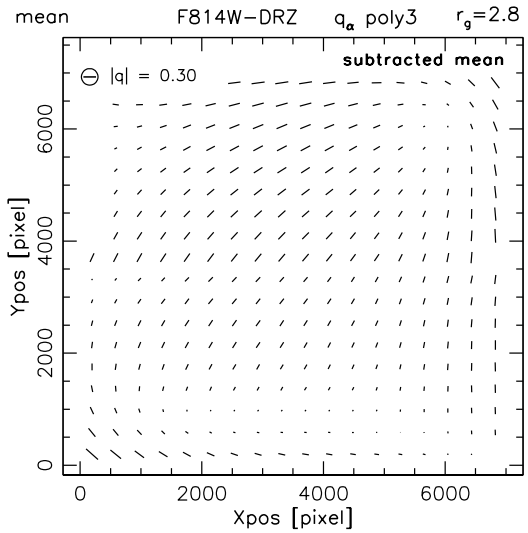


Figure 7.12: Mean PSF model computed from all F814W *DRZ*-PSF models for $r_g = 2.8$ pixels. This model is subtracted during the first step of the PCA.

For the F814W star fields, we plot the subtracted mean PSF model in Fig. 7.12, and the first four singular vectors in Fig. 7.13. The first singular vector closely resembles what has been labelled a typical PSF pattern with negative focus offset in Sect. 6.2.2 (compare to Fig. 6.5). Consistent between different filters about 60% of the total PSF variation (variance of the models in coefficient space) occurs in the direction of this first principal component, which can be seen from the normalised eigenvalues $\lambda_l/M$ plotted in Fig. 7.14 and tabulated in Tab. 7.2. Given that the first eigenvalue exceeds all higher eigenvalues by at least one order of magnitude, the first principal component by far represents the most important term. However, it is unable to describe the full PSF variation, where due to the rather slow decrease of the eigenvalues $\lambda_l/M$ for $2 \leq l \lesssim 23$ (see Fig. 7.14), 12 (24) principal components are required to capture 90% (99%) of the total variance.

We plot the coefficients $y_{lj}$ of the PSF models projected onto the parameter space spanned by the first four singular vectors in Fig. 7.15. Except for a low number of outliers the apparent distribution of occurring PSF models seems to be sampled well by the star fields confirming the applicability of our PSF correction scheme. We note that there are indications for substructure in the model distribution within the plane spanned by the first and third singular vectors. This possibly indicates some non-linear dependence, which would not be accounted for by the PCA.

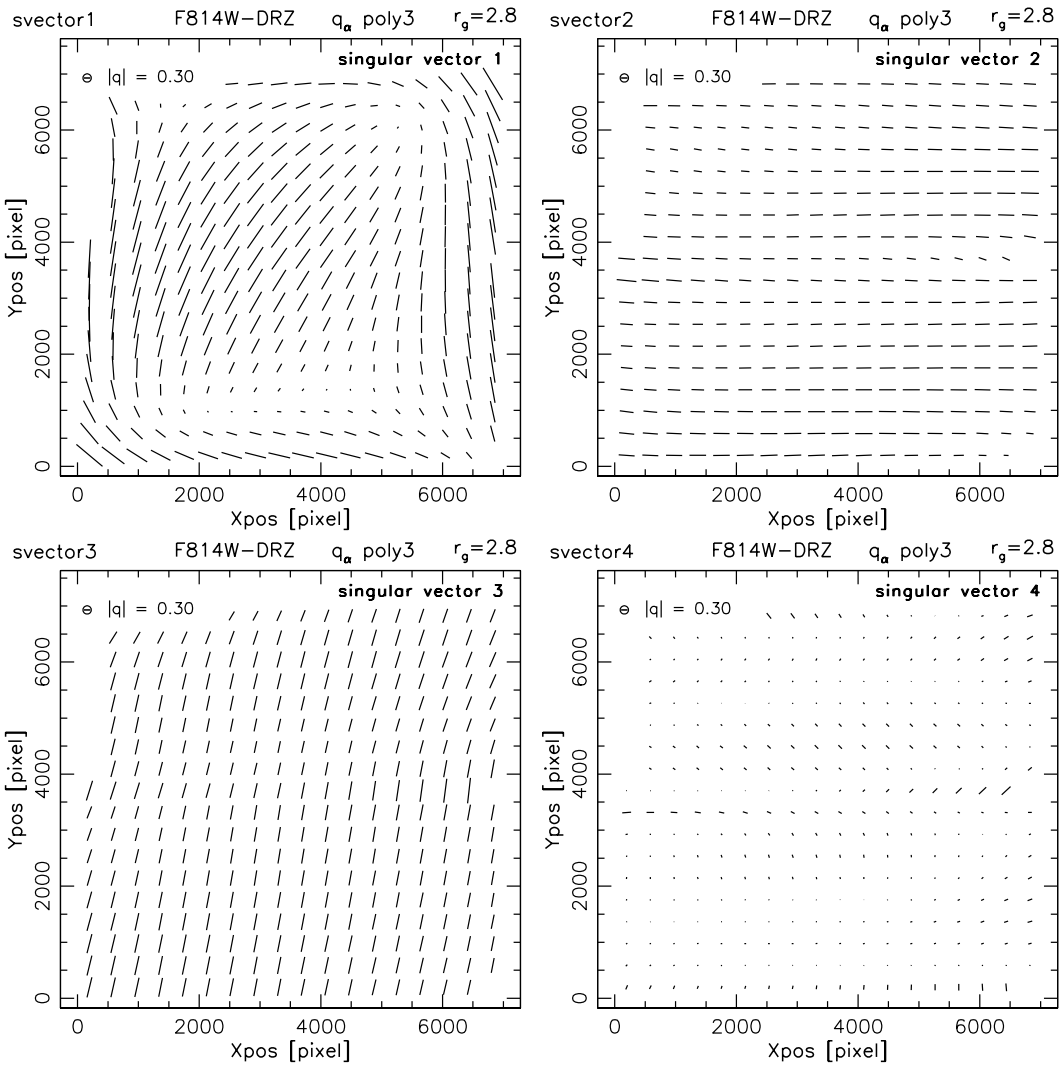


Figure 7.13: The first four singular vectors for the F814W *DRZ*-PSF models for $r_g = 2.8$ pixels.

However, due to the dominance of the first principal component we did not attempt to correct for this effect.

In order to further illustrate the relative impact of the different principal components we pick six PSF models according to their position projected onto the first principal component $y_1 = y_{1j}$, but randomly concerning the higher principal components. In Fig. 7.16 we plot these models as well as a reconstruction using only the first principal component ($L = l_{\max} = 1$) and residuals after subtraction of this reconstruction. The first principal component already provides a good approximation for the overall coherent pattern. However, if residuals should be suppressed with high accuracy, a high number of principal components has to be taken into account ($L \gtrsim 20$). This can be seen from the also shown residuals for $L = 10$, which provides only moderate improvement compared to $L = 1$.

As an additional test we perform the analysis using the covariance matrix instead of the

Table 7.2: Eigenvalues $\lambda_l/M$ of the first 10 principal components for filters F606W, F775W, and F814W, for filter scale $r_g = 2.8$ pixels.

| $l$ | $\lambda_l^{606}/M$ | $\lambda_l^{775}/M$ | $\lambda_l^{814}/M$ |
|---|---|---|---|
| 1 | 0.665 | 0.588 | 0.637 |
| 2 | 0.038 | 0.056 | 0.040 |
| 3 | 0.034 | 0.044 | 0.038 |
| 4 | 0.029 | 0.042 | 0.032 |
| 5 | 0.027 | 0.040 | 0.031 |
| 6 | 0.025 | 0.028 | 0.023 |
| 7 | 0.024 | 0.022 | 0.023 |
| 8 | 0.020 | 0.021 | 0.020 |
| 9 | 0.019 | 0.019 | 0.018 |
| 10 | 0.015 | 0.016 | 0.016 |

correlation matrix, with very similar overall results. The covariance analysis behaves mildly less stable for high principal components $l \gtrsim 15$, on average leading to slightly stronger residuals if a large number of principal components are considered.

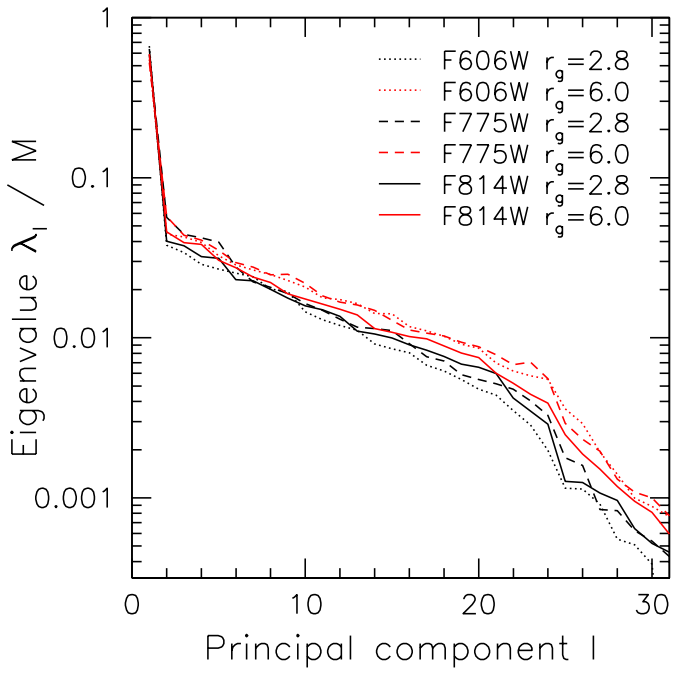


Figure 7.14: Eigenvalues $\lambda_l/M$ of the first 30 principal components for filters F606W, F775W, and F814W, for filter scales $r_g = (2.8, 6.0)$ pixels.

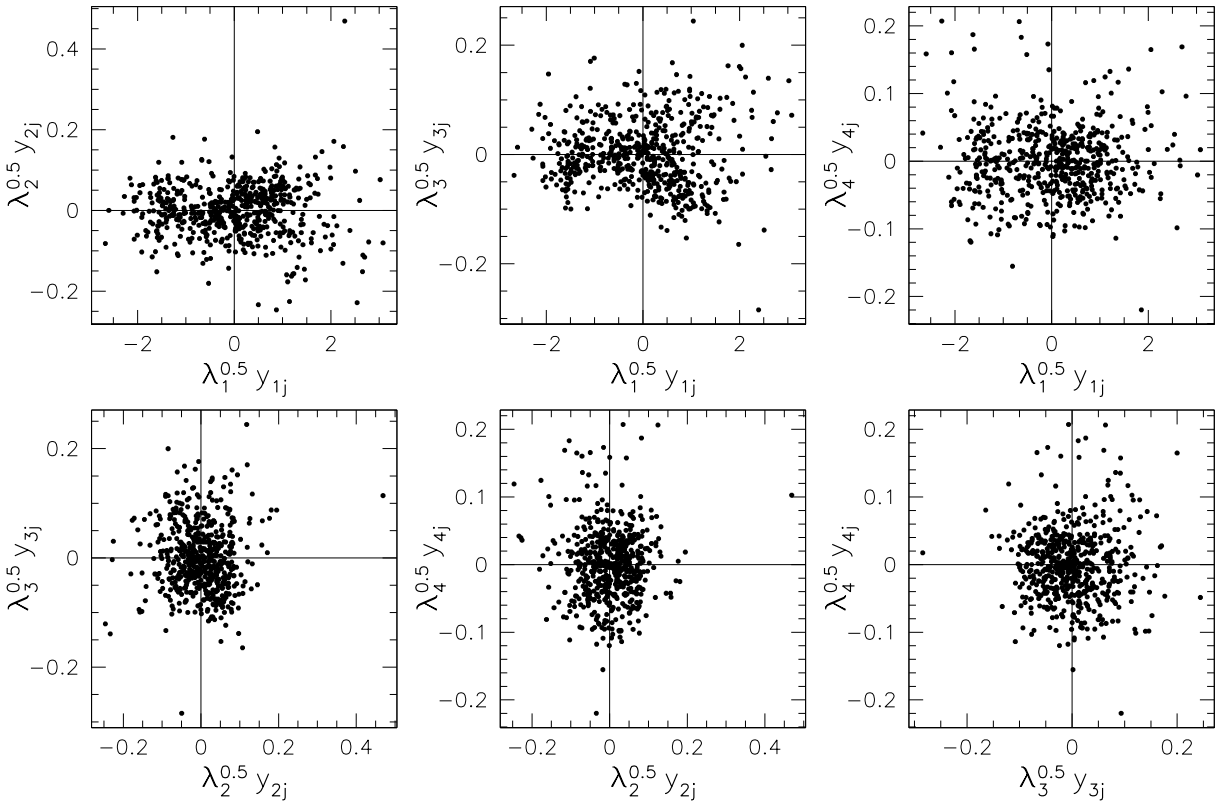


Figure 7.15: Location of the F814W stellar field *DRZ*-PSF models in the parameter space spanned by the first four singular vectors (principal components), scaled with the singular values $s_{ll} = \sqrt{\lambda_l}$ to illustrate their relative importance. Note the different scaling of the axes in the different panels and the apparent substructure in the plane spanned by the first and the third singular vector (*top middle*).

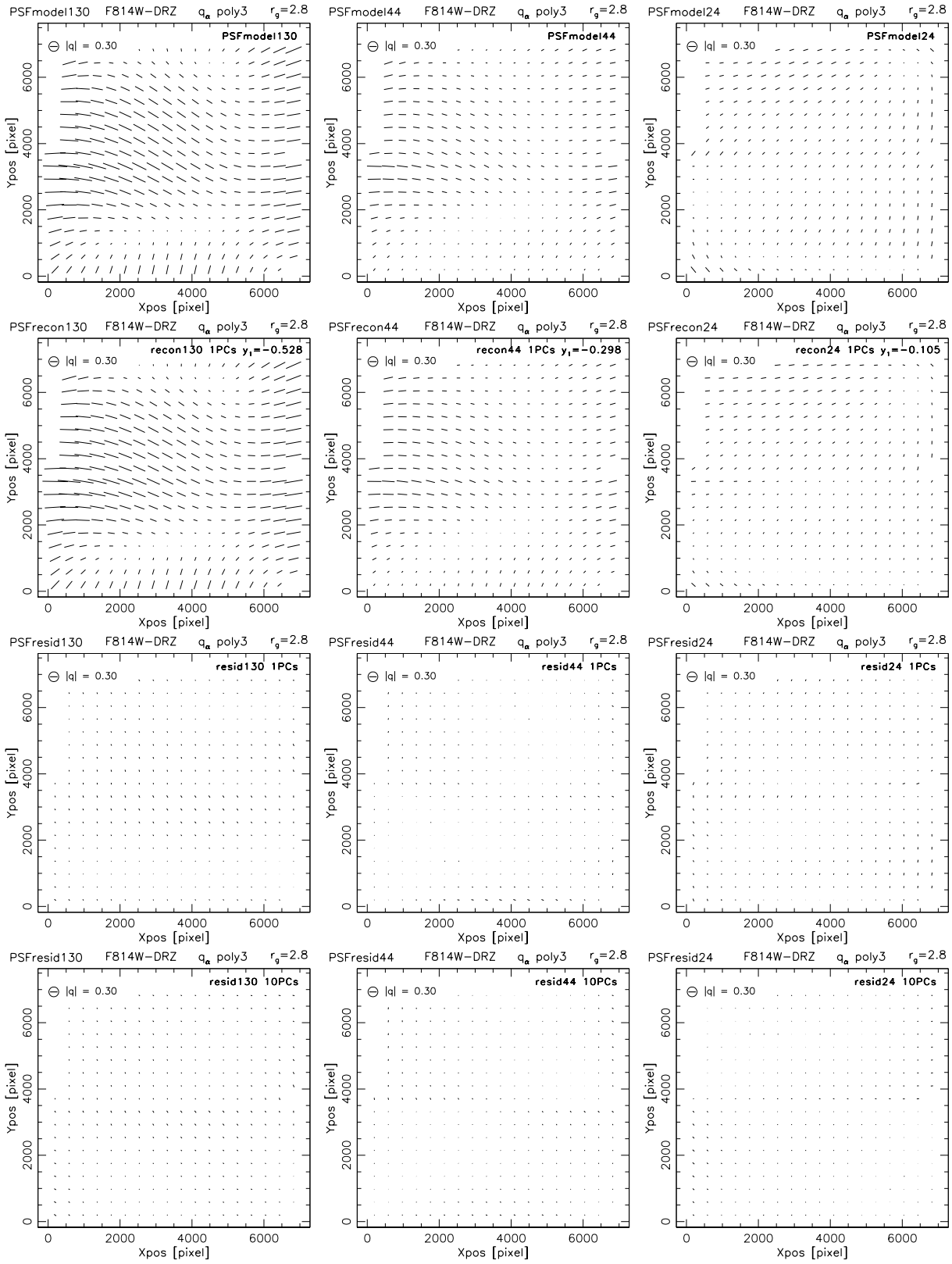


Figure 7.16: PSF models (*1st row*), PCA reconstruction using only the first principal component $L = 1$ (*2nd row*), residuals for $L = 1$ (*3rd row*), and residuals for $L = 10$ (*4th row*) for six F814W stellar field *DRZ*-exposures, of which three are shown on the next page. All models have been computed for a filter scale $r_g = 2.8$ pixels. (*Continued on the next page*)

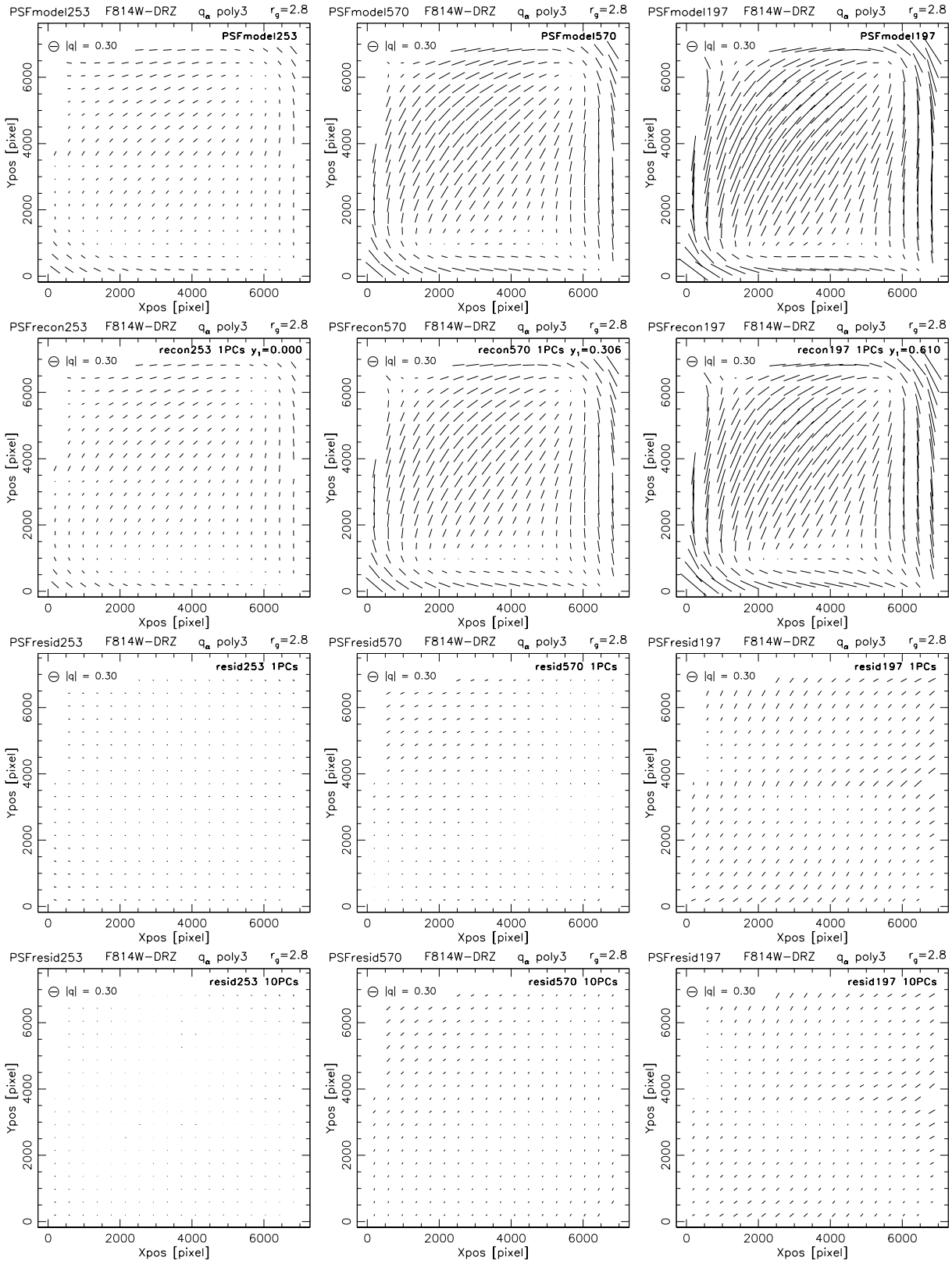


Figure 7.16: (*continued*) The fields are sorted according to their position $y_1$ along the first principal component, which relates to the focus position. The increase from $L = 1$ to $L = 10$ principal components reduces the residuals only moderately. For a robust suppression $L \gtrsim 20$ is required.

## 7.8 Conclusions

In this chapter we have presented an independent weak lensing analysis of the ACS COSMOS Survey. Compared to the data sets analysed in Chapter 6, COSMOS provides an increase in sky area of approximatly a factor seven. The increased sensitivity reveals previously undetectable indications for remaining systematics, which could not be identified in the short time remaining for the analysis. Therefore, the results presented here are only preliminary, and further tests, which will hopefully yield a catalogue free of detectable systematics, are planned for the time after this thesis write-up.

As a first result, we reconstruct the projected mass in the COSMOS field. Our results agree well with the dark matter maps and baryonic tracers presented by Massey et al. (2007b). Additonally, our 2D cosmological parameter estimation yields $\sigma_8 = 0.71 \pm 0.09$ for $\Omega_m = 0.24$, which is in good agreement with the WMAP-3 results. It is slightly lower than most of the recent ground-based shear estimates, e.g. $\sigma_8(\Omega_m/0.24)^{0.59} = 0.84 \pm 0.05$ found by Benjamin et al. (2007). This is not too surprising given the lack of exceptionally massive structures in the COSMOS field, which still suffers from significant sampling variance. Surprisingly however, Massey et al. (2007c) derive a significantly higher value for $\sigma_8$ from their cosmic shear analysis of the COSMOS field yielding $\sigma_8 = 0.90 \pm 0.083\,(\text{stat.}) \pm 0.104\,(\text{syst.})$ for a similar 2D analysis and $\sigma_8 = 0.96 \pm 0.037\,(\text{stat.})^{+0.058}_{-0.039}\,(\text{syst.})$ for a 3D analysis, both for $\Omega_m = 0.24$. We do expect variations within the errors given that both analyses are based on independent data reduction pipelines, shape measurement and PSF correction methods, and different selection criteria. However, the large discrepancy might suggest that further systematic errors may be present in one or both of the analyses. Our preliminary analysis suggests that this difference rather originates from the shear measurement than the estimates of the photometric redshift distribution. Note that both analyses still suffer from B-mode signals at small scales. If the origin for the B-modes can be identified and corrected, the difference in $\sigma_8$ might become less significant.

In any case it will be important to understand the cause for the different results. While STEP tests the actual shape measurement in shear pipelines on simulated data, this is only one step of a cosmic shear analysis. Comparisons of different pipelines on the same dataset as done here are an important additional test to verify the creditability of cosmological weak lensing studies. In order to understand the reason for the different estimates it might be helpful to perform a direct comparison of the shear catalogues.

Using a principal component analysis (PCA) we have been able to verify that most of the PSF variation occurs in a one-dimesional parameter space, which can be identified as the focus position. This is an important confirmation for the applicability of our PSF correction scheme. Higher principal components do play a role if very high accuracy is sought. For a future analysis we are considering to upgrade our PSF correction scheme with the PCA, which will allow the inclusion of higher principal components in the fit depending on the number of stars present in the field. A similar correction scheme will surely be necessary for dedicated future weak lensing missions. In addition, the PCA will allow us to split the galaxy field ACS tiles into groups with similar PSF properties, which could prove helpful in order to identify the origin of the B-mode component.

Possibly the detected B-mode signal could also be related to changes of the ACS camera

distortion. We have reported on a possible medium-term variation in Sect. 6.1.2. In addition, Anderson (2006, 2007) find indications for variations of the linear distortion terms, where they detect both a long-term trend and short-term breathing-induced variations. For COSMOS, long-term variations are unproblematic given that each COSMOS tile was observed within one orbit and the overall distortion is only of order $\sim 10^{-4}$, about two orders of magnitude below the cosmic shear signal. However, breathing induced variations might lead to significant misalignments between the individual exposures, which would be uncorrected by our pipeline. This effect could significantly degrade the PSF in the co-added frame, which would not be taken into account by our PSF correction scheme. Hence, it could possibly cause the detected B-mode signal.

# Chapter 8

# Other ACS projects

Besides the major ACS science projects described in Chapters 6 and 7, parts of the developed ACS data reduction and shear measurement pipeline have also been used in further studies led by some of my collaborators. In addition, we are still working in further gravitational lensing studies using ACS data. Here I will briefly summarise several of these projects, following a chronological order. For details the reader is referred to the corresponding papers.

## 8.1 Measuring the mass distribution of the merging galaxy cluster 1E0657–56 with strong and weak lensing

Bradač, Clowe, Gonzalez, Marshall, Forman, Jones, Markevitch, Randall, Schrabback, & Zaritsky (2006) study the strong and weak lensing signal of the merging galaxy cluster 1E0657–56, dubbed the "Bullet cluster", and compare it to the emission of hot X-ray gas. In this cluster, which is located at a redshift $z = 0.296$, recently two sub-components merged nearly in the plane of the sky, where the sub-cluster left the core of the main cluster with a relative velocity of $4500^{+1100}_{-800}\,\mathrm{km\,s^{-1}}$ as deduced from the gas bow shock seen in X-rays. Due to dissipation the gas is slowed down and trails behind the galaxies, which follow basically collisionless trajectories.

Using new HST/ACS images, Bradač et al. (2006) and Clowe et al. (2006) have been able to study the mass distribution of the system using gravitational lensing. While Clowe et al. (2006) uses pure weak lensing constraints, Bradač et al. (2006) combine weak and strong lensing measurements. I contributed to this work during the reduction of the ACS images, where Maruša Bradač's pipeline was based on our Mark-I pipeline.

The result of the analysis is illustrated in Figure 8.1 showing that the major mass component resides with the galaxies and *not* the gas, which contains most of the baryonic mass. This observation is consistent with the picture that galaxies are surrounded by (nearly) collisionless dark matter halos, which follow the trajectories of the stellar component. Hence, it is currently considered to be the strongest evidence for the existence of dark matter. Note that Angus et al. (2007) claim that they are able to to describe the Clowe et al. (2006) weak lensing $\kappa$-map of the system in the framework of modified Newtonian dynamics (MOND) without CDM, if neutrinos

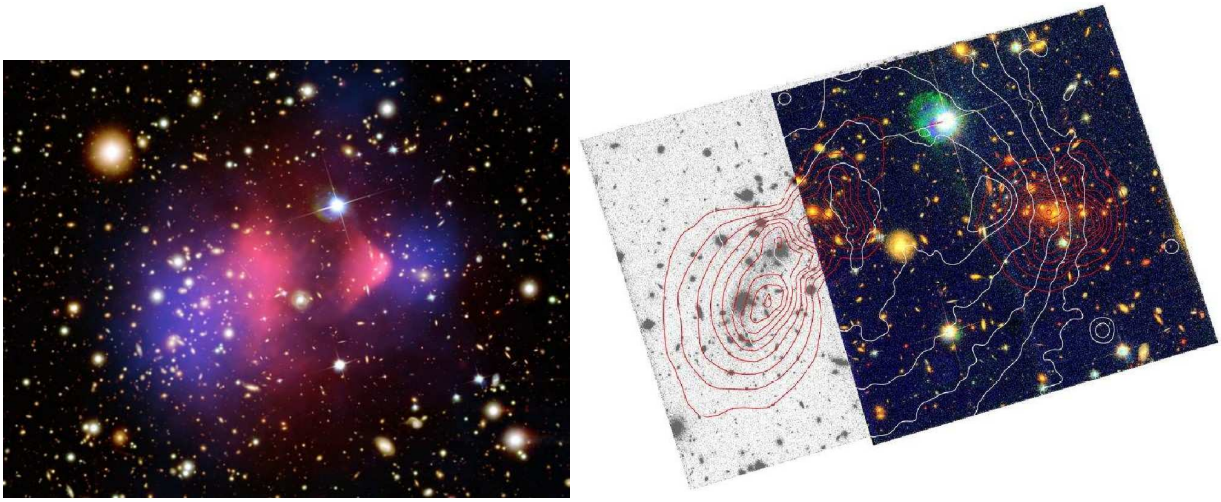

Figure 8.1: The merging "Bullet" galaxy cluster 1E0657–56, *Left*: Press-release image, where the central region shows the HST/ACS colour image, whereas the outer regions use data from the Magellan telescope. Red overlays show the location of hot X-ray gas observed by Chandra. Blue overlays show the location of the major mass components inferred from gravitational lensing. Due to the merger the hot gas, which contains most of the baryonic mass, is observed offset from the major mass component deduced from gravitational lensing. This observation is currently considered to be the most direct evidence for the existence of (collisionless) dark matter (image courtesy: Maruša Bradač). *Right*: HST/ACS image, where the overlaid red contours show the strong and weak lensing $\kappa$–reconstruction, linearly spaced with $\Delta\kappa = 0.1$ starting at $\kappa = 0.5$ for a fiducial source redshift $z_s \to \infty$. The white contours indicate X-ray brightness measured from 500 ks Chandra ACIS-I observations. North is up and East is left, the field is $4\farcm9 \times 3\farcm2$, which corresponds to $1300 \times 830\,\mathrm{kpc}^2$ at the redshift of the cluster (Figure 4 from Bradač et al. 2006).

have masses of $\sim$ 2 eV. The Karlsruhe Tritium Neutrino Experiment[1] (KATRIN) was designed to measure the mass of the electron neutrino with an accuracy of 0.2 eV. Thus, this loophole for MOND may be closed soon. In addition, it has not been shown that MOND is also able to describe the steep inner mass profiles derived from the combined strong and weak lensing analysis.

## 8.2 Comparing X-ray and gravitational lensing mass estimates of the most X-ray luminous galaxy cluster RXJ1347.5–1145

The galaxy cluster RXJ1347.5–1145 ($z = 0.451$) is the most X-ray luminous galaxy cluster know to date. It has already been subject of numerous lensing and X-ray studies (see e.g. Gitti et al. 2007; Bradač et al. 2005; Cohen & Kneib 2002, and references therein), which however led to significantly discrepant results.

[1] http://www-ik.fzk.de/~katrin/index.html

Our collaboration successfully applied for HST/ACS observations of the cluster, which have been carried out in HST Cycle 14 (proposal 10492, PI: Thomas Erben) on March 9-11, 2006. The cluster was observed in the three filters F475W, F814W, and F850LP for 5280s each.

My task was the reduction of the data, first with an upgraded version of the Mark-I pipeline, and later the improved Mark-II pipeline. In addition, I created weak lensing catalogues from the co-added F814W image, similarly to our analysis of the COSMOS data (Chapter 7).

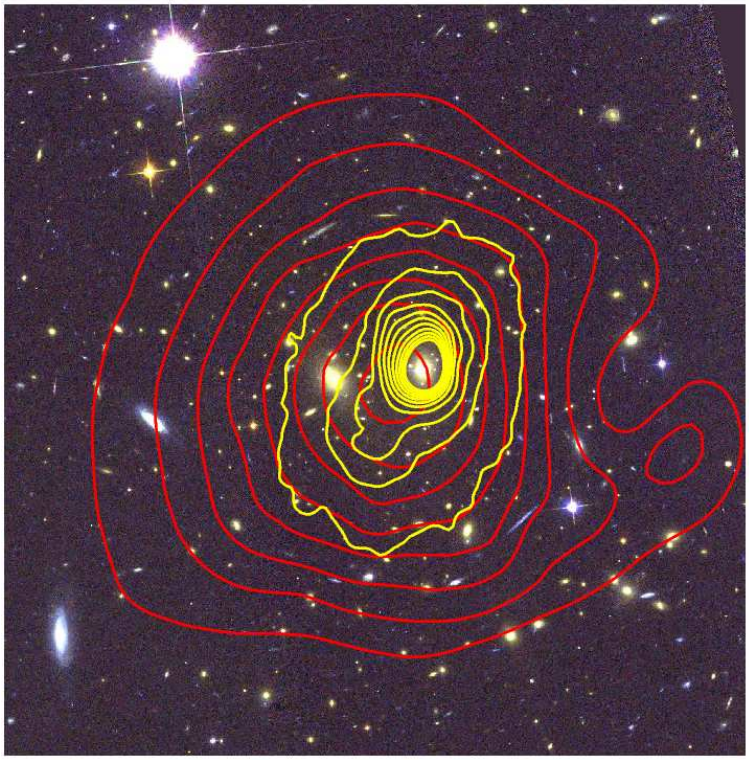

Figure 8.2: The F475W–F814W–F850LP colour composite of the cluster RXJ1347.5–1145. Overlaid in red contours is the preliminary surface mass density from the combined weak and strong lensing mass reconstruction. The contour levels are linearly spaced with $\Delta\kappa = 0.2$, starting at $\kappa = 0.5$, for a fiducial source at a redshift of $z_s \to \infty$. The linearly spaced X-ray brightness contours are overlaid in yellow and have been determined from 67 ks Chandra ACIS-I observations. North is up and East is left, the field is $2\farcm5 \times 2\farcm5$, which corresponds to $870 \times 870\,\mathrm{kpc}^2$ at the redshift of the cluster (from Bradač et al. in prep.).

The data have been used for a strong lensing analysis (Halkola et al. 2007) and a combined strong and weak lensing analysis (Bradač et al. in prep.). A central aspect of these analyses is the identification of new multiple-image candidates from the ACS data. The preliminary combined strong and weak lensing analysis yields a projected mass estimate for the cluster centre $M_L(< 350\mathrm{kpc}) = (5.9 \pm 0.5) \times 10^{14} M_\odot$, which is in in excellent agreement with X-ray mass estimates from Chandra data yielding $M_X(< 350\mathrm{kpc}) = (6.6^{+0.6}_{-0.4}) \times 10^{14} M_\odot$. Figure 8.2 shows an image of the cluster core with a preliminary $\kappa$–reconstruction using the strong and weak lensing analysis,

in comparison with X-ray estimates. For the full ACS image see Figure 3.4.

## 8.3 HAGGLeS: The HST Archive Galaxy-scale Gravitational Lens Survey

As already mentioned in Sect. 5.3, we joined forces with the HAGGLeS Project lead by Phil Marshall for the reduction of a large fraction of the ACS archive. Most of the HAGGLeS fields have been reduced at the time of the write-up using our Mark-II reduction pipeline, and are now being further analysed.

For the HAGGLeS field selection we excluded large surveys with publicly available reduced images such as GEMS, GOODS, COSMOS, EGS, and the Hubble Deep fields. Also galactic fields or observations of nearby galaxies filling the entire field-of-view have been rejected. HAGGLeS consists of two main data sets, which partially overlap:

### 8.3.1 The HAGGLeS strong lens search fields

Fields with an exposure time of at least 2 ks in two or more broad-band filters have been selected for the strong lens search. For the automatic lens search colour information is critical to reliably select multiple image candidates. The strong lens portion of HAGGLeS comprises a total of 224 fields.

Strong lens candidates identified by the lens robot are visually inspected using our web-tool (Sect. 5.3.3). A first paper describing the project, data, data reduction, and first results is currently been written (Marshall et al. in prep.).

### 8.3.2 The HAGGLeS weak lensing fields

For the cosmological weak lensing analysis we do not require observations in multiple filters, but it is crucial that we select quasi random pointings. For example, the ACS archive contains a large number of observations of galaxy clusters. If included, these fields would lead to a significant over-estimation of $\sigma_8$. To minimise potential selection bias we require that a field is either observed in parallel mode or has been pointed at a target with $z < 0.07$ or $z > 1.2$, yielding very low lensing efficiency at the target redshift. In the case of parallel observations a potential bias may arise from primary observations pointing at galaxy clusters, which could significantly affect the shear signal in the parallel field. However, it is possible to test for such a bias, e.g. by investigating the shear signal as a function primary target class. In addition, such a bias will lead to a net mean shear depending on the relative position of the cameras, e.g. a mean positive $\gamma_2$ signal for primary observations with WFPC2.

For this survey we require a minimal exposure time of 1200 s in one of the broad band filters F606W, F625W, F775W, or F814W, with a minimum number of three exposures to enable good cosmic rays rejection. With these selection criteria we estimate that the whole data set will amount to approximately 440 pointings or a total area of 1.22 deg$^2$, consisting of $\sim$ 69% parallel

and ∼ 31% primary observations. We also refer to this data set as the "Extended ACS Parallel Survey".

This survey is relatively complimentary to COSMOS: due to the many independent lines-of-sight the impact of cosmic variance will be minimal. Yet, the survey will be limited to relatively small scales, for which we expect to constrain the total matter power spectrum with high accuracy. At a typical lens redshift with high lensing efficiency ($z \sim 0.4$) the ACS field size corresponds to a physical (co-moving) separation of ∼ 1 Mpc, for which current predictions of the non-linear power spectrum seem to be sufficiently good to obtain interesting constraints on $\sigma_8$. We also expect to obtain tight constraints on the small-scale, sub-arcminute power spectrum. These cannot be used to constrain $\sigma_8$ due to the current lack of accurate theoretical predictions at a regime when baryons become important. However, these measurements can then be used to test simulations helping to understand the impact of baryons on the power spectrum.

## 8.4 STAGES: the A901/A902 super-cluster field

STAGES (HST GO-10395, PI M. E. Gray) is a $30' \times 30'$ mosaic consisting of 80 ACS/WFC tiles, each imaged for one orbit (1960 s) with four dithered exposures using the F606W filter. It has been pointed at the known galaxy super-cluster Abell 901/902 ($z = 0.16$) and is therefore not suited for cosmic shear measurement, but can be used for different weak lensing studies.

We have reduced the images using our Mark-II pipeline and created weak lensing catalogues similarly to our analysis of the COSMOS data. Figure 8.3 shows a preliminary weak lensing mass reconstruction of the field. With this study we aim to constrain the total cluster mass and projected mass distribution. We also want to verify the existence of a dark matter filament between A901a and A901b, which has been reported by Gray et al. (2002) on the basis of shallower ground-base data.

A key ingredient for further studies with the data are accurate photometric redshifts. Photometric redshifts have been measured for the field as part of the COMBO-17 project. However, these data are relatively shallow, so that redshift estimates are only available for a minor fraction of the source galaxies. Kitching et al. (2007) use the COMBO-17 redshifts in combination with the ground-based weak lensing catalogue of Brown et al. (2003) to apply the so-called shear-ratio-test for the field. Here the relative strength of the shear signal is measured as a function of redshift, which is a sensitive cosmological test. In combination with a deep photometric redshift catalogue the high-resolution ACS images would allow us to do this analysis with substantially increased statistical accuracy. The low dependence of shear measurements with our pipeline on galaxy magnitude and size, which was demonstrated for STEP3 (Sect. 4.4), would be very useful for such a 3D analysis.

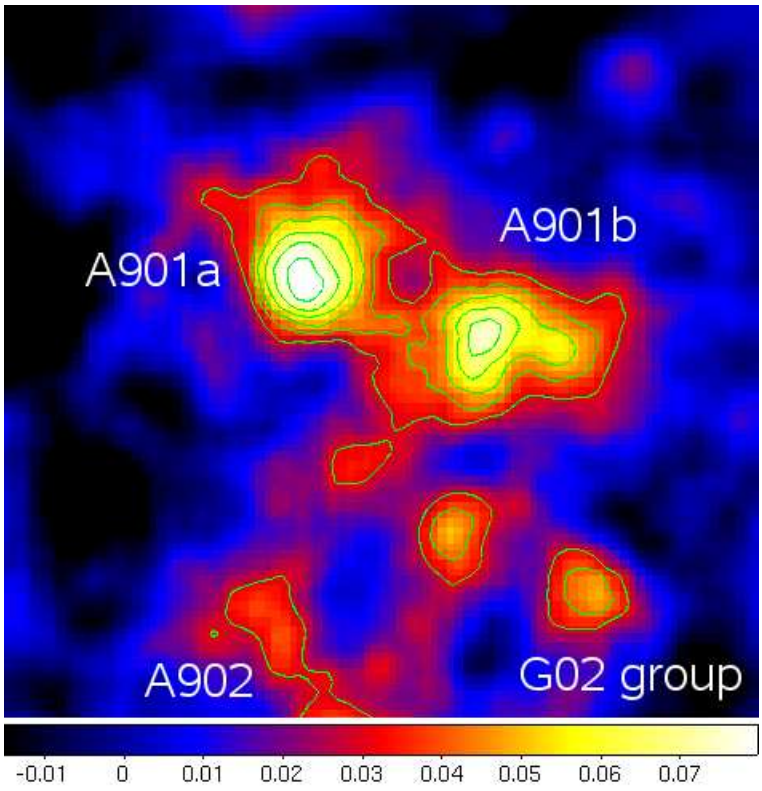


Figure 8.3: Preliminary reconstruction of the projected mass in the 30′×30′ STAGES A901/A902 super cluster field using our shear catalogue. The maximum likelihood reconstruction takes noise propagation and Wiener filtering into account as suggested by Hu & Keeton (2002), implemented by Patrick Simon, and detailed in Hetterscheidt et al. (in prep.). North is up and East left. The known galaxy clusters A901a, A901b, and A902 are marked, as well as the signal of a galaxy group discovered by Gray et al. (2002). Note the much steeper $\kappa$–scale compared to Figure 7.4. Contours show $\kappa$-levels spaced by $\Delta\kappa = 0.01$ starting at $\kappa = 0.03$.

# Chapter 9

# Conclusions and outlook

I will summarise the main results and conclusions in Sect. 9.1, and elaborate on future perspectives in Sect. 9.2. For a more detailed discussion and conclusions from the individual science projects see the concluding sections given at the end of each analysis chapter (chapters 4, 6, and 7).

## 9.1 Conclusions

With this thesis project I was given the extraordinary opportunity to contribute to the exciting field of cosmological weak lensing at a time when it was turning into a mature field of precision cosmology. Besides growing surveys, such as the ongoing CFHT Legacy Survey, this time has seen substantial development of weak lensing methods initiated and enhanced by the STEP Project, in preparation of future generations of surveys.

With the STEP blind tests we provided benchmarks quantifying the accuracy of the different weak lensing pipelines and helping to identify and eliminate systematic errors and biases. During the course of three STEP projects we successfully improved the mean shear recovery accuracy of our KSB+ pipeline from the $\sim 20\%$ to the $\sim 2\%$ level, with a $\sim \pm 5\%$ variation as a function of magnitude and size only. Similarly well tuned pipelines have the potential to serve as sufficiently accurate tools for current surveys, such as the work presented here, but also surveys as large as the CFHT Legacy Survey. For the coming generation of surveys, such as PanSTARRS-1 and VST/KIDS, a systematic accuracy of $\sim 2\%$ will be sufficient for the early phase but ultimately dominate the total error budget for the completed surveys. Proper correction for systematic errors will be even more crucial for fourth generation surveys such as DES, PanSTARRS-4, LSST, DUNE, and JDEM/SNAP, requiring sub-percent level accuracy. Due to several fundamental shortcomings and limitations we do not expect that the KSB+ formalism will be able to reliably reach this level of accuracy. This underlines the urgent need to develop and improve new methods such as the ones described by Kuijken (2006) and Nakajima & Bernstein (2007), combined with continued STEP-like tests.

Previous ground-based surveys have measured the cosmic shear signal from several tens of square degrees. Recently, Benjamin et al. (2007) presented a joint analysis of cosmic shear data

from the CFHTLS-Wide, RCS, VIRMOS-DESCART, and GaBoDS surveys, amounting to a total sky area of $\sim 100\,\mathrm{deg}^2$, from which they find $\sigma_8(\Omega_\mathrm{m}/0.24)^{0.59} = 0.84 \pm 0.05$.

For space-based surveys covering a mosaic of a single field it is difficult to provide competitive constraints on $\sigma_8$ due to strong influence of sampling variance. Especially the $0.22\,\mathrm{deg}^2$ GEMS Survey targeting the *Chandra Deep Field South* seems to suffer from strong sampling variance. For this field we obtain an estimate for the power spectrum normalisation of $\sigma_8 = 0.59^{+0.13}_{-0.17}\,(\mathrm{stat}) \pm 0.07\,(\mathrm{sys})$, for a fixed matter density $\Omega_\mathrm{m} = 0.24$[1] assuming Gaussian sampling variance (see Sect. 6.5). This estimate agrees only marginally with the WMAP-3 result of $\sigma_8 = 0.761^{+0.049}_{-0.048}$ (Spergel et al. 2007) and is significantly below the value found by Benjamin et al. (2007). From this discrepancy we conclude that there is a significant under-density of compact foreground structures in the CDFS. This is also consistent with results from Phleps et al. (2007), who find a significant depletion of red galaxies in the field. Note that Heymans et al. (2005) originally derived a higher value $\sigma_8 = 0.79 \pm 0.15$ (for $\Omega_\mathrm{m} = 0.24$) from the GEMS data. While we have been able to show that their and our shear measurements agree with a relative accuracy of $\sim 3\%$, we found that their $\sigma_8$ estimate is most probably biased due to an under-estimation of the mean redshift of the survey.

Studies performing ray-tracing through N-body simulations indicate that non-linear evolution leads to significant non-Gaussian sampling variance (Kilbinger & Schneider 2005; Semboloni et al. 2007; Hartlap et al. in prep), which suggests that we actually under-estimate the statistical uncertainty. The frank conclusion is that the sky coverage of GEMS is too small to yield representative cosmological parameter constraints using cosmic shear. The concluding picture is that the line-of-sight in the CDFS mostly passes through voids, whereas compact structures are rare. Following from the preliminary ray-tracing comparison by Hartlap et al. (in prep.), this seems to be a peculiar, but not extraordinary rare configuration, assuming a WMAP-3 cosmology.

Note that our $\sigma_8$ estimate from the CDFS was more discrepant with other weak lensing results at the time of the analysis. For example, early results from the CFHTLS yielded significantly higher $\sigma_8$ estimates of $\sigma_8 = 0.86 \pm 0.05$ (Semboloni et al. 2006) and $\sigma_8 = 0.85 \pm 0.06$ (Hoekstra et al. 2006) computed for $\Omega_\mathrm{m} = 0.3$, which corresponds to $\sigma_8 = 0.98 \pm 0.06$ and $\sigma_8 = 0.97 \pm 0.07$ for $\Omega_\mathrm{m} = 0.24$. However, with the new Benjamin et al. (2007) analysis, which makes use of a carefully calibrated redshift distribution and considers recent STEP results, the tension has been significantly reduced. It will be interesting to observe if this trend towards lower $\sigma_8$ estimates from cosmological weak lensing studies continues in the post-STEP era.

We presented a preliminary analysis of the ACS/COSMOS Survey in Chapter 7. Although this is also a single mosaic field, the approximately seven times larger sky area of $1.64\,\mathrm{deg}^2$ considerably reduces the influence of sampling variance compared to GEMS. From our analysis we have been able to confirm the main features of the projected dark matter maps published by Massey et al. (2007b). Both maps show several mass peaks associated with galaxy clusters and groups, partially connected with filamentary structures (see Figure 7.4). In addition, a huge relatively empty region is visible in the lower right (south-west) quadrant of the mosaic, with

[1] Note that the results in Chapter 6 are quoted for $\Omega_\mathrm{m} = 0.3$, as traditionally done in cosmic shear studies. For the comparison presented here we follow the example of Benjamin et al. (2007) to refer to the best-fitting WMAP-3 value to ease the comparison.

a diameter $\gtrsim 9h^{-1}$ Mpc at a typical lens redshift $z \sim 0.4$ (assuming a flat ΛCDM cosmology). We expect that this line-of-sight has similar statistical properties as the GEMS Survey, being a projecting of mostly voids along the line-of-sight, but we did not test this quantitatively.

From the COSMOS data we have been able to measure the cosmic shear signal at a wide range of scales $0\farcs1 \lesssim \theta \lesssim 80'$. At small scales we detect a significant B-mode signal, where the affected scales are $\theta \lesssim 0\farcs7$ for $\xi_{\rm B}$ and $\theta \lesssim 5'$ for $\langle M_\perp^2 \rangle$. Similar indications for remaining systematics have been reported by Massey et al. (2007c) for their analysis of the data. In our preliminary cosmological parameter estimation we only use B-mode free scales, and a redshift distribution based on the public redshift catalogue by Mobasher et al. (2007). From the COSMOS data we obtain an estimate for the power spectrum normalisation $\sigma_8 = 0.71 \pm 0.09$ for $\Omega_{\rm m} = 0.24$ assuming Gaussian cosmic variance, which is fully consistent with the WMAP-3 results. Yet, our estimate agrees only marginally with recent ground-based estimates, which favour slightly higher values of $\sigma_8$. However, the fact that no extraordinarily massive galaxy cluster is present in the field at redshifts with high lensing efficiency (see e.g. Massey et al. 2007b) might suggest a $\sigma_8$ estimate rather at the low end of the expected range. Thus, we find it surprising that our measurement differs significantly from the Massey et al. (2007c) estimate for the same field, who find $\sigma_8 = 0.90 \pm 0.083\,(\text{stat.}) \pm 0.104\,(\text{syst.})$ from a similar 2D analysis and $\sigma_8 = 0.96 \pm 0.037\,(\text{stat.})^{+0.058}_{-0.039}\,(\text{syst.})$ from a tomographic analysis, both for $\Omega_{\rm m} = 0.24$. Note that differences within the statistical and systematic errors are not unexpected, given that independent data reduction and shear measurement pipelines have been applied, as well as different selection criteria. Yet, their 3D and our 2D results are clearly not consistent. Until the time of the write-up we have not been able to unambiguously identify the origin for this discrepancy, but preliminary results suggest that it is rather related to the actual shear measurement than uncertainties of the redshift distribution. We will continue to investigate this discrepancy, but note that both catalogues still contain indications for systematic at small scales. Once these are eliminated, the discrepancy might (partially) resolve.

Compared to ground-based surveys the strength of current space-based weak lensing measurements is clearly given by the strongly increased galaxy number density. This is crucial for dark matter mapping which requires local shear information, but also helpful to constrain the cosmic shear signal at small scales. Measurements of the cosmic shear signal at sub-arcminute scale (corresponding to physical separations $\lesssim 300$ kpc for typical lens redshifts), are only moderately useful to constrain $\sigma_8$ due to uncertainties in theoretical predictions which arise from the influence of baryons (Rudd et al. 2007). However, measurements of the small-scale signal can be used to actually study the inter-relation of dark and baryonic matter. Also, they are useful to estimate the achievable accuracy of local weak lensing corrections, being relevant for example for type Ia supernovae studies. To a certain degree such measurements can be derived from mosaic observations such as GEMS and COSMOS. However, non-linear structure growth is expected to mix power from different scales, so that the small-scale signal measured from a largely under-dense field such as GEMS cannot be expected to be truly representative. For this purpose a shear measurement from a large number of random pointings as provided by the Extended ACS Parallel Survey (Sect. 8.3.2) is expected to be more useful, given that it minimises the error due to sampling variance. In addition, the field-of-view of ACS is large enough to provide additional shear estimates in the angular range $1' \lesssim \theta \lesssim 4'$ from single pointings, which can be used to

constrain $\sigma_8$.

In Chapter 6 we have already investigated a sample of 59 early fields from the ACS Parallel Survey. From these data we clearly detect a significant shear signal (Figure 6.25), which we however do not yet use to constrain $\sigma_8$ because of remaining systematics in the data, manifesting in a significant average alignment of the galaxies with the image y–axis. Several tests indicate that this spurious signal is not related to the degradation of the ACS charge transfer efficiency, which leads to a similar signature for later observations such as COSMOS, but is caused by the poor data quality of a large fraction of the data. For these fields the lack of dithering leads to various artifacts such as bad columns in the reduced data, which seem to be responsible for the false signal. Due to these findings we spent a substantial effort into further improving our data reduction pipeline (to the Mark-II state), which should allow us to reliably reject affected galaxies. However, the analysis of the Extended ACS Parallel Survey, which comprises approximately 440 independent fields, is only just starting. Thus, the improved accuracy of the updated pipeline still has to be demonstrated.

Cosmological weak lensing studies with ACS, such as the one presented here, but also the work by Heymans et al. (2005); Rhodes et al. (2007); Leauthaud et al. (2007) and Massey et al. (2007c) play a pathfinder role for dedicated future cosmic shear missions from space such as DUNE or JDEM/SNAP: Firstly, current surveys act as proof of concept for envisaged future projects. They also provide first estimates for the small-scale signal, which can be used as input to estimate the accuracy of future studies. Furthermore, current projects with ACS yield substantial technical expertise, which will be very valuable for the planning, conduction, and analysis of future surveys. Following from the experience with ACS future mission should for example aim to achieve maximal thermal stability to minimise temporal variations of the point-spread-function. Also, it will be crucial to use hardened CCD chips, which are subject to less CTE degradation. Concerning the analysis of future surveys, tools such as our PSF interpolation scheme (Sect. 6.2.4), possibly upgraded using a principal component analysis (PCA) similarly to the one described in Sect. 7.7, will be very valuable to achieve the systematic accuracy sought.

In addition to the cosmological weak lensing studies, parts of our ACS data reduction and weak lensing pipeline have also been used for studies of galaxy clusters, led by some of my collaborators. Here the high resolution and sensitivity of HST/ACS enables detailed studies of the total matter distribution using strong and weak gravitational lensing. These include investigations of the galaxy clusters 1E0657–56 (Sect. 8.1, Bradač et al. 2006) and RXJ1347.5–1145 (Sect. 8.2, Halkola et al. 2007, Bradač et al. in prep.), where the first one yielded the currently most direct evidence for the existence of dark matter, and the second one allows for a very accurate comparison of X-ray and gravitational lensing mass estimates.

## 9.2 Outlook

The results of this thesis project provide the starting point for several future projects:

It will be one of the first goals to improve the COSMOS shear catalogue, ideally to achieve a B-mode signal consistent with zero. An upgrade of the PSF correction scheme using the PCA results might be a useful tool to reach this goal. In addition, I plan to investigate if changes in the

ACS field distortion could be responsible for the systematic signal. If this is the case, a further upgrade of our pipeline and re-reduction of the data will be required. Once an improved catalogue is found, it can be used for several interesting science applications, such as a tomographic analysis which might resolve some of the discrepancy to the Massey et al. (2007c) results. In addition, we plan to use it for a detailed comparison with ground-based shear estimates from the CFHTLS Deep Survey and galaxy-galaxy lensing studies.

The progress of our study of the STAGES A901/A902 field (Sect. 8.4) depends on the availability of good photometric redshifts. If we are granted access to the COMBO-17 redshift catalogue of the field, we will be able to study the detailed mass distribution of the clusters in the field. In addition, we are aiming at measuring the shear signal of A901 as a function of source redshift. This geometric shear-ratio test can be used to constrain cosmological parameters including the dark energy equation-of-state parameter $w$ as demonstrated by Kitching et al. (2007) from a shallower ground-based catalogue of the field. The accuracy of our analysis would then be limited by the depth of the COMBO-17 redshift catalogue, so ideally one would aim to obtain deep multi-colour ground-based data from a wide-field imager on a telescope in the 6–8m class.

After completing the data reduction we are currently starting the analysis of the Extended ACS Parallel Survey. This survey will provide an interesting comparison to COSMOS, and possibly help to identify the origin of the COSMOS B-mode signal. Once free of systematics, we want to constrain the small-scale power spectrum from the data with high accuracy, providing constraints on $\sigma_8$ and the inter-play of baryons and dark matter. We also plan to conduct a galaxy-galaxy lensing study from the survey.

The combined data from COSMOS, GEMS, and the Extended ACS Parallel Survey will form the largest space-based dataset for cosmological weak lensing measurement for several years. After the loss of ACS, the Wide Field Camera 3, which is currently scheduled for installation on board HST in August 2008, will constitute an instrument with similar weak lensing capabilities as ACS. It will be very powerful for studies of galaxy clusters, but due to its slightly smaller field-of-view and optical sensitivity, no significant improvement for cosmic shear measurements is expected compared to ACS. On the other hand large dedicated ground-based surveys are either already on their way (CFHTLS[2]) or soon to begin (PanSTARRS-1[3], VST/KIDS[4], DES[5]). Therefore, cosmic shear will mostly become the domain of wide-field ground-based surveys for several years. The extreme accuracy sought for detailed studies of dark energy might, however, only be reachable using a dedicated space-based mission such as DUNE[6] or one of the Joint Dark Energy Missions (JDEM) SNAP[7] and DESTINY[8], which are currently proposed to funding agencies.

[2] http://www.cfht.hawaii.edu/Science/CFHLS/
[3] http://www.ps1sc.org/
[4] http://www.astro-wise.org/projects/KIDS/
[5] http://www.darkenergysurvey.org/
[6] http://www.dune-mission.net/
[7] http://snap.lbl.gov/
[8] http://www.noao.edu/noao/staff/lauer/destiny.htm

# Appendix A

# The KSB+ formalism

In this section I will outline the technique developed by Kaiser, Squires, & Broadhurst (1995), Luppino & Kaiser (1997), Hoekstra et al. (1998) for the point-spread-function (PSF) correction of galaxy ellipticities, closely following the description in Section 4.6.2 of Bartelmann & Schneider (2001).

The observed brightness distribution $I^{\rm obs}(\boldsymbol{\theta})$ of a galaxy image is given as the convolution of the PSF unaffected brightness distribution $I(\boldsymbol{\theta})$ with the PSF $P(\boldsymbol{\theta})$

$$I^{\rm obs}(\boldsymbol{\theta}) = \int {\rm d}^2\varphi \, I(\boldsymbol{\varphi}) P(\boldsymbol{\theta} - \boldsymbol{\varphi}) \, , . \tag{A.1}$$

In the KSB formalism it is assumed that the anisotropic part of $P$ is small and that $P$ can therefore by decomposed into an isotropic part $P^{\rm iso}$ and an anisotropic part $q$, such that

$$P(\boldsymbol{\theta}) = \int {\rm d}^2\varphi \, q(\boldsymbol{\varphi}) P^{\rm iso}(\boldsymbol{\theta} - \boldsymbol{\varphi}) \, , \tag{A.2}$$

where $P^{\rm iso}$ and $q$ are both normalised to unity and have vanishing first moments.

The coordinate system is chosen such that the image center is located at the origin. The position of the image center is definded by a vanishing first brightness moment

$$\int {\rm d}^2\theta \, W(\theta^2) \boldsymbol{\theta} I(\boldsymbol{\theta}) = 0 \, , \tag{A.3}$$

where $W(\theta^2)$ is a weight function, which truncates the integration for large distances $\theta = |\boldsymbol{\theta}|$ from the image center. Since gravitational lensing conserves surface brightness, the center of the image is in principle mapped onto the center of the source. Although this is not strictly true anymore due to the introduction of the weight function $W(\theta^2)$, deviations are expected to be very small. We will assume that all image centers are located at the origin of the corresponding coordinate systems.

Galaxy ellipticities are defined in terms of the second–order brightness moments

$$Q_{ij} = \int {\rm d}^2\theta \, W(\theta^2) \theta_i \theta_j I(\boldsymbol{\theta}) \, , \; i, j \in \{1, 2\} \tag{A.4}$$

as

$$e = \frac{Q_{11} - Q_{22} + 2\mathrm{i}Q_{12}}{Q_{11} + Q_{22}} \,. \tag{A.5}$$

## A.1 Influence of PSF anisotropy

By inserting (A.2), we can rewrite (A.1) as

$$I^{\mathrm{obs}}(\boldsymbol{\theta}) = \int \mathrm{d}^2\varphi \; q(\boldsymbol{\theta} - \boldsymbol{\varphi}) I^{\mathrm{iso}}(\boldsymbol{\varphi}) \,, \tag{A.6}$$

where we have definded the brightness profile

$$I^{\mathrm{iso}}(\boldsymbol{\theta}) = \int \mathrm{d}^2\varphi \, I(\boldsymbol{\varphi}) P^{\mathrm{iso}}(\boldsymbol{\theta} - \boldsymbol{\varphi}) \,, \tag{A.7}$$

which would be observed if the true image would only be smeared by an isotropic PSF. Inserting (A.7) into (A.6) it can be shown that

$$\int \mathrm{d}^2\theta \, f(\boldsymbol{\theta}) I^{\mathrm{obs}}(\boldsymbol{\theta}) = \int \mathrm{d}^2\varphi \, I^{\mathrm{iso}}(\boldsymbol{\varphi}) f(\boldsymbol{\varphi}) + \frac{1}{2} q_{kl} \int \mathrm{d}^2\varphi \, I^{\mathrm{iso}}(\boldsymbol{\varphi}) \frac{\partial^2 f}{\partial\varphi_k \partial\varphi_l} + \mathcal{O}(q^2) \,, \tag{A.8}$$

with

$$q_{kl} = \int \mathrm{d}^2\varphi \, q(\boldsymbol{\varphi}) \varphi_k \varphi_l \,, \tag{A.9}$$

holds for an arbitrary function $f(\boldsymbol{\theta})$. Here we used that $q$ is normalized and has vanishing first moments. In the KSB formalism it is assumed that the anisotropy of the PSF is weak. Therefore, only terms linear in $q$ are considered henceforth. By inserting $f(\boldsymbol{\theta}) = \theta_i \theta_j W(\theta^2)$ into (A.8), we find that the second–order brightness moments $Q^{\mathrm{obs}}$ and $Q^{\mathrm{iso}}$ are interrelated by

$$Q^{\mathrm{iso}}_{ij} = Q^{\mathrm{obs}}_{ij} - \frac{1}{2} q_{kl} \int \mathrm{d}^2\varphi I^{\mathrm{obs}}(\boldsymbol{\varphi}) \frac{\partial^2}{\partial\varphi_k \partial\varphi_l} \left[ \varphi_i \varphi_j W(\varphi^2) \right] \,, \tag{A.10}$$

where we used Einstein summation convention. By calculating the relevant combinations of $Q_{ij}$

$$\begin{aligned} \mathrm{tr}(Q^{\mathrm{iso}}) &= \mathrm{tr}(Q^{\mathrm{obs}}) - x_\alpha q_\alpha \,, \\ (Q^{\mathrm{iso}}_{11} - Q^{\mathrm{iso}}_{22}) &= (Q^{\mathrm{obs}}_{11} - Q^{\mathrm{obs}}_{22}) - X_{1\alpha} q_\alpha \,, \\ 2Q^{\mathrm{iso}}_{12} &= 2Q^{\mathrm{obs}}_{12} - X_{2\alpha} q_\alpha \,, \end{aligned} \tag{A.11}$$

where we defined

$$X_{\alpha\beta} \equiv \int \mathrm{d}^2\varphi I^{\mathrm{obs}}(\boldsymbol{\varphi}) \left[ \left( W + 2|\boldsymbol{\varphi}|^2 W' \right) \delta_{\alpha\beta} + \eta_\alpha(\boldsymbol{\varphi}) \eta_\beta(\boldsymbol{\varphi}) W'' \right] \,, \tag{A.12}$$

$$q_1 \equiv q_{11} - q_{22} \,, \tag{A.13}$$

$$q_2 \equiv 2q_{12} \,, \tag{A.14}$$

$$x_\alpha \equiv \int \mathrm{d}^2\varphi I^{\mathrm{obs}}(\boldsymbol{\varphi}) \eta_\alpha(\boldsymbol{\varphi}) \left( 2W' + |\boldsymbol{\varphi}|^2 W'' \right) \,, \tag{A.15}$$

with the Kronecker symbol $\delta_{\alpha\beta}$ and

$$\eta_1(\boldsymbol{\varphi}) = \varphi_1^2 - \varphi_2^2\,, \quad \eta_2(\boldsymbol{\varphi}) = 2\varphi_1\varphi_2\,, \tag{A.16}$$

we find that the ellipticities $e^{\rm iso}$ and $e^{\rm obs}$, which were defined in (A.5), are interrelated as

$$e_\alpha^{\rm iso} = e_\alpha^{\rm obs} - P_{\alpha\beta}^{\rm sm} q_\beta\,. \tag{A.17}$$

Here we defined the *smear polarisability*

$$P_{\alpha\beta}^{\rm sm} = \left({\rm tr}Q^{\rm obs}\right)^{-1}\left(X_{\alpha\beta} - e_\alpha^{\rm obs} x_\beta\right) \tag{A.18}$$

which characterises the response of the ellipticity to a PSF anisotropy.

The anisotropy kernel $q$ has to be measured from the observed shape of stellar images. Since stars are point-like sources which are not effected by lensing, they would have zero ellipticity in the absence of PSF anisotropy and thus $e^{\rm iso,*} = 0$. Here the asterix indicates that stellar images are considered. Therefore the anisotropy kernel at the stellar position is given by

$$q_\alpha = (P_{\alpha\beta}^{\rm sm,*})^{-1} e_\beta^{\rm obs,*}\,. \tag{A.19}$$

## A.2 Influence of PSF smearing

As the next step we relate the intrinsic brightness distribution with $I^{\rm iso}$. Inserting the brightness distribution of a lensed image as given in (3.11) into (A.7) and transforming to source coordinates yields

$$\begin{aligned} I^{\rm iso}(\boldsymbol{\theta}) &= \int {\rm d}^2\varphi\, I^{\rm s}(\mathcal{A}\boldsymbol{\varphi}) P^{\rm iso}(\boldsymbol{\theta} - \boldsymbol{\varphi}) \\ &= \frac{1}{{\rm det}\mathcal{A}} \int {\rm d}^2\zeta\, I^{\rm s}(\boldsymbol{\zeta}) P^{\rm iso}(\boldsymbol{\theta} - \mathcal{A}^{-1}\boldsymbol{\zeta}) \equiv \hat{I}(\mathcal{A}\boldsymbol{\theta})\,. \end{aligned} \tag{A.20}$$

In the last step we defined the brightness moment

$$\hat{I}(\boldsymbol{\theta}) = \int {\rm d}^2\varphi I^{\rm s}(\boldsymbol{\varphi})\hat{P}(\boldsymbol{\theta} - \boldsymbol{\varphi}) \quad \text{with} \quad \hat{P}(\boldsymbol{\theta}) \equiv \frac{1}{{\rm det}\mathcal{A}} P^{\rm iso}(\mathcal{A}^{-1}\boldsymbol{\theta})\,, \tag{A.21}$$

where the normalised function $\hat{P}$ has zero mean and is anisotropic in the presence of shear.

In order to find a relation between the ellipticities of $I^{\rm iso}$ and $\hat{I}$, we consider the second-order brightness moments of the latter as definded in (A.4)

$$\hat{Q}_{ij} = \int {\rm d}^2\beta\, \beta_i\beta_j \hat{I}(\boldsymbol{\beta}) W(\beta^2)\,. \tag{A.22}$$

In the weak lensing regime, and thus for small distortions, one can employ a Taylor expansion of the weight function $W(\beta)$ in (A.22) to first order, yielding the following relation between the ellipticities $\hat{e}$ and $e^{\rm iso}$:

$$e_\alpha^{\rm iso} - \hat{e}_\alpha = P_{\alpha\beta}^{\rm sh} g_\beta\,, \tag{A.23}$$

where we have defined the *shear polarisability* $P^{\rm sh}_{\alpha\beta}$ as

$$P^{\rm sh}_{\alpha\beta} = 2\delta_{\alpha\beta} - 2e^{\rm iso}_\alpha e^{\rm iso}_\beta + e^{\rm iso}_\alpha M_\beta + D_{\alpha\beta} \quad \text{, with} \tag{A.24}$$

$$M_\beta = -\frac{2}{{\rm tr}Q^{\rm iso}} \int {\rm d}^2\theta\, |\boldsymbol{\theta}|^2 I^{\rm iso}(\boldsymbol{\theta}) W' \eta_\alpha(\boldsymbol{\theta}) \quad \text{and}$$

$$D_{\alpha\beta} = \frac{2}{{\rm tr}Q^{\rm iso}} \int {\rm d}^2\theta\, I^{\rm iso}(\boldsymbol{\theta}) W' \eta_\alpha(\boldsymbol{\theta}) \eta_\beta(\boldsymbol{\theta})\,. \tag{A.25}$$

Although $P^{\rm sh}_{\alpha\beta}$ is defined in terms of $I^{\rm iso}$, we can directly calculate this tensor from the brightness profile $I^{\rm obs}$, since the difference only yields terms in second order of $q$.

We can decompose $\hat{P}$ into an isotropic and an anisotropic part analogously to (A.2)

$$\hat{P}(\boldsymbol{\theta}) = \int {\rm d}^2\varphi\, \hat{q}(\boldsymbol{\varphi}) \hat{P}^{\rm iso}(\boldsymbol{\theta} - \boldsymbol{\varphi})\,. \tag{A.26}$$

If we then define the brightness profile

$$\hat{I}^0(\boldsymbol{\theta}) = \int {\rm d}^2\varphi\, I^{\rm s}(\boldsymbol{\varphi}) \hat{P}^{\rm iso}(\boldsymbol{\theta} - \boldsymbol{\varphi})\,, \tag{A.27}$$

which would be observed from a source only smeared by an isotropic PSF, we find

$$\hat{I}(\boldsymbol{\theta}) = \int {\rm d}^2\varphi\, \hat{I}^0(\boldsymbol{\varphi}) \hat{q}(\boldsymbol{\theta} - \boldsymbol{\varphi})\,. \tag{A.28}$$

Since the relation between $\hat{I}$ and $\hat{I}^0$ is the same as the one between $I^{\rm obs}$ and $I^{\rm iso}$, the corresponding ellipticities fulfill in analogy to (A.17):

$$\hat{e}^0_\alpha = \hat{e}_\alpha - P^{\rm sm}_{\alpha\beta} \hat{q}_\beta\,, \tag{A.29}$$

where $P^{\rm sm}$ in principle has to be calculated from $\hat{I}$. However, we can again calculate $P^{\rm sm}$ from the observed brightness distribution $I^{\rm obs}$, since differences are of second order in $q$, and are therefore neglected.

Combining (A.23) with (A.29) we find

$$e^{\rm iso}_\alpha = \hat{e}^0_\alpha + P^{\rm sh}_{\alpha\beta} g_\beta + P^{\rm sm}_{\alpha\beta} \hat{q}_\beta\,. \tag{A.30}$$

From the fact that $\hat{e}^0_\alpha$ and $e^{\rm iso}_\alpha$ both vanish for stellar images follows

$$\hat{q}_\alpha = -\left(P^{\rm sm,*}\right)^{-1}_{\alpha\beta} P^{\rm sh,*}_{\beta\gamma} g_\gamma\,. \tag{A.31}$$

If we then define

$$P^g_{\alpha\beta} = P^{\rm sh}_{\alpha\beta} - P^{\rm sm}_{\alpha\gamma} \left[\left(P^{\rm sm,*}\right)^{-1}_{\gamma\delta} P^{\rm sh,*}_{\delta\beta}\right]\,, \tag{A.32}$$

and combine Eqs. (A.17) and (A.30), we finally obtain

$$\hat{e}^0_\alpha = e^{\rm obs}_\alpha - P^{\rm sm}_{\alpha\beta} q_\beta - P^g_{\alpha\beta} g_\beta\,. \tag{A.33}$$

This equation interrelates the observed ellipticity to the ellipticity of the source under the influence of an anisotropic PSF and a gravitational shear. Since the expectation value of $\hat{e}^0$ is zero, $e^{\rm obs}$ yields an estimate of the reduced shear $g$, if the PSF anisotropy is corrected.

# Bibliography


Adami, C., Mazure, A., Ilbert, O., et al. 2005, A&A, 443, 805

Albrecht, A., Bernstein, G., Cahn, R., et al. 2006, astro-ph/0609591

Anderson, J. 2006, in The 2005 HST Calibration Workshop: Hubble After the Transition to Two-Gyro Mode, ed. A. M. Koekemoer, P. Goudfrooij, & L. L. Dressel, p.11

Anderson, J. 2007, Instrument Science Rep. ACS 2007-08 (Baltimore: STScI), http://www.stsci.edu/hst/acs/documents/isrs/isr0708.pdf

Anderson, J. & King, I. R. 2006, Instrument Science Rep. ACS 2006-01 (Baltimore: STScI), http://www.stsci.edu/hst/acs/documents/isrs/isr0601.pdf

Angus, G. W., Shan, H. Y., Zhao, H. S., & Famaey, B. 2007, ApJ, 654, L13

Baade, W. 1956, PASP, 68, 5

Bacon, D., Refregier, A., & Ellis, R. 2000, MNRAS, 318, 625

Bacon, D. J., Massey, R. J., Refregier, A. R., & Ellis, R. S. 2003, MNRAS, 344, 673

Bacon, D. J., Refregier, A., Clowe, D., & Ellis, R. S. 2001, MNRAS, 325, 1065

Bahcall, N. A., Dong, F., Bode, P., et al. 2003, ApJ, 585, 182

Bartelmann, M. & Schneider, P. 2001, Phys. Rep., 340, 291

Baugh, C. M. & Efstathiou, G. 1994, MNRAS, 267, 323

Benjamin, J., Heymans, C., Semboloni, E., et al. 2007, MNRAS accepted (also astro-ph/0703570)

Bennett, C. L., Halpern, M., Hinshaw, G., et al. 2003, ApJS, 148, 1

Bernstein, G. M. & Jarvis, M. 2002, AJ, 123, 583

Bertin, E. & Arnouts, S. 1996, A&AS, 117, 393

Bonamente, M., Joy, M. K., LaRoque, S. J., et al. 2006, ApJ, 647, 25

Bradač, M., Clowe, D., Gonzalez, A. H., et al. 2006, ApJ, 652, 937

Bradač, M., Erben, T., Schneider, P., et al. 2005, A&A, 437, 49

Bradač, M., Lombardi, M., & Schneider, P. 2004, A&A, 424, 13

Brainerd, T., Blandford, R. D., & Smail, I. 1996, ApJ, 466, 623

Bridle, S., Gull, S., Bardeau, S., & J.P., K. 2002, in Natarajan P., ed., Proc. Yale Cosmology Workshop, The Shapes of Galaxies and Their Dark Halos. World Scientific, New Haven.

Brown, M. L., Taylor, A. N., Bacon, D. J., et al. 2003, MNRAS, 341, 100

Brown, M. L., Taylor, A. N., Hambly, N. C., & Dye, S. 2002, MNRAS, 333, 501

Bunker, A. J., Stanway, E. R., Ellis, R. S., McMahon, R. G., & McCarthy, P. J. 2003, MNRAS, 342, L47

Casertano, S., de Mello, D., Dickinson, M., et al. 2000, AJ, 120, 2747

Casertano, S., Ratnatunga, K. U., & Griffiths, R. E. 2003, ApJ, 598, L71

Clowe, D., Bradač, M., Gonzalez, A. H., et al. 2006, ApJ, 648, L109

Coe, D., Benítez, N., Sánchez, S. F., et al. 2006, AJ, 132, 926

Cohen, J. G. & Kneib, J.-P. 2002, ApJ, 573, 524

Cole, S., Percival, W. J., Peacock, J. A., et al. 2005, MNRAS, 362, 505

Cox, C. 1997, Instrument Science Rep. OSG-CAL-97-06 (Baltimore: STScI), http://www.stsci.edu/ hst/observatory/documents/isrs/velocity.pdf

Cox, C. & Gilliland, R. L. 2002, in The 2002 HST Calibration Workshop. (Baltimore: STScI), p.58

Cristiani, S., Appenzeller, I., Arnouts, S., et al. 2000, A&A, 359, 489

Crittenden, R. G., Natarajan, P., Pen, U.-L., & Theuns, T. 2002, ApJ, 568, 20

Croom, S. M., Warren, S. J., & Glazebrook, K. 2001, MNRAS, 328, 150

de Bernardis, P., Ade, P. A. R., Bock, J. J., et al. 2000, Nature, 404, 955

Desjacques, V. & Nusser, A. 2005, MNRAS, 361, 1257

Dickinson, M., Stern, D., Giavalisco, M., et al. 2004, ApJ, 600, L99

Dodelson, S. 2003, Modern Cosmology (Elsevier)

Dye, S., Taylor, A. N., Greve, T. R., et al. 2002, A&A, 386, 12

Dye, S., Taylor, A. N., Thommes, E. M., et al. 2001, MNRAS, 321, 685

Efstathiou, G., Bond, J. R., & White, S. D. M. 1992, MNRAS, 258, 1P

Einstein, A. 1916, Annalen der Physik, 49, 769

Eisenstein, D. J., Zehavi, I., Hogg, D. W., et al. 2005, ApJ, 633, 560

Erben, T., van Waerbeke, L., Bertin, E., Mellier, Y., & Schneider, P. 2001, A&A, 366, 717

Fixsen, D. J., Cheng, E. S., Gales, J. M., et al. 1996, ApJ, 473, 576

Fort, B., Mellier, Y., & Dantel-Fort, M. 1997, A&A, 321, 353

Freedman, W. L., Madore, B. F., Gibson, B. K., et al. 2001, ApJ, 553, 47

Fruchter, A. S. & Hook, R. N. 2002, PASP, 114, 144

Gavazzi, R., Treu, T., Rhodes, J. D., et al. 2007, ApJ, 667, 176

Giacconi, R., Rosati, P., Tozzi, P., et al. 2001, ApJ, 551, 624

Giavalisco, M., Ferguson, H. C., Koekemoer, A. M., et al. 2004, ApJ, 600, L93

Gilli, R., Cimatti, A., Daddi, E., et al. 2003, ApJ, 592, 721

Gilli, R., Daddi, E., Zamorani, G., et al. 2005, A&A, 430, 811

Gitti, M., Piffaretti, R., & Schindler, S. 2007, A&A, 472, 383

Gnedin, N. Y. & Hamilton, A. J. S. 2002, MNRAS, 334, 107

Gray, M. E., Taylor, A. N., Meisenheimer, K., et al. 2002, ApJ, 568, 141

Grazian, A., Fontana, A., de Santis, C., et al. 2006, A&A, 449, 951

Hämmerle, H., Miralles, J.-M., Schneider, P., et al. 2002, A&A, 385, 743

Halkola, A., Hildebrandt, H., Schrabback, T., et al. 2007, A&A submitted

Hamana, T., Miyazaki, S., Shimasaku, K., et al. 2003, ApJ, 597, 98

Hanany, S., Ade, P., Balbi, A., et al. 2000, ApJ, 545, L5

Hartlap, J., Simon, P., & Schneider, P. 2007, A&A, 464, 399

Henry, J. P. 2004, ApJ, 609, 603

Hetterscheidt, M. 2007, PhD thesis, Rheinische Friedrich-Wilhelms-Universität Bonn, Bonn, Germany

Hetterscheidt, M., Simon, P., Schirmer, M., et al. 2007, A&A, 468, 859

Heymans, C., Bell, E. F., Rix, H.-W., et al. 2006a, MNRAS, 371, L60

Heymans, C., Brown, M., Heavens, A., et al. 2004, MNRAS, 347, 895

Heymans, C., Brown, M. L., Barden, M., et al. 2005, MNRAS, 361, 160

Heymans, C. & Heavens, A. 2003, MNRAS, 339, 711

Heymans, C., Van Waerbeke, L., Bacon, D., et al. 2006b, MNRAS, 368, 1323

Heymans, C., White, M., Heavens, A., Vale, C., & van Waerbeke, L. 2006c, MNRAS, 371, 750

Hildebrandt, H., Erben, T., Dietrich, J. P., et al. 2006, A&A, 452, 1121

Hinshaw, G., Nolta, M. R., Bennett, C. L., et al. 2007, ApJS, 170, 288

Hinshaw, G., Spergel, D. N., Verde, L., et al. 2003, ApJS, 148, 135

Hirata, C. & Seljak, U. 2003, MNRAS, 343, 459

Hoekstra, H. 2004, MNRAS, 347, 1337

Hoekstra, H., Franx, M., Kuijken, K., & Squires, G. 1998, ApJ, 504, 636

Hoekstra, H., Mellier, Y., van Waerbeke, L., et al. 2006, ApJ, 647, 116

Hoekstra, H., Yee, H. K. C., & Gladders, M. D. 2002a, ApJ, 577, 595

Hoekstra, H., Yee, H. K. C., Gladders, M. D., et al. 2002b, ApJ, 572, 55

Hu, W. & Keeton, C. R. 2002, Phys. Rev. D, 66, 063506

Hubble, E. 1929, Proceedings of the National Academy of Science, 15, 168

Huterer, D., Takada, M., Bernstein, G., & Jain, B. 2006, MNRAS, 366, 101

Jain, B., Seljak, U., & White, S. 2000, ApJ, 530, 547

Jarvis, M., Bernstein, G. M., Fischer, P., et al. 2003, AJ, 125, 1014

Jarvis, M. & Jain, B. 2004, ApJ submitted (also astro-ph/0412234)

Jarvis, M., Jain, B., Bernstein, G., & Dolney, D. 2006, ApJ, 644, 71

Jee, M. J., Ford, H. C., Illingworth, G. D., et al. 2007, ApJ, 661, 728

Jee, M. J., White, R. L., Benítez, N., et al. 2005a, ApJ, 618, 46

Jee, M. J., White, R. L., Ford, H. C., et al. 2005b, ApJ, 634, 813

Jee, M. J., White, R. L., Ford, H. C., et al. 2006, ApJ, 642, 720

Jena, T., Norman, M. L., Tytler, D., et al. 2005, MNRAS, 361, 70

Jones, W. C., Ade, P. A. R., Bock, J. J., et al. 2006, ApJ, 647, 823

Kaiser, N. 1995, ApJ, 439, L1

Kaiser, N. 1998, ApJ, 498, 26

Kaiser, N. 2000, ApJ, 537, 555

Kaiser, N. & Squires, G. 1993, ApJ, 404, 441

Kaiser, N., Squires, G., & Broadhurst, T. 1995, ApJ, 449, 460

Kaiser, N., Wilson, G., & Luppino, G. 2000, astro-ph/0003338

Kilbinger, M. & Schneider, P. 2005, A&A, 442, 69

Kilbinger, M., Schneider, P., & Eifler, T. 2006, A&A, 457, 15

King, L. & Schneider, P. 2002, A&A, 396, 411

Kitching, T. D., Heavens, A. F., Taylor, A. N., et al. 2007, MNRAS, 138

Knop, R. A., Aldering, G., Amanullah, R., et al. 2003, ApJ, 598, 102

Koekemoer, A., Gonzaga, S., Fruchter, A., et al. 2002, HST Dither Handbook, Version 2.0, STScI, Baltimore

Koekemoer, A. M., Aussel, H., Calzetti, D., et al. 2007, ApJS, 172, 196

Koekemoer, A. M., Fruchter, A. S., Hook, R. N., & Hack, W. 2002, in The 2002 HST Calibration Workshop. Edited by S. Arribas, A. Koekemoer, and B. Whitmore. (Baltimore: STScI), p.337

Kolb, E. W., Matarrese, S., & Riotto, A. 2006, New Journal of Physics, 8, 322

Krist, J. 2003, Instrument Science Rep. ACS 2003-06 (Baltimore: STScI), http://www.stsci.edu/hst/acs/documents/isrs/isr0306.pdf

Kuijken, K. 2006, A&A, 456, 827

Le Fèvre, O., Vettolani, G., Paltani, S., et al. 2004, A&A, 428, 1043

Leauthaud, A., Massey, R., Kneib, J.-P., et al. 2007, ApJS, 172, 219

Leonard, A., Goldberg, D. M., Haaga, J. L., & Massey, R. 2007, ApJ, 666, 51

Lombardi, M., Rosati, P., Blakeslee, J. P., et al. 2005, ApJ, 623, 42

Luppino, G. A. & Kaiser, N. 1997, ApJ, 475, 20

Mandelbaum, R., Hirata, C. M., Ishak, M., Seljak, U., & Brinkmann, J. 2006, MNRAS, 367, 611

Maoli, R., van Waerbeke, L., Mellier, Y., et al. 2001, A&A, 368, 766

Massey, R., Heymans, C., Bergé, J., et al. 2007a, MNRAS, 376, 13

Massey, R. & Refregier, A. 2005, MNRAS, 363, 197

Massey, R., Refregier, A., Bacon, D. J., Ellis, R., & Brown, M. L. 2005, MNRAS, 359, 1277

Massey, R., Refregier, A., Conselice, C. J., David, J., & Bacon, J. 2004, MNRAS, 348, 214

Massey, R., Rhodes, J., Ellis, R., et al. 2007b, Nature, 445, 286

Massey, R., Rhodes, J., Leauthaud, A., et al. 2007c, ApJS, 172, 239

Meurer, G. R., Lindler, D. J., Blakeslee, J., et al. 2003, in Future EUV/UV and Visible Space Astrophysics Missions and Instrumentation. Edited by J. Chris Blades, Oswald H. W. Siegmund. Proceedings of the SPIE, Volume 4854, p.507

Mignoli, M., Cimatti, A., Zamorani, G., et al. 2005, A&A, 437, 883

Miralles, J.-M., Erben, T., Hämmerle, H., et al. 2005, A&A, 432, 797

Mobasher, B., Capak, P., Scoville, N. Z., et al. 2007, ApJS, 172, 117

Mutchler, M. & Sirianni, M. 2005, Instrument Science Rep. ACS 2005-03 (Baltimore: STScI), http://www.stsci.edu/hst/acs/documents/isrs/isr0503.pdf

Nakajima, R. & Bernstein, G. 2007, AJ, 133, 1763

Oguri, M. 2007, ApJ, 660, 1

Olsen, L. F., Miralles, J.-M., da Costa, L., et al. 2006a, A&A, 452, 119

Olsen, L. F., Miralles, J.-M., da Costa, L., et al. 2006b, A&A, 456, 881

Page, L., Hinshaw, G., Komatsu, E., et al. 2007, ApJS, 170, 335

Pavlovsky, C., Biretta, J., Boffi, F., et al. 2003, ACS Instrument Handbook, Version 4.0, STScI, Baltimore

Pavlovsky, C., Koekemoer, A., Mack, J., et al. 2006a, ACS Data Handbook, Version 5.0, (Baltimore: STScI)

Pavlovsky, C. et al. 2006b, ACS Instrument Handbook, Version 7.1, STScI, Baltimore

Peacock, J., Schneider, P., Efstathiou, G., et al. 2006, http://www.stecf.org/coordination/esa_eso/cosmology.php

Peacock, J. A. 1999, Cosmological physics (Cambridge University Press)

Peacock, J. A. & Dodds, S. J. 1996, MNRAS, 280, L19

Penzias, A. A. & Wilson, R. W. 1965, ApJ, 142, 419

Percival, W. J., Nichol, R. C., Eisenstein, D. J., et al. 2007, ApJ, 657, 645

Perlmutter, S., Aldering, G., Goldhaber, G., et al. 1999, ApJ, 517, 565

Phleps, S., Wolf, C., Peacock, J. A., Meisenheimer, K., & van Kampen, E. 2007, A&A, 468, 113

Pirzkal, N., Collodel, L., Erben, T., et al. 2001, A&A, 375, 351

Pirzkal, N., Sahu, K. C., Burgasser, A., et al. 2005, ApJ, 622, 319

Randall, S. W., Markevitch, M., Clowe, D., Gonzalez, A. H., & Bradac, M. 2007, astro-ph/0704.0261, 704

Refregier, A. 2003, ARA&A, 41, 645

Refregier, A. & Bacon, D. 2003, MNRAS, 338, 48

Refregier, A., Massey, R., Rhodes, J., et al. 2004, AJ, 127, 3102

Refregier, A., Rhodes, J., & Groth, E. J. 2002, ApJ, 572, L131

Reiprich, T. H. & Böhringer, H. 2002, ApJ, 567, 716

Rhodes, J., Massey, R., Albert, J., et al. 2005, in The 2005 HST Calibration Workshop. Edited by A. Koekemoer, P. Goudfrooij, and L. Dressel. (Baltimore: STScI), p.21

Rhodes, J., Refregier, A., Collins, N. R., et al. 2004, ApJ, 605, 29

Rhodes, J., Refregier, A., & Groth, E. J. 2000, ApJ, 536, 79

Rhodes, J., Refregier, A., & Groth, E. J. 2001, ApJ, 552, L85

Rhodes, J. D., Massey, R. J., Albert, J., et al. 2007, ApJS, 172, 203

Riess, A. 2004, Instrument Science Rep. ACS 2003-09 (Baltimore: STScI), http://www.stsci.edu/hst/acs/documents/isrs/isr0309.pdf

Riess, A. & Mack, J. 2004, Instrument Science Rep. ACS 2004-06 (Baltimore: STScI), http://www.stsci.edu/hst/acs/documents/isrs/isr0406.pdf

Riess, A. G., Filippenko, A. V., Challis, P., et al. 1998, AJ, 116, 1009

Riess, A. G., Li, W., Stetson, P. B., et al. 2005, ApJ, 627, 579

Rix, H.-W., Barden, M., Beckwith, S. V. W., et al. 2004, ApJS, 152, 163

Robertson, H. P. 1935, ApJ, 82, 284

Rudd, D. H., Zentner, A. R., & Kravtsov, A. V. 2007, ApJ submitted (also astro-ph/0703741)

Schlegel, D. J., Finkbeiner, D. P., & Davis, M. 1998, ApJ, 500, 525

Schneider, P. 1996, MNRAS, 283, 837

Schneider, P., Ehlers, J., & Falco, E. E. 1992, Gravitational Lenses (Springer Verlag, Heidelberg)

Schneider, P. & Kilbinger, M. 2007, A&A, 462, 841

Schneider, P., Kochanek, C. S., & Wambsganss, J. 2006, Saas-Fee Advanced Course 33: Gravitational Lensing: Strong, Weak and Micro (Springer Verlag, Berlin)

Schneider, P., van Waerbeke, L., Jain, B., & Kruse, G. 1998, MNRAS, 296, 873

Schneider, P., van Waerbeke, L., & Mellier, Y. 2002, A&A, 389, 729

Schrabback, T., Erben, T., Simon, P., et al. 2007, A&A, 468, 823

Seitz, C. & Schneider, P. 1995, A&A, 297, 287

Seitz, C. & Schneider, P. 1997, A&A, 318, 687

Seitz, S. & Schneider, P. 2001, A&A, 374, 740

Seljak, U., Makarov, A., McDonald, P., et al. 2005, Phys. Rev. D, 71, 103515

Semboloni, E., Mellier, Y., van Waerbeke, L., et al. 2006, A&A, 452, 51

Semboloni, E., van Waerbeke, L., Heymans, C., et al. 2007, MNRAS, 375, L6

Sievers, J. L., Bond, J. R., Cartwright, J. K., et al. 2003, ApJ, 591, 599

Simon, P., King, L. J., & Schneider, P. 2004, A&A, 417, 873

Smith, R. E., Peacock, J. A., Jenkins, A., et al. 2003, MNRAS, 341, 1311

Spergel, D. N., Bean, R., Doré, O., et al. 2007, ApJS, 170, 377

Spergel, D. N., Verde, L., Peiris, H. V., et al. 2003, ApJS, 148, 175

Springel, V., White, S. D. M., Jenkins, A., et al. 2005, Nature, 435, 629

Stanway, E. R., Bunker, A. J., McMahon, R. G., et al. 2004, ApJ, 607, 704

Starck, J.-L., Pires, S., & Réfrégier, A. 2006, A&A, 451, 1139

Strolger, L.-G., Riess, A. G., Dahlen, T., et al. 2004, ApJ, 613, 200

Sugiyama, N. 1995, ApJS, 100, 281

Szokoly, G. P., Bergeron, J., Hasinger, G., et al. 2004, ApJS, 155, 271

Taylor, A. N., Dye, S., Broadhurst, T. J., Benitez, N., & van Kampen, E. 1998, ApJ, 501, 539

Tegmark, M., Blanton, M. R., Strauss, M. A., et al. 2004a, ApJ, 606, 702

Tegmark, M., Strauss, M. A., Blanton, M. R., et al. 2004b, Phys. Rev. D, 69, 103501

Tereno, I., Doré, O., Van Waerbeke, L., & Mellier, Y. 2005, A&A, 429, 383

van der Wel, A., Franx, M., van Dokkum, P. G., & Rix, H.-W. 2004, ApJ, 601, L5

Van Waerbeke, L. & Mellier, Y. 2003, preprint astro-ph/0305089

Van Waerbeke, L., Mellier, Y., Erben, T., et al. 2000, A&A, 358, 30

Van Waerbeke, L., Mellier, Y., & Hoekstra, H. 2005, A&A, 429, 75

Van Waerbeke, L., Mellier, Y., Pelló, R., et al. 2002, A&A, 393, 369

Van Waerbeke, L., Mellier, Y., Radovich, M., et al. 2001, A&A, 374, 757

van Waerbeke, L., White, M., Hoekstra, H., & Heymans, C. 2006, Astroparticle Physics, 26, 91

Vanzella, E., Cristiani, S., Dickinson, M., et al. 2005, A&A, 434, 53

Vanzella, E., Cristiani, S., Dickinson, M., et al. 2006, A&A, 454, 423

Viana, P. T. P., Kay, S. T., Liddle, A. R., Muanwong, O., & Thomas, P. A. 2003, MNRAS, 346, 319

Walker, A. G. 1936, Proc. Lond. Math. Soc. (2), 42, 90

Wiltshire, D. L. 2007, New J. Phys. accepted (also gr-qc/0702082)

Wittman, D., Tyson, J. A., Margoniner, V. E., et al. 2001, ApJ, 557, 89

Wittman, D. M., Tyson, J. A., Kirkman, D., Dell'Antonio, I., & Bernstein, G. 2000, Nature, 405, 143

Wolf, C., Meisenheimer, K., Kleinheinrich, M., et al. 2004, A&A, 421, 913

Wolf, C., Meisenheimer, K., Röser, H.-J., et al. 2001, A&A, 365, 681

Wood-Vasey, W. M., Miknaitis, G., Stubbs, C. W., et al. 2007, ApJ, 666, 694

# Acknowledgements

I deeply appreciate the help and contributions received from many people during this project. First of all I want to thank my supervisor Professor Peter Schneider, who gave me the opportunity to work on this exciting project, always having time for advice when needed. I also like to thank him for careful reading of my manuscripts, including this thesis. Special thanks go to Patrick Simon and Thomas Erben, who provided me with essential software tools and contributed several central parts of the analysis. Joan-Marc Miralles and Catherine Heymans helped me to figure out many weak lensing-related aspects of ACS, especially in the early phase of this work, which I highly appreciate. I want to thank Marco Hetterscheidt for many fruitful KSB-related discussions, Tim Eifler for sharing his code on model predictions, Jan Hartlap for providing ray-tracing comparisons, and Hendrik Hildebrandt for help with photo-zs and ground-based catalogues. I also want to thank Fabrice Brimioulle, Jörg Dietrich, Bob Fosbury, Wolfram Freudling, Mike Lerchster, Matteo Maturi, and Norbert Pirzkal for their contributions and comments to the ACS-related projects. Furthermore, I strongly appreciate the productive work in the HAGGLeS collaboration with Phil Marshall, Chris Fassnacht, Eric Morganson, and Maruša Bradač. Finally, I want to thank Ludovic van Waerbeke, Richard Massey, William High, Catherine Heymans, and Jason Rhodes for creating the STEP1–3 image simulations and performing the joint analysis of the catalogues created in the STEP blind tests.

I like to specially thank Professor Yannick Mellier for being co-referee for this thesis, as well as Professor Manuel Drees and Professor Carl-Friedrich Bödigheimer for being members of the thesis committee.

During the time of this PhD project I deeply enjoyed the cordial atmosphere at AIfA, for which I kindly thank all colleagues, especially my former and current office mates Anja von der Linden, Lars Bährens, Leonardo Castañeda, Tim Eifler, and Daniela Wuttke. Besides the already mentioned previous and current members of the AIfA Lensing Group I want to thank Nadya Ben Bekhti, Alex Böhnert, Jacqueline Chen, Doug Clowe, Oliver Czoske, Helen Eckmiller, Xinzhong Er, Peter Erni, Aleksi Halkola, Hannelore Hämmerle, Philippe Heraudeau, Karianne Holhjem, Patrick Hudelot, Daniel Hudson, Holger Israel, Benjamin Joachimi, Martin Kilbinger, Lindsay King, Martina Kleinheinrich, Guoliang Li, Marco Lombardi, Rupal Mittal, Oxana Nenestyan, Emilio Pastor Mira, Jasmin Pielorz, Thomas Reiprich, Philipp Richter, Jens Rödiger, Mischa Schirmer, Ylva Schuberth, Elisabetta Semboloni, Sherry Suyu, Ismael Tereno, Peter Watts, Donate Weghorn, Benjamin Winkel, Olaf Wucknitz, and Yuying Zhang for many interesting discussions and the excellent atmosphere in the group. I am also grateful to the HOLIGRAIL team members for taking up the idea of lens monitoring at Hoher List and investing a lot of their time

into this project. Special thanks go to Kathy Schrüfer, Christina Stein-Schmitz, and Elisabeth Danne for a lot of help with administrative matters, and Olli Cordes, Günther Lay, Ole Marggraf, and Uwe Naß for computer administration.

This work is based on observations made with the NASA/ESA Hubble Space Telescope, obtained from the data archives at the Space Telescope European Coordinating Facility and the Space Telescope Science Institute, which is operated by the Association of Universities for Research in Astronomy, Inc., under NASA contract NAS 5-26555. This research made extensive use of software packages developed by TERAPIX and the Leiden Data Analysis Center, as well as the NASA ADS service and the photometric redshifts provided by the GOODS-MUSIC sample (Grazian et al. 2006) and the COSMOS team (Mobasher et al. 2007). It was partially conducted on the SLAC computing farm and the AIfA computer cluster.

I am very grateful to the Studienstiftung des deutschen Volkes (German National Merit Foundation) for a scholarship and mentoring during this PhD project. I acknowledge support from Bonn University through the Research Group "Dark Matter & Dark Energy: The future of the Universe" and the Deutsche Forschungsgemeinschaft through SFB/Transregio 33 "The Dark Universe". I want to thank JPL/NASA for travel support for the "2007 STEP/Weak Lensing from Space" Workshop and acknowledge support by the International Max Planck Research School for Radio and Infrared Astronomy. This work was supported by the German Ministry for Science and Education (BMBF) through DESY under project 05AV5PDA/3, and by the Deutsche Forschungsgemeinschaft under projects SCHN 342/6–1, ER 327/2–1.

Finally, I want thank my parents for their encouragement and Evelyn for her love and patience in the final phase of this PhD project.